Universidad Autónoma de Madrid

Frontiers in Plasmonics: Transformation Optics, Magnetic Plasmons, Brownian Ratchets and Quantum Phenomena.

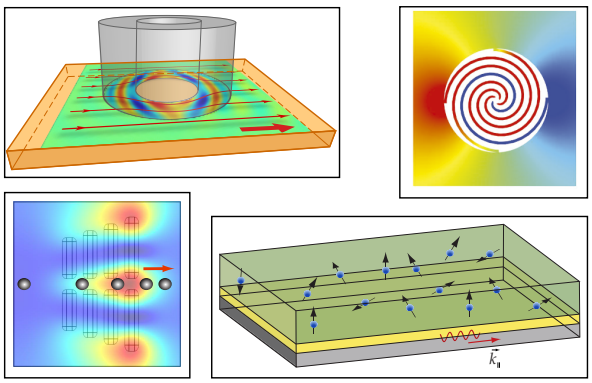

Paloma Arroyo Huidobro

Universidad Autónoma de Madrid

Departamento de Física Teórica de la Materia Condensada

Condensed Matter Physics Center (IFIMAC)

Tesis doctoral dirigida por:

Francisco José García Vidal

Madrid, Noviembre de 2013

Contents

Abstract

English

This Thesis is devoted to various topics that lay at the frontier of the Plasmonics research field. All of them are based on the remarkable properties featured by surface plasmons. Surface plasmons are surface electromagnetic waves supported by metallic nanostructures that are capable of concentrating the electromagnetic fields at scales beyond the diffraction limit.

First, we deal with the potentiality of propagating surface plasmons as a new route for devising photonic circuits, where the subwavelength field confinement could lead to more compact devices. For this purpose, we apply the theoretical framework of Transformation Optics to mold the flow of plasmons through the design of plasmonic elements. We present a number of potential devices and perform a detailed analysis of their performances.

Next, we consider the transfer of the properties featured by surface plasmons to lower frequency regimes based on the concept of *spoof* plasmons. In particular, we demonstrate the emergence of localized surface plasmon modes of geometrical origin in metallic particles whose surface is periodically textured at a subwavelenght scale. We study in detail a novel magnetic mode appearing in such structures, which features subwavelength confinement and has no analogue in conventional particle plasmonics. This magnetic localized surface plasmon has been experimentally demonstrated, proving the predictive value of our theory.

Next, we present a work framed within the area of plasmonic-based optical trapping, where the field enhancement localized at metallic antennas is used to trap nanoscopic objects with subwavelength control. In particular, we propose a Brownian ratchet based on an array of optical antennas. This device goes beyond conventional nano-optical trapping, as it enables not only the trapping of dielectric or biological targets at subwavelength volumes but also their directed transport over long distances.

Abstract

Finally, we address the topic quantum emitters interacting with the electromagnetic modes supported by flat plasmonic structures. The subwavelength confinement of the fields enhances the interaction strength between photons and quantum emitters. By means of an appropriate quantum formalism we treat the different regimes that emerge in these systems. We show that an individual quantum emitter placed in the close vicinity of metal/dielectric interfaces may undergo reversible dynamics. We also demonstrate that the coupling between two distant emitters can be mediated by a plasmonic mode, in particular, the surface plasmons propagating along graphene sheets and ribbons. In addition, we study the regime where an ensemble of quantum emitters coherently exchanges energy with a surface plasmon propagating along a metal/dielectric interface.

Castellano

Esta tesis está dedicada a cuatro temas que se encuentran en la frontera del campo de investigación denominado Plasmónica. Los distintos temas que hemos considerado se basan en las propiedades características de los plasmones de superficie. Los plasmones de superficie son ondas electromagnéticas de superficie confinadas en nano-estructuras metálicas, capaces de confinar el campo electromagnético a escalas nanométricas, más allá del límite fundamental de la difracción.

En primer lugar, hemos considerado la potencialidad de los plasmones de superficie para generar una nueva ruta hacia el diseño de circuitos fotónicos. Con este objetivo, aplicamos el marco teórico de la Óptica de Transformación al diseño de elementos plasmónicos que controlen la propagación de plasmones de superficie en la interfaz entre un metal y un dieléctrico. En concreto, presentamos una serie de dispositivos con distintas funcionalidades, haciendo un análisis detallado de sus respectivos funcionamientos.

En segundo lugar, basándonos en el concepto de plasmones *spoof*, estudiamos la posibilidad de transferir las propiedades características de los plasmones de superficie a regímenes de frecuencia más bajos. En particular, demostramos la emergencia de un plasmón superficial localizado de carácter magnético dipolar que no tiene analogía en los plasmones localizados canónicos que aparecen a frecuencias más altas. Su origen es geométrico y aparece en partículas metálicas cuya superficie está corrugada periódicamente a escalas menores que la longitud de onda relevante. Estudiamos este modo magnético en detalle, viendo que presenta confinamiento a escalas menores que la longitud de onda. Además, este modo magnético ha sido experimentalmente verificado, lo que prueba el valor predictivo de nuestra teoría.

Por otra parte, presentamos una propuesta enmarcada en el campo del control de objetos nanoscópicos mediante estructuras plasmónicas, que se basa en los altos campos electromagnéticos localizados en antenas metálicas. Nuestra propuesta va más allá de los dispositivos convencionales para atrapar partículas de tamaño nanoscópico, ya que permite no sólo atrapar objetos sino también su transporte a lo largo de distancias largas comparadas con su tamaño. En concreto, este concepto se puede aplicar al control de partículas dieléctricas o incluso objetos biológicos.

Finalmente, estudiamos la interacción entre emisores cuánticos y los modos electromagnéticos presentes en estructuras plasmónicas. El confinamiento de los campos en escalas menores que la longitud de onda incrementa el acoplo entre los emisores cuánticos y los fotones. A través del formalismo cuántico apropiado, estudiamos los distintos regímenes que aparecen en estos sistemas. Mostramos que un sólo emisor localizado en

las cercanías de una superficie metálica puede experimentar una dinámica reversible. También probamos que el acoplo entre dos emisores distantes puede mediarse a través de un modo plasmónico, en particular, los plasmones de superficie que se propagan a través de láminas y tiras de grafeno. Además, estudiamos el acoplo coherente de energía entre una colección de emisores cuánticos y el plasmón que se propaga a través de una superficie metálica.

List of acronyms

This is a list of the acronyms used in the text (in alphabetical order).

1D	One dimension
2D	Two dimensions
3D	Three dimensions
ACS	Absorption cross section
EM	Electromagnetic
ECS	Extinction cross section
FEM	Finite Element Method
IR	Infra-red
LRSPP	Long range surface plasmon polariton
LSPs	Localized surface plasmons
MD	Molecular dynamics
ME	Modal Expansion
NV	Nitrogen-vacancy
PEC	Perfect Electrical Conductor
PMMA	Poly-methyl methacrylate
PS	Polystere
QD	Quantum dot
QE	Quantum emitter
QED	Quantum Electrodynamics
SC	Strong coupling
SCS	Scattering cross section

SPs	Surface plasmons
SPPs	Surface plasmon polaritons
SRSPP	Short range surface plasmon polariton
RF	Radio frequency
TO	Transformation Optics
UV	Ultra-violet
WC	Weak coupling

Chapter 1

General Introduction

This Thesis is devoted to four different topics that lay at the frontier of Plasmonics. The research area of Plasmonics deals with the confinement of light at dimensions much smaller than the wavelength of radiation, which allows to bring optics to the nanoscale. This is possible owing to the remarkable properties featured by *surface plasmons* (SPs), a collective excitation of the conduction electrons in a metal. An important aspect of SPs is that, by confining the electromagnetic (EM) field at the nanoscale, they overcome the diffraction limit, according to which the mode volumes of optical modes can not be smaller than $\lambda_0/(2n)$, where λ_0 is the wavelength of radiation and n is the refractive index of the medium where light propagates [1]. This fact has given rise to an intense and multidisciplinary scientific activity in the field during the last years. The prospects of Plasmonics include a series of topics as diverse as surface-enhanced spectroscopy for biosensing [2], novel devices and integrated circuits [3], near field microscopies [4] or solar energy harvesting [5].

Throughout this Thesis we address four subjects that have attracted a great attention during the course of this research work. First, we apply the theoretical framework of Transformation Optics for controlling the flow of SPs at metal surfaces, which enables the development of novel photonic circuits. Next, we explore the emergence of magnetic modes in metallic structures that are the analogues of plasmonic structures at lower frequencies. Furthermore, we consider the optical trapping and manipulation of nanoscopic objects provided by the greatly enhanced EM field close to plasmonic antennas. Finally, we study light-matter interaction in nanoscale plasmonic systems, where the sub-diffraction limited confinement of the EM fields enhances the interaction strength between photons and emitters.

In the following we give brief introductions to the different areas of Plasmonics that

are covered in this Thesis. We start by introducing the properties of SPs in Section 1.1, first giving special attention to the SPs supported by metal structures and then considering those propagating along graphene sheets. Next, in Section 1.2 we review the recently developed fields of Transformation Optics and Metamaterials. In Section 1.3 we present the concept of spoof plasmons, that allows the transfer of all the exciting prospects of Plasmonics from the optical regime to lower frequencies. A different branch of Plasmonics is considered in Section 1.4, where we deal with the trapping of nano-objects by means of metallic structures. Finally, in Section 1.5 we review the interest of Plasmonics as a platform for light-matter interaction.

1.1 Surface Plasmons

Here we first present a brief summary on the main properties of SPs in metallic structures, considering metal/dielectric interfaces and thin metal films as well as metal particles of closed surfaces. Next, we introduce the topic of graphene plasmonics, in which the material supporting SPs is a graphene sheet.

SPs arise from the interaction between EM fields and the conduction electrons in a metal [6]. Conduction electrons can be driven by an EM field, which causes them to collectively oscillate. These charge density oscillations can be sustained within the bulk of a metal as well as confined at the interface between a metal and a dielectric medium, in each case at a distinct resonance frequency. Spatially confined plasmon modes at metal/dielectric interfaces, i.e., SPs, are the object of study of the field of Plasmonics. The fact that SPs are collective excitations of photons and electrons gives rise to a major characteristic: the subwavelength nature of SPs enables a strong localization and enhancement of the EM fields in the vicinity of metal/dielectric interfaces.

As we will show below, two kinds of SPs exist, depending on the geometry of the interface under consideration. First, flat metal surfaces support the propagation of *surface plasmon polaritons* (SPPs), EM modes that propagate along the surface while featuring a subwavelength confinement to it. Many research efforts have been devoted to the implementation of SPP-based photonics [7], as metal structures can be designed to efficiently guide SPPs, by for instance, confining them in the transverse direction in one-dimensional (1D) plasmonic waveguides [8, 9]. Moreover, SPPs offer a bridge between photonics and electronics, opening up the possibility of achieving more compact devices [10]. On the other hand, metal particles of dimensions smaller than the wavelength sustain confined SP modes at optical frequencies, the so-called *localized surface plasmons* (LSPs).

The existence of SPs (both SPPs and LSPs) is a characteristic feature of the EM response of metals. The optical response can be characterized by means of the electric permittivity, $\epsilon(\omega)$. In the case of metals, $\epsilon(\omega)$ depends strongly on the frequency of light. The Drude theory, which considers a metal as a background of fixed core ions plus a free electron gas, appropriately models the fact that conduction electrons are nearly free to move within the bulk. Within this model the electric permittivity can be written as (see, for instance, Ref. [11]),

$$\epsilon(\omega) = \epsilon_\infty - \frac{\omega_p^2}{\omega^2 + i\gamma\omega}, \tag{1.1}$$

where ω_p is the plasma frequency, γ is the damping constant of electrons and ϵ_∞ is a high frequency offset. The bulk plasma frequency is characteristic of each metal and reads as,

$$\omega_p = \sqrt{\frac{ne^2}{m_e\epsilon_0}}, \tag{1.2}$$

with n being the electron density, e and m_e the electron charge and effective mass, and ϵ_0 the vacuum permittivity. For most metals, ω_p lies in the ultraviolet (UV) regime, $\omega_p \sim 10^{16}$ Hz (or, equivalently, a few eV). The real and imaginary parts of the electric permittivity for silver are plotted in Fig. 1.1 [panels (a) and (b), respectively]. The Drude model (Eq. 1.1) with parameters $\hbar\omega_p = 9$ eV, $\hbar\gamma = 0.07$ eV and $\epsilon_\infty = 4.6$ [12] is plotted as a solid black line, while the dashed lines correspond to two sets of experimental data (Johson and Christy [13] and Palik [14]). Below the plasma frequency, precisely for $\omega < \omega_p/\sqrt{\epsilon_\infty}$, the real part of $\epsilon(\omega)$ is negative, a fact that is well reproduced by the Drude model [see inset in panel (a)], and its imaginary part takes a non-zero value, reflecting the relaxation time of electrons in the lattice. On the other hand, the Drude model fails to give an accurate description at frequencies $\omega \gtrsim \omega_p/\sqrt{\epsilon_\infty}$, where the imaginary part of $\epsilon(\omega)$ increases. The reason for this is that this model neglects interband transitions. At high frequencies, photons can promote bound electrons to the conduction band. These transitions can be taken into account by adding Lorentz terms to Eq. 1.1, as follows

$$\epsilon(\omega) = \epsilon_\infty - \frac{\omega_p^2}{\omega^2 + i\gamma\omega} - \frac{\tilde{\omega}_p^2}{\omega^2 - \omega_0^2 + i\gamma_0,\omega}, \tag{1.3}$$

with $\tilde{\omega}_p$, ω_0 and γ_0 being the plasma frequency, the oscillation frequency and the damping characteristic of bound electrons, respectively. As shown in Fig. 1.1, the Drude-Lorentz model (solid blue line) yields a more accurate modeling of $\epsilon(\omega)$ at high frequencies. The characteristics of the optical response of metals are responsible for the existence of SPs.

Let us first focus our attention on the propagating SP modes, i.e., SPPs. These are bound EM modes that propagate along a metal/dielectric interface. They are p-polarized

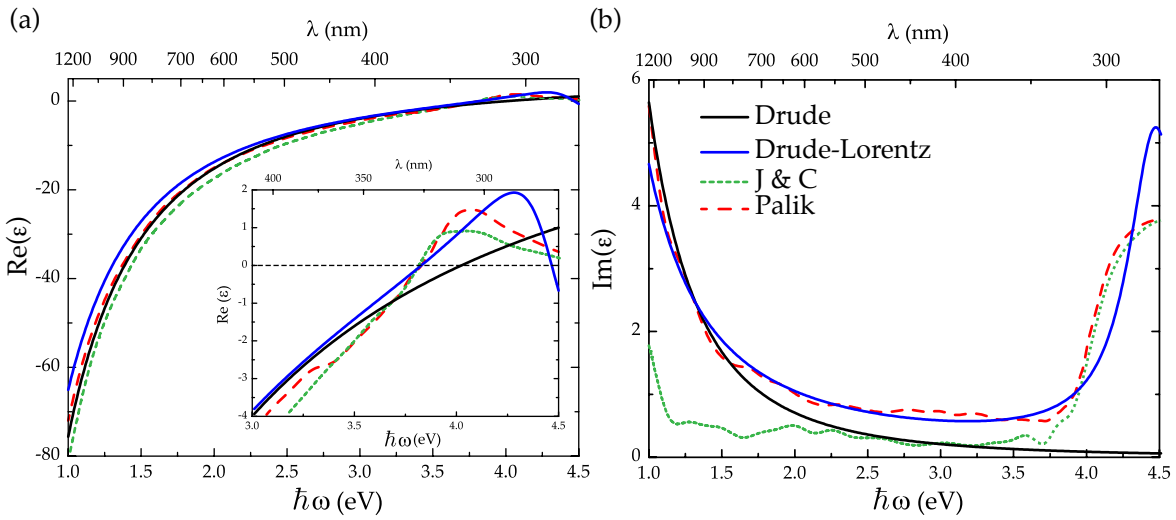

Figure 1.1: Optical response of Silver. Real (a) and imaginary (b) parts of the electric permittivity, $\epsilon(\omega)$, for silver in the optical regime. Two sets of experimental data are plotted (Johson and Christy [13] and Palik [14]) together with the Drude model, given by Eq. 1.1, and the Drude-Lorentz model, by Eq. 1.3. Note that other noble metals, such as gold, feature similar properties.

(magnetic field component lying in the plane of the interface) and their field intensity decays evanescently in the direction perpendicular to the interface. A sketch of a SPP propagating through the interface separating a metal and a dielectric (permittivities $\epsilon(\omega)$ and ϵ_d, respectively) is shown in Fig. 1.2 (a). SPPs are bound solutions of Maxwell's equations,

$$\nabla \times \nabla \times \mathbf{E}(\mathbf{r},\omega) - \frac{\omega^2}{c^2}\epsilon(\mathbf{r},\omega)\mathbf{E}(\mathbf{r},\omega) = 0\,. \tag{1.4}$$

At each side of the interface, $j = 1$ and $j = 2$, the electric field of p-polarized waves can be written as,

$$\mathbf{E}_j = \begin{pmatrix} E_{j,x} \\ 0 \\ E_{j,z} \end{pmatrix} e^{i(k_x x + k_{j,z} z - \omega t)}\,, \tag{1.5}$$

where k_x is the wave vector component along the propagation direction and $k_{z,j}$ satisfies,

$$k_{z,j} = \sqrt{\epsilon_j(\omega)k_0^2 - k_x^2}\,, \tag{1.6}$$

with $k_0 = \omega/c$ being the free space wavenumber. The dispersion relation of SPPs can be derived by imposing the appropriate boundary conditions for the continuity of the EM

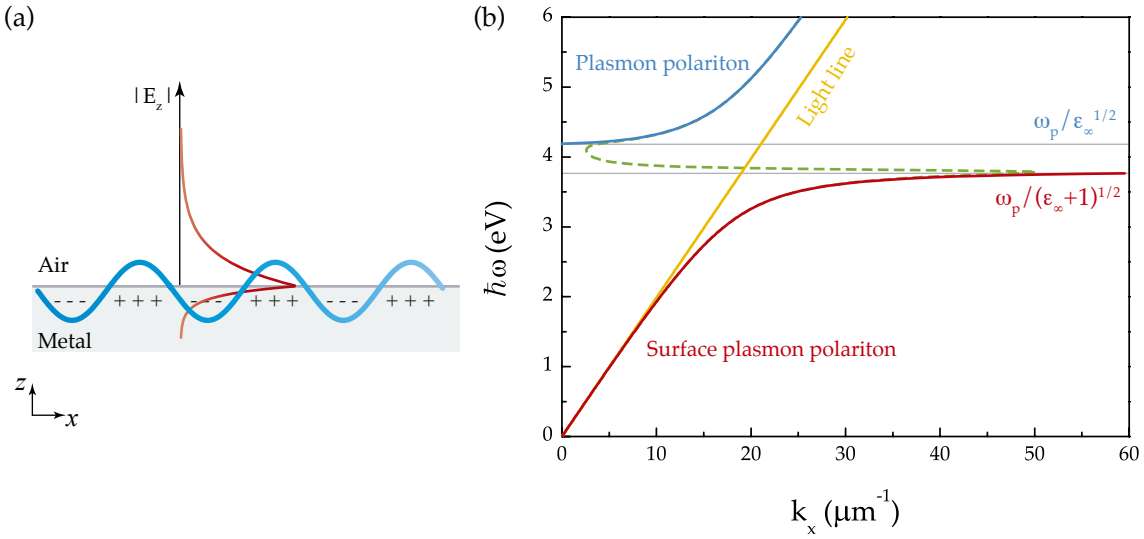

Figure 1.2: SPPs propagating along a metal/dielectric (air) interface. (a) SPPs have a mixed nature between light and charges. (b) Dispersion relation (energy versus parallel momentum) for the EM modes supported by a silver/air interface. We take the Drude model for the permittivity of Silver, with the same parameters as in Fig. 1.1, and plot two cases: a lossless ($\gamma = 0$, solid lines) and a lossy metal (dashed line). The light line, given by $\omega = ck_x$, is also given. The SPP branch lies below the light line and approaches the SP resonance frequency, $\omega_{sp} = \omega_p/\sqrt{\epsilon_\infty + 1}$. The plasmon polariton branch sets off at the bulk plasmon resonance frequency, $\omega_p/\sqrt{\epsilon_\infty}$, approaches the light line from above as the frequency increases.

field at the interface, yielding,

$$k_x(\omega) = k_0\sqrt{\frac{\epsilon(\omega)\epsilon_d}{\epsilon(\omega)+\epsilon_d}}\,, \tag{1.7}$$

where we have made the substitution $\epsilon_1(\omega) = \epsilon(\omega)$ and $\epsilon_2(\omega) = \epsilon_d$. SPP modes propagating along the interface have a real k_x, with $k_x > k_0$, and imaginary $k_{j,z}$, i.e., they are evanescent modes.

The dispersion relation given by Eq. 1.7 is plotted in Fig. 1.2 (b) for a silver/air interface. We take $\epsilon_d = 1$ and the Drude model for silver (Eq. 1.1). According to Eq. 1.7, and assuming a lossless metal, $\gamma = 0$, frequencies below $\omega_{sp} = \omega_p/\sqrt{\epsilon_\infty + 1}$ yield $k_x > k_0$, i.e., the mode lies below the light line ($\omega = ck_x$, plotted as yellow line in the figure). This is the SPP branch (see the red line). At low frequencies, $\omega \ll \omega_{sp}$, $|\epsilon(\omega)| \gg 1$ and $k_x \approx k_0$, meaning that the SPP is poorly confined to the metal. As the frequency increases, $|\epsilon(\omega)|$ decreases and $k_x \gtrsim k_0$, leading to an increase in the binding of the mode to the interface: the confinement of the SPP in the perpendicular direction reaches subwavelength values.

Finally, as the frequency approaches the SP resonance, ω_{sp}, the parallel momentum k_x increases asymptotically. This asymptote is avoided when a lossy metal is considered ($\gamma \neq 0$, dashed line). In this case, the SPP branch experiences a back-bending and joins the plasmon polariton branch above the light line (blue line). When losses are taken into account, the parallel wave vector of the SPP, k_x, acquires an imaginary part that imposes a finite propagation length for the SPP,

$$L_p = \frac{1}{\mathrm{Im}(k_x)}. \tag{1.8}$$

As the frequency increases, SPPs become more confined and absorption in the metal increases, thereby reducing the propagation length. Thus, there is a trade-off between confinement and propagation [6]. In addition, the fact that for SPPs $k_x > k_0$ means that they can not be excited directly with free space photons. Instead, the momentum mismatch has to be overcome by, for instance, patterning a grating in the metal surface. On the other hand, in the Otto [15] or Kretschmann [16] configurations the extra momentum is provided by another dielectric medium of refractive index n, that lowers the light line to $\omega = ck_x/n$, thus crossing the SPP dispersion. Alternatively, near field probes or quantum emitters, such as fluorescent molecules, can also be used to excite SPPs when placed in the close proximity of the interface, as they couple to all available parallel momenta.

In the above discussion we have implicitly assumed that the metal side of the interface is a semi-infinite medium. This is not generally the case in experiments, where thin metal films are usually employed. It is therefore interesting to consider the SPPs propagating along dielectric/metal/dielectric systems (see Fig. 1.3) [17]. In this case, imposing the boundary conditions leads to the following implicit equation for the dispersion relation of the SPPs,

$$1 + r_{1,2} r_{2,3} e^{2ik_{2,z}h} = 0\,, \tag{1.9}$$

where h is the thickness of the metal film and the subindexes $1, 2, 3$ refer to the upper dielectric, the metal and the lower dielectric, respectively. In addition, r_{ij} are the Fresnel coefficients for a single interface,

$$r_{ij} = \frac{\epsilon_i(\omega) k_{j,z} - \epsilon_j(\omega) k_{i,z}}{\epsilon_i(\omega) k_{j,z} + \epsilon_j(\omega) k_{i,z}}\,. \tag{1.10}$$

Assuming a symmetric configuration, where both dielectrics have permittivities $\epsilon = 1$, the wave vectors perpendicular to the interfaces are $k_z = \sqrt{k_0^2 - k_x^2}$ in the dielectric

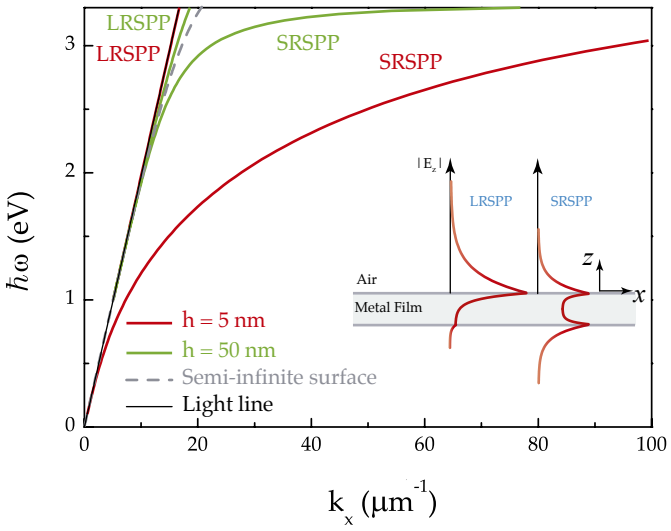

Figure 1.3: SPPs propagating along a thin metal film. The plot shows the dispersion relation of the LSRSPP and SRSPP for metal films of thicknesses $h = 5$ nm and $h = 50$ nm. The dispersion relation of a semi-infinite surface and the light line are also shown. The field distributions for the two modes are sketched in the inset, showing how the SRSPP is tightly confined to the film whereas the LRSPP is more delocalized. This justifies the fact that the LRSPP propagates longer distances than the SRSPP.

media and $k_{2,z} = \sqrt{\epsilon(\omega)k_0^2 - k_x^2}$ in the metal ($k_{z,m}$). Equation 1.9 has the following two solutions,

$$\epsilon(\omega)k_z + k_{z,m}\tanh\left(k_{z,m}h/2\right) = 0\,, \tag{1.11}$$

$$\epsilon(\omega)k_z + k_{z,m}\mathrm{cotanh}\left(k_{z,m}h/2\right) = 0\,. \tag{1.12}$$

Thus, thin metal films support the propagation of two modes, as shown in Fig. 1.3. When compared to the dispersion relation of the semi-infinite surface considered above, one of the modes lies closer to the light line while the other lies at higher wave vectors. The first one, which is the solution of the first equation above, is the long range SPP (LRSPP). This mode lies very close to the light line, thus being poorly confined to the film. On the other hand, the mode retrieved from the second equation is the short range SPP (SRSPP), which displays very large wave vectors, $k_x \gg k_0$. This means that this mode is greatly confined to the metal film. Indeed, the confinement increases when decreasing the thickness of the film (compare the lines for $h = 5$ nm and $h = 50$ nm). Increasing the confinement implies increasing the losses, and the propagation length of the SRSPPs is very short (hence the naming). Finally, for $h \gtrsim 200$ nm, the LRSPP and

SRSPP converge to the dispersion relation of the semi-infinite surface.

A different kind of SPs arises in metal particles with closed surfaces [18]. When light impinges on a metallic particle of dimensions much smaller than the wavelength of radiation, the electron gas in the metal gets polarized, with polarization charges localized at the surface. As a consequence, a restoring force emerges and originates a plasmon oscillation that is confined at the surface of the metal nanoparticle. This resonance is the LSP [19], and, differently from SPPs, can be directly excited by light [see Fig. 1.4 (a)]. An insightful model for understanding the LSP resonance is that of a Rayleigh spherical particle (dimensions $\ll$ wavelength of the incident light). In the quasi-static limit, the optical response of a subwavelength particle is determined by its polarizability [1],

$$\alpha = 4\pi R^3 \frac{\epsilon_m(\omega) - \epsilon_d}{\epsilon_m(\omega) + 2\epsilon_d}\,, \tag{1.13}$$

with R being the radius of the particle and ϵ_d being the electric permittivity of the surrounding medium. From the above expression, it is clear that the polarizability is resonant under the condition $\epsilon_m(\omega) + 2\epsilon_d = 0$, which for a lossless Drude model results in the following resonance frequency

$$\omega_{LSP} = \frac{\omega_p}{\sqrt{\epsilon_\infty + 2\epsilon_d}}\,. \tag{1.14}$$

The resonance in the polarizability implies an enhancement of the dipolar EM field generated by the metal particle. In general, the resonance frequency of LSPs is determined by the shape, size and optical properties of the metal nanoparticle.

Metal nanoparticles supporting LSPs have enabled the development of optical antennas. These are the nanoscale analogue of classical antennas working in the microwave and radio frequency (RF) regimes. They are designed to "efficiently convert free-propagating optical radiation to localized energy, and vice-versa" [20]. Thus, optical antennas enhance the interaction between nanoscale objects and propagating EM fields. As depicted in Fig. 1.4 (b), a metal nanoparticle (or nanostructures of various geometries) plays the role of the optical antenna [21–27], while the nanoscale object may be a quantum emitter or absorber, such as a molecule or a quantum dot [28, 29]. The working principle of optical antennas is possible owing to the large EM field enhancements confined to subwavelength volumes generated by the dipolar LSPs supported by metal nanoparticles. Hence, the finite permittivity of metals in the optical regime has a fundamental implication in the design of optical antennas. As we have seen, LSPs resonances are strongly dependent on the material. Therefore, classical antennas can not be simply scaled down to nanometer sizes to work as optical antennas. The size, shape and EM properties need to be taken

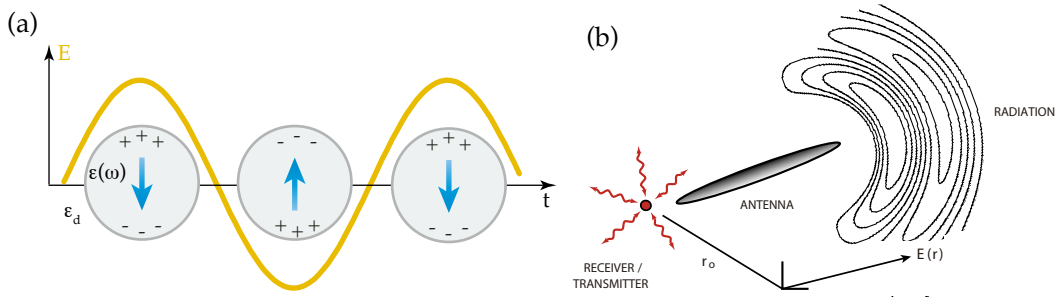

Figure 1.4: LSPs and optical antennas. (a) An EM field excites the LSP resonance in a metal nanoparticle. (b) A metal nanostructure plays the role of an optical antenna, that enables the interaction between a nanoscale emitter and radiation in free space. Reprinted from [20].

into account when designing optical antennas. For instance, a dipolar optical antenna resonant at $\lambda_0/2$, with λ_0 being the free space wavelength, requires a nanorod of length $\lambda_{\text{eff}}/2$, where λ_{eff} is the effective wavelength seen by the nanorod. For conventional metals, λ_{eff} is usually a factor of 2 to 6 smaller than λ_0, which yields length for the nanorod that is much smaller than $\lambda_0/2$ [30]. Other than the fundamental interest of probing plasmonic resonances [31], optical antennas are promising for a variety of applications ranging from photodetection, light emission and sensing to nano-imaging [32].

Other than metals, graphene [33] also supports SPs. This atomic-thick layer of carbon atoms arranged in a honeycomb lattice features unique optical [34] and optoelectronic properties [35]. In particular, it absorbs $\pi\alpha_0 \sim 2.3\%$ of visible light, with $\alpha_0 = e^2c/\hbar$ being the fine structure constant. Moreover, electrons in graphene display a linear dispersion relation, known as Dirac cone [see inset panel of Fig. 1.5 (a)], and have very high mobilities. In addition, the conductivity of this two-dimensional (2D) material is very sensitive to external fields, implying that the optoelectronic properties of graphene are highly tunable. In particular, the conductivity, σ, depends on the frequency, the temperature, T, and the chemical potential of the sheet, μ. The conductivity can be written as the sum of intraband and interband contributions obtained in the random phase approximation [36, 37],

$$\sigma = \sigma_{\text{intra}} + \sigma_{\text{inter}}, \tag{1.15}$$

as follows,

$$\sigma_{\text{intra}} = \frac{2ie^2t}{\hbar\pi\left[\Omega + i\gamma\right]} \ln\left[2\cosh\left(\frac{1}{2t}\right)\right], \tag{1.16}$$

$$\sigma_{\text{inter}} = \frac{e^2t}{4\hbar}\left[\frac{1}{2} + \frac{1}{\pi}\arctan\left(\frac{\Omega-2}{2t}\right) - \frac{i}{2\pi}\ln\frac{(\Omega+2)^2}{(\Omega-2)^2+(2t)^2}\right]. \tag{1.17}$$

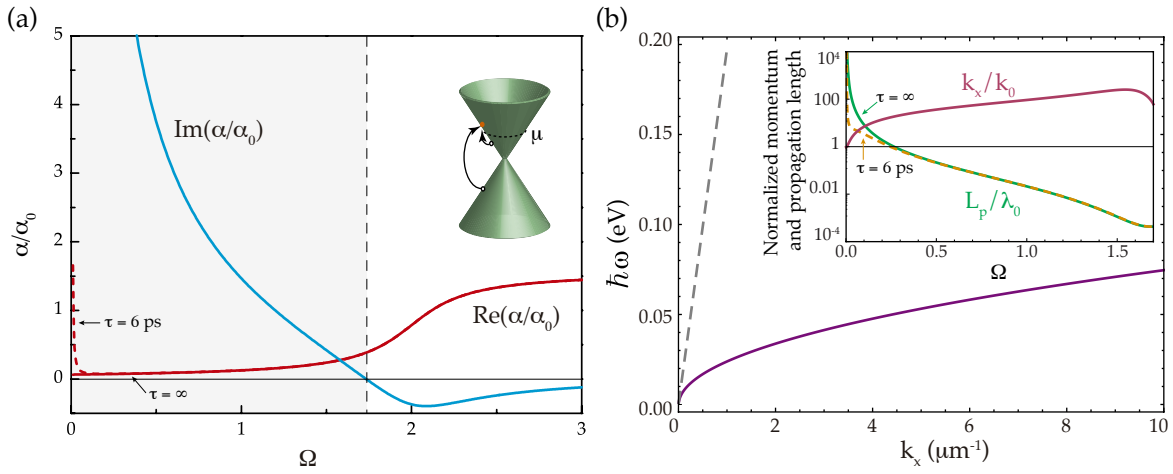

Figure 1.5: Graphene plasmonics. (a) Conductivity of a graphene sheet at $T = 300$ K and $\mu = 0.2$ eV. The real and imaginary parts of $\alpha/\alpha_0 = 2\pi\hbar\sigma/e^2$are shown. At low frequencies, the real part of the conductivity depends strongly on the electron's scattering time: the solid line corresponds to the maximum theoretical mobility of the carriers, $m = 2 \times 10^6$ cm^2/(V·s), while the dashed line corresponds to a realistic value of the mobility, $m = 2 \times 10^5$ cm^2/(V·s). (b) SPPs dispersion relation for $T = 300$ K, $\mu = 0.2$ eV and the maximum theoretical mobility. The inset shows the normalized SPP wave vector, Re$[k_x]/k_0$, and propagation length, L_p/λ_0, with $\lambda_0 = 2\pi c/\omega$. The solid and dashed curves show the propagation lenght for infinite and finite scattering time, respectively.

Here, we have used a normalized frequency, $\Omega = \hbar\omega/\mu$, and temperature $t = k_B T/\mu$. In addition, we have introduced a damping term, $\gamma = \hbar/(\mu\tau)$, where $\tau = m\mu/v_F^2$ is the carriers' scattering time (m is the mobility and v_F the Fermi velocity). The frequency dependence of the conductivity is displayed in Fig. 1.5 (a) for $T = 300$ K and $\mu = 0.2$ eV. The quantity $\alpha \equiv 2\pi\sigma/c$ is plotted in units of α_0. At low frequencies, $\hbar\omega/\mu \ll 1$, the main contributions to the conductivity are intraband transitions, and at higher frequencies, $\hbar\omega/\mu \gtrsim 1$, interband transitions dominate. Introducing a finite scattering time for the electrons results in a larger real part of $\sigma(\omega)$ only at very low frequencies (compare solid and dashed red lines), whereas at high frequencies losses depend mainly on temperature. In the limit of very low temperature and very high mobilities, Re$[\sigma(\omega)] \to 0$.

Similarly to metal surfaces, and despite being an atomically thick material, graphene also supports the propagation of SPPs. Because of the already discussed electronic properties of graphene, it is a zero-gap semiconductor. Thereby, a finite chemical potential, $\mu \neq 0$, provides a conduction band for graphene, which enables the existence of SPPs. Interestingly, μ can be controlled through, for instance, a gate voltage. These EM modes

bound to a graphene sheet were first studied theoretically in Refs. [38–42]. In experiments, graphene SPPs have been observed through infra-red (IR) spectroscopy [43] and also imaged by means of near field probes [44, 45]. The properties of SPPs propagating along a graphene sheet are determined by its conductivity (Eqs. 1.16 and 1.17). The SPP dispersion relation can be obtained by taking the zero-thickness limit in the dispersion relation of thin metal films studied in the previous Subsection. Taking the limit $k_{z,m}h \ll 1$ in Eqs. 1.12 and 1.11, we see that only the SRSPP survives, and by approximating $\mathrm{cotanh}(x) \approx 1/x$, we have

$$k_x = k_0\sqrt{1 - \frac{ic}{\epsilon\omega h}} = k_0\sqrt{1 - \frac{1}{\alpha^2}}, \tag{1.18}$$

where we have made use of the relationship between the conductivity and the electric permittivity of a 2D material, $\epsilon = 2\pi i\sigma/(\omega h)$. Bound surface waves exist only below a critical frequency, $\mathrm{Im}[\sigma(\omega)] > 0$, i.e., $\hbar\omega \approx 2\mu$. This region is pointed at in Fig. 1.5 (a) by the light grey background. Panel (b) displays the SPP dispersion relation at $\mu = 0.2$ eV and $T = 300$ K. This plot demonstrates that SPPs in graphene are tightly confined to the sheet, as it can be also seen in the inset panel, where the normalized SPP momentum, $\mathrm{Re}[k_x]/k_0$ is plotted. The inset panel also shows that including a finite scattering time results in lower SPP propagation lengths at low frequencies. Compared to metal surfaces, graphene features SPPs of appreciable propagation length at lower frequencies, since phonon excitation greatly reduces the propagation length close to optical frequencies.

The properties of SPPs in graphene have attracted great attention. The reason for this is that it may be an alternative for many of the functionalities provided by noble-metal SPPs, with the advantage of being tunable by controlling the chemical potential through, for instance, a gate potential. In particular, the interaction between nanoemitters and SPPs in graphene has been studied, showing a high degree of field confinement, as well as EM energy enhancement, in the vicinity of the sheet [46, 47]. The fluorescence quenching phenomenon in graphene, which takes place when an emitter is very close to the graphene layer, has also been considered theoretically [48, 49] and very recently observed in experiments [50].

1.2 Transformation Optics and Metamaterials

The control and manipulation of the EM fields constitutes a major aim for current technology. The way light propagates in a given medium is determined by Fermat's principle, also known as the principle of *shortest optical path*. According to this principle,

light follows the minimal optical path between two points, the optical path being the integral of the background refractive index, n, along the light trajectory. It turns out that for a spatially varying refractive index, $n(\mathbf{r})$, the shortest optical path is not a straight line, but a curved one. This is the origin of many optical phenomena, such as refraction at an interface, where the refractive index changes abruptly, or the mirage effect in a desert, where the refractive index of air continuously changes due to variations in its density.

Fermat's principle determines light propagation for a given spatial distribution of the refractive index. Conversely, the recently developed field of Transformation Optics (TO) solves the inverse problem: starting from a desired light path, TO provides a recipe for the refractive index distribution needed for light to realize that specific trajectory. This concept is indeed very general and offers us the capability to control light in any desired fashion, opening up the possibility of novel optical effects and devices. TO has emerged as a rapidly growing field thanks to the advent of metamaterials, a novel class of materials whose design flexibility has enabled the experimental realization of proposals raised by this theoretical framework.

Transformation Optics establishes a procedure that provides us with expressions for the EM material parameters, dielectric permittivity and magnetic permeability, that need to be implemented in order to obtain a medium where EM waves propagate along desired trajectories [51, 52]. It is based on the mathematical equivalence between coordinate transformations and EM material parameters. As Maxwell's equations are form-invariant under coordinate transformations, a distorted geometry in an empty space can be interpreted as a medium in a Cartesian flat space [53]. Let us consider Maxwell's equations in an arbitrary space characterized by the coordinate system $\mathbf{x}' = \{x', y', z'\}$ and some general material properties (electric permittivity $\hat{\boldsymbol{\epsilon}}'$ and magnetic permeability $\hat{\boldsymbol{\mu}}'$):

$$\nabla' \times \mathbf{E}' = -i\omega\hat{\boldsymbol{\mu}}'\mathbf{H}' \,, \tag{1.19}$$

$$\nabla' \times \mathbf{H}' = i\omega\hat{\boldsymbol{\epsilon}}'\mathbf{E}' \,. \tag{1.20}$$

This space, which can have any distorted geometry, will be referred to as *virtual space*. If a transformation $\mathbf{x} = \mathbf{x}(\mathbf{x}')$ is performed between this virtual space to a *physical space* $\mathbf{x} = \{x, y, z\}$, the form-invariance of Maxwell's equations provides the following equations in the new coordinate system [54]:

$$\nabla \times \mathbf{E} = -i\omega\hat{\boldsymbol{\mu}}\mathbf{H} \,, \tag{1.21}$$

$$\nabla \times \mathbf{H} = i\omega\hat{\boldsymbol{\epsilon}}\mathbf{E} \,. \tag{1.22}$$

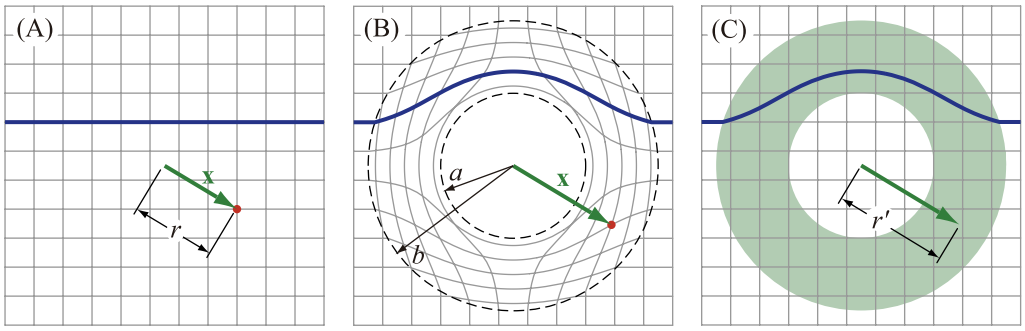

Figure 1.6: Transformation media implement coordinate transformations. Assume that an optical medium performs a coordinate transformation $\mathbf{x} = \mathbf{x}(\mathbf{x}')$ from a straight Cartesian space (a) to a space with a curved grid that excludes a circular region from it (b). When this transformation medium is implemented in an experiment (c), it ensures that light follows the curved trajectories. Since the transformation shrinks the hole in space (b) to a point in space (a), where it is made invisible, the optical medium acts as an invisibility device. Adapted from Ref. [54].

The EM properties in the transformed coordinate system, $\hat{\boldsymbol{\mu}}$ and $\hat{\boldsymbol{\epsilon}}$, can be expressed in terms of the material parameters in the original space as:

$$\hat{\boldsymbol{\epsilon}} = \hat{\boldsymbol{\epsilon}}' \frac{\hat{A}\hat{A}^T}{\det \hat{A}}; \quad \hat{\boldsymbol{\mu}} = \hat{\boldsymbol{\mu}}' \frac{\hat{A}\hat{A}^T}{\det \hat{A}}\,, \tag{1.23}$$

where $\hat{A} = \left(\frac{\partial x^i}{\partial x^{i'}}\right)$ is the Jacobian matrix of the transformation. The equations above define a set of parameters that, when implemented in a medium, ensures that light propagates following the same trajectories as in the original virtual space. In general, these parameters are inhomogeneous anisotropic tensors.

One of the most remarkable devices designed by the TO procedure described above is the invisibility cloak [51, 55]. The purpose of such a cloak is to hide from EM fields a physical object that is placed within a circular region of radius a. The cylindrical cloak is designed by taking a physical space that has a hole of radius a surrounded by a compressed region of radius b and then making a transformation to an undistorted space (virtual space). A sketch of both spaces is shown in Fig. 1.6: panel (a) presents the virtual space, where light propagates in straight lines, while panel (b) renders the physical space. A wave travelling in physical space will follow trajectories that surround the hole so that it appears to have travelled in straight lines as it would in the virtual – undistorted – space. The transformation that connects both spaces is:

$$r(r') = b/(b-a)r' + a\,. \tag{1.24}$$

This transformation squeezes all the rays in region $r < b$ in virtual space to the shell $a < r < b$ in physical space. Since the region $r < a$ lies out of the original space, any object placed within this region will be concealed by the cloak. Based on Eq. 1.23, the following set of EM parameters is retrieved from the transformation above (1.24):

$$\epsilon_r = \mu_r = (r-a)/r,\ \epsilon_\theta = \mu_\theta = r/(r-a),\ \epsilon_z = \mu_z = [b/(b-a)]^2(r-a)/r\,. \qquad (1.25)$$

Finally, to realize the cloak these parameters need to be implemented in an optical medium in real space within a shell $a < r < b$, as shown in Fig. 1.6(c). This optical medium will guide light around the circle $r = a$ as if nothing was there.

The procedure we have described for the design of a cloak is a very general way to devise optical elements with different functionalities. Other than invisibility cloaks, a wide variety of optical effects and devices has been designed by means of TO. Examples include beam shifters, dividers and rotators [56–58], beam bends [59, 60], lossless waveguide bends [61], field concentrators [62] as well as optical black holes [63]. However, the experimental realization of such devices poses non-trivial technical challenges. The electric permittivity and magnetic permeability derived with the TO formalism (see Eq. 1.23), are generally anisotropic and inhomogeneous, and often divergent, as in the case of the invisibility cloak. Hence, such optical parameters need to be tailored to vary spatially and independently throughout the material.

A new class of EM materials has offered a way to overcome the limitations of natural materials: metamaterials are artificial materials whose EM properties are given not by their atomic or chemical composition but rather by their artificial structure [64–70]. By means of subwavelength constituents, that act as artificial "atoms" or "molecules" which respond in a prescribed way to the EM fields, metamaterials can be designed to have properties that do not occur in natural materials. Two structures are usually employed as basic constituents for metamaterials: metallic wires [71], depicted in Fig. 1.7 (a), and split-ring structures [72], shown in Fig. 1.7 (b). Both wires and rings support resonances that yield different and tunable responses to EM fields. An arrangement of such basic structures acts as an homogeneous medium for EM fields as long as their sizes and spacing are much smaller than the wavelength of the EM waves. In the effective medium approximation, the collective response of the subwavelength constituents effectively yields a wide range of values of the electric permittivity, $\hat{\boldsymbol{\epsilon}}$, and the magnetic permeability, $\hat{\boldsymbol{\epsilon}}$. Then, a prescribed EM response can be obtained by an appropriate design of the metamaterial. For instance, while magnetism can only be found in nature at low frequencies below the THz regime, negative index materials with simultaneously negative electric permittivity and magnetic permeability have been realized from the optical

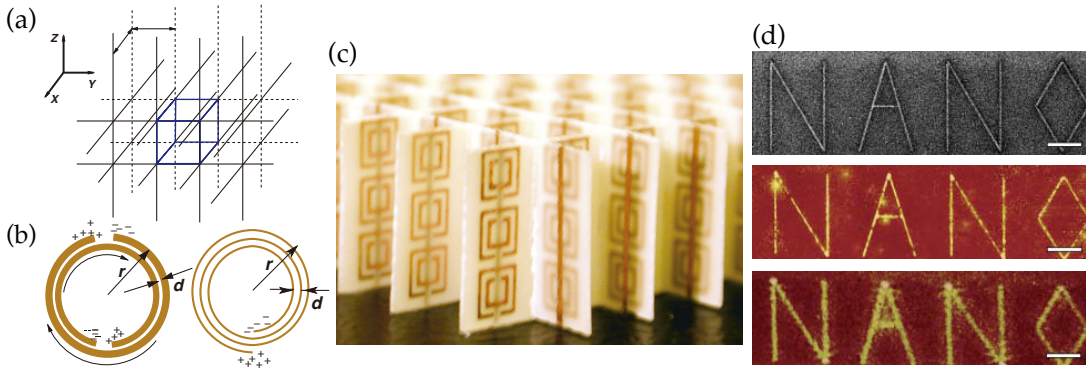

Figure 1.7: Metamaterials are artificially structured materials whose properties are determined by their subwavelength constituents, such as wires and rings. (a) Metallic wires arranged in a 3D lattice behave as an isotropic low frequency plasma [71]. (b) Split-ring resonators (left) display a magnetic moment when a magnetic field induces currents along the metal rings [72]. Swiss rolls (right) act similarly, being resonant at lower frequencies due to their higher capacitance [87]. A combination of such basic structures results in effective electric and magnetic responses. For instance, a material with a negative index of refraction at microwave frequencies was realized by means of copper split-ring resonators (c) arranged in a unit cell of 5 mm. (d) Experimental demonstration of a silver superlens that focuses propagating and evanescent waves owing to its negative index of refraction. (a-c) Reproduced from Ref. [64]. (c) Reprinted from Ref. [73] and (d) from Ref. [79].

to the GHz ranges of the spectrum, see Fig. 1.7 (c) [73–78]. Other interests within the metamaterials research field include the study of sub-diffraction limited imaging, see Fig. 1.7 (d) [79–81] and chirality [82, 83], three-dimensional (3D) metamaterials [84], active metamaterials [85] or planar photonics applications by means of metasurfaces [86].

Since the first works on TO [51, 54, 55], many efforts have been devoted to the design and fabrication of metamaterials [92] in order to enable the experimental realization of TO-based optical devices. The first transformation medium demonstrated in an experiment was an invisibility cloak in the microwave regime [88]. In the experiment, a metamaterial based on split-ring resonators was fabricated to reproduce the set of EM parameters given by Eq. 1.25 for cloaking a metallic cylinder to EM waves in the microwave regime [see Fig. 1.8 (a)]. Instead of implementing the full set of anisotropic parameters, the cloak was designed for one polarization state, such that it is sufficient to consider a reduced set of parameters: ϵ_z, μ_r and μ_θ, only μ_r being inhomogeneous. The experiment showed that the metamaterial cloak significantly reduced the scattering from a metallic cylinder [see Figs. 1.8 (b,c)]. However, the fact that the EM parameters needed

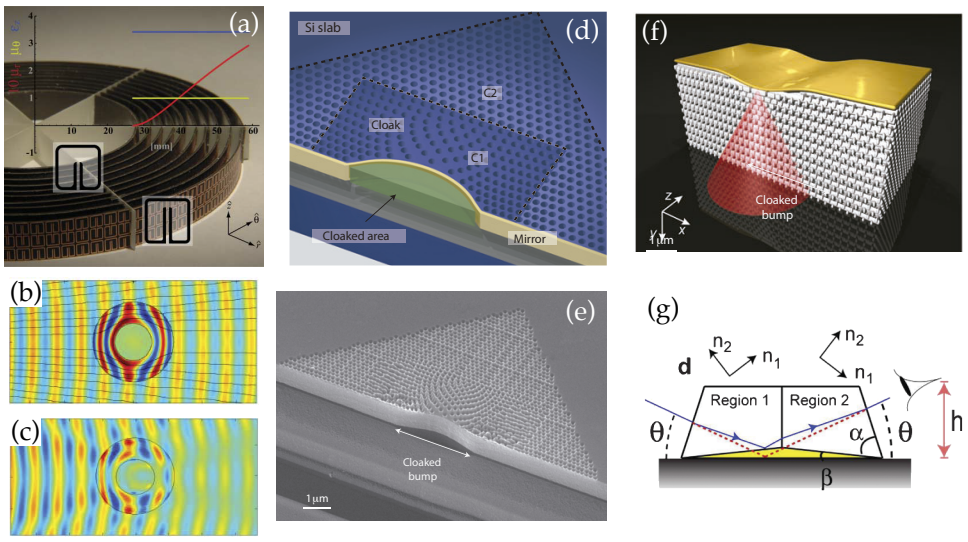

Figure 1.8: Transformation optics for real: experimental optical devices designed by means of TO. (a) Cylindrical invisibility cloak working in the microwave regime [88]. The prescribed material properties, plotted in the background, were realized by a means of a metamaterial made up of split-ring resonators. Simulated (b) and experimental (c) field pattern when the cloak is placed around a metallic cylinder (Reproduced from Ref. [88]). (d) Sketch of a broadband 2D cloak working in the near IR. The transformation medium (cloak area marked as C_1) was fabricated by milling holes with different densities in silicon. (e) Scanning electron microscopy image of the cloak. (d,e) Reprinted from Ref. [89]. (f) Schematic of a 3D cloak working in the near IR, from Ref. [90]. (g) A macroscopic carpet cloak for visible light was realized with calcite, an anisotropic material [91].

for the cloak are anisotropic and singular imply that, even in the reduced parameter set approach, the fabricated metamaterial relies on resonant metallic structures. This is generally the case for TO-based metamaterials, which are highly lossy and operate over a narrow bandwith. Moreover, the building blocks of metamaterials are much smaller than the wavelength of operation, meaning that the unit cell size of a metamaterial working in the visible range should be devised in the nanometer scale. These two factors impose technical challenges on the experimental realization of broad-band TO-devices operating at visible frequencies and with low loss. In the quest for broadband devices at optical frequencies, an alternative approach within the TO framework to the cylindrical invisibility cloak led to a rapid experimental progress. The ground-plane cloak is based on mapping a curved ground-plane into a flat one [93] and yields non-singular and material parameters. The realization of such a cloak in the microwave regime by means of a non-resonant

metamaterial [94] was followed by experiments showing broadband cloaking at near-IR frequencies [89, 95], such as the one shown in Figs. 1.8 (d,e). More recently, the concept of ground-plane cloaking has enabled a 3D broadband cloak at optical wavelengths [90], see Fig. 1.8 (f), and even macroscopic cloaks in the visible regime [91, 96], see Fig. 1.8 (g).

Transformation Optics has also found applications in Plasmonics. Since the TO framework solely relies on Maxwell's equations and coordinate transformations, it is expected to apply to all kinds of EM waves. In particular, TO has been applied to control the flow of the SPPs propagating along a metal-dielectric interface in the context of SPP-based photonics. An example of this approach is schematically depicted in Fig. 1.9 (a,b) for the case of a plasmonic ground-plane cloak. Transformation Plasmonics has paved the way for many different plasmonic functionalities at sub-wavelength scales, as shown in Refs. [97–103]. Besides metals, graphene has also been proposed as a platform for Transformation Plasmonics [104]. In this case, the inhomogeneous EM parameters devised by Transformation Plasmonics are realized by taking advantage of the possibility of tuning graphene's conductivity by varying its chemical potential. The patterning of the conductivity can then be provided in different ways, such as a bias voltage or chemical doping. In Chapter 2, which is devoted to the topic of Transformation Plasmonics as a means of controlling the propagation of SPPs at metal surfaces, we will present our research work within the field [97, 105]. In particular, we first present the TO framework as applied to Plasmonics, showing that the dielectric medium on top of the metal needs to be patterned following the TO recipes. Next, we study the functionality of several plasmonic elements and evaluate the possibility of employing conformal and quasiconformal coordinate transformations for retrieving devices with isotropic material parameters. Additionally, we shortly review the experimental implementation of Transformation Plasmonics.

At a different level, TO has also provided a framework for the design and study of complex plasmonic nanostructures. The procedure is based on mapping the singular geometry of a complex nanostructure into a simpler geometry where an analytical description is possible. This provides analytical expressions for the optical properties of metallic nanostructures with sharp corners or touching points, which are well known to efficiently harvest EM energy. This method was first employed to study the optical response of 2D metal nanostructures [106, 107], followed by its application to 3D geometries such as touching nano-spheres [108] and nanocrescents [109], as shown in Fig.

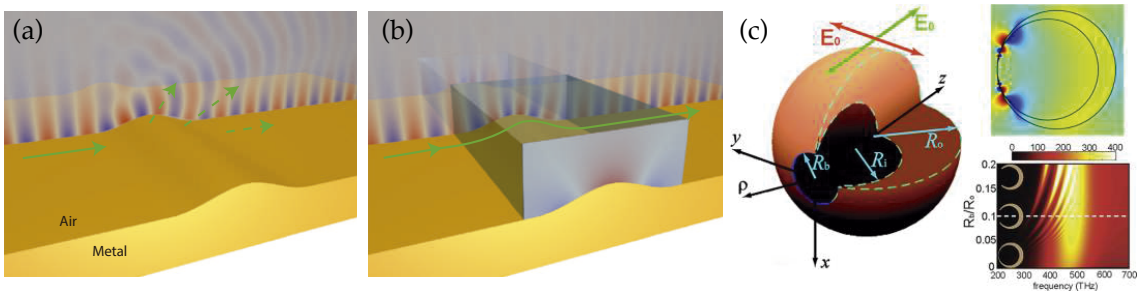

Figure 1.9: Applications of TO in Plasmonics. (a,b) As proposed in Refs. [97, 98], TO is used to reduce scattering of propagating SPPs from a surface: scattering losses experienced by SPP waves propagating along a dielectric-metal interface with a bump (a) are suppressed by covering the bump with a cloak whose refractive index spatially varies from 0.8 (blue) to 1.4 (red). (c) TO has been applied to the study of the EM field enhancement and energy harvesting in complex plasmonic nanostructures such as 3D nanocrescents. (a,b) Reproduced from Ref. [103]. (c) Reprinted from Ref. [109]

1.9 (c). In addition, TO has also been used to obtain analytical expressions and a great physical insight of non-locality on plasmonic nanostructures [110, 111] and even van der Waals forces between spherical nanoparticles [112, 113].

1.3 Geometrically-induced Surface Plasmons

The huge enhancement of EM fields generated by SPPs relies on the subwavelength confinement of the fields within the metal. For this reason, the field of Plasmonics is in principle limited to the high frequency range of the spectrum (UV, optical frequencies and near IR). At low frequencies ($\omega \ll \omega_p$), metals have a very large conductivity and the free electrons immediately respond to any EM perturbation, thereby shielding the metal from the EM field [1]. At such low frequencies, metals are said to be perfect electrical conductors (PECs). As a consequence, from the THz to the radio frequency (RF) regimes metals do not support tightly bounded surface EM modes. Instead, only poorly confined bound modes exist, such as the Zenneck [114] or Sommerfeld [115] waves, which extend mostly in the dielectric.

The concept of "spoof" plasmons was developed to overcome the limitations of conventional SPPs at low frequencies [116–118]. Spoof SPPs are surface EM modes with subwavelength confinement that arise when texturing the surface of a PEC and whose properties mimic those of conventional SPPs at optical frequencies. The main charac-

teristics of spoof SPPs can be understood by means of the simple model depicted in Fig. 1.10 (a). It consists of a perfectly conducting 2D surface pierced by a periodic array of grooves. The size, a, periodicity, d, and depth, h, of the grooves are all taken to be much smaller than the free-space wavelength of the incident wave, i.e., $a < d \ll \lambda_0$. This way, the indentations act as subwavelength cavities that couple to each other and provide the storage of EM energy at the surface needed to mimic optical SPPs. The periodic arrangement of the grooves prevents the out-coupling to free space radiation and thus enables the existence of a confined mode. Under the assumption that only the lowest order waveguide mode is excited inside the groove, the dispersion relation of such a confined mode can be written as [118],

$$k_x = k_0 \sqrt{1 + \left(\frac{a}{d}\right) \tan^2(k_0 h)}\,, \tag{1.26}$$

where $k_0 = \omega/c$ and k_x is the modal wave vector in the propagation direction. The dispersion relation given by the above equation is plotted in Fig. 1.10 (c). This dispersion relation clearly resembles that of the canonical SPPs propagating along a flat metal surface at optical frequencies (see Fig. 1.2). For this reason this geometrically induced propagating mode is termed spoof SPP. At low frequencies the spoof SPP lies close to the light line, thus being poorly confined. As the frequency increases the modal wave vector increases and the spoof SPP acquires a subwavelength confinement in the vertical direction. Finally, the dispersion relation approaches $\omega = \pi c/(2h)$ at $k_x = \pi/d$, this is, at the border of the first Brillouin zone. This cut-off arises from the periodicity and its value is given by the frequency of a cavity waveguide mode propagating inside the groove. From this simple model we see that the spoof SPP modes confined at highly conducting surfaces textured with periodic corrugations have a hybrid nature, as they feature characteristics of both surface and cavity modes.

A further step beyond this model can be taken by means of an effective medium approach [117, 118]. Owing to the fact that all the geometrical dimensions considered are subwavelength, $a < d \ll \lambda_0$, a perforated PEC surface behaves as an effective medium for EM fields. That is, the response of the system can be mapped to that of a metamaterial with homogeneous but anisotropic EM properties. For instance, the array of grooves considered in Fig. 1.10, can be mapped to an the effective medium layer on top of a perfectly conducting surface, as depicted in panel (b). The effective permittivity

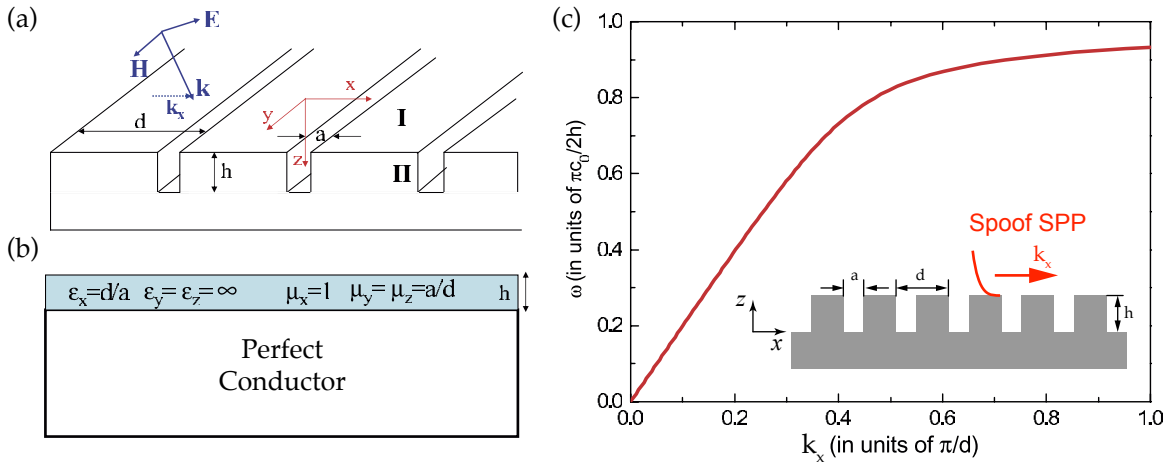

Figure 1.10: Spoof SPPs propagating along a periodic array of grooves. (a) A 1D array of grooves of width a, period d and depth h. (b) In the effective medium approach, the array of grooves behaves as a layer with homogeneous but anisotropic EM properties, on top of a perfect conductor. (c) Dispersion relation of the spoof SPPs supported by the structure shown in (a). The geometrical parameters of the grooves are $a/d = 0.2$ and $h/d = 1$. The figure has been adapted from Ref [118].

and permeability tensors of the metamaterial layer are given by,

$$\epsilon_x = \frac{a}{d}\,, \quad \epsilon_y = \epsilon_z = \infty\,; \tag{1.27}$$

$$\mu_x = 1\,, \quad \mu_y = \mu_z = \frac{d}{a}\,. \tag{1.28}$$

It is clear from this picture that the dispersion relation of spoof SPPs can be tailored by means of the geometrical parameters of the surface, which is a major advantage of the spoof SPPs concept. The analogy between conventional and spoof SPPs can be pushed forward by considering a surface pierced by a 2D array of holes [117, 118]. Different from the 1D arrays of grooves, where the first order cavity mode is always propagating, the lowest order waveguide mode in 2D arrays of holes is evanescent for $\lambda > 2a$, which imposes a cut-off frequency given by $\omega = \pi c/a$. In this case the effective medium parameters of the hole array read as,

$$\epsilon_x = \epsilon_y = \frac{\pi^2 d^2}{8a^2}\left(1 - \frac{\pi^2 c^2}{a^2}\right)\,, \tag{1.29}$$

$$\mu_x = \mu_y = \frac{8a^2}{\pi^2 d^2}\,, \tag{1.30}$$

$$\epsilon_z = \mu_z = \infty\,. \tag{1.31}$$

Interestingly, the electric permittivity, $\epsilon_{x,y}$, takes the canonical Drude form with a plasma frequency of

$$\omega_p = \frac{\pi c}{a}\,, \tag{1.32}$$

that corresponds to the cut-off frequency of the hole. This shows that the optical response of metals can be mimicked at any frequency regime by perforating a highly conducting film. Thereby, structured surfaces with tunable geometrical parameters can spoof SPPs. As a consequence, the concept of spoof SPPs enables the transfer of all the exciting prospects of SPPs to low frequency regimes, such as the THz regime, where there is a strong technological interest [119].

As we have seen above, spoof SPPs were first proposed for 2D structured flat surfaces [117, 118]. This work was followed by subsequent experimental demonstrations in the microwave [120, 121] and THz regimes [122, 123], as well as by upgrades of the original theoretical model [124, 125]. In addition, its extension to 1D geometries, where the lateral confinement opens up the possibility of designing waveguides, has been extensively studied both in theoretical and experimental works. Theoretical considerations include periodically corrugated wires [126], wedges [127], channels [128], periodic chains of dominoes [129] or metal-insulator-metal waveguides [130], as well as other proposals [131]. On the other hand, among the experimental realizations of waveguides for spoof SPPs we find helically grooved wires [132] and the experimental verification of the so-called domino plasmons [133]. In the THz and microwave regimes, where most works have focused, spoof SPPs display deep subwavelength confinement as well as long enough propagation lengths. Regarding higher frequencies, the concept of spoof SPPs has also been applied for tailoring the guiding properties of corrugated metal waveguides working at optical and telecom frequencies [134]. In addition, the concept of spoof SPPs has also enabled the interesting prospect of propagation along curved surfaces. As theoretically and experimentally demonstrated in Ref. [135], the so-called conformal surface plasmons, a kind of spoof SPPs sustained by ultra-thin films, are able to propagate along arbitrarily curved surfaces with very low propagation losses.

Finally, textured PEC particles of closed surfaces have been shown to support the localized version of spoof plasmons, with similar properties to LSPs in the optical regime [136]. For this reason, these resonances have been termed spoof-LSPs. An infinitely long PEC cylinder corrugated with a periodic array of grooves was studied in Ref. [136], where the EM response of the textured cylinder, composed of high-order order modes, was demonstrated to be equivalent to that of a Drude cylinder in the optical regime. In addition, this work also considered subwavelength particles, whose EM response is

dominated by the electrical dipole mode. While in particle plasmonics the subwavelength regime is accessible by downscaling the size of the structure, the resonance frequency of the spoof-LSPs modes scales with size. As a consequence, a different strategy is needed to reach the subwavelength regime in textured PEC particles. In particular, in Ref. [136] the subwavelength regime was reached by introducing a dielectric material of large refractive index within the grooves, thereby lowering the resonance frequency of the spoof-LSPs modes and obtaining a dipolar response. These spoof-LSPs mimic all aspects of standard LSPs in particle plasmonics. Therefore, thanks to this concept, all the phenomenology available at optical and near-IR frequencies for LSPs can be transferred to lower frequencies. Chapter 3 explores the emergence of a novel magnetic spoof-LSPs in these structures, in contrast with the purely electrical dipole character of conventional LSPs. We consider subwavelength PEC particles with periodically textured surfaces filled with a dielectric material and, by means of numerical simulations as well as an analytical model, we show that these structures support both magnetic as well as electric dipolar spoof-LSPs. Then, we show that magnetic spoof-LSPs can also be supported by purely metallic structures corrugated with very long grooves and we present the experimental verification of these resonances.

1.4 Plasmonic-based optical trapping

The optical trapping and manipulation of submicron-size particles is a cornerstone in biology and soft-condensed matter physics [137]. Conventional optical tweezers, based on strongly focused laser beams, have been extensively used for this purpose [138, 139]. As depicted in Fig. 1.11 (a), the field gradient in the converging beam gives rise to a force, $\mathbf{F}_{\text{grad}}$, that attracts the particle towards the focal point, while radiation pressure generates a force, $\mathbf{F}_{\text{scat}}$, that makes the particle move along the illumination axis. Remarkably, a 3D trap for the particle can be obtained when the gradient forces dominate. While this technique has allowed for the trapping submicron-size dielectric particles and biological objects, it provides trapping sizes intrinsically limited by diffraction. Plasmonic nanostructures have attracted significant interest as a promising system to solve this issue [140]. The sub-diffraction limited energy concentration in plasmonic systems, such as metal disks, optical antennas or metal tips [see Figs. 1.11 (b), (c) and (d), respectively] , can be exploited to create nano-optical traps capable of acting on nanometer-size objects [141–145]. The early proposal in Ref. [143] predicted the trapping of dielectric particles at the nanometer scale by means of a metal tip. Compared to conventional optical tweezers,

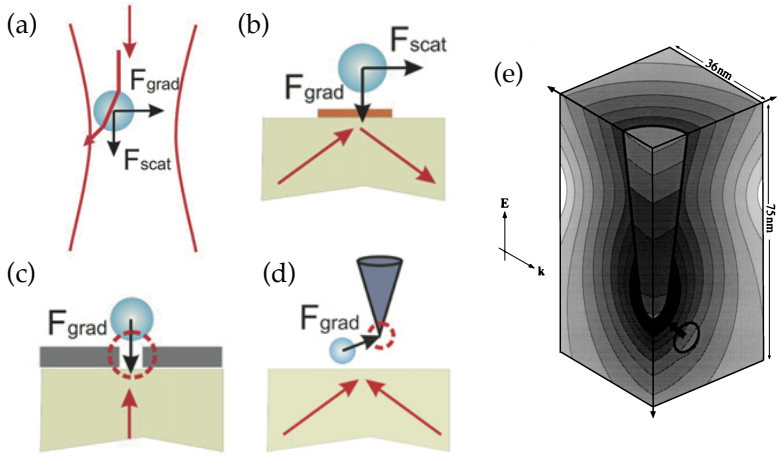

Figure 1.11: Different optical trapping configurations. (a) Conventional optical tweezers make use of a highly focused laser beam to trap small objects, such as colloidal particles or biological objects. The fundamental limitation on the size of the trapped objects set by diffraction can be overcome by means of plasmonic-based optical trapping. (b-d) The light confinement provided by SPPs propagating along patterned metal surfaces (b), as well as by the SPs localized at the subwavelength gap between two anntenas (c) or at the end of a metal tip (d), enables the trapping of objects of size as small as a few tens nanometers. (e) The near field of a gold tip of 5 nm radius displays a large field enhancement at the tip's extreme. The circle marks the position of a particle of 10 nm radius. (a-d) Reprinted from Ref. [146]. (e) Reprinted from Ref. [143].

the trapping is in this case based on the high wave vectors characteristic of evanescent waves and generated by the metal tip upon illumination, which provides light concentration beyond the diffraction limit. The huge field enhancement in a small region close to the tip, see Fig. 1.11 (e), generates strong gradient forces capable of trapping nanometer sized particles.

The first experimental demonstration of nano-optical trapping made use of patterned gold surfaces to show the trapping of micro-colloidal particles [147, 148]. In the experiment, an array of thin micrometer-sized gold disks placed on a glass substrate was covered by a solution of dielectric beads (5 μm size). The sample was then homogeneously illuminated under the SPP excitation condition, as sketched in Fig. 1.12 (a). Illumination gives rise to two forces: (i) a gradient force directed towards the gold pad and (ii) a scattering force in the direction of the parallel wave vector [see Fig. 1.11 (b)]. In the experiment, the scattering force guided the beads towards the gold disks while the gradient force, confined to the disk size, enabled their trapping thanks to the enhancement provided by

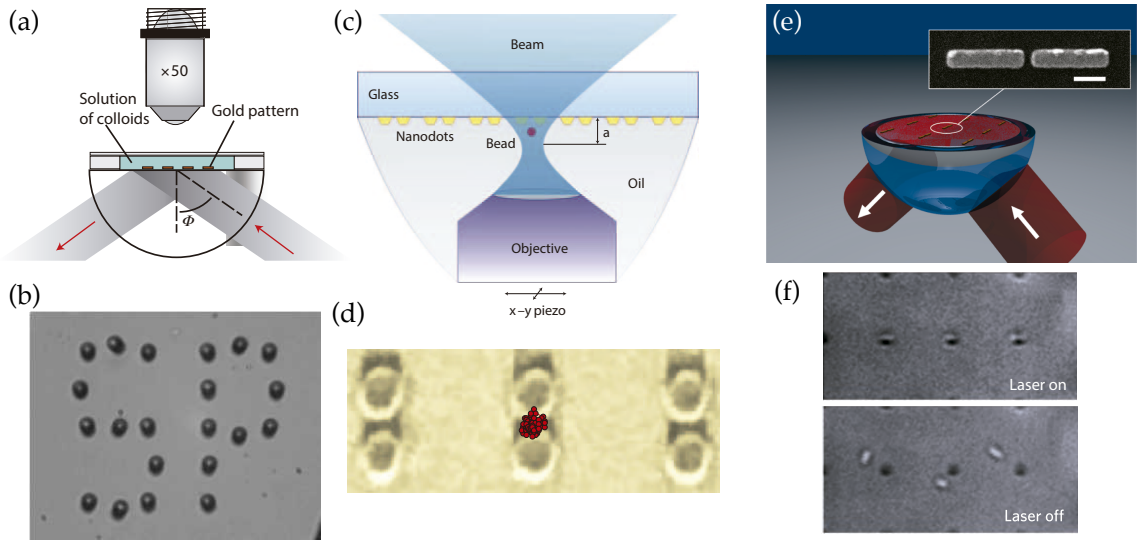

Figure 1.12: Plasmonic-based optical trapping. (a,b) In Ref. [147], a surface patterned with gold micrometer-sized disks is illuminated at the appropriate wavelength, angle and polarization for SPPs excitation. Each gold disk traps a dielectric bead of 5 μm size. (c,d) A conventional optical tweezer set up is assisted by plasmonic gap antennas to reduce the trapping volume down to subwavelength scales. Dielectric beads of 200 nm size are trapped in the gap antenna hot spot [150]. (e,f) In Ref. [151], a collection of gap antennas is illuminated by an unfocused laser beam. In this work, the parallel trapping and alignment of living bacteria was reported.

the plasmonic structure. As the same authors resported in a previous work, a plasmonic system can enhance optical forces by a factor of ~ 40 [149]. As a consequence, trapping of particles can be achieved for a reduced laser power, when compared to conventional tweezers. Interestingly, due to the small size of the metal disks compared to the illumination spot, several pads can be simultaneously illuminated and the parallel trapping of several beads can be achieved, as shown in Fig. 1.12 (b).

Further works have demonstrated the trapping of subwavelength objects by means of plasmonic antennas. The first approach towards this goal used the configuration sketched in Fig. 1.12 (c), where a conventional optical tweezer was assisted by gap antennas formed by pairs of optical antennas separated by a subwavelength gap [150]. The ability of gap antennas to concentrate light results in a trapping volume beyond the diffraction limit when the patterned structure is illuminated by a focused a laser beam. Thereby, the trapping of 200 nm dielectric beads with a 1064 nm laser field was demonstrated [see Fig. 1.12 (d)]. On the other hand, Ref. [151] reported the trapping of subwavelength particles based solely on plasmonic gap antennas. By illuminating a collection of gap antennas

under total internal refraction [see Fig. 1.12 (e)], the trapping of 200 nm polystere beads was reported. In addition, this configuration was also applied to a biological sample of living bacteria, which were effectively trapped. Interestingly, the elongated shape of the bacteria also resulted in their orientation along the longest axis of the dipole antennas. On the other hand, plasmonic gap antennas have also been used for trapping metal nanopartices of sizes as small as 10 nm, whose large polarizability enhances the optical forces [152].

As we have mentioned above, the plasmonic-based optical trapping has several advantages for the controlled immobilization of objects close to a substrate. When compared to conventional trapping schemes, plasmonic-based systems provide (i) a large field enhancement that allows for lower input powers and (ii) a sub-diffraction limited field confinement that yields nanometer-size trapping volumes. However, this technique lacks the ability to manipulate the trapped object in 3D. Such a prospect would be very interesting for instance for the manipulation of single QEs, such as atoms, QDs or NV centers. On the other hand, nano-optical trapping has potential applications in different research areas, such as lab-on-a-chip devices entirely operated with light, where plasmonic trapping could be used to immobilize cells [153], or microfluidic systems [154]. For both lab-on-a-chip and microfluidics applications, the development of optical techniques able not only to trap but also to provide a controlled manipulation of nanoscopic objects are highly desirable. There are a number of reasons why optical nano-manipulation is sought for in these fields: it can act in the single particle level, the infrastructure it requires is off-chip, and it is generally compatible with biological samples. However, up to our knowledge, any plasmonic antenna-based device lacks the functionality of object's transport over a long distance. Within this context, in Chapter 4 of this Thesis we present a proposal for a plasmonic Brownian ratchet that transforms the localized trapping based on optical antennas to enable a long distance drift of sub-micron beads [155]. This device may find applications such as the nano-manipulation of colloidal and biological objects.

Chapter 4 is framed within the context of trapping and manipulating nanoscopic particles. In particular, we present a proposal for driving dielectric nanometer-sized beads in microfluidic channels. The system is based on creating a periodic set of optical traps from an array of optical antennas with a specific geometry. Then, by externally modulating the illumination, the Brownian ratchet mechanism originates a net flow of particles into one direction. We start by detailing the design of this plasmonic Brownian ratchet: we characterize the optical response of the metallic antennas and we calculate the optical forces and trapping potential for a subwavelength dielectric bead. Next, through simulations of the system dynamics, we demonstrate a statistical directed drift into one

direction in the bead's Brownian motion.

1.5 Quantum Plasmonics

The capability of SPs of confining the EM field beyond the diffraction limit enables new ways for the quantum control of light through the interplay between *quantum emitters* (QEs) and SPs. Coherent interaction between QEs and photons is essential for quantum information processing and quantum communication technologies, which are currently being pursued [156]. A key ingredient for any quantum technology based on QEs and photons is the enhancement of light-matter interaction. In the cavity Quantum Electrodynamics (QED) approach this enhancement relies on confining photons inside a high-finesse cavity [see Fig. 1.13 (a)], which increases the interaction time between light and the emitter [157]. The emitter can be an atom (or a collection of them) [158], but also other two-level systems, such as semiconductor quantum dots (QDs) [159], nitrogen-vacancy centers in diamond (NV centers) [160] or superconducting quantum bits (qubits) [161]. The cavities consist of lossless dielectric systems with large quality factors, Q, and small mode volumes, V. Importantly, diffraction imposes a fundamental lower limit on the mode volume, $V \sim (\lambda_0/n)^3$, with λ_0 being the free space wavelength and n the refractive index of the cavity. Although the high absorption in metals is still a critical issue to overcome, Plasmonics provides a different route for the enhancement of QE-photon interactions, allowing for system sizes beyond the diffraction limit. This approach is based on positioning a QE within the hugely enhanced EM energy that is sub-diffraction confined to plasmonic nanostructures, as shown in Fig. 1.13 (b). For this reason, the study of the quantum properties of SPs and their potential as carriers of non-classical information has recently attracted great attention. The field of Quantum Plasmonics specifically deals with these issues [162].

In the last few years, SPs have been shown to preserve non-classical information, which is essential if Plasmonics is to be used as a platform for quantum applications. Pioneering work considered a pair of entangled photons generating a SPP propagating along a metallic hole array which then transforms back to photons [163–165]. The quantum state of the entangled photons, whereby two physically separated photons are linked such that the quantum description of each of them requires knowledge of the other, was shown to be transferred through the whole process. In addition, other manifestations of the quantum properties of SPPs such as squeezed states [166] and wave particle duality [167] have been demonstrated. These experiments proved that despite the mesoscopic

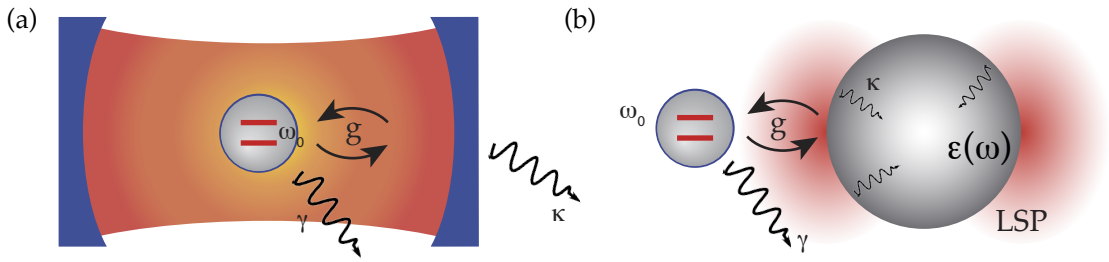

Figure 1.13: Sketches comparing two approaches for enhancing light-matter interactions. (a) Cavity QED system: a single emitter is embedded in a high finesse cavity that confines a single EM mode. (b) The large confinement of the EM field in the vicinity of a plasmonic nanostructure enhances the interaction between light and the emitter.

nature of SPPs, which involve the collective oscillation of $\sim 10^{10}$ electrons, SPP are capable of transferring entanglement and other quantum properties.

A different aspect of Quantum Plasmonics deals with the properties of plasmonic systems of very small sizes or with ultra-small gaps. Quantum size effects need to be included in the electrodynamical description of metallic nanoparticles with dimensions of the order of a few nanometers [168]. For such small sizes, the metal displays a discrete set of electronic states, which yields a shift and a broadening of the LSP resonance [169, 170]. In addition, the optical response of metal nanoparticles separated by distances $\lesssim 1$ nm is affected by the appearance of quantum tunneling, which has been theoretically [171] as well as experimentally [172, 173] investigated.

Achieving an efficient coupling between single QEs and the SPs supported by metallic nanostructures is one of the main goals of Quantum Plasmonics. A starting point for that purpose is provided by the well studied emission properties of a single emitter placed next to a metal surface [174–177]. The spontaneous decay rate of an excited state depends not only on the properties of the emitter but also on those of the EM environment [178]. This is the so-called *Purcell* effect, by which the lifetime of a QE is modified by the available EM states. The intense field and high confinement provided by SPs increase the local density of photonic states, thereby enhancing the radiative decay or, equivalently, decreasing the emitter's lifetime [179, 180]. The modification of the decay rate of a QE by the SPPs supported by a metal surface is shown in Fig. 1.14 (a). Within a close proximity to the surface the QE's decay is further enhanced by the non-radiative decay to very short-range lossy modes present in the metal. Such phenomenon is known as fluorescence quenching and is responsible for the decrease in the QE's lifetime at very close distances between the emitter and the surface [see Fig. 1.14 (b)]. Therefore,

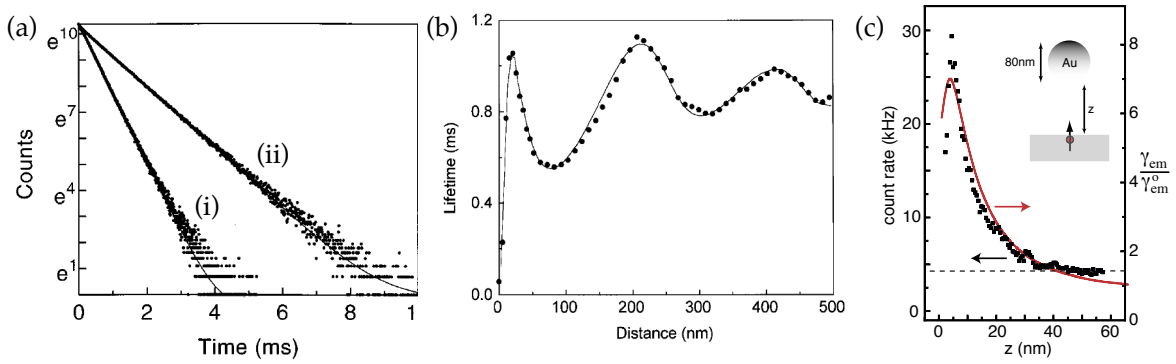

Figure 1.14: Spontaneous decay of a QE close to a plasmonic nanostructure. (a) Fluorescence lifetime of Eu^{3+} ions in the presence of (i) an optically thin silver mirror and (ii) an optically thick one. (b) Excited-state lifetime of the ions as a function of their distance to the silver optically thick film (solid line: theory, points: experiment). The oscillations at intermediate distances and the quenching of the emission at very small separations are due to variations in the local density of photonic states. (c) Fluorescence decay rate of a vertically oriented molecule as a function of its distance to a silver nanoparticle. The red line depicts the theory while the black dots stand for experimental measurements. Figures reprinted from: (a,b) Ref. [177], (c) Ref. [28].

there is an optimal distance for coupling a QE to a SPP mode. These ideas are also applicable to the LSPs supported by metal nanoparticles. The fluorescent enhancement (and quenching) of single molecules in the presence of metallic nanoparticles has been studied experimentally in Refs. [28, 29]. Figure 1.14 (c) summarizes the results of Ref. [28], where the spontaneous decay of the molecule is modified by coupling to the LSPs modes supported by the nanoparticle was demonstrated.

An important advantage of using propagating SPPs to enhance the interaction between light and single emitters is their broadband application. In particular, the fundamental mode of plasmonic waveguides, such as a metal nanowires, occurs for a broad range of frequencies. The coupling between a single QE to the SPPs propagating along metallic nanowires has been demonstrated in several works [181–183]. In Ref. [182], the fluorescence enhancement of a single QD coupled to a single SPP mode of a silver nanowire was successfully measured. A sketch of the emitter's decay channels can be seen in Fig. 1.15 (a), while Fig. 1.15 (b) displays a fluorescence image of the sample. In addition, measurements of the second order coherence function as a function of photon delay, $g^{(2)}(\tau)$ [184], were performed from the the light scattered at the end of the nanowire. Such measurements proved that the SPPs exhibit antibunching, or in other words, that the photons

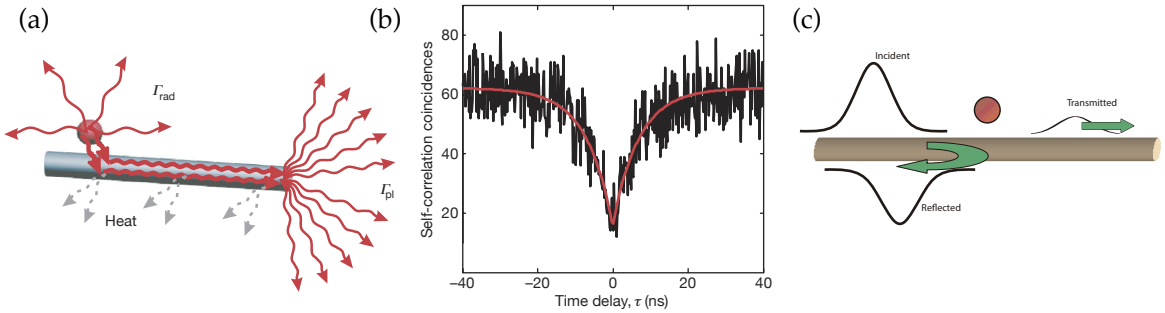

Figure 1.15: Quantum properties of single QEs coupled to plasmonic waveguides. (a) Spontaneous decay of a QE coupled to a plasmonic nanowire. In the sketch, from Ref. [182], a QD decays via radiative coupling to free space photons or SPP modes propagating through the nanowire with rates Γ_{rad} and Γ_{pl}, respectively, or it non-radiatively couples to lossy modes in the metal. (b) Second order cross-correlation as a function of the time delay between photon coincidences, $g^{(2)}(\tau)$, as measured in Ref. [182] (black line). The light emitted from a single QD couples to a silver nanowire and is finally scattered at the end of the wire, where it is collected and the photon cross-correlations are measured. (c) Proposal for a single photon transistor based on a QE coupled to a nanowire. Due to the efficient coupling between a single optical emitter and the SPPs, the emitter can act as a nonlinear switch for incident photons propagating along the wire. Figures reprinted from: (a-b) Ref. [182] and (c) Ref. [188].

emitted by the QD retain its single-photon character after being transferred through the wire by the SPP mode. This means that plasmonic wires can provide single photon sources, as has also been demonstrated in Ref. [185] using NV centers. On the other hand, alternative plasmonic systems have been proposed to provide very large fluorescent enhancements, such as hybrid waveguides [186] or plasmonic resonators [187]. Moreover, the efficient coupling between single emitters and the SPPs propagating along plasmonic waveguides enables the realization of devices, such as a single photon transistor [188, 189] [see Fig. 1.15 (c)].

In addition, SPPs have also been proposed as mediators of the interaction between several emitters. The sub-diffraction limited confinement associated with SPPs can be exploited not only to enhance the coupling between an individual QE and the photons in a single SPP mode, but also to enhance the coupling between several QEs. For instance, in Ref. [190] two emitters were connected by 1D plasmonic waveguides. After demonstrating that the coupling of a single QE to the SPP mode propagating through different waveguides (channels, wedges and wires) can be very large, plasmonic waveguides are used to provide an interaction channel between two emitters. The plasmon-mediated

coupling can be employed to efficiently couple the emitters at distances larger than the wavelength, which enables the emergence of super- and subradiance collective states with modified emission rates [191], as well as the phenomenon of resonance energy transfer. This efficient long-range interaction, which would be impossible in free space or with a dielectric fiber, was subsequently shown to produce entangled states of several QEs [192–195]. In Ref. [192], plasmon-mediated entanglement between two QEs was studied for the case of a plasmonic channel waveguide. Based on subwavelength light confinement in a plasmonic waveguide, this work presented a feasible proposal for long-distance entanglement of two qubits by using SPPs instead of photons. A large fraction of the photons radiated by one QE is captured by the SPP mode propagating through the waveguide and transferred to the second QE, thereby becoming entangled. Interestingly, entanglement can be obtained for QEs at distances larger than the operating wavelength.

So far, all the systems we have considered feature a weak light-matter coupling strength. When the interaction between light and the emitters is very strong and overcomes the system losses, the coupled system may enter into the *strong coupling* (SC) regime. Differently from the *weak coupling* (WC) regime, where the effect of the EM field is to modify the spontaneous decay rate of a QE through the already discussed Purcell effect, in the SC regime there is a reversible energy exchange between the EM field and the QEs. In order to achieve SC, such energy exchange needs to be faster than any other dissipation or decoherence mechanism in the system. The system population then exhibits coherent oscillations, which manifest themselves as a *Rabi* splitting in the energy levels. Within this regime the system composed of the EM field and the QE has to be treated as a whole and described by means of new eigenstates. The confinement and broadband characteristics of SPs in metallic nanostructures are promising tools for achieving the SC regime between QEs and EM fields. As we have mentioned already, the WC regime is interesting on its own for Quantum Plasmonics, for, e.g., efficient single photon generation [181], but entering the SC regime is a major goal of the field.

While the SC regime for an individual QE coupled to a plasmonic system has been theoretically predicted for the LSPs of metal nanoparticles [196–199] and for SPPs in several metal nanostructures [200–203], it has not yet been experimentally demonstrated. Nevertheless, the energy splitting characteristic of this regime has been observed in experiments where *ensembles* of organic molecules interact with the SPP modes propagating along a metal surface [204–206] or with SPPs supported by a metal surface drilled with a periodic array of subwavelength holes [207] and subwavelength slit arrays [208]. Moreover, organic molecules have also been used to achieve reversible switching of the ultrastrong coupling regime when placed inside a cavity [209], as well as to engineer chemical reac-

tions [210] or a material work function [211] when interacting with SPPs in hole arrays. On the other hand, the SC regime between semiconductor QDs an SPPs has also been considered, and the corresponding energy splittings characteristic of this regime have also been shown [212–215]. The usual experimental configuration is sketched in Fig. 1.16 (a): an ensemble of QEs, embedded in a dielectric host, is placed on top of a metal film. By means of a laser field, SPPs propagating along the film are excited under the Kretschmann configuration [11]. After the interaction between the QEs and the SPPs has taken place, the emitted light is measured through reflectivity from the metal film ("detection 1" in the figure) or through luminescence from the QEs ("detection 2"). Panel (c) shows typical experimental spectra (from Ref. [204]), where the reflectivity of the system is plotted as a function of energy for different excitation angles. By sampling the excitation angle, the whole SPP branch is probed as a function of the parallel $\mathbf{k}$ vector and the coupled SPP-emiter system appear as dips in reflectivity. An example of such a dispersion relation, from Ref. [214], is plotted in panel (b), displaying the characteristic anticrossing between the QE energy level (around 2.2 eV in this case) and the SPP dispersion branch. In addition, the inset panel presents the evolution of the energy splitting with the square root of the absorbance, showing that the coupling constant, g, increases with the total number of QEs, N, following $g \propto \sqrt{N}$. This dependence is characteristic of the many-emitters strong coupling regime [157]. More recently, the coherent energy exchange between QEs and SPPs has been experimentally measured in the time domain [216]. In this work, the coherent population dynamics of an ensemble of J-aggregates interacting with an SPP propagating along a metal slit array have been measured in the fs timescale for the first time.

Chapter 5 of this Thesis is devoted to the study of light-matter interaction in plasmonic systems. In particular, we address the coupling between QEs and SPPs for several configurations: (i) For an individual QE interacting with plasmonic structures we first review the modified spontaneous decay of a QE placed in the vicinity of a metal/dielectric interfaces and of a graphene sheet. Next, we revisit the problem of a QE decaying close to a metal/dielectric interface and we go beyond the spontaneous decay description, showing that that for very short distances to the metal surface, where quenching is expected, a QE of large dipole moment features reversibility its dynamics. (ii) For two QEs, we study how their interaction may be mediated by the SPPs propagating along 2D graphene sheets and 1D graphene ribbons, showing that graphene SPPs allow us to control and tailor the interaction between the QEs at deep subwavelength scales and, at the same time, at long interaction ranges [217]. (iii) Finally, we consider a collection of QEs strongly coupled to a propagating SPP. In the context of the experimental works

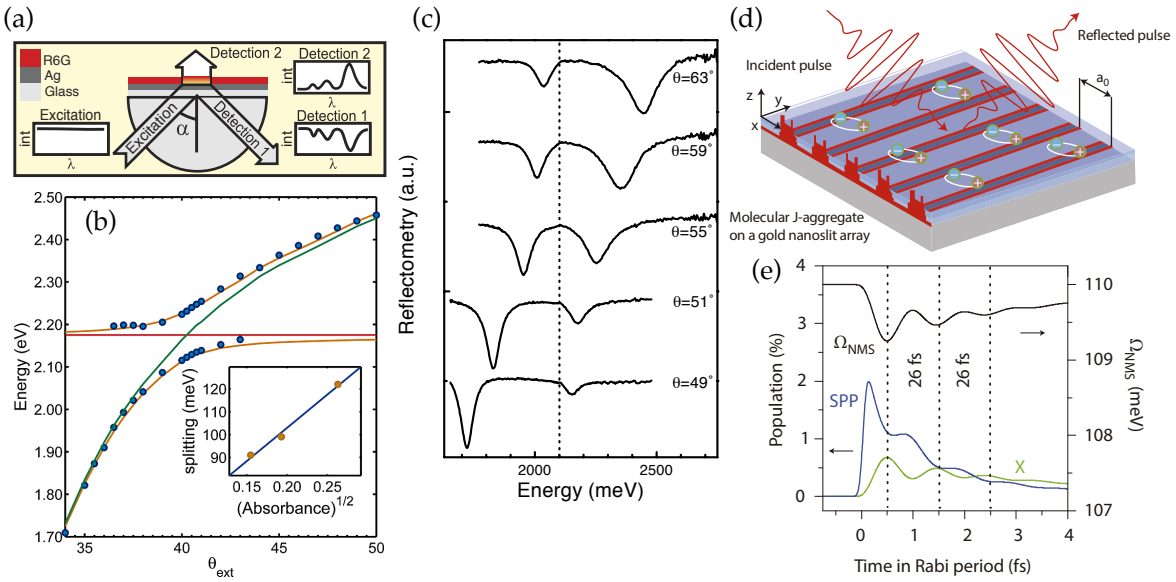

Figure 1.16: Experimental evidence of SC between a collection of QEs and propagating SPPs. (a) Experimental configuration from Ref. [205]: a sample of rhodamine molecules embedded in a dielectric host is placed on top of a silver film. Different detection methods are sketched. "Detection 1" yields the reflectivity spectrum of the system and "detection 2" gives the energies of the modes after undergoing scattering processes. (b) Characteristic energy splitting of the strongly coupled modes between a collection of QDs interacts with a silver film, from Ref. [214]. The energy level of the QDs, at $\sim$ 2.20 eV, experiences an avoided crossing with the SPP dispersion branch (green line). (c) Reflectivity measurements from Ref. [204], showing the interaction between an ensemble of J-aggregates (resonance energy $\sim$ 2.1 eV) and SPPs on a silver film. The reflectivity is plotted as a function of the incident light energy for different incident angles. The minima in these curves originate a dispersion relation equivalent to the one shown in panel (b). (e) In Ref [212], the dynamics of J-aggregates on top of a silver subwavelength slit array was measured. The experiments revealed coherent dynamics in a fs timescale (e).

reporting energy splittings and time-domain oscillations for ensembles of QEs interacting with the SPPs that propagate along a metal/dielectric interface, we develop a theoretical framework that is able to reproduce the reported phenomenology [218]. In addition, we predict the conditions under which these systems may display quantum statistical properties.

Chapter 2

Moulding the flow of surface plasmons using Transformation Optics

2.1 Introduction

In this chapter we study the application of Transformation Optics (TO) to plasmonics. One of the main goals in plasmonics is to control the flow of light at a metal surface by means of the SPPs that decorate a metal-dielectric interface. As we discussed in the introduction (see Section 1.1), in the quest for creating photonic circuits based on SPPs different waveguiding schemes have been tested during the last years [7–9]. Here we present a different strategy to tackle this problem by showing how the TO framework can be applied to efficiently mold the propagation of SPPs at a metal surface. The TO formalism, which we introduced in Section 1.2, provides us with expressions for the EM material parameters, dielectric permittivity, $\hat{\boldsymbol{\epsilon}}$, and magnetic permeability, $\hat{\boldsymbol{\mu}}$, that need to be implemented in order to obtain a medium where EM waves propagate along desired trajectories [51, 52]. This formalism is based on the form-invariance of Maxwell's equations under coordinate transformations. Hence, due to the universal character of Maxwell equations, it is expected to be valid for any EM wave.

In order to design an optical device for propagating SPPs, the fact that these EM modes are surface waves travelling along the interface between a dielectric and a metal has to be taken into account. The expressions for the EM material parameters provided by the TO formalism should, in principle, be implemented both in the dielectric and the metal sides. This fact is a severe technical challenge, as TO generally prescribes highly anisotropic and inhomogeneous $\hat{\boldsymbol{\epsilon}}$ and $\hat{\boldsymbol{\mu}}$. Moreover, since the SPP field extends over a few tens of nanometers inside the metal, $\hat{\boldsymbol{\epsilon}}$ and $\hat{\boldsymbol{\mu}}$ should be manipulated at

such length scales within the metal. However, as we demonstrated in Refs. [97, 105] and Ref. [98] showed independently, manipulating the material properties inside the metal part is not actually required: a simplified version in which only the EM properties of the dielectric side are modified leads to very accurate functionalities. Two factors determine whether this simplification is operative or not: the wavelength of the SPP and the geometry of the device under consideration. The problem of the anisotropy can be solved by choosing the appropriate coordinate transformations. When conformal and quasiconformal mappings are considered, the resulting EM parameters are isotropic. Therefore, plasmonic devices can be based on implementations of transformation media based only on isotropic dielectrics, allowing the possibility of low-loss and broad-band performances.

In this Chapter we consider the main features of TO as applied to SPPs and exemplify the theory by means of different TO devices for SPPs. We verify the results by means of finite element method (FEM) simulations [219]. The structure of the Chapter is as follows. First, we apply the general methodology of TO in Section 2.2 to the case of propagating SPPs. In particular, we study the functionality of four different potential plasmonic devices (a cylindrical cloak, a parallel shifter, a right-angle bend and a lens) at a range of wavelengths through the optical range of the spectrum. Second, we consider realistic models based on conformal and quasiconformal mappings in Section 2.3. We show that for these cases only isotropic refractive indexes need to be implemented and we apply it to the parallel shifter, the right-angle bend, the lens, a ground-plane cloak for SPPs and a plasmonic concentrator. Next, in Section 2.4 we review recent experimental implementations leading to unique SPP functionalities at optical frequencies [99, 100]. Finally, Section 2.5 summarizes the main contributions of our work in this topic.

2.2 Transformation Plasmonics

2.2.1 Transformation Optics formalism as applied to Plasmonics

As we introduced in Section 1.2, The TO framework provides tools for the design of EM media with desired functionalities. It is based on the fact that Maxwell's equations are left invariant if a mapping is performed from an empty space with a distorted geometry (virtual space) to a medium characterized by $\hat{\boldsymbol{\epsilon}}$ and $\hat{\boldsymbol{\mu}}$ placed in a flat space (physical space). A 2D transformation $\mathbf{x} = \mathbf{x}(\mathbf{x}')$ between the virtual system, $\mathbf{x}' = \{x', y'\}$, and

the physical system, $\mathbf{x} = \{x, y\}$, such as the one shown in Fig. 1.6, is described by means of its Jacobian matrix, $\hat{A} = \left(\partial x^i / \partial x^{i'}\right)$, where the index $i = 1, 2$. The empty-space Maxwell's equations in physical space can be interpreted as macroscopic equations for a medium placed in virtual space and characterized by the EM parameters given by Eq. 1.23:

$$\hat{\boldsymbol{\epsilon}}_{\mathrm{TO}} = \epsilon_0 \frac{\hat{A}\hat{A}^T}{\det \hat{A}}; \quad \hat{\boldsymbol{\mu}}_{\mathrm{TO}} = \mu_0 \frac{\hat{A}\hat{A}^T}{\det \hat{A}}. \tag{2.1}$$

In this expression, the background EM parameters of the virtual space, $\hat{\boldsymbol{\epsilon}}'$ and $\hat{\boldsymbol{\mu}}'$ in Eq. 1.23, have been replaced by the free-space values ϵ_0 and μ_0 without loosing generality and the optical medium parameters, $\hat{\boldsymbol{\epsilon}}$ and $\hat{\boldsymbol{\mu}}$ in Eq. 1.23, have been renamed as $\hat{\boldsymbol{\epsilon}}_{\mathrm{TO}}$ and $\hat{\boldsymbol{\mu}}_{\mathrm{TO}}$ for the sake of clarity. In order to get more insight, it is convenient to relate the Jacobian matrix of the coordinate transformation to its metric tensor $\hat{G} = (g_{ij})$ [1]. We have:

$$\hat{G} = \frac{\partial x^k}{\partial x^i} \frac{\partial x^k}{\partial x^j} = \left(\hat{A}^{-1}\right)^T \hat{A}^{-1}. \tag{2.2}$$

This allows us to re-express $\hat{\boldsymbol{\epsilon}}_{\mathrm{TO}}$ and $\hat{\boldsymbol{\mu}}_{\mathrm{TO}}$ in terms of the inverse metric tensor, $\hat{G}^{-1} = \hat{A}\hat{A}^T$, of the transformation:

$$\hat{\boldsymbol{\epsilon}}_{\mathrm{TO}} = \epsilon_0 \sqrt{g} \hat{G}^{-1}; \quad \hat{\boldsymbol{\mu}}_{\mathrm{TO}} = \mu_0 \sqrt{g} \hat{G}^{-1}, \tag{2.3}$$

where g is the determinant of the metric, $g = 1/(\det \hat{A})^2$. In general, the metric tensor of any 2D coordinate transformation is a 2×2 symmetric matrix. Then, as it can be readily seen from 2.3, $\hat{\boldsymbol{\epsilon}}_{\mathrm{TO}}$ and $\hat{\boldsymbol{\mu}}_{\mathrm{TO}}$ are generally anisotropic. Moreover, they are inhomogeneous and vary throughout space according to the coordinate transformation.

Since TO relies on Maxwell's equations, it applies to all kinds of EM waves and in particular to SPPs. However, we need to bear in mind the fact that SPPs are surface EM waves propagating along a metal/dielectric interface with a field distribution that is evanescent in the direction perpendicular to the interface. Therefore, an infinite number of 2D coordinate transformations should be performed, in principle, in planes parallel to the metal-dielectric interface in order to operate over the whole plasmonic field. As the SPP field extends into the dielectric and the metal, these 2D coordinate transformations should be implemented at both sides of the interface. Due to the fact that the SPP decay length in the metal (skin depth) is of a few tens of nanometers at optical wavelengths, a manipulation of the metal properties would be needed at a nanometer scale. However, a more feasible approach that consists of modifying the EM properties of the dielectric side only indeed gives very accurate results, while control over the metal is not actually

[1] The metric tensor, $\hat{G}$, is not to be confused with the Green's tensor used in other Chapters, $\hat{\mathbf{G}}(\mathbf{r}, \mathbf{r}, \omega)$

required. To illustrate the direct application of TO to SPPs and the impact of manipulating only the dielectric side, in the following Subsection we study the dependence of the efficiency on the wavelength for four different TO devices for SPPs: a cylindrical cloak, a parallel shifter, a right-angle bend and a lens.

2.2.2 Transformation Optics-based plasmonic devices

Cylindrical cloak for SPPs

As a first illustration of the methodology, we consider a 3D cylindrical cloak for SPPs travelling along the interface between a metal characterized by permittivity ϵ_m and vacuum. Figure 2.1 (a) shows a SPP that scatters with a metallic cylinder of radius a placed on the surface. A cloak placed around the cylinder, see Fig. 2.1 (b), renders the object invisible by suppressing any scattering from it. The effect of the cloak is to smoothly guide the SPP wave around the cloak, as suggested by the power flow streamlines rendered in panels (c) and (d).

As we introduced in Section 1.2, a 2D invisibility cloak was the first proposal of TO applications [51, 55] as well as the first experimental realization [88]. The cloak design is based on the coordinate transformation shown in Fig. 1.6, such that a wave travelling in physical space will follow trajectories that surround the hole so that it appears to have travelled in straight lines as it would in the virtual - undistorted - space. In order to design a 3D invisibility cloak for SPPs we take a plane parallel to the metal surface and make the 2D radial transformation $r(r') = b/(b-a)r' + a$ in the shell $a < r < b$ (see the geometry of the cloak in Fig. 2.1 (b)). In Cartesian coordinates, the transformation reads:

$$x = r(r')\frac{x'}{r'} \; ; \;\; y = r(r')\frac{y'}{r'} \; ; \;\; z = z'. \tag{2.4}$$

According to the TO equations 2.3, the EM parameters of the transformation medium are the following:

$$\hat{\boldsymbol{\epsilon}}_{\mathrm{TO}}/\epsilon_0 = \hat{\boldsymbol{\mu}}_{\mathrm{TO}}/\mu_0 = \begin{pmatrix} \epsilon_r \frac{x^2}{r^2} + \epsilon_\theta \frac{y^2}{r^2} & (\epsilon_r - \epsilon_\theta)\frac{xy}{r^2} & 0 \\ (\epsilon_r - \epsilon_\theta)\frac{xy}{r^2} & \epsilon_r \frac{y^2}{r^2} + \epsilon_\theta \frac{x^2}{r^2} & 0 \\ 0 & 0 & \epsilon_z \end{pmatrix}, \tag{2.5}$$

where ϵ_r, ϵ_θ and ϵ_z are given by Eq. 1.25. These parameters are highly anisotropic and approach singular values at the inner radius of the cloak (ϵ_{xx},$\epsilon_{yy} \to +\infty$; $\epsilon_{xy} \to -\infty$ and $\epsilon_z \to 0$). If we want to operate on a SPP, we need to cloak the field in the dielectric and metal sides as illustrated in Fig. 2.1 (e). In the dielectric side, we implement the

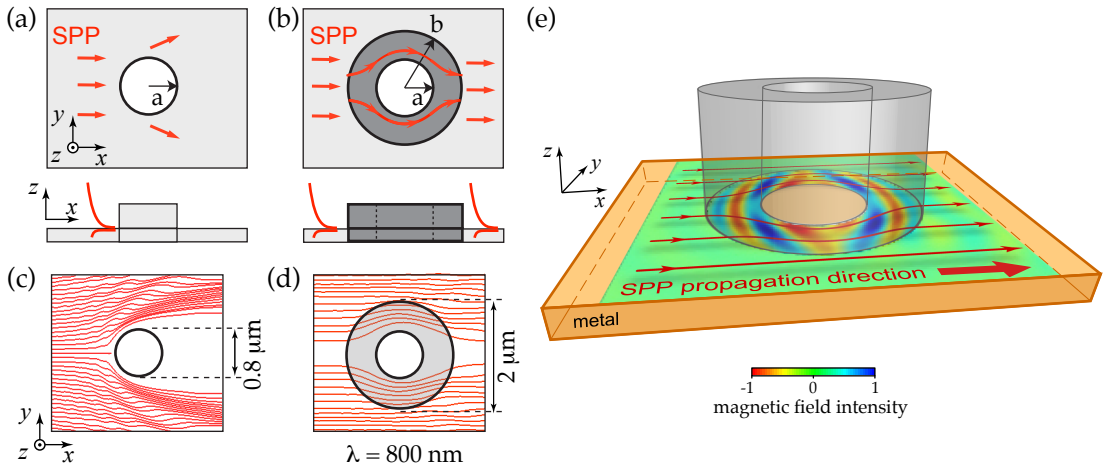

Figure 2.1: TO is used to cloak a cylinder to SPPs. (a) A SPP is propagating along an air-gold interface and scatters on a metallic cylinder of radius a. The plasmonic field intensity, shown schematically, decays exponentially away from the interface. (b) Scattering from the cylinder is suppressed by placing a cloak of outer radius b around it. The optical parameters needed to cloak the cylinder are calculated using TO and implemented in a cylindrical shell $a < r < b$ of height h_d in the dielectric side and in a shell of height h_m in the metal. (c, d) Power flow from 3D simulations at $\lambda = 800$ nm. The SPP experiences high scattering losses when it encounters the bare cylinder (c) while the cloak guides the SPP wave suppressing the scattering losses. (e) 3D SPP-cloak. The scattered magnetic field, H_y, is plotted at the dielectric-metal interface for a wavelength $\lambda = 1.5$ μm and a cloak radius $a = 1.5$ μm and height $h_d = 6$ μm.

parameters, $\hat{\boldsymbol{\epsilon}} = \hat{\boldsymbol{\epsilon}}_{\mathrm{TO}}$ and $\hat{\boldsymbol{\mu}} = \hat{\boldsymbol{\mu}}_{\mathrm{TO}}$, in a cylindrical shell of radii a and b with a height, h_d, larger than the vacuum decay length of the SPP. On the other hand, in the metal side the EM tensors need to be modified following $\hat{\boldsymbol{\epsilon}} = \hat{\boldsymbol{\epsilon}}_{\mathrm{TO}} \cdot \epsilon_m$ and $\hat{\boldsymbol{\mu}} = \hat{\boldsymbol{\mu}}_{\mathrm{TO}}$, in a cylindrical shell of the same radii but with a height h_m larger than the skin depth. If we cloaked its entire field, an incident SPP would emerge at the other side as if it had travelled through free space.

To study the effectiveness of this plasmonic device we have considered the transmittance of SPPs through the cloak and its scattering properties. We have measured the transmittance from one side of the cloak to the other as the ratio of the incident to the transmitted power flow. In order to isolate the effect of the TO medium, losses have been neglected throughout this analysis by setting the imaginary part of the metal dielectric constant to zero. Since losses are absent, 100% transmittance means that the whole plasmonic field is guided around the cylinder without any back-scattering. In the simulations, a SPP at a wavelength between 600 and 1500 nm and travelling through a

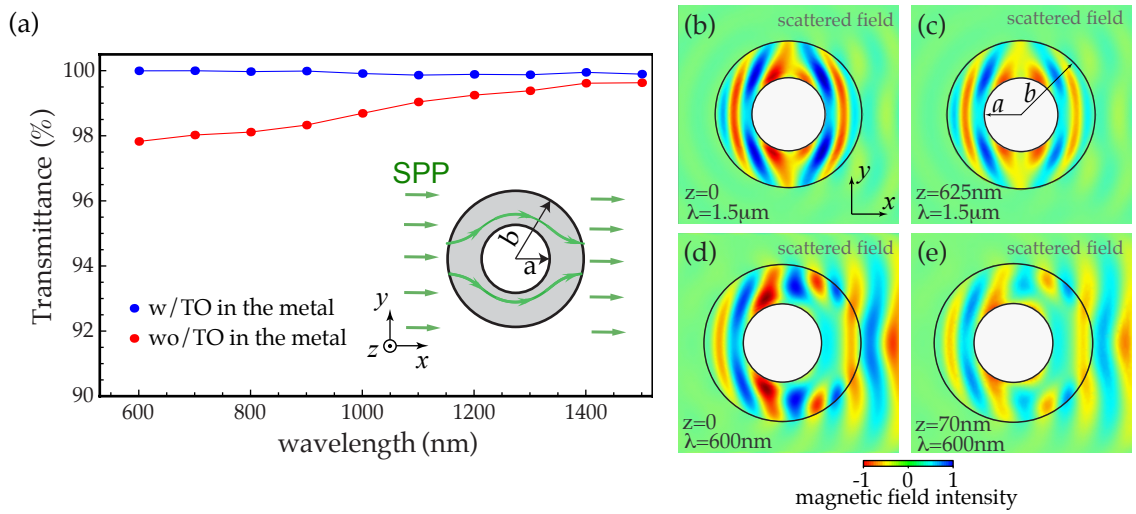

Figure 2.2: Transmittance study for a 3D cylindrical cloak for SPPs. (a) Transmittance (ratio of the incident power flow to the transmitted power flow) through the cloak for SPPs at different wavelengths. The blue and red lines show the case with and without placing a transformation medium in the metal side respectively. The in-plane size of the cloak is scaled with the wavelength as $a = b/2 = 5/6\lambda$. (e,f) Scattered H_y field at a wavelength $\lambda = 1.5$ μm and evaluated at the metal surface, $z = 0$ (e), and at $z = \delta/4 = 625$ nm (f), with δ being the vacuum decay length of the SPP into the dielectric. (g,h) The same quantity is plotted at wavelength $\lambda = 600$ nm and evaluated at $z = 0$ (g) and at $z = \delta/4 = 70$ nm (h).

gold-vacuum interface, impinges onto a cloak of size $a = b/2 = 5/6\lambda$. The height of the cloak in the dielectric side, h_d, is much larger than the vacuum decay length at a given wavelength and is chosen for convergence. The height of the cloak in the metal side, h_m, is 50 nm high at all wavelengths since the skin depth of the SPP is very similar over the wavelength range and amounts to $20-30$ nm. The transmittance spectrum is plotted in Fig. 2.2 (a) for two cases: with and without introducing a metamaterial in the metal side (blue and red lines respectively). The transmittance of the cloak in the ideal situation (blue line) where TO parameters are implemented in the metal along with the dielectric material is higher than 99% over the whole wavelength range. On the other hand, the transmittance when the metal is leaved untouched (red line) increases from 97% at 600 nm to 99% at 1500 nm. As the wavelength increases, the blue and red curves lie closer. The reason for this is that while the skin depth is approximately constant over the whole spectrum (around 20-30 nm), the vacuum decay length increases with the wavelength, varying from 250 nm for a SPP at 600 nm to 4 μm at 1500 nm. Thus, for shorter wavelengths, the part of the SPP energy carried within the metal is larger. However, although

the effectiveness of the cloak is affected by the lack of cloaking the field that resides in the metal, it is very good even at short wavelengths. Our results explain why a previous experiment on SPP cloaking at $\lambda = 500$ nm in which the metamaterial was only placed in the dielectric side was not completely successful [220].

The impact of manipulating only the dielectric side is illustrated in Fig. 2.2 (b-e) for SPP cloaks operating at $\lambda = 1.5$ μm [panels (b) and (c)] and $\lambda = 600$ nm [panels (d) and (e)]. In all cases, the prescribed $\hat{\boldsymbol{\epsilon}}_{TO}$ and $\hat{\boldsymbol{\mu}}_{TO}$ were implemented only in the dielectric side, in a cylindrical shell surrounding a perfectly conducting cylinder, leaving the metal as a continuous sheet. We present for each wavelength the y-component of the scattered magnetic field evaluated at two planes parallel to the metal-dielectric interface, one at $z = 0$ [panels (b) and (d)] and another at a height at which the SPP has decayed to a quarter of its intensity at the interface [panels (c) and (e)]. At $\lambda = 1.5$ μm, the scattered magnetic field is nearly zero out of the cloaking region and we can conclude that the performance of the cloaking device for SPPs is excellent. However, for a SPP at a wavelength of 600 nm, only partial cloaking for a SPP is achieved. The reason for this is the geometry of the cylindrical cloak which, as opposed to the beam shifter, has a discontinuity in the metal-dielectric interface. In this case, the behaviour of the cloak is very sensitive to the field propagating inside the metal because it strongly scatters at this discontinuity.

Finally, it is important to notice that a study of the scattering properties is needed for a complete analysis of the invisibility cloak. By inspection of the scattered field distribution we have seen that, when the TO recipe is not implemented in the metallic side, around 20% of the field amplitude is scattered in the forward direction. As a result, the wavefront of the SPP when passing through the simplified cloak is slightly modified. In accordance to [221], phase distortions occur for the simplified cloak and perfect cloaking is not achieved. Nevertheless, as demonstrated by our results, most of the plasmonic field is guided around the cylinder. On the other hand, we have checked the scattering properties of all the devices shown in this chapter. We have found that these effects are only relevant in the case of the cylindrical cloak. For the sake of brevity, we mention this fact here and not when discussing each device. Therefore, in the rest of the chapther, we present the transmittance and the images of the EM field as criteria for quantifying the performance of the SPP-devices.

SPP beam shifter

Another potential plasmonic device is the parallel shifter, which acts on an incident beam by translating it perpendicularly to its propagation direction. To design a 2D shifter, we take a rectangular region sized $d \times l$ [see Fig. 2.3 (a)] and map a Cartesian grid to a grid that is tilted at an angle ϕ [56]:

$$x = x' \ ; \ \ y = y' + a(x' + d) \ ; \ \ z = z', \tag{2.6}$$

where a determines the tilt angle $a = \tan\phi$. The map of this transformation is illustrated in Fig. 2.3 (b). In contrast to the transformation leading to the cylindrical cloak, Eq. 2.4, the transformation given by Eq. 2.6 is discontinuous at the frontiers of physical space, a feature that allows the transfer of the modification of the fields inside the TO medium to the wave that exits it. Because the transformed boundary is a combination of rotation and translations of the original boundary, the discontinuity does not cause reflections at the limits of the TO medium [222]. Following the TO equations (Eq. 2.3) the EM parameters of the transformation medium are:

$$\hat{\boldsymbol{\epsilon}}_{\mathrm{TO}}/\epsilon_0 = \hat{\boldsymbol{\mu}}_{\mathrm{TO}}/\mu_0 = \begin{pmatrix} 1 & a & 0 \\ a & 1+a^2 & 0 \\ 0 & 0 & 1 \end{pmatrix}. \tag{2.7}$$

A 3D SPP parallel shifter should, in principle, be composed of a slab in the dielectric side sized $d \times l \times h_d$ with permitivitty $\hat{\boldsymbol{\epsilon}}_{\mathrm{TO}}$ and permeability $\hat{\boldsymbol{\mu}}_{\mathrm{TO}}$ along with a slab in the metal film of dimensions $d \times l \times h_m$ and parameters $\hat{\boldsymbol{\epsilon}} = \hat{\boldsymbol{\epsilon}}_{\mathrm{TO}} \cdot \epsilon_m$ and $\hat{\boldsymbol{\mu}} = \hat{\boldsymbol{\mu}}_{\mathrm{TO}}$. Again, the height of the slabs at each side must be larger than the SPP decay length in that medium. In this case, the TO medium parameters are anisotropic but homogeneous and take non-singular values. A 3D view of simulation results for a SPP at $\lambda = 1.5$ μm going through a beam shifter is presented in Fig. 2.3 (c) . The incident SPP, which displays a gaussian profile, propagates in the x direction and impinges on the transformation medium. Thus, it experiences a shift of $\phi = 45°$ perpendicular to its propagation, in the y direction, and exits the shifter propagating along a direction parallel to the original incident path. Details on the geometrical parameters can be found in the caption of Fig. 2.3. In this simulation, rectangular slabs with the prescribed $\hat{\boldsymbol{\epsilon}}$ and $\hat{\boldsymbol{\mu}}$ were introduced in both the dielectric and metal sides. Note that the SPP wave fronts nicely follow the vertical lines of the transformation map shown in panel (b), which illustrates a good functionality of the device.

We have carried out simulations of this device at a range of optical wavelengths and computed the transmittance through it. For a SPP-shifter operating at a wavelength λ

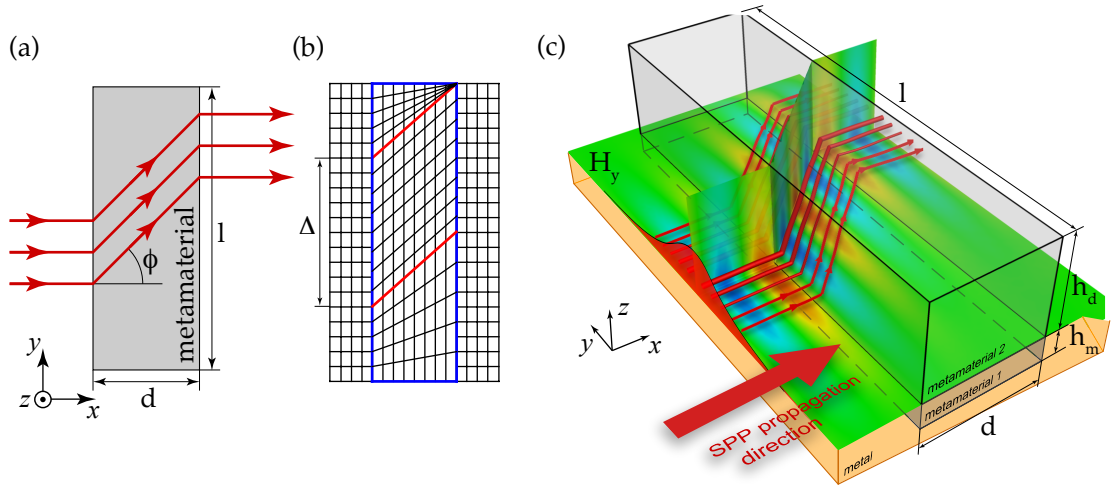

Figure 2.3: Beam shifter: a SPP with a gaussian profile of width Δ impinges on the device and experiences a shift of $\phi = 45°$. (a) Basic geometry of the 2D case. (b) Coordinate map of the transformation given by Eq. 2.6. (c) 3D view with power flow streamlines of a SPP at $\lambda = 1.5$ μm propagating on an air-gold interface. The device has in-plane dimensions 2.5μm $\times$10μm and thickness $h_d = 6$ μm and $h_m = 50$ nm. The color map represents the normalized magnetic field pattern.

the in-plane size of the device is given by $l = 20/3\lambda$ and $d = l/4$, while the width of the SPP gaussian profile is $\Delta = l - 2ad$. The blue and red spectra in Fig. 2.4 (a) show the transmittance through the beam shifter with and without introducing a transformation medium in the metal side, respectively. In the ideal situation (blue line), 100% of the SPP power flow is shifted over the whole spectra, whereas in the approximation (red line) the transmission is lowered due to the fact that the fraction of the SPP energy that is carried inside the metal is not shifted. For wavelengths larger than 900 nm the red and blue lines differ by less than 1% because most of the SPP energy is carried outside the metal. Panels (b) and (c) allow us to compare a cross-section of the 3D simulations showing the behaviour of H_y at the metal surface ($z = 0$) for $\lambda = 1500$ nm when we implement $\hat{\boldsymbol{\epsilon}}$ and $\hat{\boldsymbol{\mu}}$ in the dielectric and metal sides (b) or only in the dielectric side (c). Notice that there is almost no difference between the field distributions in both cases. On the other hand, at 800 nm the transmission is lowered to 98.5% when the metal is leaved untouched and at 600 nm it amounts to 95.5%. Although the effectiveness of the shifter at this wavelength is affected by the absence of a transformation medium in the metal side, its functionality (a shift in the SPP beam) is still very good, as can be seen by comparing panels (d) and (e). The reason for this weak wavelength dependence is clear.

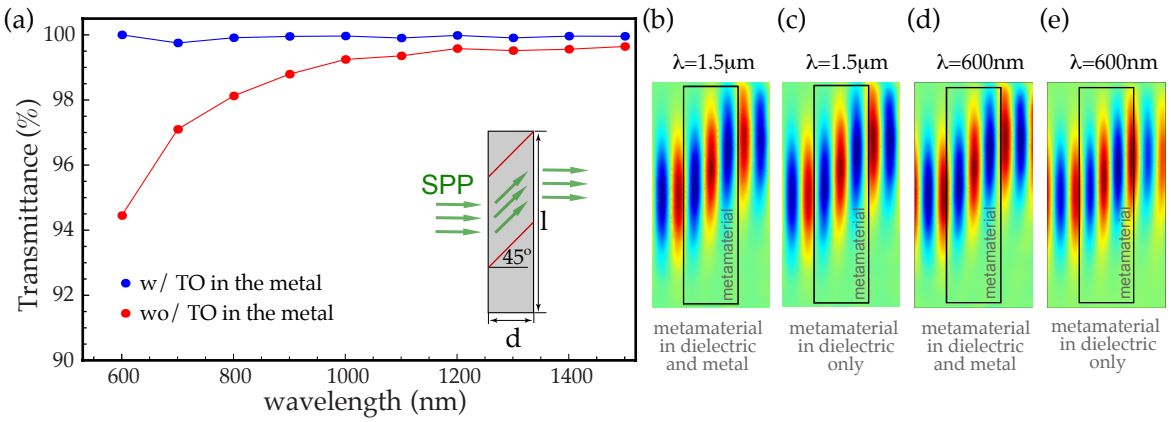

Figure 2.4: Performance of the SPP beam shifter for different wavelengths. (a) Transmittance curve of the shifter for SPPs at different wavelengths. The blue and red lines show the case with and without placing a transformation medium in the metal side, respectively. The TO parameters are implemented in a slab sized $d \times l \times h_d$ in the dielectric side and, only for the blue line, in a slab $d \times l \times h_m$ within the metal. The transmittance through the shift is measured as the ratio of the power flow that impinges the entrance face within $-\Delta/2 < y < \Delta/2$ to the power flow that exits within $0 < y < \Delta$. (b) Cross-section of the 3D beam shifter presented in Fig. 2.3 (c). H_y is evaluated at the metal surface, $z = 0$. For comparison, panel (c) shows a SPP beam shifter where the slab with the prescribed $\hat{\boldsymbol{\epsilon}}$ and $\hat{\boldsymbol{\mu}}$ has been introduced only in the dielectric side. Panels (d) and (e) render the operation of a beam shifter for a SPP at $\lambda = 600$ nm. In this case the in-plane dimensions of the rectangular slabs are 1μm $\times 4\mu$m and the thicknesses are $h_d = 600$ nm and $h_m = 50$ nm. In panel (e), only the dielectric side is manipulated.

The vacuum decay length of a SPP on a gold surface at 1.5 μm is 2.4 μm, much larger than the skin depth (23 nm) so the EM fields within the metal carry 0.01% of the total SPP energy, having practically no relevance compared to the EM fields in the dielectric. However, at $\lambda = 600$ nm, the ratio between vacuum decay length of the SPP and skin depth is reduced by a factor of 10 and the EM fields inside the metal are then relatively more important for the propagation of the SPP. For this wavelength, 1% of the SPP energy resides in the metal. Therefore, manipulation of the metal is not required since the performance of the SPP shifter is very good when the TO parameters are introduced in the dielectric side in the whole optical range.

SPP bend

The next plasmonic element we consider here is a right-angle bend. This device rotates the propagation direction of an incident SPP by $\frac{\pi}{2}$, as shown in the inset of Fig. 2.5 (a). We start by describing a 2D beam bend, which is designed by transforming a a squared region of side b in a Cartesian grid into a polar grid of squared cross-section $b \times b$ [223]. In order to bend a beam that propagates in the x direction by $\frac{\pi}{2}$, so that it exits the device propagating in the y direction, the appropriate transformation is the following:

$$r = y' \; ; \;\; \phi = \frac{\pi}{2b}(b - x') \; ; \quad z = z', \tag{2.8}$$

with $r = (x^2 + y^2)^{1/2}$ and $\phi = \arctan(y/x)$. As in the last case, this transformation is not continuous at the boundaries of the domain. The EM parameters retrieved from TO are expressed in Cartesian coordinates following 2.5 with:

$$\epsilon_r = \frac{2b}{\pi r} \; ; \;\; \epsilon_\theta = \frac{\pi r}{2b} \; ; \;\; \epsilon_z = \frac{2b}{\pi r}. \tag{2.9}$$

These tensors are singular at $r = 0$ (ϵ_r, $\epsilon_z \rightarrow +\infty$ and $\epsilon_\theta \rightarrow 0$). In order to avoid the divergence at $r = 0$ we limit the extreme values of the parameters by limiting the radius to vary from an inner value $r = a$ to the outer value $r = b$. Then the width of the bend is $\Delta = b - a$ and the curvature radius is $\rho = (a + b)/2$. According to our methodology, to design an SPP right-angle bend we need to perform the coordinate transformation in the cylindrical shell comprised between $r = a$, $r = b$, $\phi = 0$ and $\phi = \frac{\pi}{2}$. Ideally, we would need to implement the parameters $\hat{\boldsymbol{\epsilon}}_{\mathrm{TO}}$ and $\hat{\boldsymbol{\mu}}_{\mathrm{TO}}$ given by Eq. 2.5 and Eq. 2.9 within the dielectric material up to a height of h_d, while the metal optical properties should be modified following the expressions $\hat{\boldsymbol{\epsilon}} = \hat{\boldsymbol{\epsilon}}_{\mathrm{TO}} \cdot \epsilon_m$ and $\hat{\boldsymbol{\mu}} = \hat{\boldsymbol{\mu}}_{\mathrm{TO}}$ in a region of height h_m.

The performance of the SPP bend is studied in Fig. 2.5. Panel (a) shows the transmittance spectra of this device for two different situations: with and without implementing the TO parameters in the metal side (blue and red lines, respectively). The transmittance through the bend is calculated from simulations where SPPs at wavelengths ranging from 600 to 1500 nm are launched into the entrance of a bend of curvature radius $\rho = \frac{5}{2}\lambda$. The field distribution results from a simulation of an SPP at $\lambda = 900$ nm propagating in the x direction and travelling through a right angle bend of radius $\rho = 1.5$ μm is shown in Fig. 2.5 (b). The transmittance is obtained from measurements of the power flow at the entrance and exit faces of the bend. The blue line in the transmittance curve corresponds to the ideal case where the TO parameters are implemented both in the metal and dielectric sides. The transmission is over 99% for all wavelengths. On the other hand, the red line follows the transmittance through the bend when only the dielectric side is

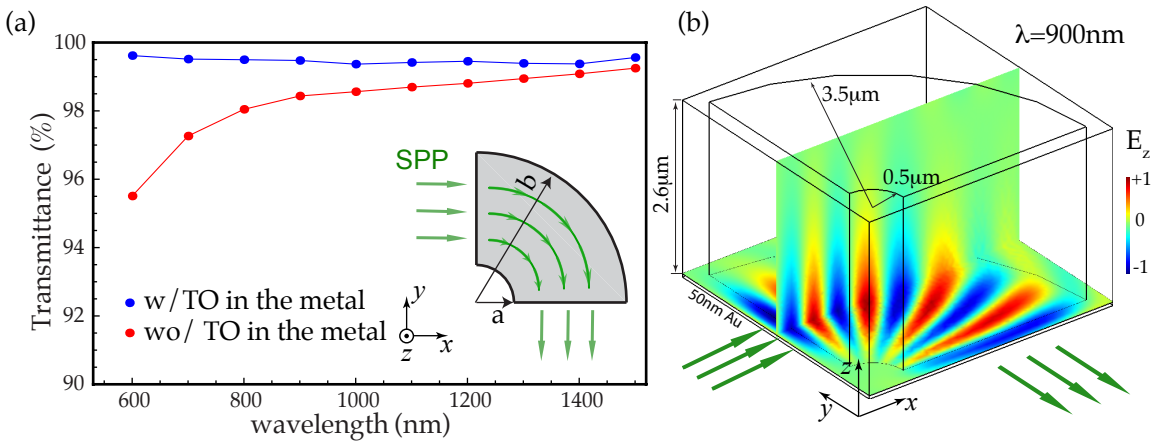

Figure 2.5: Simulation results for the SPP right-angle bend. (a) Transmission through the bend for SPPs of gaussian profiles (width Δ) at different wavelengths. The blue and red lines show the case with and without placing a transformation medium in the metal side, respectively. The bend curvature radius is $\rho = 5/2\lambda$ and the width is $\Delta = 10/3\lambda$. The inset panel shows the geometry layout from a top view. (b) z-component of the electric field for a SPP at 900 nm travelling through the bend without applying TO in the metal side.

modified. It is clearly seen that this is indeed a very good approximation, as the transmission is always higher than 95%, approaching the same results as the ideal simulations at large wavelengths. For wavelengths larger than 900 nm, the blue and red curves differ by only 2% or less, meaning that by not structuring the metal side less than 2% of the SPP powerflow will be lost. On the other hand, for short wavelengths (600-800 nm), the transmittance of the approximate situation is around 4% lower than the transmittance of the ideal blue curve, a value that corresponds to the fraction of the SPP energy that is contained in the metal. Therefore, we have shown that in the approximate but more feasible situation of structuring only the dielectric side, the performance of the SPP bend is very good over the entire wavelength range considered. However, in some cases the SPP wave fronts might suffer some distortions even though the transmittance is still very high.

SPP lens

Finally, we consider a plasmonic lens capable of focusing an incident gaussian SPP of a finite width. As described in Ref. [223], transforming a semi-circular region of radius a into a rectangular region sized $a \times 2a$ leads to a 2D rectangular lens whose focal point is located at the center of its exit face. A sketch of the geometry layout is shown in the

inset panel of Fig. 2.6 (a). Assuming an incident wave from the left ($-x$ direction), we place the lens in the $x-y$ plane in the region defined by $-a \leq x \leq 0$ and $-a \leq y \leq a$. For such a geometry, the appropriate transformation is found to be:

$$x = \frac{ax}{\sqrt{a^2 - y^2}} \; ; \;\; y = y' \; ; \;\; z = z'. \tag{2.10}$$

The TO procedure (Eq. 2.39 yield the following EM tensors in cartesian coordinates:

$$\hat{\boldsymbol{\epsilon}}_{\mathrm{TO}}/\epsilon_0 = \hat{\boldsymbol{\mu}}_{\mathrm{TO}}/\mu_0 = \begin{pmatrix} \frac{x^2y^2a^{-1}(a^2-y^2)^{-1}+a}{\sqrt{a^2-y^2}} & \frac{xy}{a\sqrt{a^2-y^2}} & 0 \\ \frac{xy}{a\sqrt{a^2-y^2}} & \frac{\sqrt{a^2-y^2}}{a} & 0 \\ 0 & 0 & \frac{\sqrt{a^2-y^2}}{a} \end{pmatrix}. \tag{2.11}$$

These parameters are inhomogeneous and anisotropic and take singular values at the boundaries of the device. As in the previous examples, the lens for SPPs consists of a rectangular slab sized $a \times 2a \times h_d$ and placed on top of the metal film, with parameters $\hat{\boldsymbol{\epsilon}}_{\mathrm{TO}}$ and $\hat{\boldsymbol{\mu}}_{\mathrm{TO}}$. In principle, a rectangular slab of dimensions $a \times 2a \times h_m$ and parameters $\hat{\boldsymbol{\epsilon}}_{\mathrm{TO}} \cdot \epsilon_m$ and $\hat{\boldsymbol{\mu}}_{\mathrm{TO}}$ should be implemented in the metal side.

We have carried out 3D simulations of a gaussian SPP width Δ travelling through the lens at a range of optical wavelengths, and we show the results in Fig. 2.6. After entering the lens, the SPP is focused at the exit side of the device and continues to propagate in cylindrical wavefronts. Panel (a) shows the transmittance through the device as a function of the SPP wavelength for a quantitative analysis of the lens effectiveness in two situations: when the TO parameters are or are not implemented in the metal side (blue and red curves, respectively). In the ideal case where transformation media are placed in the metal and dielectric sides, the transmittance is close to 100% at all wavelengths. On the other hand, the red line shows that the approximation consisting of not modifying the metal side is very good for wavelengths above 900 nm as in that wavelength range the transmittance lies above 98%. For wavelengths below 900 nm the transmittance is lowered up to an 8% compared to the ideal case because for shorter wavelengths there is a higher fraction of the SPP energy contained in the metal. However, the field patterns at these wavelengths (not shown here) reveal that the wave propagation and focusing is still very good. Panel (b) shows a plot of the field for an SPP at 900 nm travelling through the lens. While the SPP travels a distance of $a = 2250$ nm, its wavefronts are smoothly focused on a spot of the order of its wavelength.

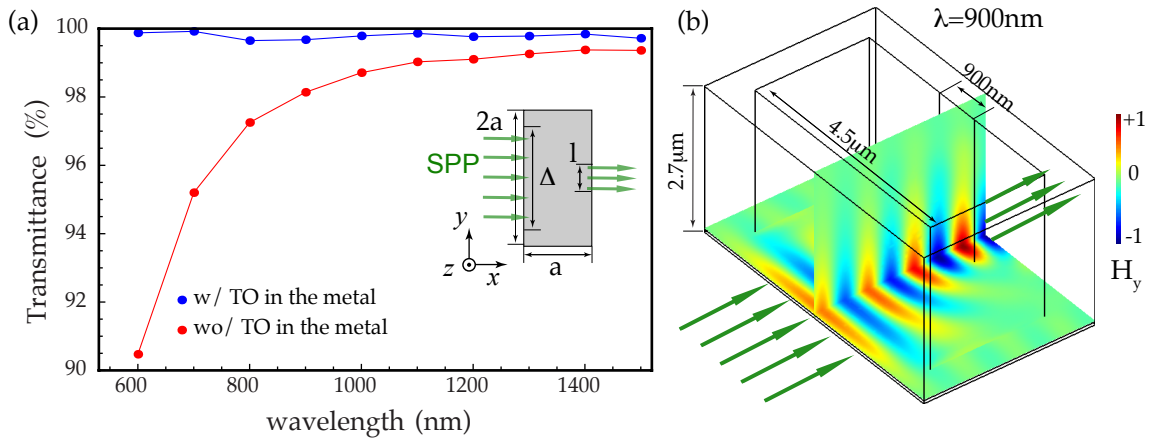

Figure 2.6: Simulation results for a 3D SPP lens. A SPP exhibiting a gaussian profile of width Δ and propagating in the x direction impinges on the lens, where it is focused to a width of the order of the wavelength. (a) Transmittance spectra through the lens for two cases: with and without placing a transformation medium in the metal side (blue and red lines respectively). The transmittance is measured as the ratio of the power flow incident on the left to the power flow that exits within a wavelength width. The in-plane size of the lens is $a \times 2a$, with $a = 2.5\lambda$, while the width of the incident beam is $\Delta = 3.75\lambda$ (see inset panel). (b) 3D view of the y-component of the magnetic field of an SPP at 900 nm travelling through the lens. In this simulation, the transformation medium was placed in the dielectric side only. Note that the lines parallel at the exit face separated by 900 nm constitute an auxiliary element to measure the transmittance and do not represent a physical boundary.

2.3 Conformal and quasiconformal mappings for realistic models

2.3.1 Conformal and quasiconformal mappings

The coordinate transformations we have considered so far present some technical problems when it comes to practical realizations as they generally yield highly anisotropic $\hat{\boldsymbol{\epsilon}}$ and $\hat{\boldsymbol{\mu}}$. However, if we choose an appropriate coordinate transformation by imposing some mathematical requirements, isotropic EM parameters may be obtained. This means that only isotropic dielectrics would be necessary to construct devices, reducing losses and opening up the possibility of broad-band performances. In particular, conformal and quasiconformal transformations give rise to isotropic material parameters, yielding easier implementations of transformation media based on isotropic dielectrics. Conformal

mappings were first investigated within this context in Ref. [55], where an invisibility device was designed by applying a transformation in the complex plane to Helmholtz's equation. This concept was also applied to design other isotropic devices, such as arbitrary waveguide bends within the limit of geometrical optics [224, 225] or directional antennas, flat lenses and beam bends [222]. Regarding plasmonic systems, conformal and quasiconfomal transformations have been employed to design light-harvesting [106] devices and ground-plane cloaks [98].

In the following we will how to derive the isotropic EM parameters that correspond to a conformal transformation within the TO framework. Let us start by assuming that the virtual and physical domains are contained in the complex planes $z = x' + iy'$ and $w = x + iy$, respectively. As we are dealing with SPPs, 2D waves extending into the third dimension (the direction perpendicular to the metal-dielectric interface), we can restrict our study to 2D transformations. A 2D coordinate transformation from virtual to physical coordinates can then be described by means of a complex function:

$$w = f(z, \overline{z}) = x(x', y') + iy(x', y'). \tag{2.12}$$

This transformation is said to be conformal if the function $f(z)$ depends on z but not on its conjugate $\overline{z}$ and is analytical, i.e. $f'(z)$ can be defined (see Appendix A.1 for more details). Then, the Cauchy-Riemann equations are satisfied ($\partial x/\partial x' = \partial y/\partial y'$ and $\partial x/\partial y' = -\partial y/\partial x'$). Consequently, the metric tensor of a conformal transformation reduces to a diagonal matrix:

$$\hat{G}^{-1} = g^{11} \cdot \mathbb{I}_{2\times 2} \quad \text{where} \quad g^{11} = (g_{11})^{-1} = \frac{\partial^2 x}{\partial x'^2} + \frac{\partial^2 x}{\partial y'^2}. \tag{2.13}$$

This means that the grid described by the transformation map $w = f(z)$ is orthogonal, i.e., the angles between coordinate lines are preserved after the mapping. According to the TO rule (Eq. 2.3), we calculate the EM parameters of the transformation medium that corresponds to a 2D conformal transformation:

$$\hat{\boldsymbol{\epsilon}}_{TO}/\epsilon_0 = \hat{\boldsymbol{\mu}}_{TO}/\mu_0 = \sqrt{g}\hat{G}^{-1} = \begin{pmatrix} 1 & 0 & 0 \\ 0 & 1 & 0 \\ 0 & 0 & \sqrt{g} \end{pmatrix}. \tag{2.14}$$

Now let us consider the case of an EM wave with the electric field polarized along the z-axis and the magnetic field in the x-y plane. The propagation of this wave is determined by the electric permittivity along the z-axis and the magnetic susceptibility tensor in the $x - y$ plane. According to the equation above, these are the following:

$$\epsilon_z = \epsilon_0\sqrt{g} \quad ; \quad \hat{\boldsymbol{\mu}} = \mu_0 \mathbb{I}_{2\times 2}. \tag{2.15}$$

This set of parameters is equivalent to an isotropic refractive index:

$$n = \sqrt{\epsilon_z \mu} = n_0 g^{1/4}, \tag{2.16}$$

where $n_0 = \sqrt{\epsilon_0 \mu_0}$ is the background refractive index. If on the other hand, the EM wave is polarized with the magnetic field along the z-axis, then $\epsilon = \epsilon_0$, $\mu_z = \mu_0 \sqrt{g}$ and $n = \sqrt{\epsilon \mu_z} = n_0 g^{1/4}$. Notice that, as shown in Appendix A.2, our approach leads to the same result as the *Optical Conformal Mapping* technique based on Helmholtz's equation [55]. Therefore, for problems where the two polarizations can be treated separately, a 2D conformal transformation leads to an isotropic transformation medium, with a refractive index defined by Eq. 2.16. On the other hand, SPPs need to be considered separately as their dispersion relation depends on the electric permittivity and the magnetic permeability rather than on the refractive index. However, we will show in the following that the propagation of an SPP in a medium with the exact diagonal anisotropic parameters (Eq. 2.14) is very similar to that in a medium with the approximate isotropic refractive index (Eq. 2.16) for a given conformal transformation.

Thus, conformal transformations lead to transformation media described by isotropic refractive indexes. However, an analytical conformal transformation is not known for every desired functionality. In those cases, quasiconformal maps are useful for designing TO media based on isotropic materials. They constitute a subset of coordinate transformations, $w = f(z, \overline{z})$, that satisfy less requirements than conformal transformations. In particular, they can depend on z and $\overline{z}$ (see Appendix A.3 for more details). In contrast to conformal transformations, quasiconformal transformations map squares in the original space to rectangles of constant aspect ratio in the transformed space. Since they are generated numerically through the minimization of, for instance, the *Modified-Liao* or *Winslow* functionals [226, 227], they are able to treat arbitrarily complex boundaries. A quasiconformal map is the optimal map of minimum anisotropy for a given domain, a fact that can be used to design isotropic transformation media. In Ref. [93], a quasiconformal map for a ground-plane cloak was obtained by minimizing the *Modified-Liao* functional with sliding boundary conditions. Applying this idea, several invisibility ground-plane cloaks operating at optical [89, 95] and microwave [94] frequencies were fabricated out of isotropic dielectric materials and a non-resonant metallic metamaterial, respectively.

In our work, we have made use of an approach to quasiconformal mapping generation that does not need of functional minimizations [228, 229] . This method takes advantage of the fact that the transformation functions, $x'(x, y)$ and $y'(x, y)$, that minimize *Winslow* functional, also solve Laplace's equation:

$$\nabla^2 x' = 0; \quad \nabla^2 y' = 0, \tag{2.17}$$

where the Laplacian, taken in the physical space, is acting on the virtual coordinates. Therefore, solving Laplace's equation in physical domain subject to sliding boundary conditions, $\vec{n} \cdot \vec{\nabla} x'^i$, leads to a quasiconformal map. Once the functions $x'(x, y)$ and $y'(x, y)$ are obtained, the gradients of the transformation can be computed in order to construct the inverse Jacobian matrix, $\hat{A}^{-1} = \partial x^{i'}/\partial x^i$. By inverting it, the Jacobian matrix needed for the TO procedure is obtained. Next, assuming that the anisotropy of the quasiconformal mapping is negligible, we can approximate its metric tensor by a diagonal matrix and define the transformation medium by means of Eq. 2.14. Again, for problems where the polarization state of the EM wave is well defined an isotropic refractive index can be defined following Eq. 2.16. In this way, a quasiconformal transformation can be used to design an isotropic TO medium defined by the index profile $n = g^{1/4}$.

In the next subsection we present several examples of isotropic implementations of plasmonic devices. We present an isotropic SPP shifter, an isotropic SPP lens, an isotropic SPP bend and an isotropic SPP lens. We quantify the quality performance of these devices and we compare them to their anisotropic counterparts shown in Section 2.2. Finally, we also consider two different realizations of a SPP ground-plane cloak in 2D and 3D.

2.3.2 Isotropic implementations of plasmonic devices

Isotropic implementation of an SPP shifter

As a first example of a plasmonic device based on isotropic dielectrics, let us consider the design of an SPP parallel shifter using a quasiconformal mapping. As in the previous examples, a TO device will be placed on top of the surface through which the SPP travels. In order to design an isotropic shifter with the same functionality as the anisotropic previously considered, we start by defining the geometry shown in the inset panel of Fig. 2.7 (a). The transformation medium, whose top view is shown in gray, is divided into three regions: an entrance for the SPP, of width $l/2$, at the left, the shifting region (at 45°), of length d, and an exit region at the right. Then, we solve Laplace's equations within the gray region with sliding boundary conditions $\vec{n} \cdot \vec{\nabla} x'$ at the lower and upper boundaries and $\vec{n} \cdot \vec{\nabla} y'$ at the left and right boundaries. The resulting quasiconformal map is plotted in Fig. 2.7 (b), where the grid corresponds to lines of $x'(x, y) = constant$ and $y'(x, y) = constant$. Following the method described above, we obtain an isotropic refractive index profile that varies between 0 and 3.5 (color map in Fig. 2.7 (b)).

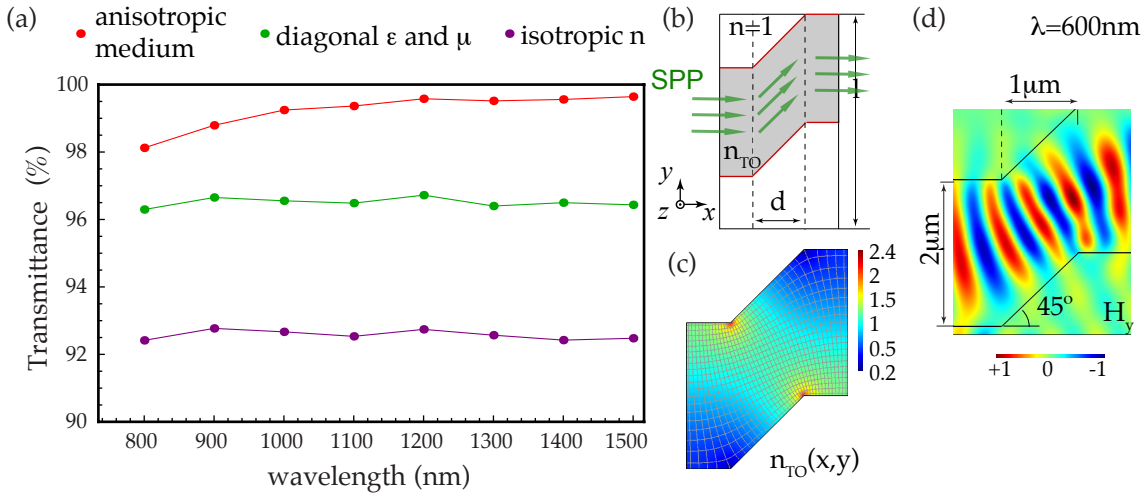

Figure 2.7: Simulation results of an isotropic SPP parallel shifter. (a) Transmittance through the shift for SPPs at different wavelengths. The blue line shows the transmission for a transformation medium characterized by anisotropic parameters (same as in Fig. 2.3). The red line corresponds to a parallel shifter characterized by an isotropic refractive index. In both cases, the TO parameters are implemented in the dielectric side only. The geometry layout is shown in the inset panel. (b) Quasiconformal map (grid) and refractive index profile (color map) of the device. (c) Magnetic field, H_y, of an SPP at 600 nm travelling through the isotropic shifter after implementing the index shown in panel b.

The transmittance curve in Fig. 2.7 (a) shows the results obtained from 3D simulations of the isotropic SPP shifter. SPPs at different wavelengths (from 800 to 1500 nm) travel along a gold-vacuum interface and impinge on the transformation medium placed on top of the gold surface. As we have previously shown, a transformation medium in the metal is not needed. The size of the device is the same as for the anisotropic shifter discussed above. The red line shows the transmittance through the shifter when the index profile $n(x, y)$ shown in panel b is implemented. The blue line shows the transmittance of the anisotropic shifter (from Fig. 2.3), allowing us to compare the efficiency of both devices. While the blue line takes transmission values above 98%, the red line lies beneath, around 92%. The are two main reasons for this feature. First, the impedance mismatch at the interfaces to free space causes losses. Second, the wave fronts of the SPP are distorted in order to follow the vertical lines of the quasiconformal map shown in panel b. This feature can be seen in Fig. 2.7 (c), were an SPP at 600 nm is guided through an isotropic beam shifter.

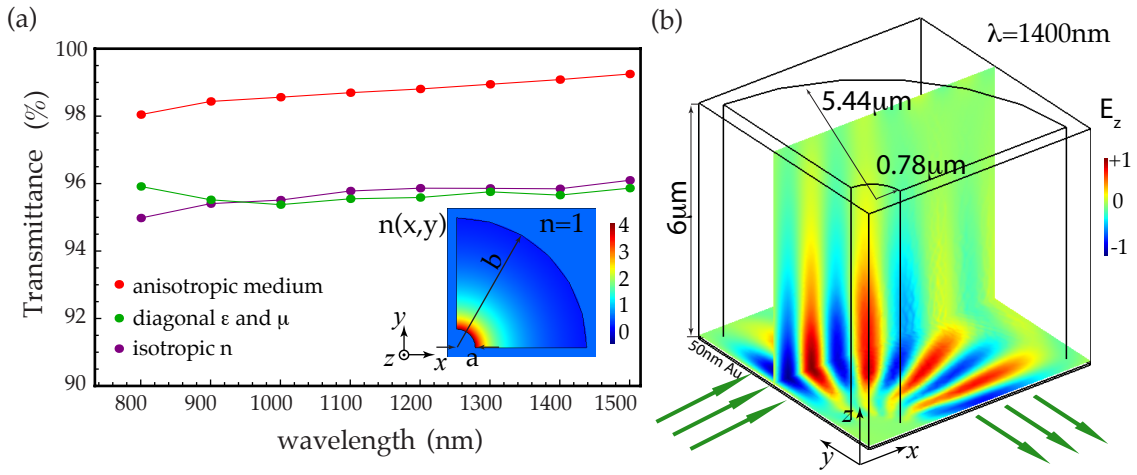

Figure 2.8: Simulation results of an SPP bend characterized by an isotropic refractive index. (a) Transmittance through the bend for SPPs at different wavelengths comparing the isotropic and anisotropic bends. The blue line corresponds to the case of a transformation medium characterized by anisotropic parameters (shown in Fig. 2.5). The red line shows the transmission of a bend characterized by an isotropic refractive index (top view plotted in the inset panel). In both cases, the TO parameters are implemented in the dielectric side only. The geometrical parameters are the same as in Fig. 2.5. (b) Electric field, E_z, of an SPP at 1400 nm travelling through the isotropic bend. Impedance mismatch occurs at the boundaries of the transformation medium and reduces the transmittance of the device.

Isotropic implementation of an SPP right-angle bend

A beam bend of the same characteristics as that discussed in Section 2.2 can also be realized with isotropic materials. By means of a conformal transformation, a more realistic optical device that bends the SPP propagation direction by a right-angle can be designed. The anisotropic parameters 2.9, yielded by the transformation 2.8, are replaced by an isotropic refractive index if a conformal transformation is made [222]:

$$n(r) = \frac{2b}{\pi r}. \tag{2.18}$$

As illustrated in the inset of Fig. 2.8 (a), the transformation medium, characterized by $n(r)$, is a cylindrical shell, $a < r < b$, of height h_d placed on top of the metal surface. This refractive index smoothly decreases from 4.46 at $r = a$ to 0.67 at $r = b$.

We have tested the functionality of the isotropic SPP bend by means of 3D simulations. The curve in Fig. 2.8 (a) compares the transmittance through the SPP bend with anisotropic parameters (blue line) and isotropic index (red line) over a wavelength

range between 800 and 1500 nm. In both cases the transmission increases with the wavelength due to the fact that the metal is leaved untouched and the energy carried by the plasmonic field contained in the metal decreases with the wavelength. However, the transmission through the isotropic bend is limited to 96% due to impedance mismatch to free space. This feature, not present for the anisotropic case, arises when conformal transformations are used. As shown in Fig. 2.8 (a), the refractive index abruptly changes from $n = 1$ to $n(r)$ at the interfaces along the entrance and exit faces of the bend. As a consequence, the SPP suffers reflections that lower the transmission. Figure 2.8 (b) illustrates the performance of the bend for a gaussian SPP at 1400 nm. After impinging on the device, close to 96% of the SPP is bent in a right angle and leaves the transformation medium through the exit face to continue its propagation through the metal.

Isotropic implementation of an SPP Lens

In this section we discuss the realization of an SPP lens with isotropic materials. The geometry and purpose of the device are the same as presented previously (see Section 2.2). An isotropic refractive index is obtained if, instead of the transformation given by Eq. 2.10, a conformal transformation between a semicircle and a rectangle is performed. In particular, we will make use of a Schwarz-Christoffel transformation as described in Ref. [222]. The refractive index profile that results from this transformation smoothly varies from 0 to 1.31 and is shown in Fig. 2.9 (b). To design the SPP lens a transformation medium with a rectangular cross-section characterized by the index distribution $n_{TO}(x, y)$ and height h_d is placed on top of a metal film. The device is surrounded by vacuum ($n = 1$).

Figure 2.9 shows the results obtained from 3D simulations of SPPs propagating through the lens. The three transmittance curves in panel (a) compare the functionality of SPP lenses characterized by different EM parameters. The red line shows the best performance as it represents the transmittance through a lens characterized by the anisotropic and singular parameters given by Eq. 2.11 (see Fig. 2.6). The green and purple lines correspond to lenses designed by means of a conformal transformation and therefore are situated at lower transmittance values due to impedance mismatch to free space. The green line accounts for the transmittance through a lens with diagonal parameters, $\hat{\boldsymbol{\epsilon}}_{\mathrm{TO}}$ and $\hat{\boldsymbol{\mu}}_{\mathrm{TO}}$, that are obtained from the conformal transformation according to Eq. 2.14. Only the third component of the tensors diagonal is different from 1, and it varies smoothly from 0 to 1.72. The purple line corresponds to the isotropic refractive index retrieved from the conformal transformation according to Eq. 2.16 and is shown in

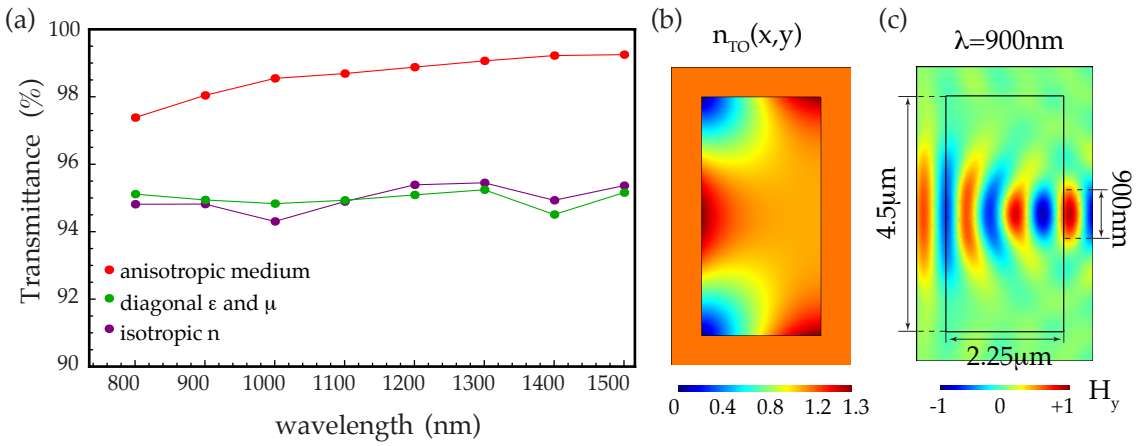

Figure 2.9: Results obtained from 3D simulations on SPPs propagating through a lens. (a) Transmittance spectra through lenses characterized by different EM parameters. Red line: anisotropic $\hat{\boldsymbol{\epsilon}}_{\mathrm{TO}}$ and $\hat{\boldsymbol{\mu}}_{\mathrm{TO}}$ (same as in Fig. 2.6). Green line: diagonal $\hat{\boldsymbol{\epsilon}}_{\mathrm{TO}}$ and $\hat{\boldsymbol{\mu}}_{\mathrm{TO}}$ resulting from a conformal transformation according to Eq. 2.14. Purple line: isotropic refractive index resulting from the same conformal transformation. (b) Refractive index profile yield by the conformal transformation. (c) Top-view of the y-component of the magnetic field. An SPP travels through a lens characterized by the refractive index shown in b and is focused within a width of the order of the wavelength.

panel (b). The two cases considered for the conformal transformation (diagonal $\hat{\boldsymbol{\epsilon}}_{\mathrm{TO}}$ and $\hat{\boldsymbol{\mu}}_{\mathrm{TO}}$ and isotropic n) give close transmittance results in this example, similarly to the SPP bend results above. Panel (c) shows the field pattern of an SPP travelling trough the isotropic lens as its wavefronts are focused on the exit face.

SPP ground-plane cloak

The TO-based approach to the design of plasmonic devices can also be applied to minimizing the scattering to the far-field of SPPs on irregular surfaces. Uneven surfaces result in strong scattering that lead to radiation of the SPP into free-space, as illustrated in Fig. 2.10 (a), where a SPP travelling along an air-gold interface encounters an obstacle. Here we model the irregularities of the metal surface as a bump of length l and height h_0, and with a shape given by $z(x) = h_0 \cos^2\left(\frac{\pi}{l}x\right)$. We consider a SPP at a wavelength of 700 nm, and a bump of length $l = 2$ μm and height $h_0 = 200$ nm. For these parameters, about 15% the plasmonic energy is scattered by the bump. This scattering can be supressed by means of a ground-plane cloak, whose main difference with the rest of the TO-based devices that we have considered up to here is the geometry. A ground-

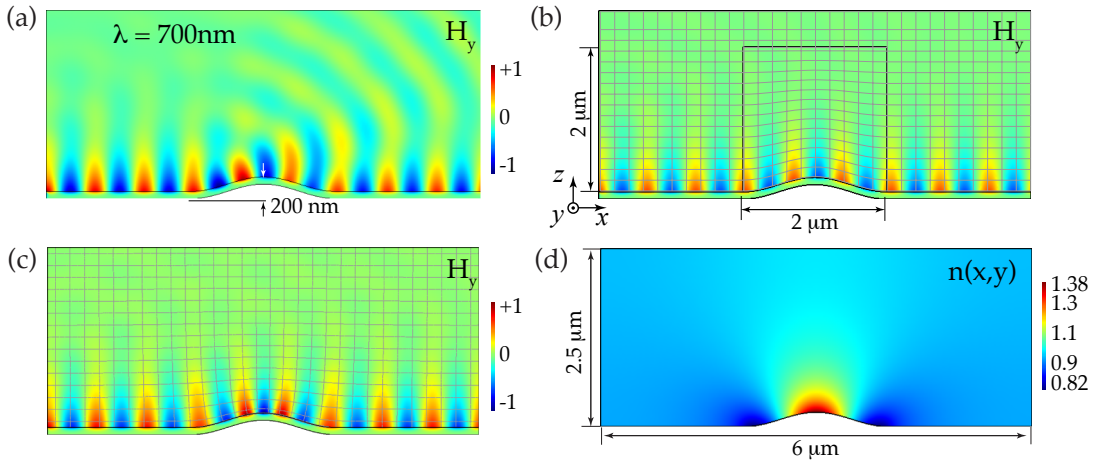

Figure 2.10: The scattering from a bump on a metal surface can be suppressed by means of a ground-plane cloak. (a) A SPP at 700 nm is scattered when it encounters a cos^2-shaped bump 200 nm high and 2 μm long in an air-gold interface. The SPP propagates in the x direction and the geometry is invariant in the y direction. (b) Scattering losses are suppressed when an anisotropic cloak (2 μm $\times$ 2 μm) is placed on top of the bump. The grid lines correspond to the coordinate map of the transfinite transformation used to derive the EM parameters of the cloak. (c) The bump is cloaked for SPPs by means of an isotropic cloak. The lines show the quasiconformal coordinate grid, that determine the refractive index profile used in the cloak and depicted in (d). In (a), (b) and (c) the color map shows the SPP magnetic field profile, H_y.

plane cloak inherently needs to be placed on a metal surface, because it mimics a highly reflective surface instead of an empty space. Taking advantage of the presence of this metal-dielectric interface, we apply directly the TO recipe previously derived for a 2D ground-plane cloak illuminated by a plane wave [93] to the case of SPP-illumination. Depending on the transformation that we choose, the material parameters of the cloak can be anisotropic or isotropic. Here we compare both cases.

The design of the anisotropic cloak involves transforming a rectangular region of a Cartesian space sized $l \times h$ into a region of the same shape except that its bottom boundary follows the shape of the bump. The simplest mapping that can be done between these two spaces is a transfinite transformation:

$$x = x',\ y = y',\ z = z' + h_0 \left(1 - \frac{z'}{h}\right) \cos^2\left(\frac{\pi}{l} x'\right). \tag{2.19}$$

The transformed coordinate grid when $l = 2$ μm and $h_0 = 200$ nm is depicted with gray lines in Fig. 2.10 (b). When applying the TO procedure, this transformation leads to the

following material parameters:

$$\hat{\boldsymbol{\epsilon}}_{\mathrm{TO}} = \hat{\boldsymbol{\mu}}_{\mathrm{TO}} = \frac{1}{\Delta}\begin{pmatrix} 1 & 0 & f_{xz} \\ 0 & 1 & 0 \\ f_{xz} & 0 & f_{zz}, \end{pmatrix} \tag{2.20}$$

where $\Delta = \frac{\partial z}{\partial z'}$, $f_{xz} = \frac{\partial z}{\partial x'}$ and $f_{zz} = {f_{xz}}^2 + \Delta^2$. When a medium with the prescribed anisotropic $\hat{\boldsymbol{\epsilon}}_{\mathrm{TO}}$ and $\hat{\boldsymbol{\mu}}_{\mathrm{TO}}$ is placed on top of the bump, a SPP smoothly travels through it without any scattering. This is confirmed by the 2D simulation illustrated in Fig. 2.10 (b), where the magnetic field, H_y, of a SPP at 700 nm going through the cloak is shown.

On the other hand, the same functionality can be achieved by means of an isotropic cloak. In order to design the isotropic ground-plane cloak, the transfinite transformation has to be replaced by a quasiconformal one. In this case, the transformation medium is sized $h' \times l'$. The quasiconformal map (shown in panel c) was generated by solving Laplace's equation with sliding boundary conditions $\vec{n} \cdot \vec{\nabla} x'$ (at the lower and upper boundaries) and $\vec{n} \cdot \vec{\nabla} y'$ (at the left and right boundaries). The effect of a ground-plane cloak is achieved by setting $y' = 0$ at the lower boundary so that the bump is mapped onto a flat surface. In contrast to the previous transformation, and as can be seen in panel (c), the new coordinate grid (gray lines) preserves the right-angles. When the TO procedure is followed, this fact results in an isotropic refractive index $n(x, y)$ for the cloak illustrated in panel (d). The index profile is smooth, ranging from 0.82 to 1.38, and it recovers the background value $n = 1$ at the outer boundaries of the cloak. The wave fronts of a SPP travelling through the cloak follow the transformed grid while it smoothly goes through the bump without scattering, as illustrated for $\lambda = 700$ nm in panel (c).

Using the same tools, a ground-plane cloak can also be devised for hiding a 3D bump on a metal surface. Let us consider the bump shown in Fig. 2.11, which is described by $z = z' + h_0\left(1 - \frac{z'}{h}\right)\cos^2\left(\frac{2\pi}{l}x'\right)\cos^2\left(\frac{2\pi}{l}y'\right)$. As a proof of principle we present an anisotropic 3D cloak, whose design involves a transfinite transformation analogous to the 2D case. The transformation is in this case:

$$x = x' \ , \ y = y' \ , \ z = z' + h_0\left(1 - \frac{z'}{h}\right)\cos^2\left(\frac{2\pi}{l}x'\right)\cos^2\left(\frac{2\pi}{l}y'\right). \tag{2.21}$$

According to the TO rules, the prescribed material parameters are the following:

$$\hat{\boldsymbol{\epsilon}}_{\mathrm{TO}} = \hat{\boldsymbol{\mu}}_{\mathrm{TO}} = \frac{1}{\Delta}\begin{pmatrix} 1 & 0 & f_{xz} \\ 0 & 1 & f_{yz} \\ f_{xz} & f_{yz} & f_{zz} \end{pmatrix}, \tag{2.22}$$

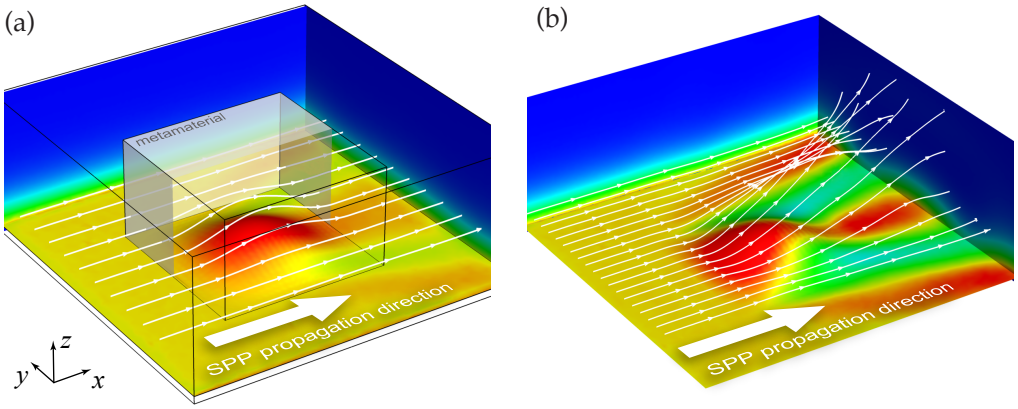

Figure 2.11: (a) Power flow distribution (color map) and power flow lines of a 3D ground-plane cloak placed over a 3D $\cos^2$-shaped gold bump of dimensions 1250 nm $\times$ 1250 nm $\times$ 200 nm. (c) Power flow for the 3D gold scatterer without the cloak.

where $\Delta = \frac{\partial z}{\partial z'}$, $f_{xz} = \frac{\partial z}{\partial x'}$, $f_{yz} = \frac{\partial z}{\partial y'}$ and $f_{zz} = {f_{xz}}^2 + {f_{yz}}^2 + \Delta^2$. We present in Fig. 2.11 (a) a simulation that confirms the effectiveness of the 3D cloak for a SPP operating at $\lambda = 600$ nm. The color map and the streamlines represent the density and the direction of the power flow of the SPP, respectively. The SPP is guided around the bump and continues travelling along the gold-vacuum interface. For comparison, Fig. 2.11 (b) shows a SPP scattering from the gold bump when the cloak is not present. We see that the fraction of the SPP that impinges directly into the bump is scattered upwards. As in the 2D geometry, this radiation into free space is totally suppressed when the cloak is present.

Proposal for a plasmonic concentrator

Finally, we present here a proposal for the experimental realization of a plasmonic field concentrator. The purpose of this device is to enhance the EM energy density of incident SPPs at a given area. The design of the concentrator is based on the implementation of the refractive index profile, $n(r)$, shown in Fig. 2.12 (a) in a circular region $R_1 < r < R_2$ surrounding a dielectric core of index n_c. The index profile varies radially following $n(r) = n_b R_2/r$, with n_b being the background index, such that the index landscape is continuous at the outer radius, $r = R_2$. In order to ensure that it is also continuous at the inner radius, this value has to be chosen as $R_1 = R_2 n_b/n_c$. When this index profile is implemented by means of dielectric materials on top of a metal surface, it acts as a

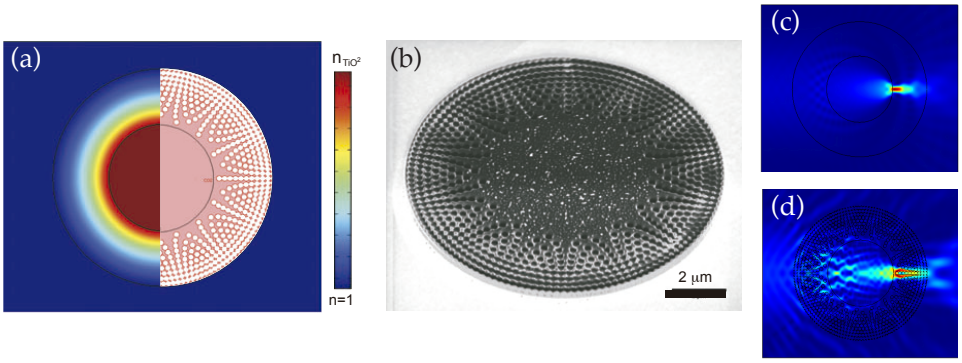

Figure 2.12: A plasmonic concentrator is achieved by means of an effective medium. (a) The index profile (left hand side) smoothly varies from $n_{\mathrm{TiO_2}}$ at the center to $n = 1$ at the outer edge. This profile is realized by drilling holes of constant radius in a dielectric disk (right hand side), such that their density distribution reproduces the refractive index landscape. (b) Sample fabricated by Prof. Quidant's group at ICFO by focused ion beam milling of a TiO_2 layer on top of a gold surface. (c) Simulation results showing concentration for SPPs at $\lambda = 1.5$ μm. (d) Performance of the effective medium approach. (a,b) Reproduced from Ref. [101].

lens for impinging SPPs, concentrating plasmonic energy in a focus at the inner radius. In principle, the plasmonic concentrator can be sub-wavelength, the only factor limiting this fact being fabrication issues.

In order to realize the index profile, $n(r)$, we propose the patterning of a dielectric material placed on top of the metal surface. This leads to an isotropic metamaterial that effectively reproduces the index profile. To design the patterning we make use of an effective medium approach. The schematic in Fig. 2.12 (a) represents a dielectric disk drilled with holes such that the refractive index profile shown at the left hand side of the panel is reproduced. For the effective medium we have considered a circular arrangement of air holes in the dielectric material surrounding a core without holes (index n_c). The effective refractive index is given by:

$$n = f + (1 - f)n_c, \tag{2.23}$$

where f is the filling fraction. Let r_0 be the radius of the holes and $\mathrm{d}r$ and $\mathrm{d}\theta$ the radial and angular separations between holes, respectively. Then, the filling fraction reads as:

$$f = \frac{\pi r_0^2}{r\mathrm{d}r\mathrm{d}\theta}. \tag{2.24}$$

Following this design, a sample was fabricated by the group of Professor Quidant at ICFO. Focused ion beam was used to drill holes on a TiO_2 layer on top of a gold surface,

as shown in Fig. 2.12 (c). The size of the disk is $R_2 = 6$ μm and the inner core of constant index has a radius $R_1 = 3$ μm, while the radius of the air holes is 105 nm. The core region $r < R_1$ has a refractive index $n = 2.35$ and holes of constant radius but varying density collectively behave as an effective medium with a gradually varying refractive index up to $n = 1$ at $r = R_2$. Simulation results demonstrating plasmonic concentration of EM energy at 1.5 μm can be seen in Fig. 2.12 (c) for an ideal device. On the other hand, Fig. 2.12 (d) shows the effect of realizing such a device by means of the effective medium. As the simulation shows, although the presence of the structured dielectric introduces scattering losses, plasmonic concentration is still achieved.

2.4 Experimental realization of plasmonic devices

The different examples presented in Sections 2.2 and 2.3 illustrate the power of Transformation Plasmonics to fully control SPP flow and design complex functionalities that would not be achievable otherwise. However, the experimental implementation of such control is conditioned by the possibility to match the required material parameters. In this Section, we briefly review recent experimental advances towards the realization of complex SPP functionalities (see Ref. [101]). We first discuss the plasmonic broadband carpet cloak realized in Ref. [99]. Next, we review the experimental realization of the plasmonic Luneburg lens presented in Ref. [100].

We start by reviewing here a carpet cloak that mimics a Bragg reflector for SPPs at visible frequencies [99]. With a design similar to the ground-plane cloak for SPPs presented in Section 2.2 to suppress scattering from an uneven metallic surface, in this experiment the cloak is placed as shown in Fig. 2.13 (a), such that SPPs are launched along an air/gold interface towards a curved Bragg reflector covered by the cloak. The effect of the cloak is then to mimic a flat Bragg reflector. In order to meet experimentally the index profile needed for the cloak [similar to the one shown in Fig. 2.10 (d)], the cloak was realized by structuring a flat gold surface with TiO_2 protrusions. A curved Bragg reflector consisting of 15 gold lines (section = 150 nm $\times$150 nm) periodically separated by half of the SPP wavelength was also fabricated. A scanning electron microscopy image of the sample can be seen in Fig. 2.13 (b). The refractive index profile was reproduced by placing each of the TiO_2 pillars at the nodes of a quasi-conformal grid. In the experiment, SPPs at $\lambda = 800$ nm propagating along the gold/air interface were launched onto the cloak as sketched in 2.13 (b) after excitation through a lithographically structured line defect. The propagation of the SPP waves was measured by means of leakage radiation

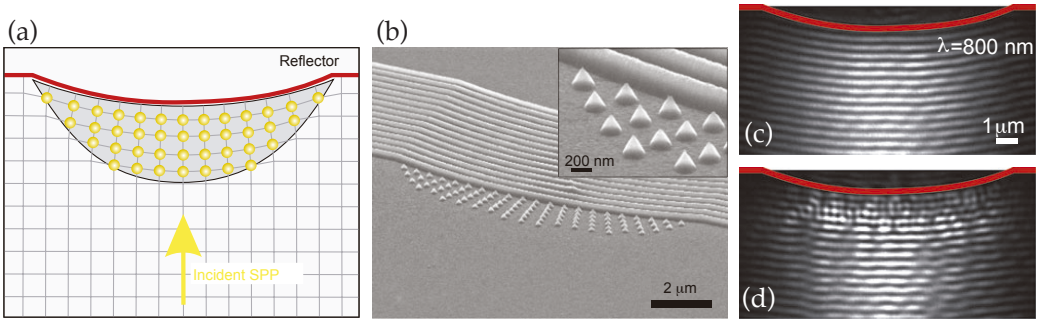

Figure 2.13: Experimental realization of a plasmonic broadband carpet cloak mimicking a flat Bragg reflector [99]. (a) Sketch of the cloak, designed by a quasiconformal map. When the device is placed in front of a curved Bragg mirror, incident SPPs are reflected as if the mirror was flat. (b) Scanning electron microscopy image of the sample. TiO_2 pillars on top of the gold surface were employed to realize the spatial variation of the isotropic index profile given by the quasiconformal map shown in (a). The Bragg mirror consists of gold lines fabricated on top of the gold substrate and separated by half the SPP wavelength. (c) Leakage radiation microscopy image showing the reflection of SPPs at $\lambda = 800$ nm on a bare curved Bragg mirror. (d) The carpet cloak on the curved Bragg mirror generates SPP plane wave fronts, mimicking the effect of a flat Bragg mirror. All the panels in this figure have been adapted from Ref. [99]

microscopy. Figure 2.13 (c) presents a leakage radiation image of SPPs at 800 nm impinging on a bare curved mirror: the reflected wave front is curved due to reflection into different directions of the SPPs depending on their relative angle to the normal of the mirror. On the other hand, placing the fabricated cloak in front of the mirror results in a plane wave front: SPPs are reflected as if they were impinging on a flat Bragg reflector. In addition, a broadband performance of the cloak was demonstrated in this work, showing an efficient performance for SPPs of wavelengths ranging from 750 nm to 850 nm.

Finally, we present the design of a plasmonic Luneburg lens for SPPs propagating on a metal surface, demonstrated experimentally together with a plasmonic Eaton lens in Ref. [100]. A planar Lubeburg lens is a circle of radius R characterized by the following refractive index:

$$n(r) = \sqrt{2 - (r/R)^2}, \tag{2.25}$$

where r is the distance to the center of the lens. This index profile focuses an incident SPP to a point in the perimeter of the lens on the opposite side of the circle. Following the methodology introduced in this chapter, in order to desgin a plasmonic Luneburg

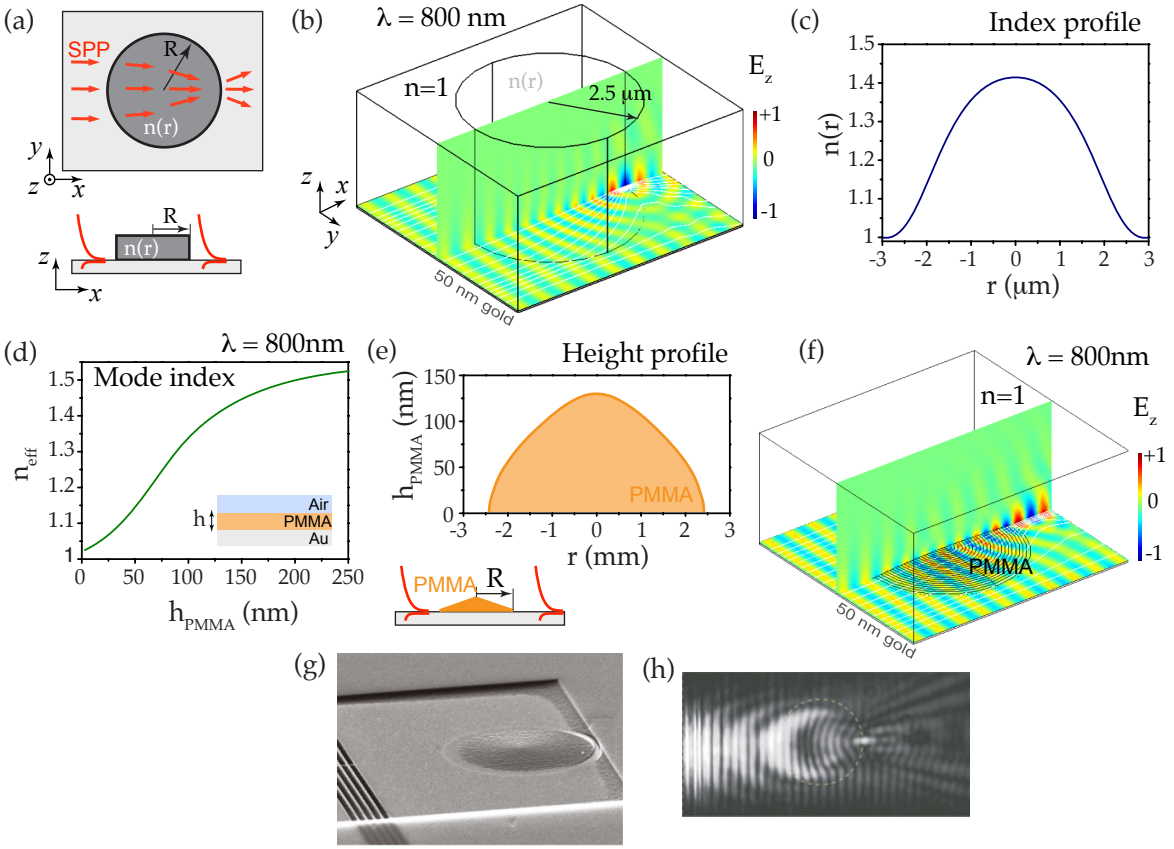

Figure 2.14: A plasmonic Luneburg lens is used to focus an incident SPP. (a) Schematic of a lens of radius R in top and side views. The transformation medium is a cylinder of radius R with height larger than the SPP decay length in the dielectric side of the interface. (b) Full-wave simulation of a lens for a SPP at 800 nm. The radius of the lens is $R = 2.5$ μm and its height is 3 μm. (c) Refractive index as a function of the distance to the center of the lens, r, for $R = 2.5$ μm. (d) Relation between the SPP mode index at 800 nm and the height of a PMMA layer placed on a gold surface. (e) Sketch of a lens that consists of a PMMA disc on the gold surface and height of the layer as a function of the distance to the center of the lens. (f) 3D simulation of a PMMA layer shaped according to panel (e) acting as a Luneburg lens for SPPs at 800 nm. Both (b) and (f) show the SPP electric field, E_z. (g) In Ref. [100], the lens was realized by 3D lithography of the PMMA on top of the gold layer and the SPP field was measured by leakage radiation microscopy (h), revealing SPP focusing at $\lambda = 800$ nm. (g,h) Reprinted from Ref. [100].

lens, let us assume a metamaterial that reproduces the refractive index $n(r)$ given above. As sketched in Fig. 2.14 (a), the metamaterial is a cylinder of radius R placed on top of a gold surface with a height that needs to be larger than the SPP vacuum decay length, similar to the previous examples. Panel (b) demonstrates a plasmonic Luneburg lens of radius $R = 2.5$ μm operating at $\lambda = 800$ nm when the spatial variation of the index $n(r)$ [shown in (c)] is implemented in the metamaterial region. The SPP electric field and power flow lines obtained from 3D simulations show the focusing of SPPs travelling along an air-gold interface at the perimeter of the lens.

This plasmonic element was experimentally demonstrated in Ref. [100] by means of a strategy that involves the effective mode index of SPPs. Instead of spatially engineering the optical properties of the dielectric, the height of a thin dielectric layer on top of the metal is varied. The index profile 2.25 is reproduced by the effective mode index of the SPP. The mode index for an air/PMMA/gold structure for SPPs at 800 nm is plotted in Fig. 2.14 (d) as a function of the PMMA height, h. In a dielectric/dielectric/metal structure with electric permittivities ϵ_1, ϵ_2 and ϵ_3, respectively, SPPs at frequency $\omega = ck_0$ propagate with an effective mode index $n_{\text{eff}} = k/k_0$ determined by the parallel wavevector k. The SPP dispersion relation is given by:

$$\tanh(k_2\epsilon_2 h) = \frac{\epsilon_3 k_{z,1} k_{z,2} + \epsilon_1 k_{z,2} k_{z,3}}{\epsilon_1 \epsilon_3 k_{z,2}^2/\epsilon_2 + \epsilon_2 k_{z,1} k_{z,3}}, \tag{2.26}$$

where

$$k_{z,i} = \sqrt{k^2 - \epsilon_i k_0^2}, \quad (i = 1, 2, 3). \tag{2.27}$$

In the situation under study, $\epsilon_1 = 1$, $\epsilon_2 = 2.19$ and $\epsilon_3 = \epsilon_{Au}$. For PMMA thicknesses up to 250 nm, we see in panel (b) that the index varies between 1 and 1.5, a range that is enough to reproduce the index required by the Luneburg lens. The plasmonic device, sketched in panel (e), is designed by calculating the PMMA's height at which the SPP effective mode index satisfies Eq. 2.25. This results in a variation of the PMMA height between 0 at the perimeter of the lens and 130 nm at the center. A numerical simulation of a SPP propagating through this lens can be seen in fig. 2.14 (f). A PMMA disk of 2.5 μm radius with a height modulated according to panel (e) was placed on top of a gold surface. The SPP field is smoothly focused at the perimeter of the lens in a subwavelength spot. This design of the plasmonic lens potentially allows for a broad band performance, as it only involves dielectric materials with a very low dispersion. In Ref. [100], the lens was realized by gradually varying the height of a PMMA disk on top of a thin gold film [see Fig. 2.14 (g)]. The fabricated structure was optically tested by combining fluorescence imaging and leakage radiation microscopy, successfully

demonstrating SPP focusing in the near-IR range of the spectrum [see panel (h)].

2.5 Conclusions

In conclusion, we have demonstrated that the application of the concept of TO to Plasmonics brings into the field unprecedented control over the flow of SPPs. Based on this approach, we have presented the necessary tools to design feasible plasmonic devices. When considering SPPs propagating on metal-dielectric interfaces, a direct application of TO would imply a manipulation of the optical properties of both the metal and dielectric materials. However, we have shown that modifying only the dielectric side leads to almost perfect functionalities because most of the SPP energy is carried within the dielectric medium at optical frequencies. Having proved this feature within a general framework in which the EM parameters are anisotropic, we have then presented plasmonic devices that can be made out of isotropic dielectric materials. Regarding practical implementations, this fact yields low loss and broadband performances. Making use of conformal and quasiconformal transformations, control over SPPs flow can be achieved by placing a structured dielectric layer on top of the metal surface. In particular, we have discussed different ways to reproduce the refractive index landscape in an experimental realization of plasmonic TO-based devices: either dielectric pillars fabricated on a metal surface or air holes drilled in a dielectric load, or by adjusting the effective refractive index of the SPPs through controlling the height of a dielectric layer. However, a full exploitation of Transformation Plasmonics at optical frequencies remains hindered by current limitations in nanofabrication. We expect that the flexibility of our methodology, together with an improvement in fabrication techniques, will ensure many different theoretical proposals and experimental realizations of plasmonic devices based on TO.

Chapter 3

Magnetic localized surface plasmons

3.1 Introduction

The existence of SPs propagating along metal/dielectric interfaces, SPPs, or localized at metal particles, LSPs, is limited to the high frequency range of the spectrum. At low frequencies, the surface EM waves supported by metal/dielectric interfaces are poorly confined and extend mostly in the dielectric. However, as we reviewed in the Introduction Chapter (see Subsection 1.3), "spoof" plasmons are able to transfer the properties of SPPs to low frequencies [117, 118]. These SPPs are geometrically-induced propagating surface modes that arise when a highly conducting surface is periodically corrugated on a subwavelength scale. Spoof SPPs were developed under the assumption of the metal behaving as a PEC. This approximation takes the metal as a perfectly conducting material where the EM field can not penetrate. Thus, the PEC approximation is appropriate for low frequencies where the conductivity of metals is high. An important aspect of this approximation is that it implies the scalability of the structures for different frequency regimes.

Spoof SPPs have been studied, theoretically as well as experimentally, in 2D surfaces [117, 118, 120–125] and in a variety of 1D waveguiding schemes [126–135]. Moreover, the localized version of this concept, the spoof-LSPs, have also been shown to appear for textured PEC particles of closed surfaces [136]. In this work, infinitely long subwavelength PEC cylinder corrugated with a periodic array of grooves filled with a dielectric material were studied. Such structures were shown to feature an electrical dipole response, much in the same way as the LSPs supported by metal particles in the optical regime. In this Chapter we explore the emergence of subwavelength magnetic resonances in these textured PEC particles, which are the low-frequency analogues of the subwave-

length nanoparticles studied at optical frequencies and therefore open up the possibility of magnetic LSPs.

This Chapter is organized as follows. First, in Section 3.2, we consider metal cylinders and disks corrugated with subwavelength grooves filled with a dielectric material. We study the EM response of the 2D cylinders by means of numerical simulations, showing that they support magnetic as well as electric dipole resonances, and that these are quasi-degenerate. An analytical model, developed in Section 3.3, allows us to reproduce the numerical findings and also to gain physical insight on the emergence of such EM resonances. Next, in Section 3.4 we consider corrugated metallo-dielectric disks, where the degeneracy between the electrical and magnetic modes is lifted and the magnetic resonance generates a distinct feature in the spectrum. We also develop an anisotropic metamaterial model to effectively reproduce the EM response of these structures, finding fundamental differences with respect to metal and dielectric subwavelength particles. In Section 3.5 we show that, interestingly, a magnetic resonance can also be obtained for purely metallic structures corrugated with very long grooves. We present two structures that show similar responses, but where the depth of the grooves has been increased in a different way: structures corrugated with meander-shaped and spiral-shaped grooves. Finally, in Section 3.6 we present an experimental demonstration of the magnetic LSPs, based on an ultra-thin spiral structure working in the microwave regime.

3.2 Metallo-dielectric corrugated cylinders

In this Section we study the EM response of metal cylinders corrugated with dielectric-filled subwavelength grooves (of radial and parallel walls). By inspecting the scattering cross section (SCS) and numerical eigenmodes of such structures, we show that two different modes contribute to the lowest frequency resonance appearing in the spectra. These two modes are quasi-degenerate and, while one of them has an electrical dipole character, the second one is a magnetic dipole.

We start by considering a basic 2D geometry that supports spoof-LSPs. It consists of an infinitely long metallic cylinder of radius R corrugated with a periodic array (period $d = 2\pi R/N$) of N grooves, of depth $h = R - r$ and width a, see the sketch in Fig. 3.1 (a). The number of grooves and the radius of the cylinder are chosen to yield $d \ll \lambda_0$, with λ_0 being the wavelength of the incident EM wave. The grooves are filled with a dielectric material of refractive index n_g. In this way, the resonant wavelengths, λ_{res}, can be made much larger than the size of the object and we can operate in the very

deep subwavelength regime, $R \ll \lambda_{res}$ [136]. Here, we take the metal structures as PECs, which allows for an analytical treatment and moreover is a very good approximation at sufficiently low frequency (see Appendix B for more details). We study two different cases: grooves of parallel walls [see the inset of Fig. 3.1 (a)] and radial grooves [see the inset of Fig. 3.2 (a)]. Both cases display very similar EM resonances, as we detail below, and both structures allow for an analytical treatment for their EM resonances, as we will show in the next Section.

We analyze the EM response of corrugated PEC structures by means of the SCS, which we numerically compute making use of FEM simulations [219]. In order to calculate the SCS we consider (here and throughout the Chapter) an incoming TM-polarized plane wave (magnetic field $\vec{H}$ pointing along the z direction) propagating along the x axis and with wavenumber $k_0 = \omega/c$ [see Fig. 3.1 (a)]. Under this illumination, we compute the power scattered by the structure, $P_{\rm sc}$, as a surface integral,

$$P_{\rm sc} = \int_{\delta V} \langle \mathbf{S} \rangle \cdot \mathbf{n} \, \mathrm{d}a. \tag{3.1}$$

where δV is a surface enclosing the structure. In addition, $\mathbf{S}$ stands for the Poynting vector, whose mean value reads as

$$\langle \mathbf{S} \rangle = \frac{1}{2} \mathrm{Re} \left\{ \mathbf{E} \times \mathbf{H}^* \right\}. \tag{3.2}$$

The total SCS is obtained as $P_{\rm sc}/P_0$, with $P_0 = c\epsilon_0 |\mathbf{E}|^2/2$ being the incident power. Finally, we normalize the SCS by the geometrical cross section of the structure, $\sigma_{\rm geom}$, such that the normalized SCS, σ, reads as

$$\sigma = \frac{P_{\rm sc}/P_0}{\sigma_{\rm geom}}. \tag{3.3}$$

Notice that for the 2D structures considered in this Section, $\sigma_{\rm geom} = 2R$. In addition, and since we consider PECs, the resonant wavelengths scale with R, which we take as unit length. Hence, throughout the Chapter the frequency will be expressed in terms of the dimensionless quantity $k_0 R$.

The SCS spectrum for a representative textured cylinder with grooves of parallel walls and with parameters $r = 0.4R$, $N = 40$ and $a/d = 0.3$ is shown in Fig. 3.1 (a). This spectrum closely resembles what is observed for very subwavelength metal particles at optical frequencies. This analogy suggests that the first resonance peak is due to the electrical dipole resonance while the high frequency narrow peak is associated with the electrical quadrupole (see inset panel). On the other hand, a calculation of the eigenmodes of the structure reveals that the first resonance peak has contributions of

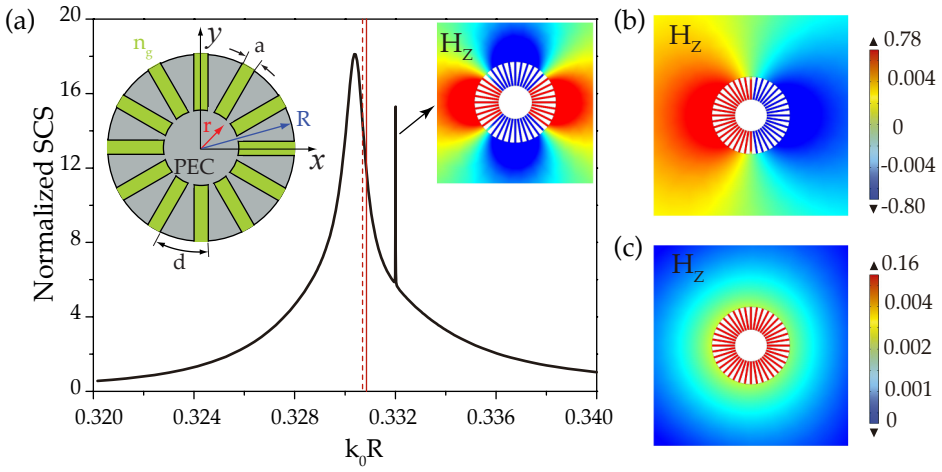

Figure 3.1: Spoof-LSPs supported by a cylinder corrugated with grooves of parallel walls. (a) SCS for a structure with parameters: $r = 0.4R$, $N = 40$, $a/d = 0.3$ and grooves filled with a material of refractive index $n_g = 8$. The low energy peak ($k_0R = 0.33$) reveals two resonances: the electrical and magnetic dipoles, whose magnetic field amplitude (H_z) are plotted in panels (c) and (c), respectively. The solid (dashed) vertical lines show the position of the electric (magnetic) resonance according to the analytical model.

two different EM modes with very similar eigenfrequencies. One of them has an electrical dipole character [see panel (b)] whereas the field pattern associated with the other one is independent of the azimuthal angle, as corresponds to a magnetic dipole pointing along the z-axis [see panel (c)].

Figure 3.2 considers a textured cylinder with the same parameters as that considered in Fig. 3.1 but with radial grooves. Panel (a) displays the SCS while panels (b) and (c) show the EM field patterns of the two eigenmodes that, similarly to the case discussed in Fig. 3.1, contribute to the first resonance peak. By comparing this figure to the case of grooves of parallel walls, it is clear that the EM response of both structures is very similar. We conclude that the only effect of the shape of the grooves is a small shift in the resonance frequencies: while for rectangular grooves the resonance is at $k_0R \sim 0.33$, for radial grooves $k_0R \sim 0.39$. Interestingly, we can see from these results that subwavelength PEC structures textured with periodic grooves display two degenerate resonances, an electrical dipole and a magnetic dipole. This behavior is at odds to what happens in standard plasmonics. As we described in Section 1.1, the optical response of subwavelength metal particles is dominated by the electrical dipole resonance. Indeed, for these particles the magnetic dipole resonance is extremely weak and does not show up in the SCS. This fact can be understood by comparing the electric and magnetic polarizabilities provided

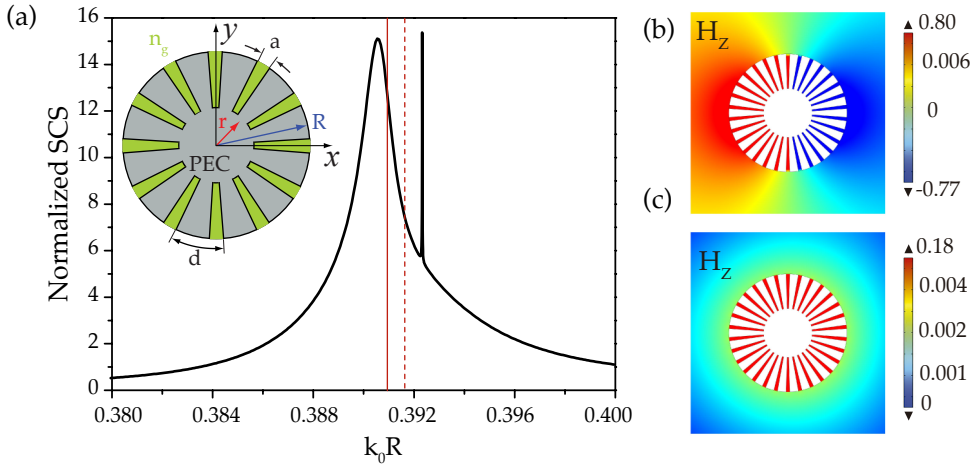

Figure 3.2: Spoof-LSPs supported by a cylinder corrugated with radial grooves filled with a material of refractive index $n_g = 8$. (a) SCS spectrum. (b,c) Field pattern (H_z) at the electric and magnetic resonances. The structure has the same parameters as in Fig. 3.1. The solid (dashed) vertical lines show the position of the electric (magnetic) resonance according to the analytical model.

by Mie theory in the quasistatic limit [230],

$$\alpha_{\mathrm{e}} = 4\pi R^3 \frac{\epsilon(\omega)-1}{\epsilon(\omega)+2}, \tag{3.4}$$

$$\alpha_{\mathrm{m}} = 4\pi R^3 \frac{(k_0 R)^2}{30}\left[\epsilon(\omega)-1\right], \tag{3.5}$$

where $\alpha_{\mathrm{e,m}}$ stand for the electric and magnetic polarizabilities, respectively, R is the radius of the particle, assumed to be in free space, and $\epsilon(\omega)$ its electric permittivity. From the above expressions, we see that $\alpha_{\mathrm{m}}/\alpha_{\mathrm{e}} \sim (k_0 R)^2$, and hence for subwavelength particles the magnetic response is much lower than the electric one.

3.3 Analytical results: Modal Expansion

Here we detail an analytical model that reproduces the EM response of the 2D corrugated cylinders discussed in the previous Section. In order to deal with the EM response of PEC cylinders corrugated with grooves, we make use of the Modal Expansion (ME) technique. The ME is based on the matching of the EM modes outside the cylinder (radial coordinate $\rho > R$) and inside the grooves ($r < \rho < R$) by means of the appropriate boundary conditions at $\rho = R$. In the following we describe the ME technique, first for

the structure with radial grooves, and then for the structure with grooves of parallel walls. Next, we derive an analytical expression for the SCS for the case of radial grooves.

Let us first consider a PEC cylinder textured with subwavelength radial grooves. In order to apply the ME technique to the EM response of this system, we take the unit cell shown in Fig. 3.3 (a). Assuming a subwavelength particle ($k_0R \ll 1$, $k_0d \ll 1$), the field inside the grooves can be approximated by the fundamental waveguide mode as

$$H_z^I = A\, H_0^{(1)}(k_0 n_g \rho) + B\, H_0^{(2)}(k_0 n_g \rho), \tag{3.6}$$

where A and B are constants and $H_n^{(1),(2)} = J_n \pm N_n$ is the Hankel function of the first (or second) kind and order n, with J_n and N_n being the Bessel functions of first and second kind, respectively. In the outer region the field can be written as

$$H_z^{II} = \sum_n A_n H_n^{(1)}(k_0\rho) e^{in\phi}, \tag{3.7}$$

where we have neglected the diffraction orders. Accordingly, E_ϕ can be expressed from H_z in each region using $E_\phi = -i/(\omega\epsilon\epsilon_0)\mathrm{d}H_z/\mathrm{d}\rho$. The resonance condition for each mode is obtained by applying the boundary conditions at $\rho = R$. This procedure yields the following transcendental equation:

$$S_n^2 \frac{H_n^{(1)}(k_0R)}{H_n^{(1)'}(k_0R)} \frac{f}{g} = -n_g \tag{3.8}$$

where $f = J_1(k_0n_gR)N_1(k_0n_gr) - J_1(k_0n_gr)N_1(k_0n_gR)$ and $g = J_0(k_0n_gR)N_1(k_0n_gr) - \ldots$ $\cdots - J_1(k_0n_gr)N_0(k_0n_gR)$. In addition, $H_n^{(1)'}(k_0R) \equiv \frac{d\,H_n^{(1)}(k_0R)}{d\,(k_0R)}$, and

$$S_n = \sqrt{\frac{a}{d}}\,\mathrm{sinc}\left(\frac{na}{2R}\right). \tag{3.9}$$

The quantity S_n contains all the information about the unit cell, and, for subwavelength texturing ($a \ll R$), its expression reduces to $S_n \approx \sqrt{a/d}$. The solution of Eq. 3.8 for a given n yields the complex resonance frequency of the mode of order n. Physically, the picture that emerges from our modelling is that of surface EM modes running around the cylinder surface, with each resonance appearing when an integer number of modal wavelengths fits into the perimeter. In the subwavelength limit, Eq. 3.8 predicts that the mode for $n = 0$ (i.e., azimuthally-independent) is very close in frequencies to the mode for $n = 1$, but with broader linewidth. The resonance frequencies of these two modes for the textured PEC cylinder considered in Fig. 3.2 are marked as vertical lines in panel (a) of that figure. As shown in the figure, the analytical result is in a very good agreement with the numerical SCS and eigenmode calculations.

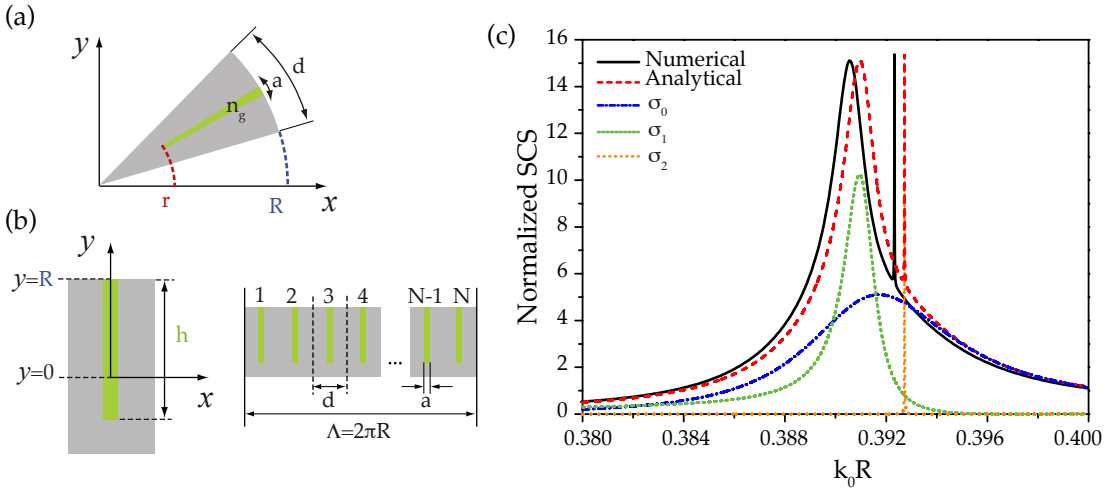

Figure 3.3: Modal Expansion technique and analytical SCS. (a,b) Unit cells used for the ME technique for the case of a cylinder corrugated with radial grooves (a) and with grooves of parallel walls (b). (c) SCS for a subwavelength PEC cylinder corrugated with radial grooves ($r = 0.4R$, $N = 40$, $a = 0.3d$ and $n_g = 8$). The solid line shows the numerically-computed SCS [same as in Fig. 3.2 (a)] while the red dashed line corresponds to the analytical SCS. The contributions of the $n = 0$, $n = 1$ and $n = 2$ modes to the analytical SCS are also shown.

Let us now apply the ME technique to the case of a PEC cylinder textured with subwavelength grooves of parallel walls. Given the rectangular shape of the grooves, in this case we proceed as follows in order to write the field within them. First, we consider an array of N grooves with parallel walls on a flat surface, as shown in Fig. 3.3 (b). Next, we apply Born von Karman boundary conditions for a super-cell of length $\Lambda = 2\pi R$ to take account of the circular geometry. This procedure leads to the following field inside the grooves:

$$H_z^I = Ae^{ik_0 n_g y' \frac{\Lambda}{2\pi}} + Be^{-ik_0 n_g y' \frac{\Lambda}{2\pi}} \tag{3.10}$$

where A and B are constants, $x' = 2\pi x/\Lambda$ and $y' = 2\pi y/\Lambda$ are the renormalized coordinates, and we have taken only the fundamental waveguide mode based on the assumption that the texturing is subwavelength. On the other hand, in the outer region the fields can be expanded in terms of the Hankel function of the first kind, $H_n^{(1)}$:

$$H_z^{II} = \sum_{-\infty}^{\infty} C_n \left(k_0 y' \frac{\Lambda}{2\pi} \right) e^{inx'} H_n^{(1)}, \tag{3.11}$$

the set C_n being constants. By applying the boundary conditions for each mode n we arrive to the following transcendental equation for the complex resonance frequency of

the EM mode with azimuthal number n:

$$S_n^2 \frac{H_n^{(1)}(k_0 R)}{H_n^{(1)'}(k_0 R)} \tan(k_0 n_g h) = -n_g, \tag{3.12}$$

where S_n is now given by

$$S_n = \sqrt{\frac{a}{d}} \operatorname{sinc}\left(\frac{n\pi a}{Nd}\right). \tag{3.13}$$

As in the case of radial grooves, the resonance condition given by Eq. 3.12 is consistent with a picture in which an EM mode runs around the cylinder surface and resonances emerge when an integer number of modal wavelengths fit into the perimeter. The tangent function in Eq. 3.12 accounts for the fact that a guided mode is traveling down the groove (of depth h and refractive index n_g), and bouncing at its bottom. Similarly to Eq. 3.8, Eq. 3.12 also predicts that the modes for $n = 0$ and $n = 1$ are very close in frequencies in the subwavelength limit, as shown by the vertical lines in Fig. 3.1 (a). Again, we can see that, despite the few ingredients it includes, our simple modelling shows a very good agreement with the numerical SCS. Furthermore, our modelling illustrates the geometrical origin of the modes and justifies their naming: magnetic dipole LSP for the $n = 0$ mode and electrical dipole LSP for the $n = 1$ mode.

Based on the analytical models for both radial and rectangular grooves, we can predict the effect of the geometrical parameters of the groove, a/d and h. As suggested by the modelling, LSP modes arise as geometrically-induced surface EM modes supported by the periodic array of grooves. From Eqs. 3.8 and 3.12, we can state that the resonance wavelength is mainly controlled by the depth of the grooves and the refractive index of the dielectric filling, following $\lambda \sim 4 n_g h$. On the other hand, the effect of the width of the grooves, a/d, is to produce a small shift in the resonance wavelength. In particular, and as we have also checked with numerical simulations, smaller values of a/d give larger resonance frequencies.

Our analytical model can be also used to calculate the SCS of corrugated particles as well as the relative contributions of each mode n to it. Here, we focus our interest on the geometry with radial grooves, as the circular symmetry of this structure allows us to write an analytical expression for the SCS based on the ME of the fields. Assuming that the field within the grooves is given by only one waveguide mode and following Ref. [136], we can write the normalized SCS as

$$\sigma = \frac{2}{k_0 R} \sum_{n=-\infty}^{\infty} |a_n|^2, \tag{3.14}$$

where the coefficient a_n for each mode n is given by:

$$a_n = -i^n \frac{\frac{a}{d} J_n(k_0 R) f - n_g J_n'(k_0 R) g}{\frac{a}{d} H_n^{(1)}(k_0 R) f - n_g H_n^{(1)'}(k_0 R) g}. \tag{3.15}$$

The SCS given by the above equations and for a subwavelength cylinder of the same parameters as that shown in Fig. 3.2 is plotted in Fig. 3.3 together with the numerically computed SCS: the two curves show a very good agreement. Moreover, the analytical expression for the SCS allows us to separate the contribution of each mode, which can be written as:

$$\sigma_0 = \frac{2}{k_0 R} |a_0|^2, \ \sigma_n = 2 \frac{2}{k_0 R} |a_n|^2 \, (n \neq 0) \tag{3.16}$$

In the SCS plot we present the contributions of the $n = 0$, $n = 1$ and $n = 2$ modes (σ_0, σ_1 and σ_2, respectively). It is clear from this figure that the main contributions to the SCS of 2D subwavelength cylinders come from the two lower order modes. The magnetic and electric dipoles ($n = 0$ and $n = 1$) are very close in frequencies with the magnetic resonance being broader, and both of them contribute to the low energy peak. Thus, the analytical model confirms the findings obtained in the previous Section from the numerical results. Notice that equivalent results are to be expected for the case of rectangular grooves.

3.4 Metallo-dielectric corrugated disks

Here we study the 3D counterpart of the corrugated PEC cylinders studied in the previous Sections. Going from the infinitely long textured cylinder to a 3D corrugated disk of finite thickness L has a fundamental consequence. Not only do the resonances shift when the particle's size is reduced, as usual in particle plasmonics, but also the magnetic and electric LSP split in such a way that the former shifts to higher frequencies than the latter. In the following we first discuss the SCS obtained for PEC disks corrugated with dielectric-filled grooves of parallel walls. Then, we compare the EM resonances supported by these structures with the electric and magnetic dipole modes displayed by subwalength dielectric particles. We focus on the different frequency ordering of the resonances and give a detailed explanation for this fact. Finally, we present a metamaterial interpretation for the corrugated PEC structures.

The SCSs for two disks of different L are shown in Fig. 3.4 (a). The disks are corrugated with grooves of parallel walls filled with a dielectric material and with the same parameters considered in Fig. 3.1. As in the 2D case, in the 3D FEM simulations we

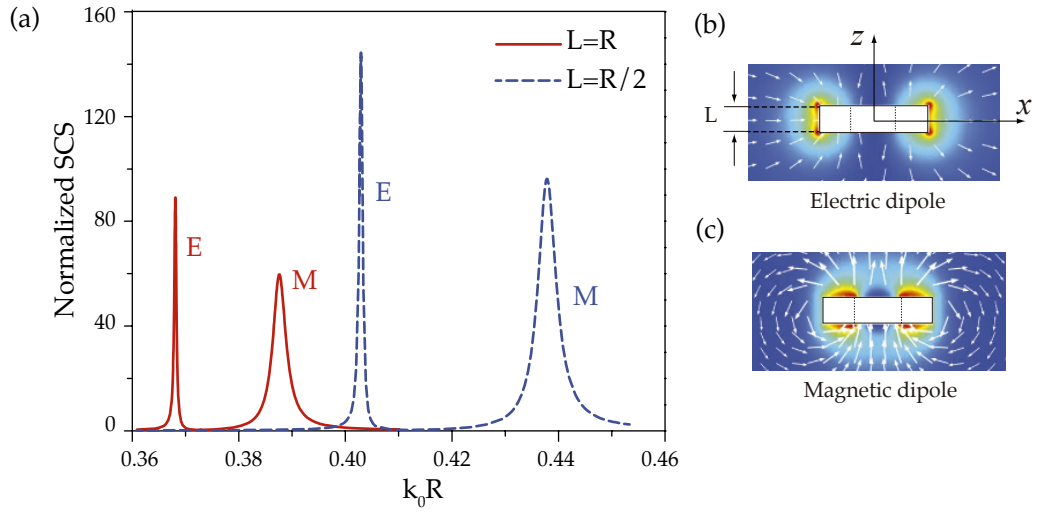

Figure 3.4: Magnetic LSPs in subwavelength PEC disks corrugated with grooves of parallel walls and filled with a dielectric. Structures of finite thickness and with the same r, N, a/d and n_g as in Fig. 3.1 are considered. (a) SCS for corrugated disks of thickness $L = R$ (solid red line) and $L = R/2$ (dashed blue line). (b,c) Near field distribution of the electric (b) and magnetic (c) dipole resonances for a disk of thickness $L = R/2$. The arrows show the electric field lines and the color map shows the norm of the electric field in panel (b) and the magnetic field lines and magnetic field, respectively, in (c).

have considered an incident wave polarized with the magnetic field pointing in the z direction and propagating along the x axis, see Fig. 3.4. The SCS is calculated following Eq. 3.3, where the geometrical normalization factor is in this case $\sigma_{\text{geom}} = 2RL$. Two distinct peaks can be seen in the SCS plot for disks of finite thickness ($L = R$ in solid red and $L = R/2$ in dashed blue). By looking at the field patterns at these resonances, displayed in panels (b) and (c) for $L = R/2$ case, it is clear that the peak at a low frequency corresponds to the electric LSP while the one at a higher frequency is the magnetic LSP. This picture is reinforced by analyzing the vectorial plots also displayed in those panels [E-field lines for the low frequency peak, (b), and H-field lines for the high frequency peak, (c)]. In the first case (b), the arrows go from one end of the structure to the other, as corresponds to an electrical dipole, whereas in panel (c) the arrows show how the magnetic field is circulating around the disk, as in a magnetic dipole. Hence, while subwavelength corrugated infinitely long cylinders present a magnetic LSP that is very close in frequencies to the electric LSP, finite corrugated disks support a magnetic LSP at a different frequency than the electric LSP.

It is known that purely dielectric particles of subwavelength sizes and large refractive

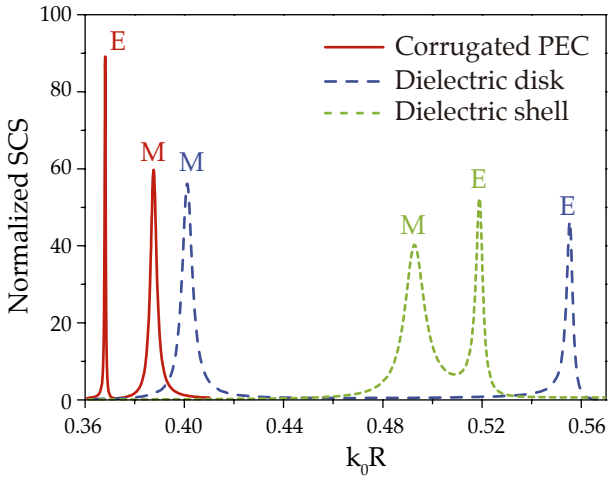

Figure 3.5: Electric and magnetic dipole resonances in subwavelength dielectric particles. The plot shows the SCS for: (i) a corrugated disk of $L = R$ and with the same parameters as in Fig. 3.4 (solid red), (ii) a dielectric disk of the same size and $n_g = 8$ (dashed blue), and (iii) a PEC core of radius r with a dielectric shell of radius R and $n_g = 8$ (short dashes, green).

index also display magnetic and electric dipole modes [231, 232]. It is therefore relevant to compare the EM modes supported by corrugated metal cylinders with those emerging in subwavelength dielectric particles in the same frequency range. Figure 3.5 compares the calculated SCS for three different structures: (i) a PEC disk corrugated with grooves filled with a dielectric material of index n_g, as in Fig. 3.4, (ii) a dielectric disk of radius R and refractive index given by n_g, and (iii) a dielectric shell of width h surrounding a PEC core of radius r. As opposed to the modes for the corrugated PEC disk, for dielectric particles the magnetic dipole resonance lies at lower energies than the electric dipole resonance, as well as for the core-shell structure. The physical origin of this opposite frequency ordering for metallic and dielectric disks is related to the dissimilar shapes of the corresponding electric field line patterns (see Section 3.8 for more details). This distinct behavior implies that the corrugated PEC structure cannot be interpreted as an effective isotropic dielectric medium. Rather than that, in the effective medium limit, $\lambda \gg R$, the region with grooves can be mapped into a metamaterial with both anisotropic permittivity and permeability tensors.

In the following we give a detailed account of the anisotropic metamaterial equivalence for corrugated metal structures. Since the PEC particles we are concerned with in this Chapter are corrugated at a subwavelength scale ($d \ll \lambda_0$), the region with grooves can be interpreted as an effective medium layer. Let us consider once again the case of radial

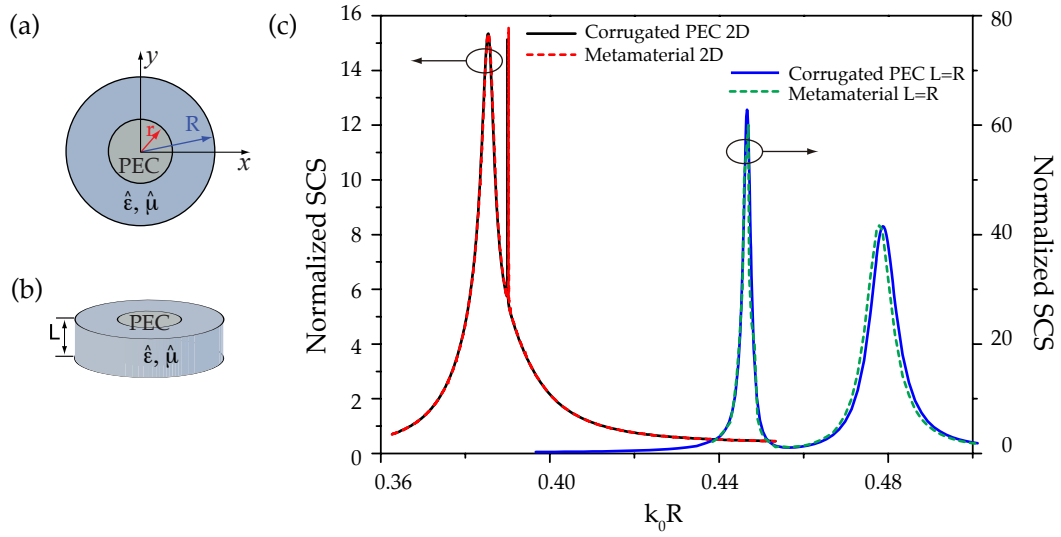

Figure 3.6: Metamaterial approximation for corrugated PEC structures. In the effective medium approximation corrugated PEC particles behave as an inhomogeneous and anisotropic layer of thickness $R - r$ wrapped around a PEC inner core. (a) and (b) depict the geometry of the metamaterial models in 2D and 3D, respectively. (c) SCS for corrugated PEC cylinders with radial grooves ($r = 0.4R$, $N = 40$, $a = 0.8d$ and $n_g = 8$) and disks (same parameters, thickness $L = R$) together with the SCS in the effective medium approximation for both cases.

grooves, which as we showed in Sections 3.2 and 3.3, features the same EM resonances as the case of rectangular grooves considered in this Section. Taking advantage of the circular symmetry displayed by PEC particles corrugated with radial grooves, we obtain the EM tensors of the effective medium under TM incidence by averaging $1/\epsilon$ in the azimuthal direction and by considering that the mode propagates with velocity c/n_g in the radial and vertical directions. In cylindrical coordinates they read:

$$\epsilon_r = \infty,\ \epsilon_\phi = n_g^2 d/a,\ \epsilon_z = \infty, \tag{3.17}$$

$$\mu_r = a/d,\ \mu_\phi = 1,\ \mu_z = a/d. \tag{3.18}$$

These permittivity and permeability tensors, $\hat{\boldsymbol{\epsilon}}$ and $\hat{\boldsymbol{\mu}}$, represent a metamaterial with anisotropic and inhomogeneous EM properties. Note that an equivalent expression could be derived to map the response of PEC particles corrugated with rectangular grooves.

We have tested the validity of this approach for infinitely long cylinders and for disks of finite thickness by means of numerical simulations. The results are illustrated in Fig. 3.6. The geometries under consideration are depicted in panels (a) and (b): first, in the 2D case it consists of a PEC core of radius r surrounded by a metamaterial shell

of width $R - r$ (a); second, in the 3D case we deal with a shell of width $R - r$ and thickness L surrounding the PEC core (b). The plot in panel (c) shows the computed SCS. In the 2D case, the plot shows the SCS for the same subwavelength corrugated cylinder considered in Fig. 3.2 (black solid line) together with the SCS obtained in the metamaterial approximation (red dashed line). We can observe that the two lines virtually coincide. Regarding the effective medium approximation for the 3D corrugated disks of thickness L, we have assumed that the 3D permittivity and permeability tensors can be approximated by the 2D ones (Eqs. 3.17 and 3.18) and we have implemented them in a shell of width $R-r$ and thickness L. In the figure, the SCS for the corrugated PEC particle is shown as a blue solid line, while the effective medium approximation corresponds to the dashed green line. In both cases the low energy peak corresponds to the electric LSP while the high energy peak is the magnetic LSP (similar to the results for rectangular grooves presented in Fig. 3.4). The agreement between the two lines demonstrates the fact that the EM response of subwavelength corrugated PEC particles can be understood as that of an anisotropic and inhomogeneous layer coating a PEC core rather than as a isotropic dielectric shell surrounding a PEC particle.

3.5 Metallic corrugated cylinders and disks

In the previous Sections we showed that PEC structures corrugated with subwavelength grooves filled with a dielectric material support magnetic spoof-LSPs. Although these magnetic LSP modes (and those supported by dielectric particles) are very promising in order to create dipolar magnetic resonances, they rely on the inclusion of a dielectric material with a very high n_g, which could limit their feasible implementation. Building up magnetic LSP modes supported by purely metallic structures would be more convenient from the fabrication point of view. Our analytical model (see Section 3.3), gives a clue on how to proceed. Equation 3.12, which applies to cylinders corrugated with rectangular grooves, predicts that, in the subwavelength limit, the positions of the complex resonance frequencies are mainly controlled by the product $n_g \cdot h$. Therefore, an interesting design is to replace the grooves with $h \leq R$ and filled with a dielectric material by very long empty grooves that posses an effective length much larger than R. In order to achieve a depth $h > R$, the grooves of parallel walls need to be bended and warped within the particle's volume. Note that purely metallic structures displaying magnetic resonances have been explored before both in the microwave and metamaterials areas of research. Spiral structures of varied geometries have been traditionally used as

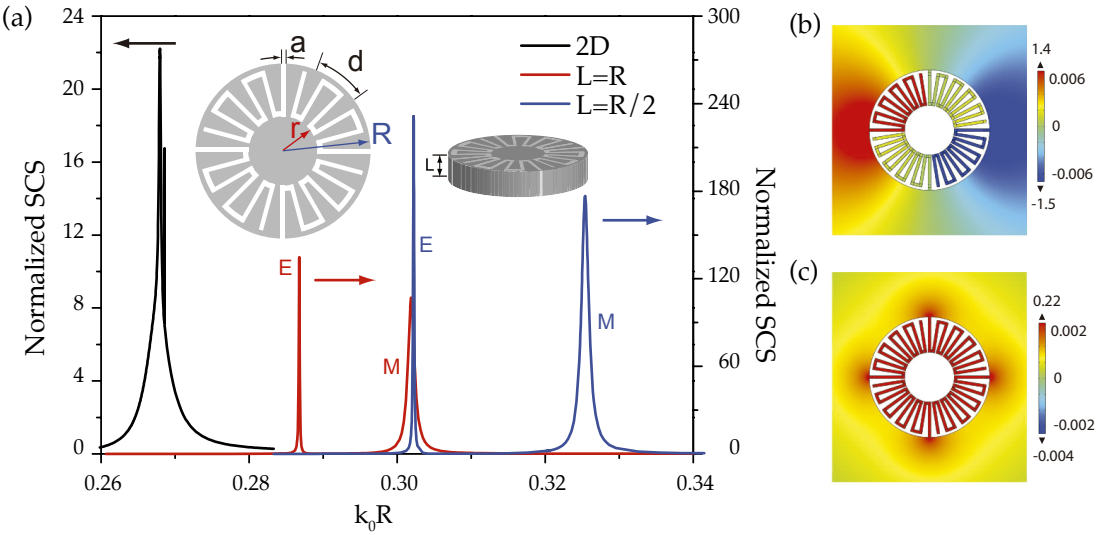

Figure 3.7: Magnetic LSPs in PEC subwavelength structures without dielectric filling. (a) The plot shows the SCS for an infinite cylinder (black line) and disks of thicknesses $L = R$ (red line) and $L = R/2$ (blue line), corrugated with four meanders and with parameters: $N = 40$, $a = 0.3d$, $n_g = 1$ and effective depth $h_m \approx 6R$. (b,c) Field pattern (H_z amplitude) for the 2D case at the dominant peak in the SCS, $k_0R = 0.268$, showing the electric dipole (b) and magnetic dipole modes (c), respectively.

frequency-independent antennas or for polarization control at low frequencies [233–235]. More recently, spiral-based metamaterials like Swiss-rolls [72] or one-spiral resonators [236, 237] have been introduced in order to improve the magnetic response of split-ring resonators [72].

Here we introduce two novel structures that exploit the basic idea of using very long grooves: PEC cylinders or disks corrugated with meanders and with spiral grooves. In principle, it is not clear whether the hypothesis that bent grooves behave like straight larger ones is valid, due to possible internal reflections at the bends. However, our numerical results confirm the validity of this approach. In Fig. 3.7 we present detailed results on the LSP modes in PEC structures corrugated with meanders. The geometry we are considering is sketched as an inset: a cylinder of radius R is textured with four meander-shaped grooves of effective depth $h_m \approx N(R - r)/4$. The computed SCS for such a structure is plotted as a black line for the 2D case. Similarly to the already discussed PEC cylinder with filled grooves, the SCS shows a dominant peak that reveals electrical dipole and magnetic dipole field patterns, as shown in panels (b) and (c). A rough estimation based on Eq. 3.12 (where h is substituted by h_m) predicts spectral

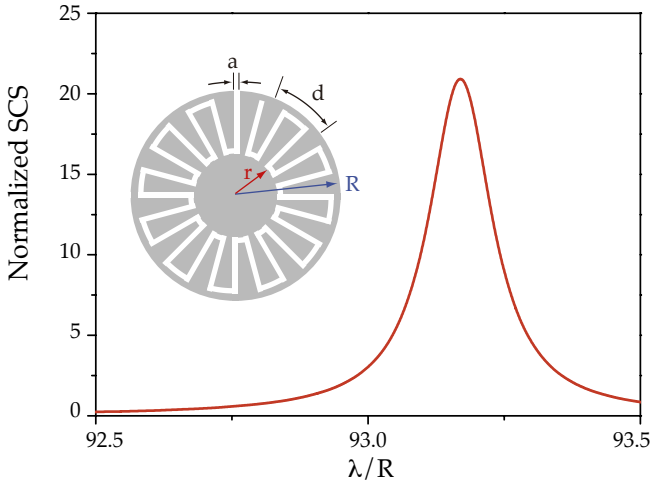

Figure 3.8: Deeply subwavelength magnetic LSP in a PEC subwavelength structures without dielectric filling. The plot shows the SCS for an infinite cylinder corrugated with just one meander and with the same parameters as considered in Fig. 3.7.

locations of these two dipolar modes at $k_0 R = \pi R/(2h_m) \approx 0.262$, very close to the numerical value, 0.268. Moreover, 3D structures corrugated with meanders also behave similar to PEC disks corrugated with filled grooves. In particular, the SCS for disks with meanders ($L = R$ in red and $L = R/2$ in blue), shows a shift in the resonant modes, with the magnetic LSP spectrally located at higher frequencies than the electrical LSP. In addition, our design allows us to create EM modes whose resonant wavelengths can be made much larger than the size of the object. This is illustrated Figure 3.8, where the normalized SCS of an infinite cylinder corrugated with only one very long meander displays a resonance at a wavelength that is around 100 times larger than the radius.

A different way of achieving grooves of very long depth is based on a spiral geometry. As the meander structure, it mimics the EM response of a corrugated cylinder with shallow grooves and filled with a dielectric. The structure consists of a PEC cylinder of radius R drilled with four spiral-shaped grooves that are wrapped around a small PEC cylinder of radius r [see the geometry sketch in Fig. 3.9 (a)]. Each spiral groove has width a and depth $h = 5R$, and two neighbouring arms are separated by a distance d. The plot in panel (a) presents the computed SCS for 2D cylinders (black line), and 3D disks of thicknesses $L = R$ (red line) and $L = R/2$ (blue line). As in the previously discussed cases, the dominant peak in the 2D SCS shows two quasi-degenerate electric and a magnetic LSPs (H_z for these modes is depicted in panels b and c). The 3D cases present a shift of the resonances that takes the magnetic LSP mode to higher frequencies

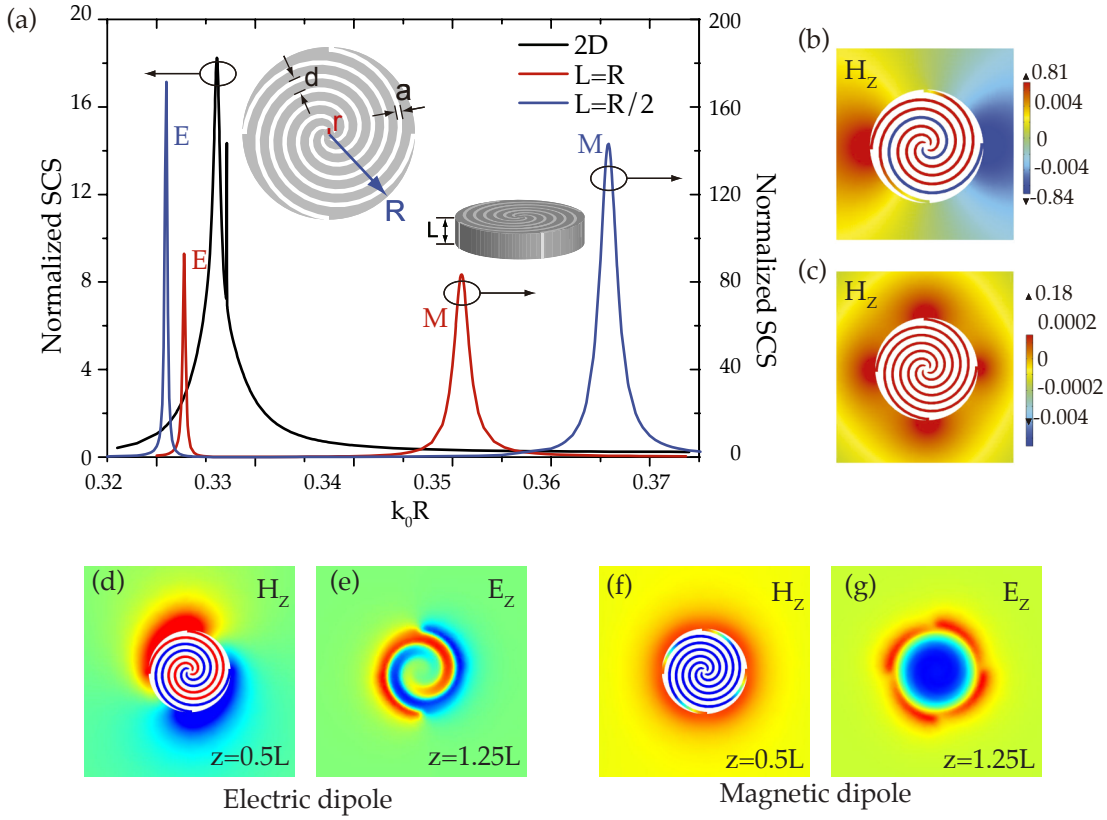

Figure 3.9: Particles corrugated with spiral-shaped grooves. (a) The plot shows the SCS for the 2D case (black line) and disks of thicknesses $L = R$ (red line) and $L = R/2$ (blue line), with parameters: $d = 0.159R$, $a = 0.33d$, $r = 0.063R$, $h_m = 5R$ and $n_g = 1$. All the parameters are shown in the geometry sketch. (b,c) Field pattern for the two quasi-degenerate modes at $k_0R = 0.3245$ for an infinitely long spiral structure showing the electric and magnetic dipoles, respectively. (d,e) Near-field distributions of a 3D PEC disk corrugated with spiral grooves at the electric LSP resonant frequency ($k_0R = 0.32$) on two plane cuts. The magnetic field, H_z is plotted in the $x-y$ plane at $z = L/2$ (d) and the electric field, E_z, is plotted at $z = 1.25L$ (e). (f,g) The same as panels (d,e) but for the magnetic LSP ($k_0R = 0.32$): H_z at $z = L/2$ (f) and E_z at $z = 1.25L$ (g). The thickness of the disk in panels (d-g) is $L = R/2$.

than the electric LSP. Plots of the near-field distribution at both LSP modes for a 3D disk corrugated with spiral-shaped grooves are also presented in the figure. Panels (d) and (f) show the z component of the magnetic field, H_z, at a plane cut in the middle of the disk ($z = L/2$) for the electric (d) and magnetic (f) LSPs. For both resonances, the near field resembles that of the 2D case [see panels (b) and (c)], and the electric-dipole and magnetic-dipole characters are clear. These characters are still clear for both resonances when the electric field is plotted on top of the disk, in a plane at a distance

$0.25R$ from its the upper face. The pattern of E_z at $z = 1.25L$ is shown for the electric LSP and the magnetic LSP in panels (e) and (g), respectively. Finally, note that the spiral structure presented in Fig. 3.9 is just a particular case of the general idea the emergence of magnetic spoof-LSPs in purely metallic structures corrugated with very long grooves.

With the results presented in this Section, we have demonstrated that our hypothesis behind the design of the meanders and spirals geometries is correct and magnetic LSP modes can be supported by purely metallic structures. Additionally, the origin of these EM resonances is purely geometrical and, hence, our design is not limited by material properties. Indeed, and as we show in the following, spoof LSP modes are not limited to PEC structures and hence very low frequencies. By considering realistic metal properties, we have checked that these modes exist for a broad range of frequencies.

In order to illustrate the range of validity of the PEC approximation, we now present calculations where the effect of both metal absorption and finite permittivity have been taken into account. We model the metal as silver with a Drude permittivity with parameters, $\omega_p = 1.37 \times 10^{16}$ Hz, $\gamma = 2.73 \times 10^{13}$ Hz, as given in Ref. [238] (see Appendix B for more details), and analyze the extinction cross section (ECS) for different frequency regimes. The ECS is the sum of the scattering and absorption (ACS) cross sections. In particular, here we consider the 2D meanders structure presented in Fig. 3.7 (a), with the PEC replaced by silver. The simulation results for particles of radius $R = 10$ mm (b), $R = 1$ mm (c), $R = 100$ μm (d), $R = 10$ μm (e) and $R = 1$ μm (f), with all the other geometrical parameters scaled accordingly, are presented in Fig. 3.10. The structures are resonant for $\sim$ 1 GHz, $\sim$ 10 GHz, $\sim$ 100 GHz, $\sim$ 1 THz and $\sim$ 10 THz, respectively. Considering realistic metal properties results in three main effects. First, due to its extremely narrow band, the quadrupole mode disappears from the spectrum when metal absorption is included. Second, as the frequency increases, the resonance peak is red-shifted with respect to the estimation given by the PEC approximation. This shift is most noticeable for the case of $R = 1$ μm, for which the PEC approximation predicts a resonance frequency of 12.8 THz, while the real metal simulation yields a resonance at 9.5 THz. Third, absorption starts to dominate scattering: whereas in the GHz regime the ECS is dominated by the scattering contribution, in the IR regime absorption is the main contribution to the ECS. These results prove that, although the PEC approach losses quantitative prediction power as the frequency increases, it is able to capture the main ingredients of the resonance behaviour of corrugated metal particles for frequencies ranging from the GHz to the THz and mid-IR regimes.

Moreover, we have also checked the effects of realistic metal properties on the results

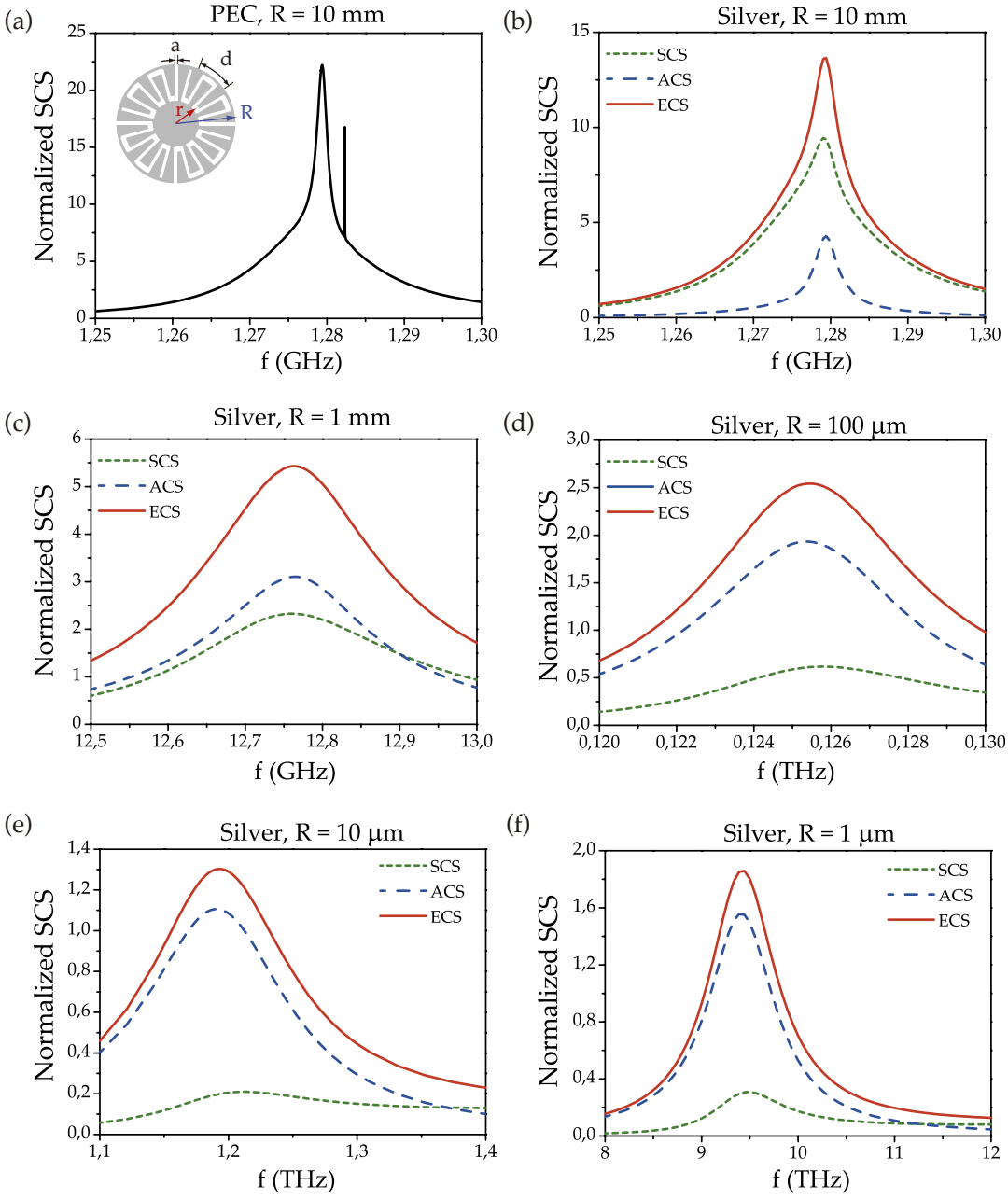

Figure 3.10: Effect of realistic permittivity in cylinders corrugated with meanders. (a) Normalized SCS for a 2D PEC cylinder corrugated with meander-like grooves (same as in Fig. 3.7). The radius of the cylinder is $R = 10$ mm. (b) Normalized SCS, ACS and ECS for a corrugated cylinder made of silver and with radius $R = 10$ mm. The plot shows a very good agreement with the PEC approximation in panel (a). (c-f) Effect of the realistic conductivity for corrugated cylinders with radius $R = 1$ mm (c), $R = 100$ μm (d), $R = 10$ μm (e) and $R = 1$ μm (f). The geometrical parameters in all cases are $r = 0.4R$, $N = 40$, $a = 0.3d$, $n_g = 1$ and effective depth $h_m \approx 6R$. The electric permittivity of silver is modeled with a Drude formula with parameters given by Ref. [238] (see Fig. B.1 for a plot).

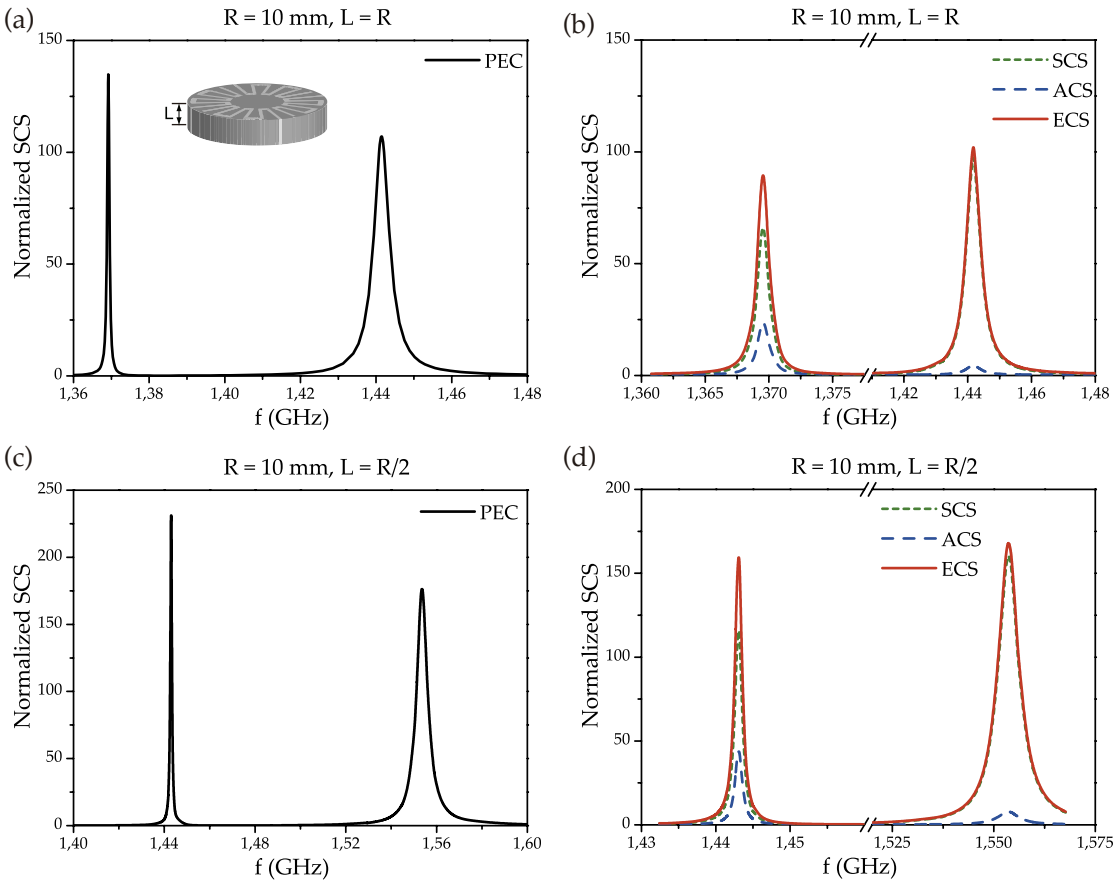

Figure 3.11: Effect of realistic permittivity in disks corrugated with meanders. (a,b) Disks of thickness $L = R$. (c,d) Disks of thickness $L = R/2$. Panels (a) and (c) show the SCS in the PEC approximation as a reference. Panels (b) and (d) present the SCS, ACS and ECS for corrugated silver particles in the GHz regime. In all cases the radius of the disk is $R = 10$ mm and the other geometrical parameters are $r = 0.4R$, $N = 40$, $a = 0.3d$, $n_g = 1$ and effective depth $h_m \approx 6R$.

for the 3D disks presented in Fig. 3.7 (b). Corrugated disks of thickness $L = R$ and $L = R/2$ are studied in panels (a,b) and (c,d) of Fig. 3.11, respectively. In this case we present results in the GHz regime, which corresponds to millimeter-sized structures. Despite the inclusion of metal absorption losses, scattering dominates absorption for this frequency range. From this figure it is clear that magnetic and electric spoof LSP modes survive for real metals. With these results we have confirmed that, as expected, the PEC approximation is very accurate for our structures at low frequencies.

3.6 Experimental verification

In this Section we discuss the experimental verification of our results carried out by the group of Professor Cui at Southeast University in China. In these experiments, ultra-thin metallic spiral structures were used to provide experimental proof on the magnetic spoof-LSPs. For practical reasons, the experiments were performed in the microwave regime but, as we have shown, magnetic LSP modes can also be devised at higher frequencies (THz up to mid-IR energies) by just a proper down scaling of the structure analyzed in this experimental study. The fabricated structure consists of four metallic spiral arms wrapped 1.5 turns around a small metallic disk of radius r such that the particle has an outer radius R (see the geometry sketch in Fig. 3.12). Each strip has width w and two neighboring arms are separated by a distance d. The textured copper disks (radius $R = 9.5$ mm) have a thickness that is much smaller than the radius: $L = 0.035$ mm. The whole ultra-thin structure is fabricated on top of a dielectric substrate using the standard printed circuit board fabrication process. The substrate has a thickness $t_s = 0.8$ mm and a dielectric permittivity $\epsilon_s = 3.5$.

The measured near field spectrum for the ultra-thin spiral structure is presented in Fig. 3.12 (a) as a red solid line. The EM response of the structure is measured by means of a transmitting antenna that is placed 3 mm away from one side of the sample to excite the modes, and a receiving antenna that is located at the other side of the sample to detect the resonance spectrum. In the plot, we can clearly observe two distinctive resonance peaks at frequencies $f = 1.1$ GHz ($k_0 R = 0.22$) and $f = 1.87$ GHz ($k_0 R = 0.37$). To reveal the physical nature of these two resonances, we have calculated the ECS spectrum for the same structure (see black dashed line in the figure). It shows two resonances whose spectral locations are in excellent agreement with the experimental results. In this case, the ECS, has been calculated by means of full wave simulations [239] in which both the metal absorption and the presence of a dielectric substrate are fully taken into account. The simulated field patterns at the two resonances are plotted in panels (b) and (c). Similarly to the behavior previously discussed for PEC disks corrugated with meanders and spirals, these plots show that the first resonance is due to the electrical LSP (b) while the second peak emerges from the magnetic LSP (c). In addition these field patterns closely resemble those plotted in Fig. 3.9 [panels (e) and (g)] for the spiral structures of thickness $L = R/2$ considered in the previous Section. The measured near field distributions for the spiral structure are rendered in panels (d) and (e). The local z component of the electric field for both the electric and magnetic dipole LSP resonances

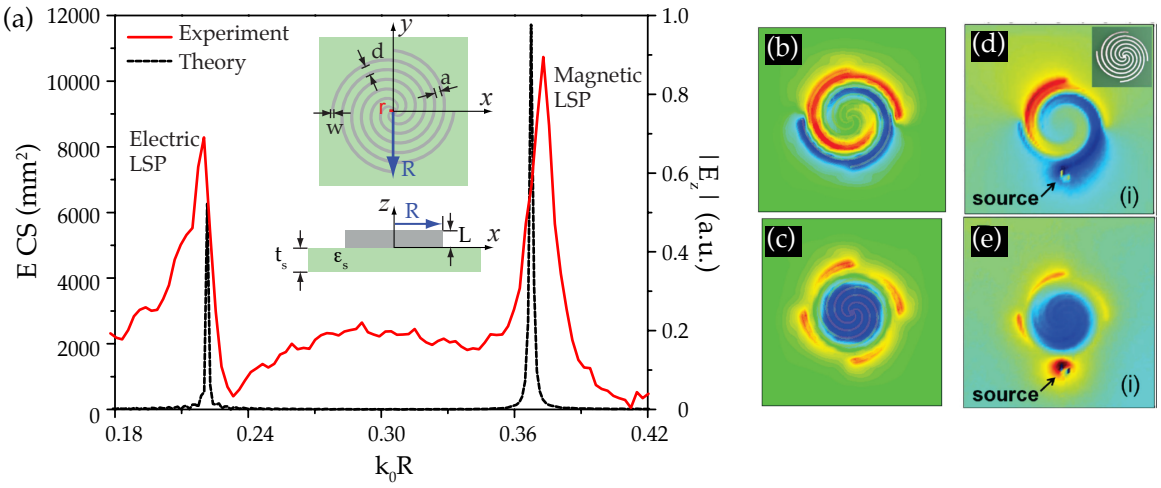

Figure 3.12: Resonance spectrum for subwavelength ultra-thin textured metallic disks. (a) Experimental near field spectrum ($|E_z|$ is measured) and calculated ECS spectrum. The inset panels show a sketch of the structure, which is placed on top a dielectric of thickness $t_s = 0.8$ mm and $\epsilon_s = 3.5$. The parameters of the fabricated structure are: $R = 9.5$ mm, $r = 0.6$ mm, $d = 1.508$ mm, $a = 1.008$ mm and $L = 0.035$ mm. (b,c) Calculated near-field distribution of the E_z field component at the electric (b) and magnetic (c) LSPs in a $x - y$ plane cut 1.5 mm above the ultra-thin disk. In the color scale, red and blue indicate positive and negative values, respectively. (d,e) Measured near field distribution of the LSP. The same quantities as in panels (b,c) are plotted. A photograph of the sample is rendered in panel (d)

are shown in (d) and (e), respectively. By comparing panels (d) and (e) to the numerical results shown in (b) and (c), we conclude that the agreement between the simulation results and the experimental images is remarkable. For the electric LSP mode (d), we notice that two equivalent electric currents propagate along two curved routes on the metallic surface with opposite directions, resembling an electric dipole. On the other hand, for the magnetic-dipole mode, we can see in (e) that the circulating E_z field varies between negative and positive, which is analogous to the current generated by a magnetic moment. Hence, these experimental results show that electric and magnetic LSP resonances also exist for ultra-thin ($L \ll R$) metal films and, therefore, meander and spiral structures can be used as building blocks in the design of 2D metamaterials (i.e., metasurfaces) [86, 240].

3.7 Conclusions

To summarize, in this Chapter we have developed the concept of magnetic localized surface plasmons. The results presented here add the important ingredient of magnetism to the field of particle plasmonics. We have first studied PEC particles corrugated with subwavelength grooves filled with dielectrics. By means of numerical simulations as well as an analytical model, we have shown that, unlike conventional subwavelength plasmonic particles, the EM response of these corrugated structures consists of two quasi-degenerate modes. We have discussed throughout the Chapter that one of the modes is an electrical dipole LSP while the second one is a magnetic dipole LSP, and that they have a geometrical origin. We have studied how for 3D structures the quasi-degeneracy is lifted and the magnetic-LSP acquires a higher resonance frequency than the electrical-LSP. The response of PEC structures corrugated with grooves can not be mapped to that of isotropic dielectric materials, but rather to that of an anisotropic metamaterial.

In addition, we have shown that magnetic-LSP modes can also be supported by purely metallic structures. Based on the analytical model, we have found an equivalence between structures corrugated with shallow grooves filled with dielectrics and structures corrugated with long empty grooves. In this case, the EM resonances can be controlled by means of only geometrical parameters, without requiring a dielectric material of high refractive index. We have presented two different structures of this kind. In the first one the deep grooves are achieved by bending them in a meander shape, while in the second one a spiral shape is used for this purpose. Finally, we have presented an experimental verification of our findings based on an ultra-thin spiral structure working in the microwave regime.

3.8 Appendix: Frequency ordering of the modes

In this Appendix we present a detailed study on the origin of the different frequency ordering of the EM dipole modes occurring in corrugated PEC structures and in subwavelength dielectric particles. In particular, we present a physical argument based on the variational formulation of EM that explains why the electric dipole mode of corrugated metallic disks has lower frequency than the magnetic dipole mode, whereas the opposite frequency ordering is displayed for the modes of dielectric disks.

The precise magnitude of the eigenvalue associated to an eigenmode supported by any of the structures considered in this Chapter is dictated by the spatial distribution

of its corresponding electric field **E**. This fact can be best appreciated by means of the variational formulation of electrodynamics. According to this formulation [241], the lowest frequency eigenmode minimizes the following functional

$$U\left[\mathbf{E}\right] = \frac{\int \mathrm{d}\mathbf{r}^3 \left|\nabla \times \mathbf{E}\right|^2}{\int \mathrm{d}\mathbf{r}^3 \, \epsilon(\mathbf{r}) |\mathbf{E}(\mathbf{r})|^2}. \tag{3.19}$$

Similarly, the next eigenmode minimizes the functional within the subspace orthogonal to the first eigenmode. Moreover, the frequency ω corresponding to a given eigenmode can be computed by evaluation of the functional at the field **E** corresponding to the mode:

$$\left(\frac{\omega}{c}\right)^2 = U\left[\mathbf{E}\right]. \tag{3.20}$$

Importantly, the functional is directly related to the electric field curl, the latter being linked to the geometry and curvature of the field lines. Thus, inspection of the field line patterns of the eigenmodes, e.g. the presence or absence of vortices, provides a physical clue to the magnitude and ordering of the corresponding eigenvalues.

Since we have already computed the eigenmodes of the different structures under consideration with FEM calculations, it is straightforward to numerically evaluate Eq. 3.20 to determine the eigenvalues by means of the variational theorem. In order to understand the different frequency ordering of the modes of 3D structures, our argument starts by considering 2D cylinders. For the metallic corrugated structure presented in Fig. 3.1, the eigenvalues retrieved using Eq. 3.20 are consistent with those previously found. The eigenvalues corresponding to the magnetic and electric modes, given in Table 3.1, differ by less than 2 parts in 1000, confirming the quasi-degeneracy already discussed throughout the Chapter for infinitely long corrugated cylinders. For a 2D dielectric cylinder of the same radius and refractive index $n_g = 8$, the eigenvalues determined with

Eigenvalues, $k_0 R$:

	Corrugated PEC		Dielectric	
Mode	Cylinder	Disk	Cylinder	Disk
Magnetic-LSP	0.330	0.384	0.291	0.394
Electric-LSP	0.327	0.368	0.470	0.558

Table 3.1: Eigenvalues, $k_0 R$, of the magnetic and the electric modes for the corrugated PEC and dielectric particles studied in Figs. 3.13 and 3.14. The eigenvalues are calculated using Eq. 3.20.

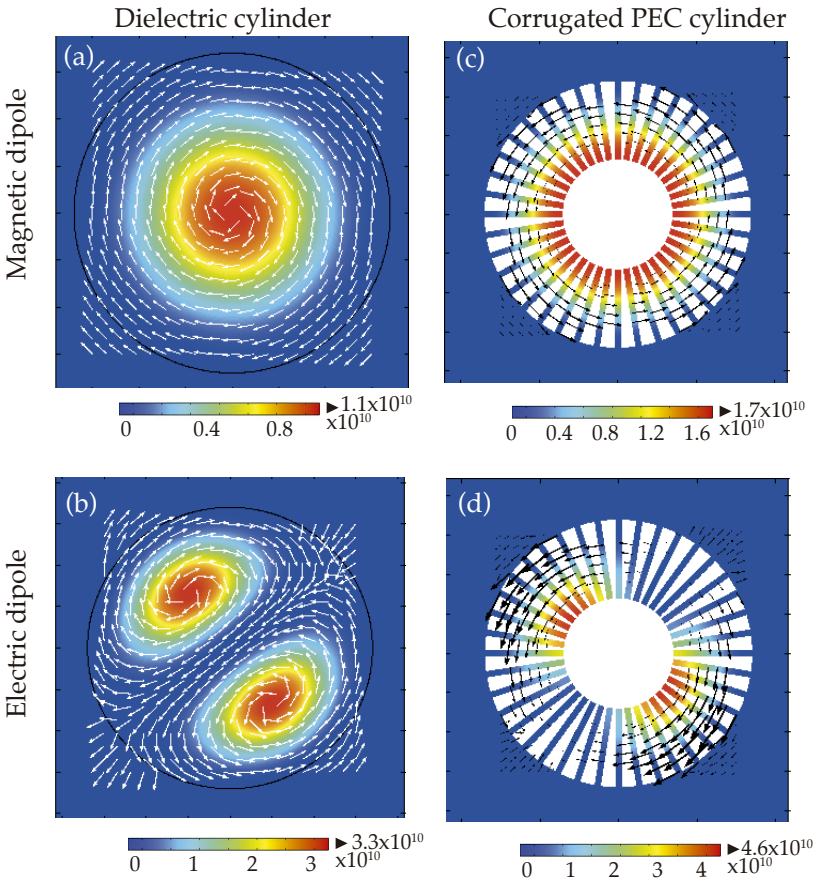

Figure 3.13: The curl field for 2D structures: a dielectric cylinder and a subwavelength PEC cylinder corrugated with grooves. The arrows represent the (Ex, Ey) components of the electric field, while the color map represents the squared rotational of the electric field normalized to the EM energy of the mode. Panels (a) and (b) render the rotational fields for the n=0 (a) and n=1 (b) modes of a dielectric cylinder, while panels (c) and (d) correspond to the n=0 (c) and n=1 (d) modes supported by a corrugated metallic cylinder.

the FEM calculation and via Eq. 3.20 are again consistent, and they present a different behaviour than that for the corrugated metallic cylinder. Now the magnetic and electric modes are not degenerate (see Table 3.1). Their frequency difference is large, the electric mode having a frequency 60% higher than the magnetic one. As mentioned above, this contrasting behaviour can be ascribed to the field line patterns of the various eigenmodes, which are rendered in Fig. 3.13. The magnetic mode of the dielectric cylinder (panel a) displays one vortex with azimuthal symmetry, whereas the electric mode (panel b) presents two counter-rotating vortices with enhanced electric field curl which, according to Eq. 3.20, rises its frequency value. This reasoning explains the frequency ordering

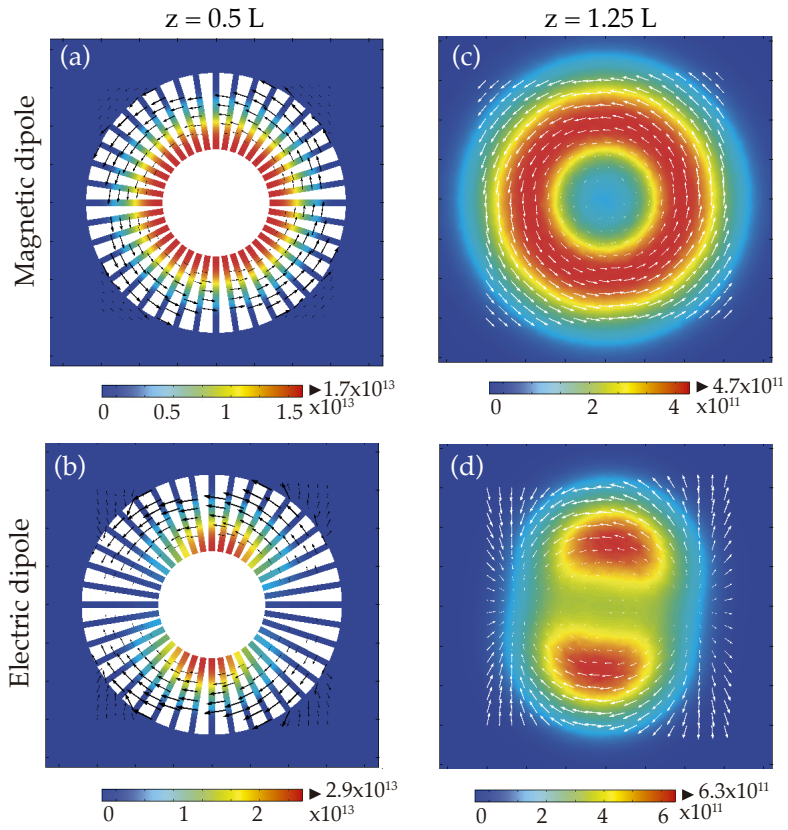

Figure 3.14: The curl field for a 3D subwavelength PEC disk corrugated with grooves. The figure shows the electric field lines [(Ex, Ey), arrows] and the normalized squared rotational of the electric field (color map) for a 3D disk of L = R at two different cut planes parallel to the disk lid: modes $n = 0$ (a) and $n = 1$ (b) at the middle of the disk and modes $n = 0$ (c) and $n = 1$ (d) at a plane cut on top of the disk separated a distance $0.25L$ from it.

of the magnetic and electric dipole modes for a dielectric cylinder. On the other hand, the corrugated metallic cylinder presents a very different electric field line geometry. In this structure the presence of the grooves imposes a circulating pattern around the inner metallic core for both the magnetic and electric modes (panels c and d). Although the quasi-degeneracy in the metallic case cannot be understood from the qualitative aspect of the field patterns alone, the full evaluation of the functional as well as the analytical model presented in the presented in Section 3.3 predict precisely this behaviour.

When going from 2D corrugated metallic cylinders to 3D disks, it remains to be explained why the quasi-degeneracy is lifted and why, as a difference to the dielectric structures, the magnetic mode is the one which acquires a higher frequency. We have first computed the eigenvalues for a corrugated metallic disk of thickness $L = R$ by

means of the variational theorem. The results, presented in Table 3.1, confirm that both modes rise their frequencies as compared to the 2D case: the magnetic mode increases its frequency a 22% from its 2D value and the electric mode frequency increases a 10%. Notice that the evaluation of the functional requires an integration to all space (see Eq. 3.20) and that not all regions of space contribute equally to the integral. In fact, the region comprising the inner part of the grooves is responsible for about 80% of the total amount. Interestingly, if the functional is evaluated by integration only within this region, the quasi-degeneracy is not lifted. This is a consequence of the fact that the field within the grooves is almost the same for the 2D and 3D cases (compare Figs. 3.13 and 3.14). Thereby, we expect that the reason behind the degeneracy lift when going from 2D to 3D stems from the fields outside the disk. We have checked this by separating the integrals in Eq. 3.20 in three contributions corresponding to: (i) the grooves, (ii) the regions above and below the disk lids, and (iii) the rest. It turns out that region (ii) is the second in importance when the functional is evaluated. On this basis we analyze the value of the electric field curl for both the electric and magnetic modes in this region, i.e., in a plane parallel to the disk lid and above it, as shown in Fig. 3.14 (c) and (d). The magnetic mode displays a distinct vortex (panel c) which is absent for the electric mode (panel d). Thus, according to Eq. 3.20, when the corresponding electric field curls are integrated on top of the lids, the magnetic mode increases its frequency more than the electric mode. Finally, the corresponding computation has been performed for dielectric structures and the resulting eigenvalues are shown in Table 3.1. In a similar way to metallic structures, the transition from 2D to 3D rises the frequencies of both modes, namely a 35% increase for the magnetic dipole and a 20% for the electric dipole. However, as we have shown above, the modes of dielectric cylinders are not degenerate but, instead, display a large frequency difference, the electric one having a 60% higher frequency. As a consequence, the blueshifts are now unable to revert the frequency ordering of the modes, and the magnetic dipole remains the ground mode.

Chapter 4

Plasmonic Brownian ratchet

4.1 Introduction

The plasmonic-based optical trapping and transport of nanoscopic objects finds many applications in microfluidics and lap-on-a-chip systems [153]. As we introduced in Section 1.4, the extremely enhanced EM energy in plasmonic antennas enables the trapping of Rayleigh dielectric particles and biological objects within subwavelength volumes [140]. In principle, plasmonic antennas are designed to generate highly localized gradient forces for trapping the targeted objects into a single point fixed by the fabricated nanostructure [147–151]. The controlled transport and manipulation of these targets over long distances is desirable for lap-on-a-chip applications and especially for on-chip sorting. This long-distance transport has been shown for nanoscopic metal particles, whose large polarizability greatly enhances the scattering forces that push the particles on flat substrates along the illumination direction [242, 243]. In contrast, dielectric and biological objects lack a large polarizability and different strategies need to be developed in order to achieve a controlled transport of such objects.

Thermal noise induced by random collision of the liquid molecules [244], is usually an obstacle for controlling particle flow at nanoscopic scales and is to be suppressed for any particle manipulation technology. By taking advantage of these thermal fluctuations instead suppressing them, here we address the issue of dielectric particle transport over long distances in plasmonic structures. Although the second law of thermodynamics states that temperature-governed fluctuating forces originate no net motion in the large scale, by driving an anisotropic system out of thermodynamic equilibrium work can be performed out of thermal noise. This is the working principle of the so-called Brownian ratchets [245, 246].

The attention raised by Brownian ratchets spans over different fields [247]. For instance, they have been of fundamental interest in biology because they play a role in biological protein motors, as was experimentally investigated in Ref. [248] for an actomyosin motor. Brownian ratchets have also attracted great interest as the basic working principle of practical devices inspired in biological physics or motivated by biological applications. The reason for this is that they enable a net transport of objects in the micro and nanoscales, which can be used to pump nanoscale motors or to sort different kinds of particles. The directed drift of Brownian particles has been reported for different systems, such as for colloidal particles in the presence of asymmetric electrodes [249], for dielectric particles in an optical ratchet [250], for DNA in electrochemical systems [251, 252], for charged phospholipids in a 2D fluid bilayer embedded in an array of asymmetric titanium dioxide barriers [253] or for colloidal particles in microfluidic systems [254]. While these experiments rely on a dynamical modulation of an external driving to take the system out of equilibrium, Brownian ratchets based on non-conservative stationary forces, where the system is taken out of equilibrium by time reversal symmetry breaking, are also possible. In Ref. [255], a deterministic ratchet that makes use of non-conservative optical forces in a specific arrangement of stationary optical lattices was theoretically demonstrated. In addition, the quest for self-propelling microdevices has lead to the experimental demonstration of a bacterial driven micro-motor, where the propelling force generated by flagellar bacterial motors act as a non-conservative force [256]. Finally, and at a different level, mesoscopic Brownian motors, such as organic electronic ratchets and spin ratchets, have also been experimentally demonstrated, showing that they are great candidates to power nanodevices and electronic circuits [257–261].

In this Chapter, we present a proof of principle demonstration of a light-driven nanoscale Brownian ratchet based on plasmonic interactions. This plasmonic Brownian ratchet makes use of plasmonic-based optical forces, which first enable the trapping of a subwavelength dielectric bead and then drive it a long distance displacement in a single device at room temperature. By means of an array of plasmonic structures with broken spatial symmetry, we generate a set of anisotropic traps for dielectric beads. This trapping potential is repeatedly excited by turning on and off a laser field, thus taking the system out of equilibrium and yielding a directed drift of particles into one direction, as sketched in Fig. 4.1. In addition, we demonstrate this mechanism by means of molecular dynamics (MD) simulations, showing the rectified Brownian motion of a dielectric bead in the absence of any external bias.

The Chapter is organized as follows. In Section 4.2 we characterize the plasmonic system that will be the base for the Brownian ratchet. In order to study the properties

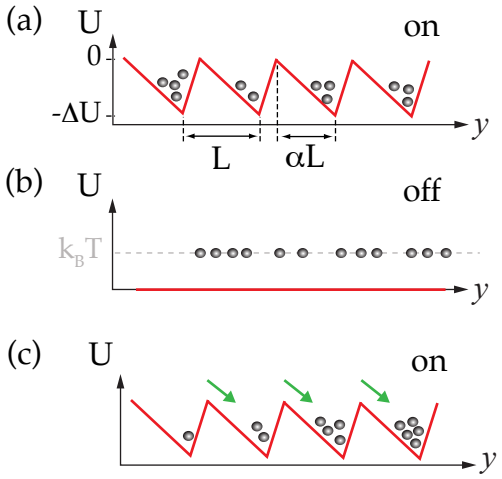

Figure 4.1: Sketch of the ratchet mechanism: by periodically turning on and off a plasmonic-based optical potential the Brownian diffusion of a dielectric particle is biased into one direction. (a) A periodic set of anisotropic optical traps is generated by illuminating a periodic array of plasmonic nanostructures with a laser field. The potential wells act as nanotweezers for a dielectric bead. (b) When the illumination is off, the particles are free to diffuse over the sample. (c) Due to the anisotropy in the potential, turning the illumination on again results in an enhanced probability for the particle to move forwards. Thereby, the Brownian motion of the particle is rectified into one direction.

of the nano-optical traps generated by the proposed plasmonic structure, we first discuss the EM fields and optical forces in Subsection 4.2.1. In Subsection 4.2.2 we study the trapping potential felt by a dielectric bead in the presence of the plasmonic system and we discuss the geometrical parameters appropriate for the design of the Brownian ratchet. Next, in Section 4.3, we simulate the dynamics of a subwavelength dielectric bead in the plasmonic Brownian ratchet. First, in Subsection 4.3.1 we briefly review the MD simulation technique, and in Subsection 4.3.2 we present the simulation results and we discuss the relevant parameters that play a role in the dynamics.

4.2 Characterization of the plasmonic system

We start by describing the plasmonic system that is the base for the Brownian ratchet proposed in this Chapter. It consists of an array of plasmonic nanostructures that is designed to bias the Brownian motion of subwavelength dielectric beads. The design of the plasmonic Brownian ratchet is based on (i) anisotropic trapping, generated by geometrical asymmetry, and (ii) a periodic modulation in time of the interaction, achieved

by switching the illumination on and off in periodic cycles. Hence, we need a 1D array of anisotropic nano-optical traps in one direction.

To fulfill these requirements we propose the periodic array of plasmonic nanostructures shown in Fig. 4.2. The unit cell, whose side view is shown in panel (b), is formed by a collection of metallic dipole antennas (dielectric permittivity ϵ_m) of gradually varying lengths and with deep subwavelength spacing [1]. In our design, we have taken in particular four optical dipole antennas. Each dipole antenna has a subwavelength gap d and is separated from its nearest neighbour by g. The nanorods composing the dipole antennas have width w, height h and varying lengths: L in one side of the group and

$$L_0 = L - 3(\mathrm{w} + g)\tan(\theta) \tag{4.1}$$

in another. The angle θ, shown in panel (a), characterizes the asymmetry of the structure. The array of nanostructures, with period Λ, lies on top of a glass substrate and is immersed in water containing a solution of dielectric beads at room temperature. The system is illuminated with a normally incident plane wave (intensity I_0) with the electric field polarized along the dipole antennas axis (E_x), as depicted in panel (b), such that the near field within the gaps is efficiently enhanced and dielectric beads can be trapped in the EM hot spots. For this purpose, the geometrical parameters ($L = 225$ nm, $d = 40$ nm, $\mathrm{w} = 50$ nm, $g = 25$ nm and $h = 30$ nm) are chosen to maximize the field enhancement at an IR excitation wavelength of $\lambda = 1500$ nm. Finally, note that although more complex structures could also be devised, the arrangement of optical antennas of different lengths that we propose provides the required trapping and anisotropy, as we will see in the following.

In this Section we characterize the trapping properties of the plasmonic system described above. We first study the EM fields and optical forces generated by the plasmonic system upon illumination in Subsection 4.2.1, detailing the calculation method and discussing the results. Next, in Subsection 4.2.2, we study the trapping potential derived from the calculated optical forces and we discuss the appropriate geometrical parameters for the ratchet device.

4.2.1 Plasmonic-based optical forces

In order to characterize the properties of the nanotweezers, we start by studying the optical forces generated by the plasmonic system on a subwavelength dielectric bead. At first, we focus on a single array element, i.e. the four dipole antennas that compose an

[1] Note that a similar nanostructure has been studied in Ref. [262]

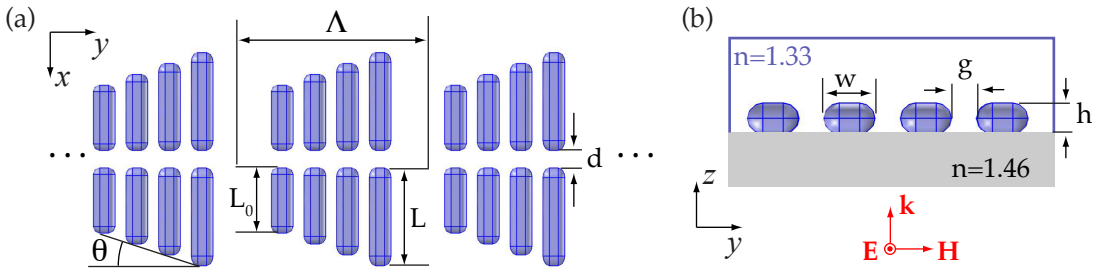

Figure 4.2: Plasmonic system that enables the Brownian ratchet device. (a) Top view of the plasmonic system: a periodic array of plasmonic structures formed by four optical dipole antennas. Each dipole antenna consists of two nanorods separated by a subwavelength gap d. The length of the dipole antennas varies gradually, thereby generating a geometrical asymmetry that is characterized by angle θ. (b) Side view of the periodic array unit cell: the plasmonic structure is placed on top of a glass substrate and embedded in water. The width of the nanorods is w and the separation between nearest neighbors is g. The system is placed in the $x-y$ plane such that the dipole antennas' long axis lies along the x axis while the nanostructure's symmetry axis corresponds to the y axis. The illumination is a plane wave that is turned on and off in periodic cycles.

unit cell. A dielectric bead in the presence of the plasmonic structure experiences a force that enables its trapping. This force is completely determined by the system EM fields, which are contained in the Maxwell stress tensor [1, 11],

$$\hat{\mathbf{T}}(\mathbf{r},t) = \left[\epsilon_0\epsilon\mathbf{E}\mathbf{E} + \mu_0\mu\mathbf{H}\mathbf{H} - \frac{1}{2}(\epsilon_0\epsilon|\mathbf{E}|^2 + \mu_0\mu|\mathbf{H}|^2)\hat{\mathbf{I}}\right] , \tag{4.2}$$

where ϵ and μ are the permittivity and permeability of the medium surrounding the object. The integration of this tensor on an arbitrary surface δV that encloses the particle yields the force exterted on it as follows,

$$\mathbf{F} = \int_{\delta V} \left\langle \hat{\mathbf{T}}(\mathbf{r}) \right\rangle \cdot \mathbf{n}(\mathbf{r})\, \mathrm{d}a\,, \tag{4.3}$$

where $\mathbf{n}(\mathbf{r})$ is the normal to the integration surface and $\langle ... \rangle$ stands for time average. Under the dipole approximation, the above equation reduces to a simpler expression in terms of the bead's polarizability, $\alpha(\omega)$ (as defined in Eq. 1.13), and the electric field gradient, as follows

$$\mathbf{F} = \frac{\mathrm{Re}\left[\alpha(\omega)\right]}{4}\nabla\mathbf{E}(\mathbf{r})\,. \tag{4.4}$$

Although this approximation usually works very well for particles of sizes much smaller than the wavelength (Rayleigh limit), we have checked that in this case the above equation fails to give an accurate value for the force at the EM hot spots. The reason for this

is that in these areas field variations occur in a scale that is comparable to the particle's size and the dipole approximation fails. Therefore, in oder to obtain the force field, we employ the Maxwell stress tensor method and calculate the tensor $\hat{\mathbf{T}}(\mathbf{r})$ for different positions of the particle's center, as we detail below.

As a first step to determine the optical forces acting on the bead we calculate the EM fields generated by the plasmonic structure upon illumination. To calculate the fields we make use of FEM simulations [219], that we briefly describe in the following. In the simulations, the group of four dipole antennas lies on top of a glass substrate (refractive index $n_1 = 1.46$) and is immersed in water ($n_2 = 1.33$), as shown in Fig. 4.2 (b). We simulate the antennas as real metal structures, including absorption. We take them as gold nanorods with permittivity $\epsilon_m(\omega)$ as given by the Drude-Lorentz model with parameters taken from Ref. [12]. In particular, $\epsilon_m = -103.6 + 8.8i$ at the illumination wavelength. The plasmonic structure is illuminated by means of a plane wave under normal incidence. The incident wave propagates in the z direction and is polarized along the dipole antennas' axis. Its electric field reads as

$$\mathbf{E}_0 = E_0 \mathbf{u}_x \cdot \begin{cases} e^{-ik_0 n_1 z} + r_{12}\, e^{ik_0 n_1 z} & z \leq 0\,, \\ t_{12}\, e^{-ik_0 n_2 z} & z > 0\,, \end{cases} \tag{4.5}$$

where $k_0 = 2\pi/\lambda$, E_0 is the amplitude and $\mathbf{u}_x$ is the unit vector in the x direction. In addition, r_{12} and t_{12} are the Fresnel coefficients for the glass/water interface, given by

$$r_{12} = \frac{n_2 - n_1}{n_2 + n_1}, \quad t_{12} = \frac{2n_1}{n_2 + n_1}. \tag{4.6}$$

Finally, in order to avoid reflections at the frontiers of the simulation domain we employ the appropriate boundary conditions, namely perfectly matched layers [219].

The simulated electric field is plotted in Fig. 4.3 for two different configurations of the nanostructure with different symmetries. Panels (a) and (c) correspond to the case where $\theta = 0°$ and show a top and a side view, respectively. In panel (a), the plot displays a symmetric field pattern with respect to the x axis. The greatly enhanced electric field at the dipole antennas' gap [see panel (c)] act as a nanotweezer for dielectric beads. On the other hand, panels (b) and (d) present the electric field for a structure with $\theta = 18°$. In this case, the field pattern reveals that the EM field is greatly enhanced in a hot spot located at the longest antenna's gap. The presence of the neighbouring antennas, with slightly different resonance frequencies due to their slightly different lengths, results in a continuous and asymmetric field profile along the y direction. As we will see below, the Brownian ratchet mechanism is ultimately based on this anisotropic field profile.

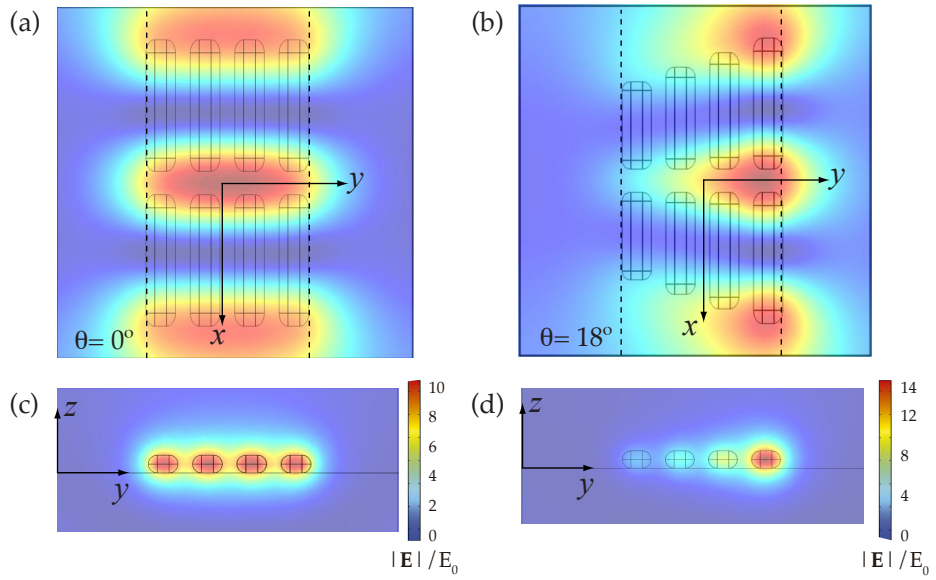

Figure 4.3: EM fields generated by the plasmonic nanostructure composed of four dipole antennas. Two nanostructures are compared: a symmetric geometry (a,c), $\theta = 0°$, and one with an asymmetric geometry (b,d), $\theta = 18°$. In panels (a) and (b) the plot shows electric field enhancement, $|\mathbf{E}|/E_0$, at a plane cut at $z = 90$ nm. The antennas lie on top of a water/glass interface at $z = 0$ (see Fig. 4.2). Panels (c) and (d) render a side view at plane $x = 0$. The illumination is a plane wave under normal incidence polarized along the dipole antennas' axis. The excitation wavelength is $\lambda = 1500$ nm. The geometrical parameters are: $L = 225$ nm, $d = 40$ nm, w $= 50$ nm, $g = 25$ nm and $h = 30$ nm. L_0 depends on the value of θ following Eq. 4.1: $L_0 = L$ in panels (a,c) and $L_0 = 150$ nm in panels (b,d).

We now consider the forces experienced by a subwavelength dielectric bead in the presence of the plasmon-based nanotweezers. As we have already mentioned, the integration of the Maxwell stress tensor, which is determined by the EM fields through Eq. 4.2, on a surface δV enclosing the bead yields the optical forces acting on the bead. Here we detail the calculation methods employed to derive the optical forces.

Our purpose is to calculate the force field as a bead that is placed above the plasmonic nanostructure moves along its symmetry axis, i.e., the y axis. We consider a polystere (PS) bead of refractive index $n = 1.59$ and radius $\sigma = 50$ nm. Its center is placed $x = 0$, $z = 90$ nm, such that the lowest point of the bead is separated 10 nm from the plasmonic nanostructure. The y position of the bead is varied to sample a grid,

$$y_i = y_0 + (i-1)\Delta y\,, \tag{4.7}$$

with $\Delta y = 10$ nm and $i = 1, ...N$. For each position of the bead, y_i, we run a FEM simulation of the EM fields as explained above. Note that the simulations have to include

the PS bead in order to take into account the perturbation of the EM field produced by its presence. In addition, we make use of an auxiliary boundary to perform the integral of the Maxwell stress tensor in Eq. 4.3. In particular, we use a cube of side 104 nm and centered at the bead's center. Thereby, we can write the y component of the force from Eq. 4.3 in terms of surface integrals on the box faces as

$$\begin{aligned}\mathbf{F}_y(\mathbf{r}) &= \int_{S_{+x}} \left\langle \hat{\mathbf{T}}_{yx}(\mathbf{r},t) \right\rangle \mathrm{d}y\mathrm{d}z - \int_{S_{-x}} \left\langle \hat{\mathbf{T}}_{yx}(\mathbf{r},t) \right\rangle \mathrm{d}y\mathrm{d}z + \\ &+ \int_{S_{+y}} \left\langle \hat{\mathbf{T}}_{yy}(\mathbf{r},t) \right\rangle \mathrm{d}x\mathrm{d}z - \int_{S_{-y}} \left\langle \hat{\mathbf{T}}_{yy}(\mathbf{r},t) \right\rangle \mathrm{d}x\mathrm{d}z + \\ &+ \int_{S_{+z}} \left\langle \hat{\mathbf{T}}_{yz}(\mathbf{r},t) \right\rangle \mathrm{d}x\mathrm{d}y - \int_{S_{-z}} \left\langle \hat{\mathbf{T}}_{yz}(\mathbf{r},t) \right\rangle \mathrm{d}x\mathrm{d}y\,. \end{aligned} \tag{4.8}$$

Here, the symbol $\int_{S_{\pm x,y,z}}$ stands for the surface integration on the cube's face that is normal to the x, y or z axis, respectively, and whose normal vector $n(\mathbf{r})$ points in the positive direction of the axis for the "+" case and in the negative direction for the "−". Equivalently, similar expressions can be written for $\mathbf{F}_x$ and $\mathbf{F}_z$. In the above equation, $\hat{\mathbf{T}}_{ij}(\mathbf{r},t)$ are the different Cartesian components of the Maxwell stress tensor. From Eq. 4.2, we can explicitly write the time average of each of the tensor components as

$$\begin{aligned}
\left\langle \hat{\mathbf{T}}_{xx}(\mathbf{r},t) \right\rangle &= \frac{1}{2}\mathrm{Re}\left[\epsilon_0\epsilon(E_x^* E_x - \frac{1}{2}|\mathbf{E}|^2) + \mu_0\mu(H_x^* H_x - \frac{1}{2}|\mathbf{H}|^2)\right], \\
\left\langle \hat{\mathbf{T}}_{xy}(\mathbf{r},t) \right\rangle &= \frac{1}{2}\mathrm{Re}\left[\epsilon_0\epsilon E_x^* E_y + \mu_0\mu H_x^* H_y\right], \\
\left\langle \hat{\mathbf{T}}_{xz}(\mathbf{r},t) \right\rangle &= \frac{1}{2}\mathrm{Re}\left[\epsilon_0\epsilon E_x^* E_z + \mu_0\mu H_x^* H_z\right], \\
\left\langle \hat{\mathbf{T}}_{yx}(\mathbf{r},t) \right\rangle &= \frac{1}{2}\mathrm{Re}\left[\epsilon_0\epsilon E_y^* E_x + \mu_0\mu H_y^* H_x\right], \\
\left\langle \hat{\mathbf{T}}_{yy}(\mathbf{r},t) \right\rangle &= \frac{1}{2}\mathrm{Re}\left[\epsilon_0\epsilon(E_y^* E_y - \frac{1}{2}|\mathbf{E}|^2) + \mu_0\mu(H_y^* H_y - \frac{1}{2}|\mathbf{H}|^2)\right], \\
\left\langle \hat{\mathbf{T}}_{yz}(\mathbf{r},t) \right\rangle &= \frac{1}{2}\mathrm{Re}\left[\epsilon_0\epsilon E_y^* E_z + \mu_0\mu H_y^* H_z\right], \\
\left\langle \hat{\mathbf{T}}_{zx}(\mathbf{r},t) \right\rangle &= \frac{1}{2}\mathrm{Re}\left[\epsilon_0\epsilon E_z^* E_x + \mu_0\mu H_z^* H_x\right], \\
\left\langle \hat{\mathbf{T}}_{zy}(\mathbf{r},t) \right\rangle &= \frac{1}{2}\mathrm{Re}\left[\epsilon_0\epsilon E_z^* E_y + \mu_0\mu H_z^* H_y\right], \\
\left\langle \hat{\mathbf{T}}_{zz}(\mathbf{r},t) \right\rangle &= \frac{1}{2}\mathrm{Re}\left[\epsilon_0\epsilon(E_z^* E_z - \frac{1}{2}|\mathbf{E}|^2) + \mu_0\mu(H_z^* H_z - \frac{1}{2}|\mathbf{H}|^2)\right].
\end{aligned} \tag{4.9}$$

In summary, by calculating the EM fields and Maxwell stress tensor for each position of the bead, y_i, and then integrating the tensor following Eq. 4.8 and equivalent expressions for the x and z components of the force, we are able to obtain the force field.

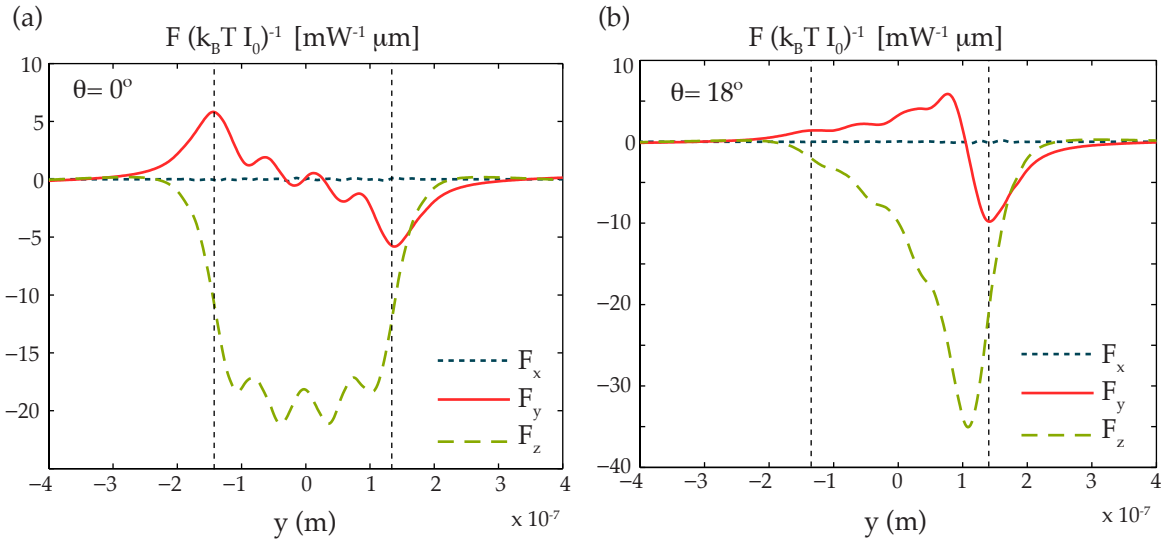

Figure 4.4: Optical forces experienced by a PS bead above the plasmonic nanostructure composed of four dipole antennas. (a) Symmetric nanostructure, with $\theta = 0°$. (b) Asymmetric nanostructure, with $\theta = 18°$. The dashed vertical lines point at the antennas boundaries as a reference to compare with the field patterns in Fig. 4.3.

Figure 4.4 shows the force field calculated by the above described procedure for a PS bead in the presence of the two plasmonic nanostructures considered in Fig. 4.3. The forces are normalized to the thermal energy, k_BT, with k_B being Boltzmann's constant and T the temperature, and to the intensity of the incident EM wave, $I_0 = nc\epsilon_0|E_0|^2/2$. In both cases, the force in the vertical direction, $\mathbf{F}_z$, attracts the particle towards the structure, while the force in the x direction is $\mathbf{F}_x \ll \mathbf{F}_y, \mathbf{F}_z$. Accordingly to the already discussed field pattern, the force field shown in panel (a) has inversion symmetry, as a particle moving towards the right from the left end is attracted towards the hot spot in the same way as a particle moving from the right end and towards the left. On the other hand, the forces in panel (b) reflect the geometrical asymmetry of the nanostructure. As it can be seen from the figure, $\mathbf{F}_y$ guides the particle towards the hot spot shown in Fig. 4.3 (b), as it is positive for y values at the left of the hot spot, and negative when the bead is at the right of the hot spot. However, in this case the force lacks inversion symmetry. Finally, note that $\mathbf{F}_y$ is the relevant component of the force for the study of the Brownian ratchet mechanism.

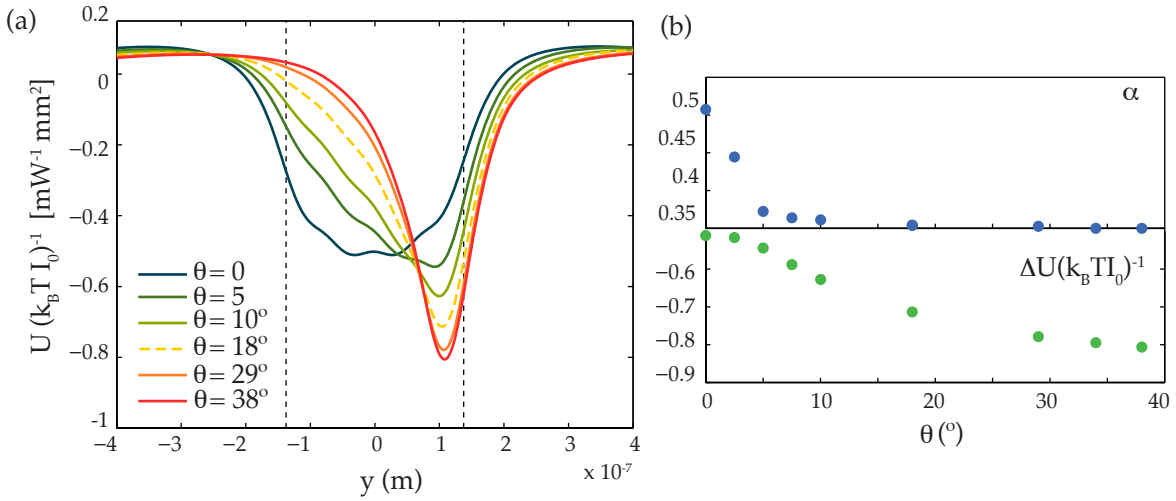

Figure 4.5: Optical trapping potential experienced by a PS bead above the plasmonic nanostructure. (a) The trapping potential is plotted for several values of the geometrical asymmetry (parametrized by θ). The dashed vertical lines point to the antennas boundaries for reference. (b) Evolution of the potential asymmetry parameter, α (upper panel), and depth of the potential well, ΔU (lower panel), as a function of θ. The geometrical parameters of the plasmonic nanostructure are given in Fig. 4.3.

4.2.2 Trapping potential

Let us now study the trapping properties of the plasmon-based tweezers by means of the optical potential, which can be determined from the EM forces discussed in the previous Subsection. In particular, a line integration of the force yields the potential energy needed to move the particle from infinity to a position $\mathbf{r}$ [11]:

$$U(\mathbf{r}) = \int_{-\infty}^{\mathbf{r}} \mathbf{F}(\mathbf{r}') \cdot \mathrm{d}\mathbf{r}' \,. \tag{4.10}$$

Since we are interested in a bead that moves along nanostructure's symmetry axis, we can write the above equation as

$$U(y) = \int_{-\infty}^{y} \mathbf{F}_y(y') \, \mathrm{d}y' \,, \tag{4.11}$$

where the force $\mathbf{F}_y$ is given by Eq. 4.8 and the integral runs over the grid positions of the bead given by Eq. 4.7.

By means of this procedure, we have obtained the results displayed in Fig. 4.5. Panel (a) shows the potential $U(y)$ experienced by a PS bead in the presence of the plasmonic structure for several values of the angle θ. The curves demonstrate that the asymmetric geometry yields the anisotropy in the trapping potential. We have characterized the

asymmetry of the potential by means of a parameter, α, sketched in Fig. 4.1 (a). This parameter is defined as

$$\alpha = 0.5 - \frac{y_{\min}}{L}\,, \tag{4.12}$$

where $y_{\min}$ is the position of the potential minimum and $L = 8 \times 10^{-7}$ m, with the antennas centered as shown by the vertical dashed lines in the figure. Since the potential is not periodic, we have chosen L such that $U(-L/2) = U(L/2)$. The evolution of α with θ is shown in the upper inset of panel (b), while the lower inset shows the evolution of the potential depth, ΔU. The case $\theta = 0°$ corresponds to a symmetric structure, which leads to a symmetric potential ($\alpha = 0.5$). Increasing θ makes the potential more anisotropic (α decreases) by moving the hot spot towards the longest antenna's gap and, at the same time, it increases the depth of the potential well. For $\theta \approx 18°$ [corresponding $U(y)$ plotted as a yellow dashed line in panel (a)], α saturates at ≈ 0.36. The reason for this is that for larger values of θ, the dipole antennas are too different in length and they decouple to very different resonance frequencies. These results show that the plasmonic structure with $\theta = 18°$ is convenient for the design of a plasmonic ratchet as it gives a maximum anisotropy and values of the potential depth, $\Delta U \approx k_B T I_0$ [mW$^{-1}\mu$m^2], of the order of the thermal energy for illumination intensities $I_0 \approx 1$ mW/μm^2.

The design of a Brownian ratchet requires a periodic set of anisotropic traps. Hence, we now consider a periodic arrangement of the plasmonic nanostructures, as sketched in Fig. 4.2 (a). Figure 4.6 (a) shows the trapping potential calculated for a periodic array for different values of the period, Λ. These curves stem from simulations of the plasmonic nanostructure subjected to periodic boundary conditions in the y direction. The depth of these potential wells is plotted in Fig. 4.6 (b) as a function of the period. As shown by this figure, placing the plasmonic structures in a periodic array gives rise to a coupling between them, yielding an oscillation of the potential depth with Λ. The potential depth is maximum for $\Lambda \approx 1$ μm, minimum for $\Lambda \approx 1.4$ μm and approaches the ΔU value that corresponds to the single structure when the period is large enough. This oscillation with Λ is due to an interference effect in the far-field interaction between the plasmonic nanostructures. For values of $\Lambda \geq 900$ nm, the far-field coupling also results in two local maxima in the shape of the potential $U(y)$, as can be seen in panel (a). Such maxima at the sides of the absolute minimum of the potential may prevent particle trapping, which would reduce the effectiveness of a Brownian ratchet device. Therefore, a period of $\Lambda = 800$ nm is appropriate for the design of a plasmonic ratchet [plotted dashed yellow line in panel (a)], since it provides a deep optical trap without any local maxima. In the following Section we study the dynamics of a dielectric bead in the presence of a

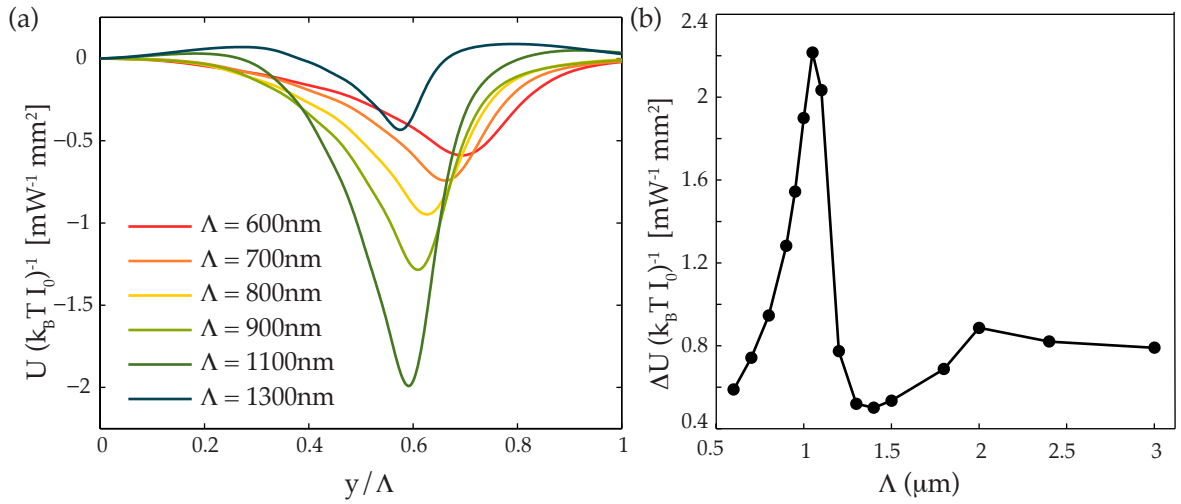

Figure 4.6: Unit cell of the trapping potential generated by a periodic array of plasmonic structures. Each structure is characterized by an asymmetry given by $\theta = 18°$ and geometrical parameters as given in the caption of Fig. 4.3. (a) The anisotropic trapping potential is shown for different values of the period, Λ. (b) Evolution of the potential depth with the array period.

periodic array of nano-optical traps.

4.3 Plasmonic Brownian ratchet dynamics

In this Section we study the dynamics of the system. In order to demonstrate the Brownian ratchet operation, we have carried out MD simulations for a diffusive bead in the presence of the plasmonic structure while the trapping is periodically turned on and off. In the following we first briefly review the MD simulation technique in Subsection 4.3.1. Next, in Subsection 4.3.2 we present the statistics of the simulation results, discussing the parameters that play a role in the dynamics of the ratchet mechanism.

4.3.1 A brief review on the molecular dynamics simulation technique

In the MD simulation technique, the classical equations motion of a given system are integrated throughout time [263]. In our work we have carried out MD simulations of a single particle, characterized by mass m, position $\mathbf{r}$ and momentum $\mathbf{p}$. The particle undergoes Brownian motion at temperature T and is subjected to the plasmonic potential. The system dynamics is obtained from the simulated trajectories, which are defined from the resulting positions and momenta. The equations of motion of the particle can

be written from Newton's law as

$$m\ddot{\mathbf{r}} = \mathbf{f}\,, \tag{4.13}$$

where $\mathbf{f}$ represents all the forces exerted by the system on the particle. Alternatively, the equations of motion can be cast as a set of two first order differential equations:

$$\dot{\mathbf{r}} = \frac{\mathbf{p}}{m}\,, \tag{4.14}$$

$$\dot{\mathbf{p}} = -\nabla_{\mathbf{r}} U = \mathbf{f}\,, \tag{4.15}$$

where U is the potential.

In order to simulate the Brownian dynamics of a single bead in the presence of the optical potential at a constant temperature, T, we make use of the Langevin equation [264] and write Eq. 4.13 as follows

$$m\ddot{\mathbf{r}} = \mathbf{F} - \gamma m\dot{\mathbf{r}} + \sqrt{2\alpha\gamma m k_B T}R(t)\,. \tag{4.16}$$

Here, $\mathbf{F}$ is the plasmonic force discussed in the previous Section, k_B is Boltzman's constant and α is a dimensionality factor that takes the values $\alpha = 1, 2, 3$ for 1D, 2D and 3D, respectively. The term $\gamma m\dot{\mathbf{r}}$ corresponds to the drag force of the bead in water. The friction coefficient, γ, is given by

$$\gamma = 6\pi\sigma\eta/m\,, \tag{4.17}$$

where η is the viscous coefficient of the medium and σ, is the radius of the particle. The interplay between the diffusion constant of the particle,

$$D = \frac{k_B T}{m\gamma}\,, \tag{4.18}$$

and the magnitude of the external forces dominates the dynamics. By defining the time needed for a particle to diffuse its own radius, $\tau_\sigma = \sigma^2/D$, two regimes can be distinguished. For small values of γ, i.e. $\gamma\tau_\sigma \ll 1$, the particle undergoes inertial dynamics, dominated by the external forces. On the other hand, the diffusive or Brownian regime takes place for $\gamma\tau_\sigma \gg 1$. Finally, the last term in Eq. 4.16 is the Langevin expression that accounts for the Brownian motion of the particles in the fluid by means of a stochastic force: $R(t)$ is a delta-correlated Gaussian function with zero mean, i.e.,

$$\langle R(t)\rangle = 0\,, \tag{4.19}$$

$$\langle R(t)R(t')\rangle = \delta(t - t')\,. \tag{4.20}$$

The Brownian dynamics of the system is then simulated by numerically solving Eq. 4.16. We do so by integrating the equations of motion 4.13-4.15 using finite differences [263]. In particular, we make use of Leapfrog algorithm, which is based on a Taylor expansion of the position, $\mathbf{r}$, and velocity, $\mathbf{v}$ around time t as follows

$$\mathbf{v}(t + \Delta t/2) = \mathbf{v}(t - \Delta t/2) + \frac{\mathbf{f}(t)}{m}\Delta t + O(\Delta t^2)\,, \tag{4.21}$$

$$\mathbf{r}(t + \Delta t) = \mathbf{r}(t) + \mathbf{v}(t + \Delta t/2)\Delta t + O(\Delta t^2)\,. \tag{4.22}$$

Thereby, in each simulation step we evaluate the velocity at half-integer time steps, $t+\Delta t/2$, and then use them to compute the position at time $t+\Delta t$. In addition, Brownian motion is simulated by taking R as a random number from a gaussian distribution in each step of the algorithm.

4.3.2 System dynamics

For a proof of concept design of the ratchet, we consider the asymmetric nanostructure discussed in the previous Section, with $\theta = 18°$ and with the geometrical parameters given in the caption of Fig. 4.3. We take an array of such a nanostructure with period $\Lambda = 800$ nm, which yields to the potential $U(y)$ plotted as a yellow line in Fig. 4.6 (a). To ensure a highly efficient trapping, we take an irradiance $I_0 = 75\text{mW}/\mu\text{m}^2$, although this device also works for lower laser powers. As we are interested in the Brownian ratchet mechanism, we consider the dynamics in 1D along the direction of optical traps, i.e., the y direction. By doing so, we are assuming that the beads can only move along the y direction, which could be done by, for instance, placing the structure in a thin microfluidic channel. Thereby, Eq. 4.16 reduces to

$$m\ddot{y} = \mathbf{F}_y - \gamma m\dot{y} + \sqrt{2\gamma m k_B T}R(t)\,, \tag{4.23}$$

with $\mathbf{F}_y$ being the optical force calculated from Eq. 4.8. The friction coefficient, γ, is obtained from Eq. 4.17 with $\eta = 1 \times 10^{-3}$ kg/(m s) being water's viscous coefficient and $\sigma = 50$ nm the radius of the particle. The mass of particle is obtained from PS density, $\rho = 1050$ kg/m^3. With these parameters we have $\gamma\tau_\sigma \sim 10^6$, ensuring that the dynamics of the bead is diffusive. In addition, we assume a low density of particles in the water solution, such that they are non-interacting. This allows us to simulate the dynamics of the system by solving the above equation for a single particle for N realizations of the system. In each realization, the initial conditions of the particle are random, such that we explore the statistics of the system.

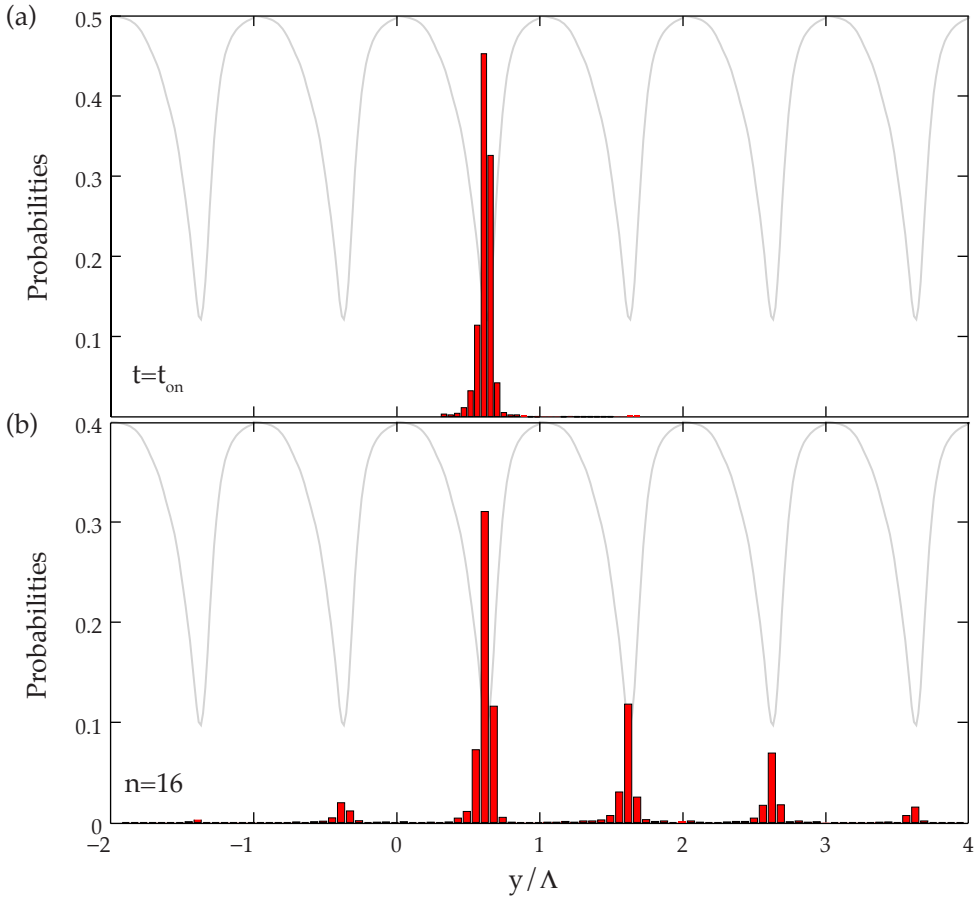

Figure 4.7: Plasmonic Brownian ratchet dynamics for $N = 4000$ realizations of the system. One PS bead is embedded in water at room temperature and subjected to the time-modulated plasmonic potential. (a) Initial situation: The particle probability distribution is centered at the trapping position of the nanotweezer ($0 \leq y \leq \Lambda$) after a time $t_{\text{on}} = 2{\times}10^4\tau_0$. (b) Final situation: After 16 on-off cycles ($t_{\text{off}} = 8 \cdot 10^3\tau_0$), the probability for the particle to show a directed motion in the forward direction is 40%. The gray line represents the plasmonic potential in arbitrary units ($\Delta U = 75 k_B T$).

Initially, the bead is placed within a unit cell ($0 \leq y \leq \Lambda$) of the anisotropic periodic potential, with random position and velocity. During time t_{on}, an external laser excites the set of optical traps. Despite the anisotropy, there are no large-scale gradients in the system and hence no statistical net motion of the particle is to be expected. When t_{on} is long enough, the bead falls into the potential minimum as $\Delta U \gg k_B T$. In our calculations we have used $t_{\text{on}} = 2 \times 10^4 \tau_0$, with

$$\tau_0 = \sqrt{\frac{m\sigma^2}{k_B T}} = 5.7 \times 10^{-7}\,\text{s}\ , \tag{4.24}$$

which yields $t_{on} = 11$ ms. Figure 4.7 (a) presents a histogram of $N = 4000$ realizations of the particle's position at a time $t = t_{on}$ showing a distribution around the potential minimum.

During the ratchet operation, the system is driven out of equilibrium by a repeated modulation of the potential in time. By assuming that the trapping potential is well characterized by parameters α and ΔU, we can give some analytical predictions on the dynamics of the system. When the potential is off, the particle is free to diffuse around the potential minimum. Due to the spatial anisotropy, the characteristic time,

$$\tau_F = \frac{\alpha^2 \Lambda^2}{2D}, \tag{4.25}$$

needed for the particle to travel to the neighbouring unit cell in the forward direction (distance $\alpha\Lambda$), is shorter than the characteristic time,

$$\tau_B = \frac{(1-\alpha)^2 \Lambda^2}{2D}, \tag{4.26}$$

to travel backwards [distance $(1-\alpha)\Lambda$]. If the potential is switched off for a time t_{off} satisfying $\tau_B \gg t_{off} \gg \tau_F$, the probability of the particle moving forward is enhanced while that of moving backward is suppressed. Thus, after one cycle, trapping the particle in the potential minimum located in the forward direction is more likely than in the backward direction and repeating the cycle causes a directed drift of the particle for a statistical ensemble. The probability of the bead moving forward in a single cycle, P, can be quantified. Let us assume that at $t = t_{on}$ the probability distribution is of the form (see e.g. Ref. [250]),

$$P(y) = \frac{1}{\sqrt{\pi\beta^2}} e^{-(y-\langle y\rangle)^2/\beta^2}, \tag{4.27}$$

where $\beta^2 = 4Dt_{off}$ and the mean value of the distribution corresponds to the potential minimum, $\langle y\rangle = (1-\alpha)\Lambda$, with the unit cell centered as shown in Fig. 4.7. Then, P can be written as the probability of the particle being at $y \geq \Lambda$,

$$P = \int_{\Lambda}^{\infty} P(y) = \frac{1}{2}\mathrm{erfc}\left(\frac{\alpha\Lambda}{\beta}\right). \tag{4.28}$$

Making use of Eq. 4.25 and the expression for β, we can write

$$P = \frac{1}{2}\mathrm{erfc}\left(\sqrt{\frac{\tau_F}{2t_{off}}}\right) \approx \frac{1}{2}\exp\left(-\frac{\tau_F}{t_{off}}\right), \tag{4.29}$$

where we have assumed $t_{off} \gg \tau_F$. We see from the above expression that t_{off} is a relevant parameter for the dynamics of the system, as it will determine wether the probability of moving forward in each cycle is enhanced or supressed.

Net particle drift, $P_F - P_B$, for different values of t_{off}:				
t_{off}/τ_0	6×10^3	8×10^3	1×10^4	1.5×10^4
$P_F - P_B$	0.135	0.231	0.111	0.102

Table 4.1: Particle drift for different values of the time the laser is off: $P_F - P_B$ after 16 on-off cycles and N=1000 realizations is shown for different values of t_{off}, showing that $t_{off} = 8 \cdot 10^3 \tau_0$ maximizes the particle flux.

Let us now discuss the simulation results for a statistical ensemble of N realizations. In order to characterize the dynamics for different values of t_{off}, we start by defining the probabilities of moving forward, $P_F = N_F/N$, and backward, $P_B = N_B/N$, (N_F and N_B being the number of realizations where the particle is at $y \geq \Lambda$ and $y \leq 0$, respectively). Table 4.1 presents the MD simulation results for the particle's net drift, $P_F - P_B$, for different values of t_{off} and after 16 on-off cycles, showing that $t_{off} = 8 \cdot 10^3 \tau_0$ maximizes the particle flux. The other values of t_{off} considered, are either too small for allowing the particle to diffuse to the forward unit cell, or too large and the probability of diffusing backwards is enhanced together with that of diffusing forward. On the other hand, for the parameters used in our calculations, we have $\tau_F \sim 6$ ms and $\tau_B \sim 20$ ms, while the optimal value of t_{off} is 4.5 ms. It can be seen that this value of t_{off} does not satisfy the condition $\tau_B \gg t_{off} \gg \tau_F$, as we predicted with the simple analytical modeling. The reason for this disagreement may come from the fact that the potential has a complex shaped that is not accurately described by only two parameters, α and ΔU. Assuming that α has a different effective value, the values of τ_F and τ_B would change too. The condition $\tau_B \gg t_{off} \gg \tau_F$ would be satisfied for instance for $\alpha = 0.3$, which yields $\tau_F \sim 4$ ms and $\tau_B \sim 23$ ms. Therefore, we take the value $t_{off} = 8 \cdot 10^3 \tau_0$ and study the dynamics of the system.

Figure 4.7 (b) shows a histogram of the particle's positions after 16 on-off cycles with $t_{off} = 8 \cdot 10^3 \tau_0$. The total simulation time is then given by

$$t = 16 t_{on} + 15 t_{off} = 0.26\,\text{s}, \tag{4.30}$$

as we record the positions after the particles have been trapped again. In this calculation, $N = 4000$ realizations of the system have been simulated, in order to show converged statistical results. The histogram shows a statistical directed motion into the forward direction, which demonstrates the Brownian ratchet mechanism. As shown in the figure, and despite the fact that there are no temperature gradients or applied forces in the

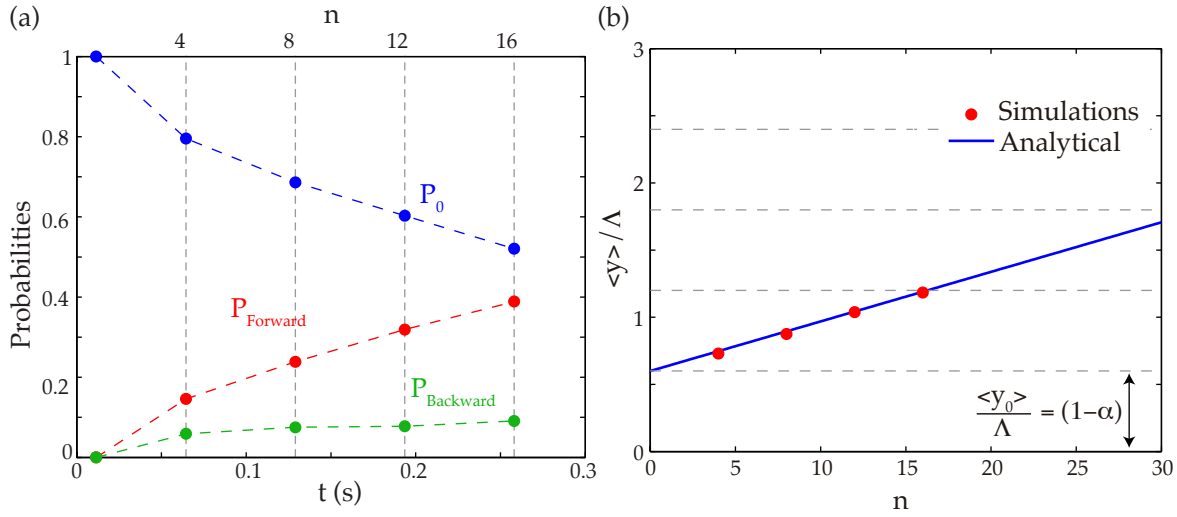

Figure 4.8: Evolution of the dynamics with the number of cycles. (a) Time evolution of the probabilities for the particles to move forward (P_{F}), backward (P_{B}) or to remain in the initial unit cell (P_0). The simulation results at 1, 4, 12 and 16 on-off cycles are shown as circles. The lines are a guide-to-the-eye. (b) Mean value of the bead's position as a function of the number of on-off cycles. The simulation results for 4, 8, 12 and 16 cycles are shown as red circles and Eq. 4.31 is shown as a blue line. From this result we can estimate the number of cycles needed for the bead's mean position to reach, e.g. the fifth potential well in the forward direction as $n \sim 10^2$. The dashed gray lines show the positions of the potential minima.

large scale, the particle's drift is biased into one direction through the combined action of anisotropy and out-of-equilibrium dynamics. Notice that the probability distribution around each trapping site is asymmetric, which may reflect the potential anisotropy. The time evolution of the probabilities of moving forward and backwards, together with P_0, the probability of remaining in the initial unit cell, are shown in Fig. 4.8 (a). In the plot we show with circles the probabilities after 4, 8, 12 and 16 on-off cycles, revealing that P_{F} increases with the number of on-off cycles up to 40% whereas P_{B} saturates at around 10% for 4 cycles. Due to the statistical origin of the ratchet, a large number of repetitions is needed to observe directed motion.

In addition, from our results we can also predict the time evolution of the dynamics for a large number of cycles. In particular, we consider the evolution of the mean particle position, $\langle y \rangle$, with the number of cycles, n. The red circles in Fig. 4.8 (b) show $\langle y \rangle$ obtained from the simulation results for different values of n, displaying a linear increase with the number of cycles. Hence, we can write $\langle y \rangle$ as a function of n in terms of the distance to the neighbouring unit cell in the forward direction, $\alpha\Lambda$, and the probability

of moving forward in each cycle, P, given by Eq. 4.25. We have

$$\langle y \rangle = \langle y_0 \rangle + n\alpha' \Lambda P \tag{4.31}$$

where $\langle y_0 \rangle$ is the mean initial position, $\langle y_0 \rangle = (1 - \alpha)\Lambda$. With the previously discussed values, $\tau_F = 6$ ms and $t_{off} = 4.5$ ms, we have $P = 0.13$ and α' is left as a fitting parameter. The fit of the simulation results to Eq. 4.31 is shown as a blue line in the figure, with $\alpha' = 0.3$, a value that is very close to the theoretical value, $\alpha = 0.36$. Thereby we can estimate the number of cycles needed for the the bead's mean position to travel a certain number of unit cells. For instance, we can predict that in $\sim 10^2$ cycles, that is $t = 1.6$ s, the bead's mean position will reach the fifth potential well in the forward direction.

Finally, we discuss some issues related to the practical implementation of the plasmonic ratchet. It should be noted that the performance of the device can be affected by thermal-induced dynamics, as light coupling to LSPs in metallic particles leads to heat dissipation into the surroundings [265]. These effects should be minimized in an experiment by (i) reducing heat absorption in the metal by low illumination intensities, (ii) a careful design of the plasmonic structure (for instance, a substrate with a high thermal conductivity can work as a heat sink [266]) and (iii) considering thin fluidic cells [151]. This last point has another advantage, as it prevents beads from escaping in the vertical direction when the illumination is turned off.

4.4 Conclusions

To summarize, in this Chapter we have presented a proposal for transport of subwavelength dielectric particles in a plasmonic system that takes advantage of random thermal motion. This plasmonic Brownian ratchet only requires the periodic modulation in time of the large field enhancement generated in asymmetric plasmonic structures upon illumination. Here we have studied a proof of principles device, based on an array of plasmonic nanostructures composed of four dipole antennas of gradually varying lengths. We have shown that the nano-optical traps supported by such plasmonic nanostructures enable the trapping of a dielectric bead and we have characterized the optical trapping potential. In addition, by means of MD simulations, we have demonstrated the statistical rectification of the Brownian motion of a sub-micrometer bead in the absence of an external bias or a large scale temperature gradient. The use of plasmonic structures allows to overcome the limitations of conventional techniques for light-based manipulation of particles, permitting to control the flow of subwavelength particles. Moreover, the proposed plasmonic brownian ratchet is a flexible device, as, for instance, the particle's

propagation direction can be reversed by just tuning the wavelength. In particular, due to the slightly different resonance frequency of the dipole antennas, the anisotropy of the trapping potential can be reversed by exciting the shortest antenna instead of the longest one.

Chapter 5

Coupling between quantum emitters and propagating surface plasmons

5.1 Introduction

This Chapter addresses the topic of light-matter coupling in plasmonic systems. As we introduced in Section 1.5, one of the main goals of Quantum Plasmonics is to provide an efficient and controlled coupling between QEs and SPPs. The sub-diffraction limited confinement of the EM field provided by SPPs enables new routes for the control of the interaction between QEs and photons. Plasmonic surface modes, through their small mode volumes and large enhancements of the EM field, offer a different way to the control of light-matter interaction, which has been extensively studied in the field of cavity QED and is interesting both from a fundamental point of view and for applications in quantum technologies [156].

As we have already reviewed, the coupling between light and QEs can be separated into two different regimes depending on the interplay between the coupling strength and the system losses. In the WC regime the QE undergoes an irreversible decay from the excited to the ground state. The effect of the EM field is to modify the spontaneous decay rate, or inversely the lifetime, of the QE via the Purcell effect [178]. On the other hand, when the coupling strength overcomes all the dissipation mechanisms, the QE-field system enters into the SC regime, where a reversible energy exchange takes place. While the modification of the spontaneous decay rate of an individual QE close to plasmonic systems has been demonstrated many times since the pioneering experiments [174–177], the observation of the SC regime remains elusive. Only theoretical works have considered the SC between QEs and LSPs in metal nanoparticles [196–199] or SPPs in

plasmonic waveguides and surfaces [200–203]. On the other hand, the SC regime has been observed in experiments where a collection of QEs interacts with the SPP modes supported by different metallic nanostructures [204–215]. In this kind of systems, the real-time observation of the coherent QE-SPP dynamics has also been reported [216]. In this Chapter we study the coupling between QEs and the EM field in plasmonic systems of different configurations: individual emitters in the vicinity of plasmonic structures, two QEs coupled through a plasmonic mode and a collection of QEs strongly coupled to a propagating SPP.

This Chapter is structured as follows. We start by reviewing the theoretical framework necessary to study the coupling of a QE to the EM field in inhomogeneous environments in Section 5.2. Next, in Section 5.3 we consider the particular case of an individual QE coupled to plasmonic media. We first consider the modified spontaneous decay rate of the emitter in the vicinity of different plasmonic structures (Subsection 5.3.1). In particular, we consider a semi-infinite metal surface and a graphene sheet, paying particular attention to the coupling to the SPPs supported by those systems. Next, in Subsection 5.3.2, we revisit the problem of an individual QE interacting with layered metallic structures and we exactly solve for the dynamics of the system, showing that reversible dynamics takes place under some conditions. In Section 5.4 we study the interaction between two QEs mediated by SPPs, considering the particular case of the SPPs supported by graphene sheets (Subsection 5.4.2) and ribbons (Subsection 5.4.3). Finally, in Section 5.5 we study the the SC phenomenon between ensembles of QEs and propagating SPPs observed in metal surfaces. For that purpose we develop a quantum framework that accounts for the coherent coupling between QEs and SPPs and incorporates the presence of dissipation and dephasing (Subsections 5.5.1 and 5.5.2). In addition, the quantum framework can deal with complex aspects such as saturation effects and quantum statistics, which we present in Subsection 5.5.3.

5.2 A quantum emitter coupled to the electromagnetic field

We begin by presenting the theoretical formalism that allows us to deal with the coupling of QEs to the EM modes supported by the flat plasmonic nanostructures studied in this Chapter. A proper treatment of a QE interacting with the EM field requires a QED formalism in which both the emitter's energy levels and the EM field are quantized. In Subsection 5.2.1 we present the QED treatment of a QE that has discrete energy states

and couples to the EM field by emitting (or absorbing) photons. We start by deriving the Hamiltonian of the system. Next, we consider the case of an individual QE and present a formalism to deal with the dynamics of the QE's population. In the case of a weak coupling strength between the QE and the EM field, we derive the spontaneous decay rate of the QE. In addition, in Subsection 5.2.2 we briefly review the classical picture of a dipole emitter radiating in inhomogeneous environments. We consider the modification in the dipole's rate of energy dissipation and we find that this quantity has the same expression as the normalized spontaneous decay rate derived within the QED formalism.

5.2.1 Quantum formalism

Let us start by considering here the QED formalism that handles the QE-field coupled system. In particular, we are interested in the interaction between QEs and the EM modes supported by plasmonic structures. Such plasmonic media are characterized by a frequency-dependent and spatially inhomogeneous, complex permittivity $\epsilon(\mathbf{r}, \omega)$. As we described in Section 1.1, in the optical regime flat metal/dielectric interfaces (as well as graphene sheets at lower frequencies) support the propagation of SPPs. While at frequencies well below ω_{sp}, the character of the SPPs is predominantly photon-like, as the frequency increases the SPPs are more plasmon-like and ohmic losses in the metal start to be important. This means that depending on the frequency regime under consideration, the importance of absorption varies significantly. When SPPs are more photon-like, losses in the metal can be treated perturbatively. On the other hand, at higher frequencies absorption can even play a role in the QE-field interaction and losses in the metal need to be appropriately handled. In the following, we first introduce a canonical quantization scheme appropriate for systems where losses can be neglected or introduced perturbatively. Next, we upgrade the formalism by means of a macroscopic QED approach that is able to deal with QEs in the presence of dispersive and absorbing media.

A quantum emitter interacting with the electromagnetic field in the presence of non-absorbing media

The Hamiltonian that describes a QE coupled to the EM field in the absence of losses is composed of three terms: the QE's excitation Hamiltonian, the continuum of EM modes and an interaction term. First, the QE's term is needed. The QE is represented under the two-level system approximation: it possesses two energy levels (ground, $|g\rangle$, and excited, $|e\rangle$, states) with an optically active transition between them at frequency ω_0. Within

this scheme, the Hamiltonian for the QE reads as

$$H_0 = \hbar\omega_0\sigma^\dagger\sigma\,. \tag{5.1}$$

Here, $\sigma = |g\rangle\langle e|$ and $\sigma^\dagger = |e\rangle\langle g|$ describe the QE's raising and lowering operators, respectively, that satisfy fermionic anticommutating algebra, i.e. $\left[\sigma,\sigma^\dagger\right]_+ = 1$. The two level-system description assumes a large separation between the electronic energy levels of the QE, with only one possible transition at the resonance frequency. While being usually a good approximation for semiconductor QDs or NV centers, it is just a first approximation for complex organic molecules, where non-radiative decay channels associated with vibro-rotational levels are important.

The second term corresponds to the quantized EM field in a lossless medium. The canonical quantization procedure [267] involves an expansion over a set of normal modes $\mathbf{u}_{\mathbf{k},\lambda}(\mathbf{r},\omega)$ labeled by the wave vector, $\mathbf{k}$, and the polarization state, $\lambda = 1, 2$. By defining the creation and annihilation operators of the EM field, ${a^\dagger}_{\mathbf{k},\lambda}$ and $a_{\mathbf{k},\lambda}$, which satisfy bosonic commutator relations, $\left[a_{\mathbf{k},\lambda}, {a^\dagger}_{\mathbf{k}',\lambda'}\right] = \delta_{\mathbf{k},\mathbf{k}'}\delta_{\lambda,\lambda'}$, we can write the electric field as follows

$$\mathbf{E}(\mathbf{r}) = \sum_{\mathbf{k},\lambda}\left[\mathbf{u}_{\mathbf{k},\lambda}(\mathbf{r},\omega)a_{\mathbf{k},\lambda} + \mathbf{u}^*_{\mathbf{k},\lambda}(\mathbf{r},\omega){a^\dagger}_{\mathbf{k},\lambda}\right]. \tag{5.2}$$

where the normal modes evolve in time following $\mathbf{u}_{\mathbf{k},\lambda}(\mathbf{r},t) = \mathbf{u}_{\mathbf{k},\lambda}(\mathbf{r},\omega)e^{i\omega t}$. In free-space, a canonical basis is that of plane waves with wave vectors $\mathbf{k}$ quantized in a 3D box of volume $V = L^3$. For each wave vector, which satisfy the dispersion relation $k^2 = \omega^2_{\mathbf{k}}/c^2$, there are two polarization states with unit vectors $\hat{\mathbf{u}}_{\mathbf{k},\lambda}$ such that $\hat{\mathbf{u}}_{\mathbf{k},\lambda}\cdot\hat{\mathbf{u}}_{\mathbf{k},\lambda'} = \delta_{\lambda,\lambda'}$ and $\hat{\mathbf{u}}_{\mathbf{k},\lambda}\cdot\mathbf{k} = 0$. This yields

$$\mathbf{E}(\mathbf{r}) = \sum_{\mathbf{k},\lambda}\sqrt{\frac{\hbar\omega_{\mathbf{k}}}{2\epsilon_0 V}}\hat{\mathbf{u}}_{\mathbf{k},\lambda}\left[e^{i\mathbf{k}\mathbf{r}}a_{\mathbf{k},\lambda} + e^{-i\mathbf{k}\mathbf{r}}{a^\dagger}_{\mathbf{k},\lambda}\right]. \tag{5.3}$$

By means of operators ${a^\dagger}_{\mathbf{k},\lambda}$ and $a_{\mathbf{k},\lambda}$, the free-energy Hamiltonian of the EM field can be written as

$$H_{\mathrm{EM}} = \sum_{\mathbf{k},\lambda}\hbar\omega_{\mathbf{k}}a^\dagger_{\mathbf{k},\lambda}a_{\mathbf{k},\lambda}\,. \tag{5.4}$$

Note that in the equation above the sum stands for

$$\sum_{\mathbf{k},\lambda} = \frac{V}{(2\pi)^3}\sum_{\lambda=1,2}\int \mathrm{d}^3\mathbf{k}\,. \tag{5.5}$$

The interaction term in the dipole approximation can be written from $H_{\mathrm{I}} = -\boldsymbol{\mu}_{eg}\cdot\mathbf{E}$, where $\boldsymbol{\mu}_{eg} = \boldsymbol{\mu}(\sigma + \sigma^\dagger)$ is the dipole moment operator with $\boldsymbol{\mu} = \langle e|\boldsymbol{\mu}_{eg}|g\rangle = \langle g|\boldsymbol{\mu}_{eg}|e\rangle$.

We have

$$H_{\mathrm{I}} = \sum_{\mathbf{k},\lambda} \hbar g_{\mathbf{k},\lambda} \left[\left(\sigma + \sigma^{\dagger} \right) \left(e^{i\mathbf{kr}} a_{\mathbf{k},\lambda} + e^{-i\mathbf{kr}} a^{\dagger}{}_{\mathbf{k},\lambda} \right) \right], \tag{5.6}$$

where $g_{\mathbf{k},\sigma}$ is the coupling constant. From Eq. 5.3 we can write

$$g_{\mathbf{k},\lambda} = \sqrt{\frac{\omega_{\mathbf{k}}}{2\hbar\epsilon_0 V}} \boldsymbol{\mu} \cdot \hat{\mathbf{u}}_{\mathbf{k},\lambda} \,. \tag{5.7}$$

We see in expression 5.6 that there are two types of interaction processes: while the terms $a\sigma^{\dagger}$ and $a^{\dagger}\sigma$ conserve the number of excitations, the terms $a^{\dagger}\sigma^{\dagger}$ and $a\sigma$ do not do so. By writing H_{I} in the interaction picture,

$$H_{\mathrm{I}}(t) = \sum_{\mathbf{k},\lambda} \hbar g_{\mathbf{k},\lambda} \left[\left(\sigma e^{-i\omega_0 t} + \sigma^{\dagger} e^{i\omega_0 t} \right) \left(e^{i(\mathbf{kr}-\omega_{\mathbf{k}} t)} a_{\mathbf{k},\lambda} + e^{-i(\mathbf{kr}-\omega_{\mathbf{k}} t)} a^{\dagger}{}_{\mathbf{k},\lambda} \right) \right], \tag{5.8}$$

the non-conserving processes can be identified as fast oscillating terms. The so-called *rotating wave* approximation states that those terms can be neglected as long as $|g_{\mathbf{k},\sigma}| \ll \omega_0 + \omega_{\mathbf{k}}$. Under this assumption, the Hamiltonian can finally be written as

$$H = \hbar\omega_0 \sigma^{\dagger}\sigma + \sum_{\mathbf{k},\lambda} \hbar\omega_{\mathbf{k}} a^{\dagger}_{\mathbf{k},\lambda} a_{\mathbf{k},\lambda} + \sum_{\mathbf{k},\lambda} \hbar g_{\mathbf{k},\lambda} \left[\sigma^{\dagger} a_{\mathbf{k},\lambda} + \sigma a^{\dagger}{}_{\mathbf{k},\lambda} \right]. \tag{5.9}$$

The Hamiltonian above describes a QE interacting with a set of EM modes [1]. This formalism can deal with the dynamics of QEs coupled to the EM field. However, the quantization procedure that we have made use of is limited to the case of non-absorbing media.

A quantum emitter interacting with the electromagnetic field in the presence of absorbing media

We now upgrade the QED framework in order to consider the interaction between QEs and the EM field in the presence of dispersive and absorbing media. Including absorption in the quantum formalism requires a reconsideration of the quantization procedure of the EM-field [268, 269]. Now we briefly review the macroscopic approach to QED in absorbing media, a detailed account of which can be found in Ref. [270]. This approach is based on the quantization of the macroscopic Maxwell's equations through the consideration of an overall system composed of the EM field and the medium, including its dissipative part.

[1] Note that Hamiltonian 5.9 is usually referred to as *Jaynes-Cummings* model for the case of a single EM mode

Let us first consider the quantization of the EM field. In the presence of dispersing and absorbing media of dielectric function $\epsilon(\mathbf{r},\omega)$, the field Hamiltonian derived in the above (Eq. 5.4) needs to be replaced by the following expression

$$H_{\mathrm{EM}} = \sum_{\lambda} \int \mathrm{d}^3\mathbf{r} \int_0^{\infty} \mathrm{d}\omega\, \hbar\omega\, \mathbf{f}_{\lambda}^{\dagger}(\mathbf{r},\omega)\cdot\mathbf{f}_{\lambda}(\mathbf{r},\omega), \tag{5.10}$$

where we have introduced a continuum set of bosonic field operators, $\mathbf{f}_{\lambda}(\mathbf{r},\omega)$ and $\mathbf{f}_{\lambda}^{\dagger}(\mathbf{r},\omega)$. These operators are associated with the elementary excitations of the field-matter composed system. The electric field can be expressed in terms of the bosonic operators as

$$\mathbf{E}(\mathbf{r},\omega) = i\sqrt{\frac{\hbar}{\pi\epsilon_0}} \sum_{\lambda} \frac{\omega^2}{c^2} \int \mathrm{d}^3\mathbf{r}'\, \sqrt{\mathrm{Im}\left[\epsilon(\mathbf{r}',\omega)\right]}\hat{\mathbf{G}}_{\lambda}(\mathbf{r},\mathbf{r}',\omega)\cdot\mathbf{f}_{\lambda}(\mathbf{r}',\omega), \tag{5.11}$$

with $\hat{\mathbf{G}}(\mathbf{r},\mathbf{r},\omega) = \sum_{\lambda}\hat{\mathbf{G}}_{\lambda}(\mathbf{r},\mathbf{r},\omega)$ being the Green's function of the classical treatment of the field generated by a dipole, which reads as

$$\nabla\times\nabla\times\hat{\mathbf{G}}(\mathbf{r},\mathbf{r}_0,\omega) - \frac{\omega^2}{c^2}\epsilon(\mathbf{r},\omega)\hat{\mathbf{G}}(\mathbf{r},\mathbf{r}_0,\omega) = \hat{\mathbf{I}}\delta(\mathbf{r}-\mathbf{r}_0). \tag{5.12}$$

The electric field operator is then given by $\mathbf{E}(\mathbf{r}) = \mathbf{E}^{(+)}(\mathbf{r}) + \mathbf{E}^{(-)}(\mathbf{r})$, with

$$\mathbf{E}^{(+)}(\mathbf{r}) = \int_0^{\infty} \mathrm{d}\omega\, \mathbf{E}(\mathbf{r},\omega). \tag{5.13}$$

and $\mathbf{E}^{(-)}(\mathbf{r}) = \left[\mathbf{E}^{(+)}(\mathbf{r})\right]^{\dagger}$. Accordingly, the magnetic field satisfies an equivalent relation between $\mathbf{B}(\mathbf{r})$ and $\mathbf{B}(\mathbf{r},\omega)$, with $\mathbf{B}(\mathbf{r},\omega) = (i\omega)^{-1}\boldsymbol{\nabla}\times\mathbf{E}(\mathbf{r},\omega)$.

Next, in order to include the QE and its interaction with the EM field we follow the standard procedure and consider the minimal coupling Hamiltonian where the QE (or an ensemble of them) is considered to be composed of a collection of point charges q_α located at points $\mathbf{r}_\alpha$ and with momentum $\mathbf{p}_\alpha$. The Hamiltonian reads as

$$\begin{aligned} H &= \sum_{\lambda}\int \mathrm{d}^3\mathbf{r}\int_0^{\infty}\mathrm{d}\omega\,\hbar\omega\,\mathbf{f}_{\lambda}^{\dagger}(\mathbf{r},\omega)\cdot\mathbf{f}_{\lambda}(\mathbf{r},\omega) + \sum_{\alpha}\frac{1}{2m_\alpha}\left[\mathbf{p}_\alpha - q_\alpha\mathbf{A}(\mathbf{r}_\alpha)\right]^2 \\ &+ \frac{1}{2}\int \mathrm{d}^3\mathbf{r}\rho_A(\mathbf{r})_A\phi_A(\mathbf{r}) + \int \mathrm{d}^3\mathbf{r}\rho_A(\mathbf{r})\phi(\mathbf{r})\,. \end{aligned} \tag{5.14}$$

Here, the first term is the EM energy in the absence of any extra charges (Eq. 5.10), while the rest of the terms account for the effect of such charges in the medium-assisted QE-field interaction. The second term corresponds to the kinetic energy of the charges, expressed by means of the vector potential, $\mathbf{A}(\mathbf{r})$. The third and fourth terms are, respectively: their Coulomb energy (with $\rho_A(\mathbf{r})$ and $\phi_A(\mathbf{r})$ being the charge density of particles

and the scalar Coulomb potential) and the interaction energy between the particles and the medium (with $\phi(\mathbf{r})$ being the field potential in the Coulomb gauge). Assuming a two-level QE at position $\mathbf{r}_0$, with resonance frequency ω_0 and described by operators $\{\sigma^\dagger, \sigma\}$, and that the already introduced electric-dipole and rotating wave approximations hold, the minimal coupling Hamiltonian can be written as

$$H = \hbar\omega_0\sigma^\dagger\sigma + \sum_\lambda \int \mathrm{d}^3\mathbf{r} \int_0^\infty \mathrm{d}\omega\, \hbar\omega\, \mathbf{f}_\lambda^\dagger(\mathbf{r},\omega)\cdot\mathbf{f}_\lambda(\mathbf{r},\omega) - \left[\sigma^\dagger\boldsymbol{\mu}\cdot\mathbf{E}^{(+)}(\mathbf{r_0}) + \sigma\mathbf{E}^{(-)}(\mathbf{r_0})\cdot\boldsymbol{\mu}\right]. \tag{5.15}$$

This equation represents a generalization of Hamiltonian 5.9 for the case of absorbing media. As we have seen, the macroscopic QED approach provides an appropriate field quantization scheme in the presence of losses and dispersion.

Dynamics of the quantum emitter's population

The Hamiltonian given by Eq. 5.15 determines the population dynamics of a QE coupled to the EM modes supported by an absorbing and dispersive medium, such as a plasmonic environment, as we will see in the following. The population of the QE experiences spontaneous emission, the process by which the QE's population decays from an excited state to the ground state through photon emission. In free space, the QE's population features an exponential decay characterized by a rate, γ_0. When the emitter is surrounded by a given environment, the EM modes available for the decay change, which determines the dynamics of the QE's population. If the system is in the WC regime, the QE decays at a modified rate. On the other hand, if the system is in the SC regime, reversible dynamics with a coherent energy transfer between the QE and the EM field takes place.

Let us start by considering a QE at position $\mathbf{r}_0$ that is initially in its excited state, while there are no photons, i.e. state $|e, 0_{\mathbf{r},\omega_\lambda}\rangle \equiv \sigma^\dagger|g\rangle|0_{\mathbf{r},\omega_\lambda}\rangle$. Then, the QE can decay through the spontaneous emission of a photon of frequency ω and polarization λ into a set of final states where the QE is in the ground state and there is one photon, i.e. $|g, 1_{\mathbf{r},\omega_\lambda}\rangle \equiv \mathbf{f}_\lambda^\dagger(\mathbf{r}_0,\omega)|g\rangle|0_{\mathbf{r},\omega_\lambda}\rangle$. In the Schrödinger picture, a state of the system can be expressed as

$$|\psi(t)\rangle = c_e(t)|e, 0_{\mathbf{r},\omega_\lambda}\rangle + \sum_\lambda \int \mathrm{d}^3\mathbf{r} \int_0^\infty \mathrm{d}\omega\, c_{\mathbf{r},\omega_\lambda}(t)|g, 1_{\mathbf{r},\omega_\lambda}\rangle, \tag{5.16}$$

where $c_e(t)$ gives the population of the QE's excited state as $n_\sigma(t) = |c_e(t)|^2$. The time evolution of the system is determined by Schrödinger equation,

$$i\hbar\frac{\mathrm{d}|\psi\rangle}{\mathrm{dt}} = H|\psi\rangle, \tag{5.17}$$

with H being the Hamiltonian given by Eq. 5.15. This formalism is known as the *Wigner-Weisskopf* problem, see for instance Ref. [270], and yields the following set of differential equations

$$\begin{aligned}\dot{\tilde{c}}_e(t) &= -\frac{1}{\sqrt{\pi\epsilon_0\hbar}}\sum_\lambda \int_0^\infty \mathrm{d}\omega\, \frac{\omega^2}{c^2}\cdot \\ &\quad \cdot \int \mathrm{d}^3\mathbf{r}\sqrt{\mathrm{Im}\left[\epsilon(\mathbf{r},\omega)\right]}\,\boldsymbol{\mu}\cdot\hat{\mathbf{G}}_\lambda(\mathbf{r}_0,\mathbf{r},\omega)\tilde{c}_{\mathbf{r},\omega_\lambda}(t)e^{-i(\omega-\omega_0)t}, \qquad (5.18)\\ \dot{\tilde{c}}_{\mathbf{r},\omega_\lambda}(t) &= \frac{1}{\sqrt{\pi\epsilon_0\hbar}}\frac{\omega^2}{c^2}\sqrt{\mathrm{Im}\left[\epsilon(\mathbf{r},\omega)\right]}\hat{\mathbf{G}}^*_\lambda(\mathbf{r}_0,\mathbf{r},\omega)\cdot\boldsymbol{\mu}\,\tilde{c}_e(t)e^{i(\omega-\omega_0)t}, \qquad (5.19)\end{aligned}$$

where we have introduced two modified coefficients, $\tilde{c}_e(t)$ and $\tilde{c}_{\mathbf{r},\omega_\lambda}(t)$, that relate to the ones in Eq. 5.16 via $c_e(t)=\tilde{c}_e(t)e^{-i\omega_0 t}$ and $c_{\mathbf{r},\omega_\lambda}(t)=\tilde{c}_{\mathbf{r},\omega_\lambda}(t)e^{-i\omega t}$. Formal integration of Eq. 5.19 with the initial condition $\tilde{c}_{\mathbf{r},\omega_\lambda}(0)=0$ yields

$$\tilde{c}_{\mathbf{r},\omega_\lambda}(t)=\frac{1}{\sqrt{\pi\epsilon_0\hbar}}\frac{\omega^2}{c^2}\sqrt{\mathrm{Im}\left[\epsilon(\mathbf{r},\omega)\right]}\,\boldsymbol{\mu}\cdot\hat{\mathbf{G}}^*_\lambda(\mathbf{r}_0,\mathbf{r},\omega)\int_0^t \mathrm{d}t'\,\tilde{c}_e(t')e^{i(\omega-\omega_0)t'}. \qquad (5.20)$$

Inserting the last expression into the equation for $\dot{\tilde{c}}_e(t)$ (5.18) leads to an integro-differential equation for the modified excited state coefficient $\tilde{c}_e(t)$, which reads as

$$\begin{aligned}\dot{\tilde{c}}_e(t) &= -\frac{1}{\pi\epsilon_0\hbar}\sum_\lambda\int_0^\infty \mathrm{d}\omega\,\frac{\omega^2}{c^2}\int \mathrm{d}^3\mathbf{r}\,\frac{\omega^2}{c^2}\mathrm{Im}\left[\epsilon(\mathbf{r},\omega)\right] \\ &\quad\times\left[\boldsymbol{\mu}\cdot\left(\hat{\mathbf{G}}_\lambda(\mathbf{r}_0,\mathbf{r},\omega)\cdot\hat{\mathbf{G}}^*_\lambda(\mathbf{r}_0,\mathbf{r},\omega)\right)\cdot\boldsymbol{\mu}\right]e^{-i(\omega-\omega_0)(t-t')}\tilde{c}_e(t). \qquad (5.21)\end{aligned}$$

Finally, making use of the relation

$$\mathrm{Im}\left\{\hat{\mathbf{G}}(\mathbf{r},\mathbf{r}',\omega)\right\}=\sum_\lambda\int \mathrm{d}\mathbf{r}''\,\frac{\omega^2}{c^2}\mathrm{Im}\left[\epsilon(\mathbf{r}'',\omega)\right]\left(\hat{\mathbf{G}}_\lambda(\mathbf{r},\mathbf{r}'',\omega)\cdot\hat{\mathbf{G}}^*_\lambda(\mathbf{r}',\mathbf{r}'',\omega)\right), \qquad (5.22)$$

we arrive to the following integro-differential equation

$$\dot{\tilde{c}}_e(t)=-\int_0^t \mathrm{d}t'\,K(t-t')\tilde{c}_e(t'), \qquad (5.23)$$

where the Kernel $K(t-t')$ is defined as

$$\begin{aligned}K(\tau) &= \frac{|\boldsymbol{\mu}|^2}{\pi\epsilon_0\hbar}\int_0^\infty \mathrm{d}\omega\,\frac{\omega^2}{c^2}\int \mathrm{d}^3\mathbf{r}\,\left[\mathbf{n}_\mu\cdot\mathrm{Im}\left\{\hat{\mathbf{G}}(\mathbf{r}_0,\mathbf{r}_0,\omega)\right\}\cdot\mathbf{n}_\mu\right]e^{-i(\omega-\omega_0)\tau} \\ &= \int_0^\infty \mathrm{d}\omega J(\omega)e^{i(\omega-\omega_0)\tau}. \qquad (5.24)\end{aligned}$$

In the last equality above, we have introduced the spectral density function, which reads as

$$J(\omega)=\frac{|\boldsymbol{\mu}|^2\omega^2}{\pi\epsilon_0\hbar c^2}\left[\mathbf{n}_\mu\cdot\mathrm{Im}\left\{\hat{\mathbf{G}}(\mathbf{r}_0,\mathbf{r}_0,\omega)\right\}\cdot\mathbf{n}_\mu\right], \qquad (5.25)$$

where $\mathbf{n}_\mu$ is the unit vector in the dipole moment direction, such that $\boldsymbol{\mu} = |\boldsymbol{\mu}|\mathbf{n}_\mu$. Expressions 5.23 - 5.25 constitute an important set of equations as they allow for the calculation of the time-evolution of the coupled QE-field system through an integration of the spectral function over the whole frequency range. These equations are exact, and solving them leads to a proper treatment of the QED dynamics of coupled systems independently of the coupling strength as long as the rotating wave approximation holds for Hamiltonian 5.15. In addition, they apply to QEs in the presence of an arbitrary configuration of absorbing materials. All the information concerning the environment is contained in the spectral density, which is fully determined by the classical Green's function of the problem.

Markov approximation

In the case of a weak coupling strength between the QE and the EM modes, the *Wigner-Weisskopf* formalism can be further simplified. We start by assuming the spectral function to be smooth around the QE's resonance frequency, ω_0, i.e., $\mathrm{d}J(\omega)/\mathrm{d}\omega \ll 1$. This is the so-called *Markov* approximation, which implies that the QE's spontaneous decay is a memoryless process. This means that the dominant contribution comes from $t \approx t'$ and the integral in Eq. 5.23 can be taken up to ∞. Then, the Kernel function given by Eq. 5.24 can be approximated to

$$K(\tau) \approx J(\omega_0) \int_0^\infty \mathrm{d}\omega\, e^{i(\omega-\omega_0)\tau} = J(\omega_0)\pi\delta(\tau) + i\Delta\omega. \tag{5.26}$$

Here, $\Delta\omega = \mathrm{P.V.}\int_0^\infty \mathrm{d}\omega J(\omega)e^{i(\omega-\omega_0)\tau}$ is the Lamb shift, which represents a small frequency shift in the QE's frequency that will be neglected here. Then, Eq. 5.23 reduces to

$$\dot{\tilde{c}}_e(t) = -J(\omega_0)\pi \int_0^\infty \mathrm{d}t'\delta(t-t')\tilde{c}_e(t) = -\frac{\Gamma(\omega_0)}{2}\tilde{c}_e(t). \tag{5.27}$$

where we have introduced the quantity $\Gamma(\omega) = 2\pi J(\omega)$. The above differential equation has an analytical solution, $\tilde{c}_e(t) = \tilde{c}_e(0)e^{-\Gamma(\omega_0)t/2}$, which implies an *irreversible* exponential decay of the QE's excited state population:

$$n_\sigma(t) = n_\sigma(0)e^{-\Gamma(\omega_0)t}, \tag{5.28}$$

from which it is clear that $\Gamma(\omega_0)$ is the spontaneous decay rate. Recalling expression 5.25 we can explicitly write $\Gamma(\omega)$ as

$$\Gamma(\omega) = \frac{2|\boldsymbol{\mu}|^2\omega^2}{\epsilon_0\hbar c^2}\left[\mathbf{n}_\mu \cdot \mathrm{Im}\left\{\hat{\mathbf{G}}(\mathbf{r}_0,\mathbf{r}_0,\omega)\right\}\cdot\mathbf{n}_\mu\right]. \tag{5.29}$$

An equivalent and particularly insightful way of writing the spontaneous decay rate (Eq. 5.29) is in terms of the local EM density of states, ρ_μ. This quantity can be written in terms of the Green's function by making use of its normal mode expansion, as shown in Appendix C. According to Eq. C.10, we have for ρ_μ:

$$\rho_\mu(\mathbf{r}_0,\omega) = \frac{6\omega}{\pi c^2}\left[\mathbf{n}_\mu \cdot \mathrm{Im}\left\{\hat{\mathbf{G}}(\mathbf{r}_0,\mathbf{r}_0,\omega)\right\}\cdot \mathbf{n}_\mu\right], \tag{5.30}$$

which allows us to write

$$\Gamma(\omega) = \frac{\pi\omega}{3\hbar\epsilon_0}|\boldsymbol{\mu}|^2\rho_\mu(\mathbf{r}_0,\omega). \tag{5.31}$$

The EM density of states represents the ability of the structure surrounding the emitter to support the EM mode into which the QE decays. In other words, the density of states is determined by the materials and geometries that constitute the environment for the QE, and it controls the spontaneous emission rate. Equation 5.29 constitutes an important result as it implies that the spontaneous decay rate, rather than being a radiative intrinsic property of atoms or molecules, is affected by the environment surrounding the emitter. This fact is clear from the above equation, where the effect of the environment is contained in the local density of states that relates to the classical Green's function through Eq. 5.30. The modification of the spontaneous emission rate is known as Purcell effect, as he was the first to point out this phenomenon in the context of a magnetic dipole in an electronic device [178].

Finally, the free-space spontaneous decay rate can be derived by particularizing the above expression for $\Gamma(\omega)$, Eq. 5.29, for the vacuum Green's function derived in Appendix C (Eq. C.24),

$$\mathrm{Im}\left\{\hat{\mathbf{G}}_0(\mathbf{r}_0,\mathbf{r}_0,\omega)\right\} = \frac{\omega}{6\pi c}. \tag{5.32}$$

Thereby we arrive to the intrinsic decay rate of a QE, which we term γ_0 and reads as

$$\gamma_0 = \frac{|\boldsymbol{\mu}|^2\omega_0^3}{3\pi\epsilon_0\hbar c^3}. \tag{5.33}$$

This expression represents the relationship between a QE's transition frequency and dipole moment, and its radiative decay rate.

5.2.2 Green's function formalism for a classical dipole coupled to the electromagnetic field

We now consider the radiation properties of an emitter coupled to the EM field within a classical framework. In particular, we follow Ref. [11] to calculate the energy dissipation

rate for an oscillating dipole, which has a very insightful expression in terms of the Green's function formalism. Let us consider an electric point dipole located at point $\mathbf{r} = \mathbf{r}_0$ and with a harmonically oscillating dipole moment $\boldsymbol{\mu}(t) = \mathrm{Re}\left[\boldsymbol{\mu}\exp\left(-i\omega t\right)\right]$, where ω is the resonance frequency. The electric field generated by the dipole within a medium characterized by the dielectric permittivity $\epsilon(\mathbf{r},\omega)$ corresponds to the solution of the wave equation

$$\nabla\times\nabla\times\mathbf{E}(\mathbf{r}) - \frac{\omega^2}{c^2}\epsilon(\mathbf{r},\omega)\mathbf{E}(\mathbf{r}) = i\omega\mu_0\mathbf{j}(\mathbf{r})\,, \tag{5.34}$$

with a current density $\mathbf{j}(\mathbf{r}) = -i\omega\boldsymbol{\mu}\delta[\mathbf{r}-\mathbf{r}_0]$, while the field $\mathbf{H}(\mathbf{r})$ satisfies

$$\nabla\times\epsilon(\mathbf{r},\omega)^{-1}\nabla\times\mathbf{H}(\mathbf{r}) - \frac{\omega^2}{c^2}\mu_0\mathbf{H}(\mathbf{r}) = \nabla\epsilon(\mathbf{r},\omega)^{-1}\mathbf{j}(\mathbf{r})\,, \tag{5.35}$$

where we have assumed a non-magnetic medium. Equivalently, the EM fields at point $\mathbf{r}$ generated by the arbitrarily oriented dipole placed at $\mathbf{r}_0$ can be written in terms of the Green's dyadic $\hat{\mathbf{G}}(\mathbf{r},\mathbf{r}_0,\omega)$ as $\mathbf{r}_0$ as

$$\mathbf{E}(\mathbf{r}) = \omega^2\mu_0\hat{\mathbf{G}}(\mathbf{r},\mathbf{r}_0,\omega)\boldsymbol{\mu}(\mathbf{r}_0)\,, \tag{5.36}$$

$$\mathbf{H}(\mathbf{r}) = -i\omega\left[\nabla\times\hat{\mathbf{G}}(\mathbf{r},\mathbf{r}_0,\omega)\right]\boldsymbol{\mu}(\mathbf{r}_0)\,, \tag{5.37}$$

where the Green's function satisfies the wave equation for a point source, given by expression 5.12.

As the dipole oscillates, it radiates energy into the surrounding medium. According to Poynting's theorem, the average power radiated by the dipole, P, has to be equal to the rate of energy dissipation, $\mathrm{d}W/\mathrm{d}t$, which is given by

$$\frac{\mathrm{d}W}{\mathrm{d}t} = -\frac{1}{2}\int_V \mathrm{Re}\{\mathbf{j}^*\cdot\mathbf{E}\}\mathrm{d}V, \tag{5.38}$$

where V is the source volume. Introducing the dipole's current density, we have for the radiated power

$$P = \frac{\omega}{2}\mathrm{Im}\{\boldsymbol{\mu}^*\cdot\mathbf{E}(\mathbf{r}_0)\}. \tag{5.39}$$

By replacing the electric field in the above expression for the radiated power with the Green's function through Eq. 5.36, we obtain

$$P = \frac{\omega^3|\boldsymbol{\mu}|^2}{2c^2\epsilon_0\epsilon}\left[\mathbf{n}_\mu\cdot\mathrm{Im}\left\{\hat{\mathbf{G}}(\mathbf{r}_0,\mathbf{r}_0,\omega)\right\}\cdot\mathbf{n}_\mu\right]. \tag{5.40}$$

This expression represents an important relation between the power radiated by a dipole and the Green's function of the system. It states that the radiated power depends on the

dipole's moment orientation, its frequency of oscillation and the imaginary part of the Green's function evaluated at the dipole's location, $\mathbf{r}_0$. The above equation is a general relation that applies not only to a dipole radiating in a homogeneous medium, such as free space or a dielectric material, but also to a dipole within an inhomogeneous environment, such as a cavity or a plasmonic structure. The characteristics of the environment are contained in the Green's function, that is specific to the problem.

When considering a dipole located in an inhomogeneous environment, it is convenient to identify two contributions to the Green's function: a free-space part and a scattered part. The first term corresponds to the direct dipole field, whereas the second one represents the field that is scattered from the environment after its former generation by the dipole. Hence, we can write the Green's function as

$$\hat{\mathbf{G}}(\mathbf{r}_0, \mathbf{r}_0, \omega) = \hat{\mathbf{G}}_0(\mathbf{r}_0, \mathbf{r}_0, \omega) + \hat{\mathbf{G}}_S(\mathbf{r}_0, \mathbf{r}_0, \omega), \tag{5.41}$$

where $\hat{\mathbf{G}}_0$ is the free space contribution and $\hat{\mathbf{G}}_S$ is the scattered part. The power dissipated by a harmonically oscillating dipole in free space can be obtained from Eq. 5.40 by using the free space Green's function (Eq. 5.32). We have

$$P_0 = \frac{\omega^4 |\boldsymbol{\mu}|^2}{12\pi c^3 \epsilon_0 \epsilon}, \tag{5.42}$$

which allows us to write the normalized rate of energy dissipation as

$$\frac{P}{P_0} = 1 + \frac{6\pi c}{\omega} \left[\mathbf{n}_\mu \cdot \mathrm{Im} \left\{ \hat{\mathbf{G}}_S(\mathbf{r}_0, \mathbf{r}_0, \omega) \right\} \cdot \mathbf{n}_\mu \right]. \tag{5.43}$$

Therefore, the change in radiated power depends on the field emitted by the dipole that is scattered by the environment and then arrives back to the dipole.

Finally, let us go back to the spontaneous decay rate of a QE derived within the QED framework in the previous Subsection (Eq. 5.29). The decay rate normalized it to its free space value, γ_0, can be written as,

$$\frac{\Gamma}{\gamma_0} = 1 + \frac{6\pi c}{\omega} \left[\mathbf{n}_\mu \cdot \mathrm{Im} \left\{ \hat{\mathbf{G}}_S(\mathbf{r}_0, \mathbf{r}_0, \omega) \right\} \cdot \mathbf{n}_\mu \right], \tag{5.44}$$

where we have made use of the separation of the Green's function in its free-space and scattered contributions according to Eq. 5.41. Interestingly, we see from this expression that the normalized spontaneous emission rate is equivalent to the normalized rate of energy dissipation given by Eq. 5.43 and derived within the classical formalism. Hence, we have

$$\frac{\Gamma}{\gamma_0} = \frac{P}{P_0}, \tag{5.45}$$

and decay rate variations in inhomogeneous systems can be determined through a calculation of the classical EM energy radiated by a dipole.

In the following, we study the coupling between QEs and the EM modes supported by plasmonic structures in several configurations. First, in Section 5.3 we consider the case of a single QE placed in front of flat plasmonic structures. Here, we first review the WC regime, where the QE features an irreversible decay that can be understood within the Markov approximation through Eq. 5.29. Next, we go beyond the Markov approximation by exactly solving the dynamics of the QE's population. The Wigner-Weiskopf formalism (Eqs. 5.23 - 5.25) allows us to do so, and thereby to determine the regions where reversible dynamics takes place. In Section 5.4 we consider the case of two QEs coupled through a plasmonic mode. In particular, we show that the interaction between two QEs can be efficiently mediated by the SPPs supported by graphene sheets and ribbons. Finally, in Section 5.5 we develop a theoretical framework to treat the SC regime between an *ensemble* of QEs and the SPPs propagating along flat metal/dielectric interfaces.

5.3 Single quantum emitter coupled to plasmonic media

In this Section we address the coupling of a single QE to flat plasmonic structures under two different regimes. First, in Subsection 5.3.1 we work under the Markov approximation, where the QE's population decays irreversibly. We review the modification of the spontaneous decay rate, Γ/γ_0, for QEs in the optical regime close to a metal/dielectric interface as well as for QEs in the THz regime in the vicinity of a graphene sheet. For both cases, we show that if the QE is placed at the appropriate distances to the plasmonic medium, its spontaneous emission can be greatly enhanced due to coupling to SPPs. Moreover, in the case of graphene, the coupling to SPPs can be tuned by means of the chemical potential of the sheet. On the other hand, when the WC regime breaks down, the decay of the QE is no longer exponential and it can not be described by a rate. In this case, the dynamics of the coupled QE-plasmonic media system can be exactly determined by means of the Wigner-Weisskopf formalism presented in the previous Section. In Subsection 5.3.2 we solve Eq. 5.23 for a QE close to a metal/dielectric interface and a thin metal film and we determine the conditions for which reversibility can be found in the dynamics.

5.3.1 Modification of the spontaneous decay rate

In this Subsection we apply Eq. 5.29 to study the modified spontaneous decay rate of a QE in an inhomogeneous plasmonic environment. As we have already described in the previous Section, for weak coupling strengths between the QE and the EM modes supported by the plasmonic environment, an exponential decay of the QE's population is expected. Such a decay is characterized by a rate, $\Gamma(\omega)$, that can be written in terms of the classical Green's function of the system (see Eq. 5.29), which contains all the information of the environment surrounding the QE. The modification of the decay rate can also be understood in terms of the local density of states, a quantity that represents the number of final states available for the spontaneous decay. Importantly, depending on the properties of the surrounding media, the local density of states can be higher or lower than that of free space [178]. In the first case, $\Gamma/\gamma_0 > 1$ and the decay rate is enhanced with respect to emission vacuum. The lifetime, $\tau = h/\Gamma$, of the emitter, is then reduced and the dipole decays faster. When there is a lower number of available states than in free space, $\Gamma/\gamma_0 < 1$ and there is an inhibition of the spontaneous emission, or, in other words, the lifetime of the emitter is increased. Plasmonic nanostructures have been shown to greatly enhance the spontaneous emission of an emitter due to the non radiative coupling to SPPs, which provide a large density of states [179, 180].

Here we consider a QE in the presence of a plasmonic media with a planar interface at $z = 0$. We study two different cases: (i) a semi-infinite metal surface of dielectric permittivity $\epsilon(\omega)$ [see Fig. 5.1(a)] and (ii) a graphene sheet of conductivity $\sigma(\omega)$ [see Fig. 5.1(b)]. According to Eq. 5.29, the QE's spontaneous decay rate is fully determined by the classical Green's tensor of the system, $\hat{\mathbf{G}}(\mathbf{r}, \mathbf{r}, \omega)$, evaluated at the emitter's frequency, ω_0, and at its location, $\mathbf{r} = \mathbf{r}_0$, with $\mathbf{r}_0 = (\mathbf{r}_\parallel, z)$. For the structures of interest here, with a single interface, it is convenient to separate the Green's function in a free-space and a scattered part, following Eq. 5.41, an thereby arriving to Eq. 5.44. The scattered Green's function, $\hat{\mathbf{G}}_S(\mathbf{r}_0, \mathbf{r}_0, \omega_0)$, in this case is indeed the reflected Green's function, $\hat{\mathbf{G}}_R(\mathbf{r}_0, \mathbf{r}_0, \omega_0)$, and we can write

$$\frac{\Gamma}{\gamma_0} = 1 + \frac{6\pi c}{\omega} \left[\mathbf{n}_\mu \cdot \mathrm{Im} \left\{ \hat{\mathbf{G}}_R(\mathbf{r}_0, \mathbf{r}_0, \omega_0) \right\} \cdot \mathbf{n}_\mu \right]. \tag{5.46}$$

Hence, the change in the QE's decay rate in the presence of a layered structure is dictated by the field emitted by itself, reflected at the interface and arriving back at it. The Green's function can be written from a plane wave expansion of s and p-polarized plane waves, as detailed in Appendix C. As any dipole moment may be considered as a combination of a perpendicular (labeled as $\perp$) and a parallel ($\parallel$) components, it is

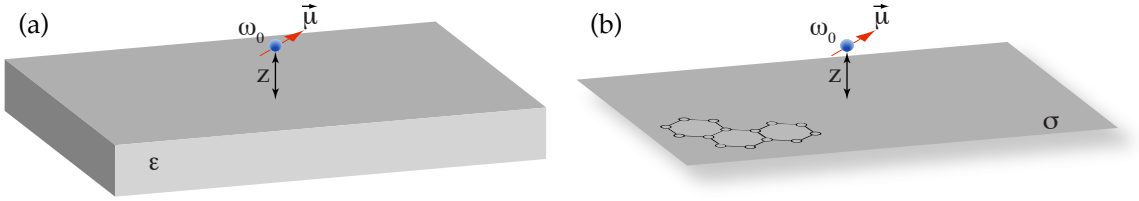

Figure 5.1: QE decaying close to two different plasmonic media: a metal surface and graphene. (a) QE of resonance frequency ω_0 and dipole moment $\boldsymbol{\mu}$ at a distance z from a semi-infinite metal region. The metal dielectric permittivity is $\epsilon(\omega)$. (b) QE located in the vicinity of a graphene sheet of conductivity $\sigma(\omega, \mu, T)$, with μ being the chemical potential and T the temperature.

sufficient to consider these two orientations. From the expressions for the Green's dyadic derived in Appendix C (Eqs. C.31 and C.32), we can write

$$\hat{\mathbf{G}}^{\parallel}(\mathbf{r}_0, \mathbf{r}_0, \omega_0) = \frac{i}{8\pi} \int_0^{\infty} \mathrm{d}k_{\parallel} \frac{k_{\parallel}}{k_z} \left[1 + q_z^2 + \left(r_s(k_{\parallel}) + q_z^2 r_p(k_{\parallel})\right) e^{2ik_z z}\right], \tag{5.47}$$

$$\hat{\mathbf{G}}^{\perp}(\mathbf{r}_0, \mathbf{r}_0, \omega_0) = \frac{i}{8\pi k_o^2} \int_0^{\infty} \mathrm{d}k_{\parallel} \frac{k_{\parallel}^3}{k_z} \left[1 - r_p(k_{\parallel}) e^{2ik_z z}\right]. \tag{5.48}$$

where $k_0 = \omega/c$ is the free-space wave number and $\mathbf{k} = (\mathbf{k}_{||}, k_z)$ is the wave vector, with $k_{||} = |\mathbf{k}_{||}|$ and $k_z = \sqrt{k_0^2 - k_{||}^2}$. In addition, $r_s(k_{\parallel})$ and $r_p(k_{\parallel})$ represent the reflection coefficients for s and p polarizations. In both equations the free-space and reflected contributions can be easily separated, and we have for the modified decay rates

$$\frac{\Gamma_{\parallel}}{\gamma_0} = 1 + \frac{3}{4} \mathrm{Re}\left[\int_0^{\infty} \mathrm{d}q \frac{q}{q_z} \left(r_s(q) + q_z^2 r_p(q)\right) e^{2ik_0 q_z z}\right], \tag{5.49}$$

$$\frac{\Gamma_{\perp}}{\gamma_0} = 1 - \frac{3}{2} \mathrm{Re}\left[\int_0^{\infty} \mathrm{d}q \frac{q^3}{q_z} r_p(q) e^{2ik_0 q_z z}\right]. \tag{5.50}$$

where we have introduced the normalized wave vectors: $q = k_{\parallel}/k_0$ and $q_z = \sqrt{1 - q^2}$. The two equations above determine the modified decay rate for a QE of dipole moment parallel or perpendicular to a planar interface. They imply that a dipole moment oriented perpendicular to the surface will couple only to the p modes supported by the layered structure, since expression 5.50 involves only r_p, while a dipole of any other orientation will couple to s as well as p modes. In the following, we make use of these expressions to study how the emission properties of a QE are modified by the presence of (i) a semi-infinite metal region and (ii) a graphene sheet.

Modified spontaneous decay rate of a QE close to a flat metal/dielectric interface

Let us first consider a QE located at a distance z of a metal/vacuum interface, as sketched in Fig. 5.1(a). The reflection coefficients are in this case determined by the wave vectors in the direction perpendicular to the interface, $q_z = \sqrt{1-q^2}$ in the dielectric region of the interface and $q_z^m = \sqrt{\epsilon(\omega)-q^2}$ in the metal region, as

$$r_p(q) = \frac{q_z^m - \epsilon(\omega) q_z}{q_z^m + \epsilon(\omega) q_z}, \quad r_s(q) = \frac{q_z^m - q_z}{q_z^m + q_z}. \tag{5.51}$$

Writing the decay rate as in Eqs. 5.49 and 5.50 provides a deep physical insight into the problem, as it allows us to examine where the radiation emitted by the QE is going, or, in other words, into which channels the QE may decay and their relative importance. The QE's dipolar field contains modes of different wave vectors, q. Those modes with q lying inside the light line, $0 < q < 1$, represent coupling of the emitter to radiation, whereas those modes with $q > 1$ correspond to energy transfer to the substrate through the near field of the dipole. There are three decay channels to point out [179, 180]:

- Far field radiation: The region of wave vectors determined by $0 < q < 1$ represents the radiation of the QE into the far field. For these modes, $q_z = \sqrt{1-q^2}$ is real, meaning that their character is propagating. The contribution of these modes to the total decay can be expressed for the different orientations as

$$\frac{\Gamma_{\text{Rad}}^{\parallel}}{\gamma_0} = 1 + \frac{3}{4}\text{Re}\left[\int_0^1 \text{d}q \frac{q}{q_z}\left(r_s(q) + q_z^2 r_p(q)\right) e^{2ik_0 q_z z}\right], \tag{5.52}$$

$$\frac{\Gamma_{\text{Rad}}^{\perp}}{\gamma_0} = 1 - \frac{3}{2}\text{Re}\left[\int_0^1 \text{d}q \frac{q^3}{q_z} r_p(q) e^{2ik_0 q_z z}\right]. \tag{5.53}$$

- Coupling to SPPs that propagate along the metal/dielectric interface. They appear as a pole in the reflection coefficient for p polarization, satisfying $q_z + \epsilon(\omega) q_z^m = 0$. Their dispersion relation, $q_{\text{spp}} = \sqrt{\epsilon/(1+\epsilon)}$, lies outside the light line and as a consequence SPPs are evanescent waves (imaginary q_z) bound to the interface (see Section 1.1). Due to their evanescent character, they can only be excited by the near field of the QE, when it is in close proximity to the metal surface. The relative weight of this channel can be calculated by evaluating the pole contribution to the integrals in Eqs. 5.49 and 5.50 to obtain

$$\frac{\Gamma_{\text{spp}}^{\parallel}}{\gamma_0} = \frac{3\pi}{2}\text{Re}\left[-iq_{\text{spp}}^3 \frac{\epsilon(\omega_0)^{1/2}}{\epsilon(\omega_0)^2 - 1} e^{-2k_0 q_{\text{spp}} \frac{z}{\sqrt{|\epsilon(\omega_0)|}}}\right], \tag{5.54}$$

$$\frac{\Gamma_{\text{spp}}^{\perp}}{\gamma_0} = 3\pi\text{Re}\left[q_{\text{spp}}^3 \frac{|\epsilon(\omega_0)|^{3/2}}{\epsilon(\omega_0)^2 - 1} e^{-2k_0 q_{\text{spp}} \frac{z}{\sqrt{|\epsilon(\omega_0)|}}}\right]. \tag{5.55}$$

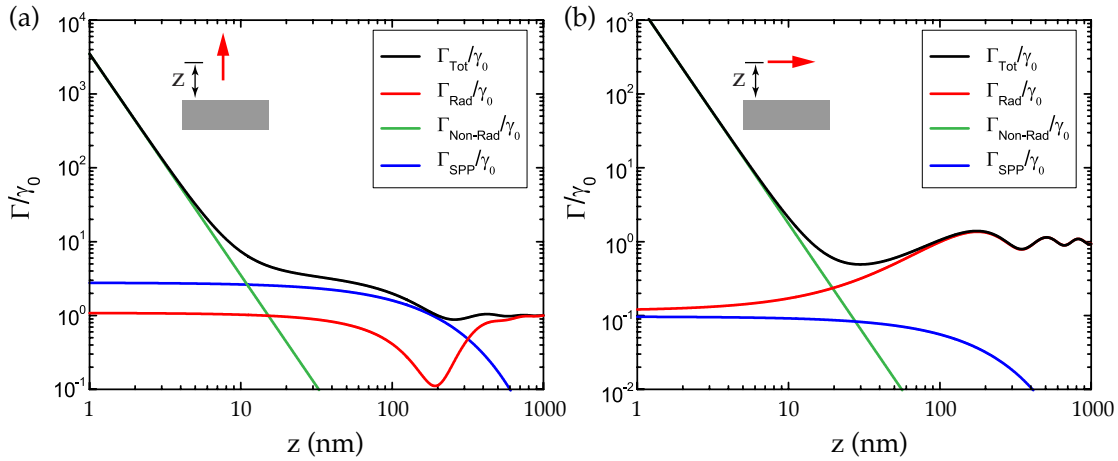

Figure 5.2: Normalized decay rate, Γ/γ_0, for a QE close to a metal surface as a function of the emitter's distance to the surface, z. The QE's resonance frequency is $\hbar\omega_0 = 2$eV and its dipole moment is perpendicular to the dielectric-metal interface in (a) and parallel to it in (b). The normalized total decay rate $\Gamma_{\text{Tot}}/\gamma_0$ (black line) is plotted together with the different contributions: radiation to free space $\Gamma_{\text{Rad}}/\gamma_0$ (red line), decay into SPPs $\Gamma_{\text{spp}}/\gamma_0$ (blue line) and decay into lossy channels $\Gamma_{\text{Non-Rad}}/\gamma_0$ (green line). The metal permittivity corresponds to silver and is taken from Ref. [14].

- Coupling to other non radiative modes. The last decay channel, which has been referred to as *lossy surface waves* [179], is relevant only for very small distances since it relies on a broad feature appearing at very large wave vectors, $q \gg 1$. The oscillating near field of the emitter induces excitations in the electronic charge density, such as electron-hole pairs, that then decay through scattering within the semi-infinite metal (impurities, phonons, surface potential...). The contribution of this non radiative decay to the total decay rate can be calculated in the quasi-static limit. For $q \gg 1$, we have $q_z \approx iq$ and $q_z^m \approx iq$ and the decay rate simplifies to

$$\frac{\Gamma^{\parallel}_{\text{Non-Rad}}}{\gamma_0} = \frac{3}{16}\frac{1}{(k_0 z)^3}\text{Im}\left(\frac{\epsilon(\omega_0)-1}{\epsilon(\omega_0)+1}\right), \tag{5.56}$$

$$\frac{\Gamma^{\perp}_{\text{Non-Rad}}}{\gamma_0} = \frac{3}{8}\frac{1}{(k_0 z)^3}\text{Im}\left(\frac{\epsilon(\omega_0)-1}{\epsilon(\omega_0)+1}\right). \tag{5.57}$$

Hence, we can write the total decay rate of the QE as a sum of three contributions as

$$\Gamma_{\text{Tot}} = \Gamma_{\text{Rad}} + \Gamma_{\text{spp}} + \Gamma_{\text{Non-Rad}} \tag{5.58}$$

where the partial contributions of each channel (Γ_{Rad}, Γ_{spp}, $\Gamma_{\text{Non-Rad}}$) are listed in Eqs. 5.52 to 5.57 for the perpendicular and parallel orientations the dipole moment. It is clear

from this set of expressions that the different contributions have a specific dependence on the distance between the QE and the metal surface, z. The modified total decay rate together with the partial decays as a function z for a QE in the optical regime (resonance frequency $\hbar\omega_0 = 2$ eV, or equivalently, $\lambda = 633$ nm) is presented in Fig. 5.2. Panel (a) corresponds to a dipole moment oriented perpendicular to the surface and panel (b) to the parallel orientation. In both panels and for large distances, radiation to free space is the main contribution to the total decay, which shows an oscillatory behaviour with z due to reflection from the interfaces. The non radiative decay to surface plasmons, with an exponential decay, is relevant at intermediate distances. Finally, non radiative coupling to losses in the metal always dominates at small distances, with a z^{-3} dependence.

Both panels of Fig. 5.2 show that the total decay rate, Γ/γ_0, is largely enhanced as the QE is brought closer to the metal surface. The near field of the dipole makes it possible for the QE to couple to non radiative modes with high q vectors, which imply large confinement of the EM field. While the so-called *lossy surface waves* also enhance the decay of the QE at very small distances to the metal surface, coupling to SPPs is of particular interest, since they enhance the decay at intermediate distances and, at the same time, they propagate through the metal surface. This means that they can act as a channel to mediate the energy transfer between several QEs, as we will see in the following Section. It is convenient to define here the β_{spp} factor as the fraction of the emitted radiation that goes into SPPs:

$$\beta_{\text{spp}} = \frac{\Gamma_{\text{spp}}}{\Gamma_{\text{Tot}}}. \tag{5.59}$$

Figure 5.3 shows β_{spp} as a function of z for a QE at $\hbar\omega_0 = 2$ eV, oriented perpendicular to the surface ($\beta_\perp$, black line) or parallel to it ($\beta_\parallel$, blue line). An isotropic average of orientations ($\beta_{\text{iso}} = 2\beta_\parallel/3 + \beta_\perp/3$) is also presented (red line). In the plot, the perpendicular dipole moment displays a region of great interest at intermediate distances $20 < z < 300$ nm, where $\beta_\perp$ is very close to 1, meaning that the total decay rate is dominated by the coupling to SPPs. On the other hand, the coupling of the parallel dipole moment to SPPs is lower. An average over all orientations, which is likely in an experiment due to the difficulty in controlling the orientation of QEs, has an intermediate value $\beta_{\text{iso}} \approx 0.3$ over a broad distance range, $20 < z < 300$ nm. This region of large β_{spp} is of particular interest in this Chapter and we will show in the following that this feature is also found for graphene SPPs.

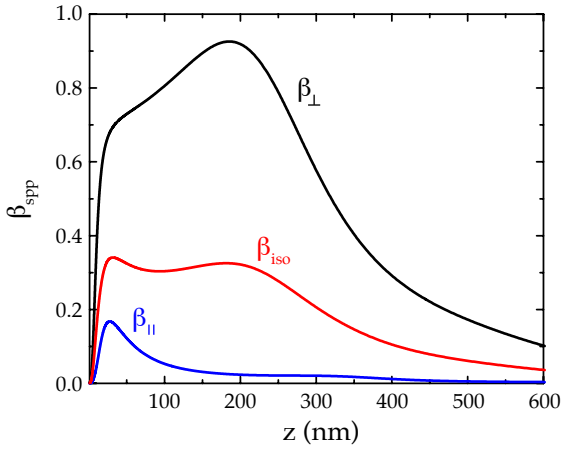

Figure 5.3: Coupling to SPPs for a QE close to a silver surface as a function of the distance z: β_{spp} represents the fraction of the emitted radiation that couples to the SPPs of the metal/dielectric interface, $\Gamma_{\text{spp}}/\Gamma_{\text{Tot}}$. The QE's resonance frequency is $\hbar\omega_0 = 2$ eV and its dipole moment is oriented perpendicular to the interface for the black line and parallel to it for the blue line, while the red line corresponds to an isotropic average of orientations.

Modified spontaneous decay rate of a QE close to a graphene sheet

Here we characterize the coupling to graphene SPPs for a QE at frequency ω_0 decaying in the vicinity of a free-standing 2D graphene sheet, as sketched in Fig. 5.1 (b). The graphene sheet has a conductivity $\sigma(\omega)$, given by Eqs. 1.16 and 1.17. As detailed in Section 1.1, this quantity depends on the chemical potential of the graphene sheet [2], μ, the temperature, which we consider to be $T = 300$ K, and the carriers' scattering time τ, for which we use a value taken from the theoretical predictions, $\tau = 6$ ps [271]. Below a critical frequency, $\hbar\omega \approx 2\mu$, $\text{Im}(\sigma) < 0$ and the graphene sheet supports the propagation of bound SPP modes.

According to Eq. 5.46, the total decay rate of a QE that is placed close to a graphene sheet is given by the imaginary part of the Green's function. Similarly to the case of a metal surface, coupling to SPPs is larger for a QE with a dipole moment oriented perpendicularly to the sheet. Hence, in the following we consider only this orientation for the dipole moment and write the modified decay rate as given in Eq. 5.50,

$$\frac{\Gamma}{\gamma_0} = 1 - \frac{3}{2}\text{Re}\left[\int_0^\infty \text{d}q \frac{q^3}{q_z} r_p(q) e^{2ik_0 q_z z}\right]. \tag{5.60}$$

The reflection coefficient, $r_p(q)$, of the graphene layer is written in terms of the normalized

[2] Not to be confused with the dipole moment used in this chapter, $\boldsymbol{\mu}$.

conductivity $\alpha = 2\pi\sigma/c$ as

$$r_p(q) = \frac{-\alpha q_z}{\alpha q_z + 1}. \tag{5.61}$$

Figure 5.4 (a) shows the total normalized decay rate (black line) for a QE of resonance frequency in the THz regime ($\nu = 2.4$ THz, $\hbar\omega_0 = 1$ meV) and for $\mu = 0.2$ eV as a function of the emitter-graphene distance z, normalized to the free-space wavelength $\lambda_0 = 124\ \mu$m. The physical parameters μ and ω_0 are chosen to provide a good compromise in the trade-off between confinement and propagation length for the graphene SPPs, as discussed in Section 1.1. Similarly to the case of a QE close to a metal surface, three different regions can be identified in the plot according to the decay mechanisms:

- A radiative region at large distances ($z \gg \lambda_0/10$ for the chosen parameters). If the QE is far enough from the graphene sheet, the total decay rate follows $\Gamma_{\mathrm{Rad}/\gamma_0}$ (blue line), which corresponds to the integration of the radiative modes ($0 < q < 1$) in Eq. 5.60.

- A region ($\lambda_0/10 < z < \lambda_0/100$) where the dominant decay channel is the coupling to graphene SPPs. In this region, the total modified decay rate follows the partial SPP decay, $\Gamma_{\text{G-SPP}}/\gamma_0$ (red line), that can be calculated from the pole contribution to Eq. 5.60 as

$$\frac{\Gamma_{\text{G-SPP}}}{\gamma_0} = \frac{3\pi}{2}\mathrm{Re}\left[i\frac{q_{\mathrm{p}}^2}{\alpha}e^{2ik_0 q_z^{\mathrm{p}} z}\right], \tag{5.62}$$

  where $q_{\mathrm{p}} = \sqrt{1-\alpha^{-2}}$ and $q_z^{\mathrm{p}} = -\alpha^{-1}$ are the normalized momentum components of the SPP (see Eq. 1.18).

- A non radiative lossy region when the QE is very close to the sheet ($z < \lambda_0/100$).

Importantly, and as the figure shows, the decay rate of the QE can be enhanced by several orders of magnitude. Here we are interested in the plasmonic region, where the graphene SPP contribution to the total decay rate yields enhancement values larger than 100 for the parameters we have chosen. It is interesting to note that the values reached by $\Gamma_{\text{G-SPP}}/\gamma_0$ are much larger than for the metal surface considered previously. However, enhancements similar to the ones obtained with graphene SPPs can also be obtained for very thin metal films [272] when the thickness is much smaller than the skin depth, which is challenging from the fabrication point of view, as opposed to the intrinsic 2D character of graphene. For higher frequencies or smaller chemical potentials, even larger

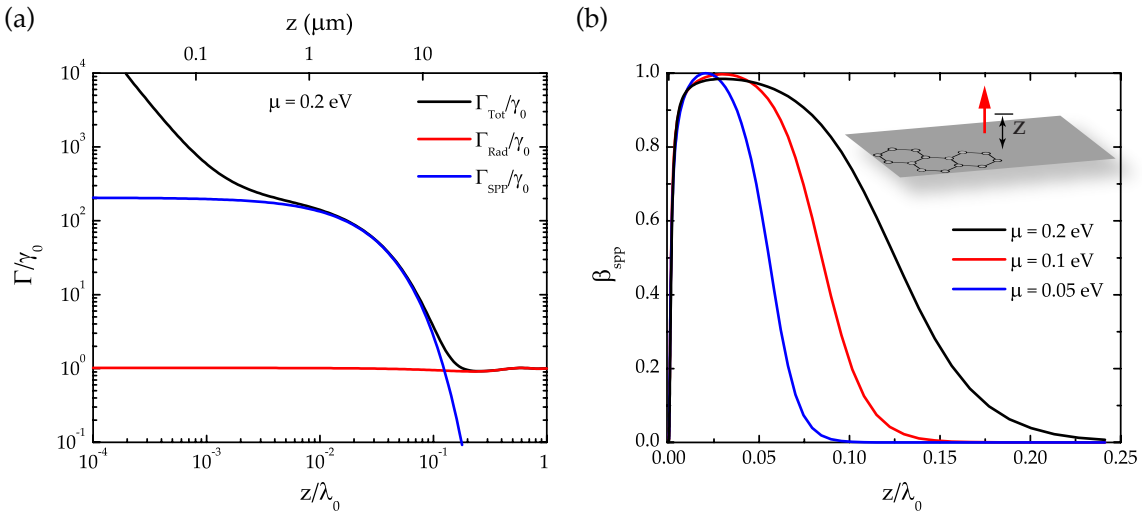

Figure 5.4: Dependence with the distance for the decay of a QE in the presence of graphene. (a) Normalized decay rate, Γ/γ_0, for a QE at $\nu = 2.4$ THz (free-space wavelength $\lambda_0 = 124$ μm) close to a graphene sheet at a chemical potential $\mu = 0.2$ eV. The black line represents the total decay rate, Γ_{Tot}/γ_0, the red line stands for the contribution of radiation to free space $\Gamma_{\text{Rad}}/\gamma_0$ and the blue line corresponds to the decay into SPPs $\Gamma_{\text{spp}}/\gamma_0$. (b) Tuning the coupling to SPPs, $\beta_{\text{spp}} = \Gamma_{\text{spp}}/\Gamma_{\text{Tot}}$, by means of the chemical potential, μ. The dipole moment is perpendicular to the graphene sheet in all cases.

enhancements of the decay rate in the plasmonic region can be obtained in graphene; for instance, $\Gamma/\gamma_0 \approx 10^3$ at $\lambda_0 = 64$ μm for the same chemical potential.

The parameter that accounts for the efficiency of the coupling to SPPs, the β factor, is in this case defined as the ratio of the emitter's decay rate through graphene SPPs to its total decay rate, $\beta_{\text{G-SPP}} = \Gamma_{\text{G-SPP}}/\Gamma_{\text{Tot}}$. Figure 5.4 (b) studies the possibility of tuning $\beta_{\text{G-SPP}}$ with the chemical potential. Three values for μ are considered: $\mu = 0.2$, 0.1 and 0.05 eV. For each value of μ there is a range of z's where $\beta_{\text{G-SPP}}$ is close to 1, which corresponds to the region where the decay rate is dominated by the plasmonic channel. This means that the region of high $\beta_{\text{G-SPP}}$ can be dynamically tuned with the chemical potential, which is in turn controlled by means of an electrostatic gating or a chemical doping. In particular, when the chemical potential is decreased to 0.1 eV (green line) and 0.05 eV (blue line), the SPP appears at larger q vectors, it is more confined to the graphene sheet, and the range of distances where $\beta_{\text{G-SPP}}$ is high is narrower. Compared to the metal/dielectric interface studied above, a graphene sheet gives very large decay rates and β factors close to 1. This is due to the huge confinement and large values of the SPP wave vectors resulting from the 2D character of graphene, which makes the

coupling to SPPs very efficient. Comparing to thin metal layers, where, as discussed in Section 1.1, the confinement can also be very large, the most important advantage of graphene is the capability of tuning the coupling to SPPs by means of a gate potential.

5.3.2 Reversible dynamics for a quantum emitter interacting with plasmonic media

Now we study the conditions for the breakdown of the Markov approximation and the appearance of reversible dynamics for an individual QE placed in the close proximity of plasmonic nanostructures. As we reviewed in the Section 1.5, experimental works where a single QE interacts with a plasmonic system include the observation of fluorescent enhancement and quenching in flat metal/dielectric interfaces [174–177, 179, 180] and metal nanoparticles [28, 29], as well as the efficient single photon generation in metal nanowires [181–183, 185–187]. All these works are examples of the WC regime, where the QE's population decays irreversibly to the plasmon mode. On the other hand, in situations where the coupling strength between the QE and the EM environment is sufficiently large to overcome dissipation and decoherence mechanisms, the QE and the EM field coherently exchange energy. In the context of plasmonic nanostructures, the SC regime has been studied in theoretical works considering a single QE interacting with the LSPs supported by metallic structures of different geometries: cigar-shaped nanoparticles [196], dimer nanoantennas [197] or spherical nanoparticles [198, 199]. In addition, SC between a single QE and a SPP mode propagating along 1D plasmonic waveguides [200, 201, 203] or 2D metal surfaces [202] has also been considered. Here we study the case of an individual QE placed close to 2D flat metal/dielectric interfaces. In particular, we consider a semi-infinite metal surface and a metal thin film, both supporting the propagation of 2D SPPs. Differently from previous works in the same system [202], where a perturbative method able to capture reversibility only up to lowest order in the coupling was used, here we treat the dynamics of the QE exactly.

In order to study the dynamics of a QE's population in the presence of the absorbing metal structure, we make use of the macroscopic QED formalism presented in Section 5.2. In the following, we use that formalism to study the dynamics of a QE coupled to the EM modes supported by a layered metallic structure. By analyzing the appearance of oscillations in the QE's population, we determine the conditions for the break down of the WC regime and the observation of reversibility in the dynamics. In addition, under some conditions we are able to map the full dynamics of the problem to a dissipative Jaynes-Cummings model. Thereby we derive analytical expressions involving the key

parameters that play a role in the onset of the reversible dynamics.

The system under study is sketched in Fig. 5.5 (a) as an inset panel. An individual QE is placed on top a of a layered dielectric/metal/dielectric structure. The thickness of the metal film is h and the dielectric permittivities of the media are $\epsilon_d/\epsilon_m/\epsilon_d$. For the dielectric media we take $\epsilon_d = 1$ and as the metal we use silver, with a dieletric funtion modeled by the Drude formula (Eq. 1.1) with the same parameters as those used in Fig. 1.1 ($\hbar\omega_p = 9$ eV, $\hbar\gamma_p = 0.07$ eV and $\epsilon_\infty = 5.6$). The QE is placed at point $\mathbf{r}_0 = (\mathbf{R}, z_0)$, where z_0 is the distance between the emitter and the upper metal/dielectric interface. The emitter is described within a two level-system approximation, $\{\sigma, \sigma^\dagger\}$, and characterized by its transition frequency ω_0 and dipole moment $\boldsymbol{\mu}$. We assume $\boldsymbol{\mu}$ to be oriented perpendicularly to the interface, but similar results could be obtained for the parallel orientation. In addition, we use the free space spontaneous decay rate, γ_0, which relates to the dipole moment through Eq. 5.33, or the QE's lifetime, $\tau_0 = \gamma_0^{-1}$, to parametrize the strength of the coupling to the EM field.

We start by briefly reviewing the theoretical framework needed to appropriately treat the interaction between the QE and the EM field in the presence of the plasmonic structure. First, we use Hamiltonian 5.15, which was derived in the previous Section within a macroscopic QED formalism and under the electric-dipole and rotating wave approximations. The dynamics of the QE-EM field combined system can then be derived by means of the already described *Wigner-Weisskopf* formalism. Assuming a state of the form given by Eq. 5.16 and applying Schrodinger's equation, the time evolution of the QE's excited state population,

$$n_\sigma(t) = |c_e(t)|^2, \tag{5.63}$$

is determined by Eq. 5.23 as

$$\dot{\tilde{c}}_e(t) = -\int_0^t \mathrm{d}t'\, K(t-t')\tilde{c}_e(t'). \tag{5.64}$$

The kernel of this integro-differential equation is defined by Eq. 5.24 as

$$K(\tau) = \int_0^\infty \mathrm{d}\omega J(\omega) e^{i(\omega-\omega_0)\tau};\;\; J(\omega) = \frac{|\boldsymbol{\mu}|^2\omega^2}{\pi\epsilon_0\hbar c^2}\left[\mathbf{n}_\mu \cdot \mathrm{Im}\left\{\hat{\mathbf{G}}(\mathbf{r}_0, \mathbf{r}_0, \omega)\right\} \cdot \mathbf{n}_\mu\right]. \tag{5.65}$$

The spectral density function, $J(\omega)$, contains all the information on both the QE-field coupling and the density of EM modes and is fully determined by the classical Green's function of the problem.

The spectral density function for the system under study is plotted in Fig. 5.5. Panel (a) displays $J(\omega)$ for a QE placed on top of a metal film of thickness $h \gg \sqrt{\epsilon_d} z_0$, such

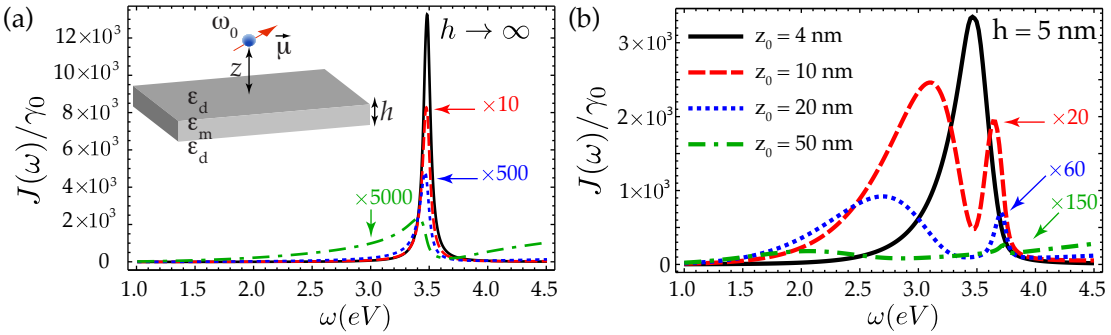

Figure 5.5: Spectral density function for a single QE near a layered metallic structure for two different values of the metal film thickness, h. An individual QE interacts with a dielectric/metal/dielectric structure, as sketched in the inset panel. (a) Spectral density for a QE close to a thick metal film ($h \gg \sqrt{\epsilon_d} z_0$). Four different separations, z_0, between the QE and the upper metal/dielectric interface are plotted. (b) Same as in (a) but for a thin metal film ($h = 5$ nm). In both panels, the spectral density is normalized to the QE's free space decay rate, γ_0, and we assume $\epsilon_d = 1$.

that it can be considered a semi-infinite metal/dielectric interface. Different values of the QE-interface distance, z_0, are plotted, starting from $z_0 = 4$ nm [3]. As the figure shows, for small separations the spectral density is strongly peaked at the SPPs cut-off frequency,

$$\omega_{sp} = \frac{\omega_p}{\sqrt{\epsilon_d + \epsilon_\infty}}, \tag{5.66}$$

anticipating that the EM modes around this frequency will dominate the dynamics. Notice however that, as we will show below, SPPs play a minor role in the process of reversible dynamics and that the key actors are the EM modes responsible for quenching of radiation. The same behaviour is observed for thin metal films ($h = 5$ nm), as shown in panel (b) for $z_0 = 4$ nm. As the QE-interface separation grows the height of the peak decreases and its width increases making the spectral density smoother for the case of a thick metal film. In contrast, for thin metal films in this intermediate regime, the spectral density splits into two contributions corresponding to the short and long range SPP modes of the thin film (see Section 1.1). The poor confinement of the SRSPP mode makes its contribution pin at ω_{sp} independently of z_0 whereas the contribution of the LRSPP mode shifts to lower frequencies as z_0 increases. Finally, at large z_0's, the spectral densities corresponding to both thick and thin metal films become very smooth without signatures of resonant peaks.

[3] We have checked that for $z_0 \geq 4$ nm non local effects do not need to be considered (see Ref. [273]).

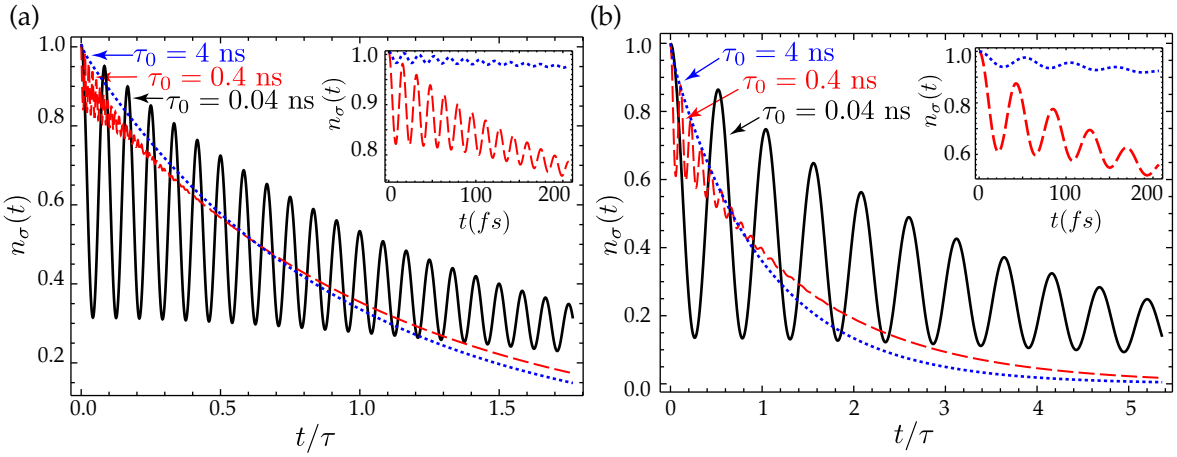

Figure 5.6: Population dynamics of an individual QE near a metal surface. (a) Dynamics of the excited state population for a QE in the optical regime, $\hbar\omega_0 = 2$ eV, placed at a distance $z_0 = 5$ nm from a metal surface. Different values for τ_0 are considered, as specified in the legend. The time-scale is normalized to the modified lifetime of the QE, $\tau = h/\Gamma(\omega_0)$. Inset panel: zoom to observe oscillations of small amplitude for two cases. (b) Same as in panel (a) but for a QE of resonance frequency $\hbar\omega_0 = 3$ eV.

Now we focus our attention on the dynamics of the single QE when it is placed at very short distances from the metal surface and quenching is expected [179, 180]. As the behaviour of $J(\omega)$ for thick and thin metal films is very similar for this range of distances, from now on we study the case of thick metal films without losing generality. In order to study the dynamics beyond the perturbative regime, we solve numerically Eq. 5.64 by using a grid-based method [274] without further approximations. Note here that this is different from Ref. [202], where an approximate method was employed.

In Fig. 5.6 we plot the excited state population dynamics for a QE placed at a distance $z_0 = 5$ nm from the metal surface. For this distance, we see in Fig. 5.5 (a) that $J(\omega)$ is strongly peaked at $\omega = \omega_{sp}$. Each panel corresponds to a different value of the QE's resonance frequency, ω_0. The timescale of both panels is normalized to the modified lifetime of the emitters, $\tau = \hbar/J(\omega_0)$, such that they appear in the same scale. In panel (a), we show the dynamics of a QE with a transition frequency lying in the optical regime, $\hbar\omega_0 = 2$ eV, and for different values of the QE's intrinsic lifetime, τ_0. For $\tau_0 = 4$ ns (dotted blue line), the population of the QE decays exponentially. This corresponds to the Markov regime, where the population features an irreversible decay (see Eq. 5.28) at a rate $\Gamma = 2\pi J(\omega_0)$. Thus, by fully solving for the dynamics we recover in this case the WC regime, where, as we have already explained, the spontaneous decay rate is

solely determined by the value of $J(\omega)$ around ω_0. For $\tau_0 = 0.4$ ns (dashed red line), however, the QE dynamics exhibits a clear deviation from the exponential decay with fast oscillations in the initial times (see inset). Finally, for the shortest τ_0 considered, 0.04 ns (black solid line), the QE dynamics displays strong oscillations, before being attenuated by the metal losses. The emergence of these oscillations as τ_0 decreases, i.e., as the dipole moment increases, is a manifestation of the coherent exchange of energy between the QE and the EM field excitations present at the metal surface. In panel (b), we plot the same cases as in panel (a) but for a QE with a transition frequency closer to the peak of the spectral density, $\hbar\omega_0 = 3eV$. The dynamics exhibits, as in panel (a), a transition from irreversible to reversible dynamics with decreasing τ_0, but showing oscillations of longer period and larger amplitude. The comparison between these two panels proves that the detuning between the peak of the spectral density and the energy of the emitter is also a very relevant parameter for determining the visibility of the oscillations.

An important question to address is the possible experimental verication of the reversible dynamics predicted by our calculations. As shown in Fig. 5.6, the timescale to observe experimentally these effects depends strongly on the intrinsic lifetime, τ_0, of the chosen QE. QEs with transition frequencies lying within the optical regime such as NV centers, QDs and J-aggregates of organic molecules, feature intrinsic lifetimes around ~ 10 μs [275], 1 ns [182] and 70 ps [276], respectively. As the figure shows, oscillations in the population of QEs at $\hbar\omega_0 = 2$ eV would be best observed for $\tau_0 = 40$ ps. Even in this case, the observation of oscillations would require sub-picosecond resolution.

So far, through the numerical integration of Eq. 5.64, we have explored the emergence of reversibility in all ranges of relevant parameters: z_0, ω_0, τ_0 [4]. The configurations that favor reversible dynamics are: ω_0's closer to ω_{sp}, the regions of very small separations and the shortest τ_0, this is, the largest dipole moments. Interestingly, in this spatial region ($\omega_0 c/\sqrt{\epsilon_d} \ll z_0$), the main contribution to the spectral density does not come from the SPP contribution (SPP pole). Instead, it stems from the EM modes having an even larger parallel momentum than SPPs, i.e., EM modes that are even more evanescent in the direction perpendicular to the metal surface than SPPs. By only considering the contribution of these EM modes, and similarly to Eq. 5.57 for the decay rate, an analytical formula for the spectral density can be obtained ($k_{||} \gg \omega_0/c$):

$$\frac{J(\omega)}{\gamma_0} = \frac{3}{16\pi}\frac{1}{(k_0 z_0)^3}\mathrm{Im}\left(\frac{\epsilon(\omega_0)-\epsilon_d}{\epsilon(\omega_0)+\epsilon_d}\right). \tag{5.67}$$

[4]Note that we have explored regions of both small distances and ω_0 close to ω_{sp} that were not accessible with the approximations used in previous works

We have checked numerically that this approximation for the spectral density gives virtually the same results as those given by Eq. 5.67, provided that the distance of the QE to the metal surface is very small. This formula for the spectral density is usually known as quasistatic approximation and it has already been used in the literature to analyze the strong modification of the QE's lifetime in the presence of metal surfaces, wires or nanoparticles [179–181, 273, 277]. However, up to our knowledge, it has never used to analyze the emergence of reversible dynamics. Notice that, as we explained in Subsection 5.3.1, the region of very short distances is generally thought to only yield quenching and strong coherent effects are unexpected. In addition, by utilizing the Drude expression for $\epsilon(\omega)$, see Eq. 1.1, it is possible to write Eq. 5.67 in terms of ω_p, γ_p and ω_{sp} as,

$$\frac{J(\omega)}{\gamma_0} = \frac{3}{16\pi}\frac{1}{(k_0 z_0)^3}\frac{2\omega_{sp}^4}{\omega_p^2}\frac{\gamma\,\omega}{\gamma^2\omega^2 + (\omega^2 - \omega_{sp}^2)^2}. \tag{5.68}$$

Furthermore, $J(\omega)$ can be expanded close to the cut-off frequency, $\omega \sim \omega_{sp}$, as

$$\frac{J(\omega)}{\gamma_0} \approx \frac{3}{16\pi}\left(\frac{c}{\omega_0 z_0}\right)^3 \omega_p \left(\frac{\omega_{sp}}{\omega_p}\right)^3 \frac{\gamma/2}{(\gamma/2)^2 + (\omega - \omega_{sp})^2}, \tag{5.69}$$

which is a Lorentzian, $J_L(\omega) = \frac{g_{\text{eff}}^2}{\pi}\frac{\gamma_{\text{eff}}/2}{(\gamma_{\text{eff}}/2)^2 + (\omega - \omega_{\text{eff}})^2}$, with parameters,

$$\omega_{\text{eff}} = \omega_{sp}\,, \tag{5.70}$$

$$\gamma_{\text{eff}} = \gamma\,, \tag{5.71}$$

$$g_{\text{eff}}^2 = \gamma_0\omega_p\frac{3}{16}\left(\frac{\omega_{sp}}{\omega_p}\right)^3\left(\frac{c}{\omega_0 z_0}\right)^3. \tag{5.72}$$

The Lorentzian spectral shape of the spectral density in Eq. 5.69 allows us to integrate the kernel in Eq. 5.65, yielding

$$K(\tau) = g_{\text{eff}}^2\, e^{-\gamma_{\text{eff}}\,\tau/2} e^{i(\omega - \omega_{\text{eff}})\tau}. \tag{5.73}$$

By using Laplace transform techniques, with $K(s) = g_{\text{eff}}^2/\left[s + \gamma_{\text{eff}} - i(\omega - \omega_{\text{eff}})\right]$, an analytical solution of the integro-differential equation given by expression 5.64 can be found to be $\tilde{c}_e(s) = \left[s + K(s)\right]^{-1}$ [267]. The QE's population is then proportional e^{iRt}, with R being the Rabi frequency, which reads as

$$R = \sqrt{g_{\text{eff}}^2 - \left[\gamma_{\text{eff}} + 2i(\omega - \omega_{\text{eff}})\right]^2/16}. \tag{5.74}$$

As a consequence, for very short QE-metal distances, the dynamical evolution of the QE dictated by the general Hamiltonian turns out to be mathematically equivalent to

the solution of the following master equation:

$$\dot{\rho} = i\left[\rho, H_{\text{eff}}\right] + \frac{\hbar\gamma_{\text{eff}}}{2}\mathcal{L}_a\left[\rho\right], \tag{5.75}$$

with $\mathcal{L}_a\left[\rho\right] = 2a\rho a^\dagger - \rho a^\dagger a - a^\dagger a\rho$ being a Lindblad term [267] and H_{eff} being

$$H_{\text{eff}} = \hbar\omega_0\sigma^\dagger\sigma + \hbar\omega_{\text{eff}}a^\dagger a + \hbar g_{\text{eff}}\left[a\sigma^\dagger + \sigma a^\dagger\right]. \tag{5.76}$$

The above master equation appears in the dissipative Jaynes-Cummings model [278], which is the cornerstone of cavity QED physics. Equation 5.75 represents the mapping of the dynamics of a QE coupled to the continuum of EM modes supported by a 2D metal surface into a Jaynes-Cummings model. Hamiltonian H_{eff} describes the coherent evolution of the combined system: the QE and a *pseudo-mode* bosonic excitation of energy $\omega_{\text{eff}} = \omega_{sp}$ (represented by the a-operator), which accounts for all the EM modes of the metal surface. The coherent coupling between the QE and this pseudo-mode is given by g_{eff} through Eq. 5.72. The Lindblad term in Eq. 5.75 describes irreversible mechanisms in the dynamics through the effective losses of the pseudomode, γ_{eff}, which are solely determined by the metal properties, γ.

The physical picture that emerges from the mathematical equivalence between the initial hamiltonian and the mapping to the Jaynes-Cummings model can be extracted from the quasistatic approximation. In this limit, the interference between the QE's dipole and its image results in a divergence of the reflected field, expressed in the resonance condition $\epsilon_m(\omega) + \epsilon_d = 0$, ultimately attenuated by the plasma losses. This resonance can be seen as that supported by a dipole-image-induced effective cavity. The strongly damped resonance interacts with the QE, being able to coherently exchange energy with it. Note that in contrast to previous studies [200–202], we have identified that in this case SPPs play no role in reversibility. This can be concluded mathematically as well from the absence of SPP contribution in the spectral density of Eq. 5.67 that describes the EM field when the QE is close to the surface.

Within the Jaynes-Cummings model, it is well-established that reversibility in the dynamics appears when the coupling strength is stronger than losses ($g_{\text{eff}} \gg \gamma_{\text{eff}}$). Thus, in Fig. 5.7 we render a (z_0, τ_0)-space diagram of the parameter $g_{\text{eff}}/\gamma_{\text{eff}}$ to get a better estimation of the optimal regions for observing reversibility [5]. Shorter τ_0's and smaller z_0's [6] increase reversibility as they increase g_{eff}. A different strategy, not explored in the figure, consists of decreasing the effective losses, $\gamma_{\text{eff}} = \gamma$, that control the timescale where

[5] We have numerically checked that the pseudomode approximation holds for $z_0 \lesssim 15$ nm.

[6] Note that for $z_0 \lesssim 4$ nm non local corrections may affect the results.

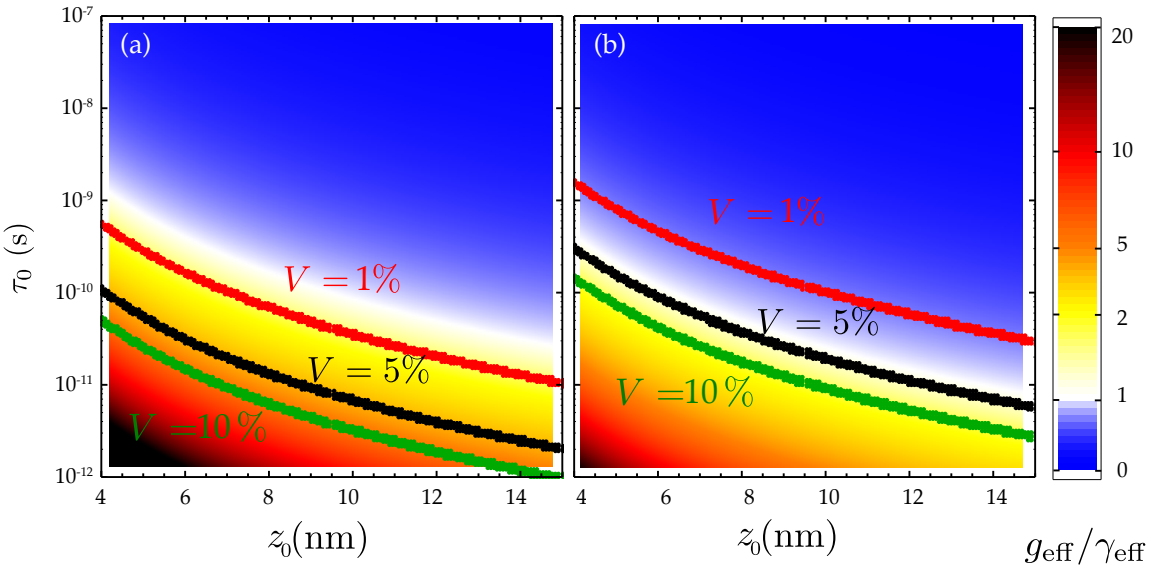

Figure 5.7: Strong and weak coupling regimes map for a QE near a metal surface. The contour plot shows the real part of the ratio $g_{\rm eff}/\gamma_{\rm eff}$ as a function of z and τ_0 for QEs of energies $\hbar\omega_0 = 2$ eV (a) and $\hbar\omega_0 = 3$ eV (b). The coloured lines highlight the lines where the visibility of the oscillations reaches 1%, 5% and 10% (red, black and green, respectively).

the oscillations get attenuated. This can be done by, e.g., lowering the temperature of the system. Finally, as we showed in the numerical results of Fig. 5.6, there is another relevant magnitude for the characterization of reversible dynamics, namely, the amplitude of the oscillations. Based on our analytical approach, we can extract an analytical formula for the visibility of the oscillations in the limit $\gamma_{\rm eff} \approx 0$,

$$V \equiv \frac{\max[n_\sigma] - \min[n_\sigma]}{\max[n_\sigma] + \min[n_\sigma]} = \frac{2g_{\rm eff}^2}{2g_{\rm eff}^2 + (\omega - \omega_{\rm eff})^2}. \tag{5.77}$$

This expression shows that there are two ways for increasing V: (i) by decreasing the effective detuning of the QE with the pseudo-mode as we showed in Figs. 5.6 (a,b); (ii) by increasing the effective coupling, as done in Fig. 5.6 by decreasing τ_0. In Fig. 5.7, we have plotted the frontiers in the phase-space diagram where $V = 1\%; 5\%$ and 10% in red, black and green, respectively. As expected from Eq. 5.77, the higher the coupling and/or the smaller the effective detuning between the modes, the better the visibility.

Moreover, the mapping of the physics to a cavity QED problem of Eq. 5.75 has also important implications when thinking of incorporating new factors that could influence the QE dynamics. For instance, the study of plasmon non-linear interaction can be done by adding simply a non-linear term, $H_{nl} = U_a(a^\dagger a)2$, in the coherent part of Eq. 5.75 whereas considering extra QE losses or pure dephasing can be done by including new

Lindblad terms, $(\gamma_\sigma/2)\mathcal{L}_\sigma[\rho]$ [218] and $(\gamma_\phi/2)\mathcal{L}_{\sigma^\dagger\sigma}[\rho]$ [279], respectively. However, note that the dynamics of the QE is dominated by the most evanescent EM modes of the continuum, and that these provide the most relevant loss mechanism, as $\gamma_p \gg \gamma_\sigma, \gamma_\phi$.

5.4 Interaction between two quantum emitters mediated by propagating surface plasmons

As we mentioned in Section 1.5, SPPs can act as mediators of the interaction between several QEs. In Ref. [190], the subwavelength light confinement in plasmonic waveguides was exploited to enhance the coupling between two distant QEs via the SPP modes propagating along the waveguides. This plasmon-mediated interaction enables an efficient coupling between the QEs at distances larger than the involved free-space wavelength, which results in the emergence of collective super- and subradiant states with modified emission rates [191]. In addition, this efficient long-range interaction mediated by SPPs can be exploited even to obtain entanglement between two QEs [192].

Motivated by this background, in this Section we consider graphene as a plasmonic media that is able to mediate the coupling between two QE. Compared to previous studies, where the plasmon-mediated interaction between two QEs was considered for SPPs in metal structures [190], the efficient and tunable coupling of an individual QE to the SPP modes propagating in a graphene sheet makes this 2D material a very interesting system for the controlled coupling between two QEs. As we have shown in Section 5.3.1, a QE placed within the appropriate distance range from a graphene sheet couples very efficiently to the SPP modes that propagate through the sheet due to the sub-diffraction limited confinement associated with SPPs. Here we aim to enhance the coupling between two QEs located near a graphene layer. In order to have graphene SPP modes with long enough propagation lengths, we work in the THz regime.

This Section is organized as follows. First, in Subsection 5.4.1, we introduce the total normalized decay factor, γ, which can be determined from the Green's function of the problem and characterizes the collective interaction of the two QEs. Next, in Subsection 5.4.2 we study the interaction between two QEs mediated by the SPPs of a 2D graphene sheet. The presence of graphene SPPs leads to interesting phenomena, such as the super- and subradiant regimes, where the radiation properties of several QEs are enhanced or suppressed. We analyze the evolution of γ with the vertical distance between the QEs and the sheet in a transmission configuration and with the in-plane distance between the emitters in a reflection configuration, as well as its tunability by means of the chem-

ical potential. Finally, we consider the coupling of two QE in 1D graphene ribbons in Subsection 5.4.3. We show that confinement in the 1D case leads to longer interaction ranges between the QEs and we study how the coupling between the QEs is affected by the presence of the ribbon's edges.

5.4.1 Interaction between two quantum emitters in inhomogeneous environments

We start by briefly presenting an extension of the theoretical formalism described in Section 5.2 to include several QEs. In order to treat the interaction among N QEs in the presence of a plasmonic media, the Hamiltonian derived within the macroscopic QED framework (Eq. 5.15) can be generalized as follows,

$$H = \sum_{i=1}^{N} \hbar\omega_i \sigma_i^\dagger \sigma_i + \sum_\lambda \int \mathrm{d}^3\mathbf{r} \int_0^\infty \mathrm{d}\omega\, \hbar\omega\, \mathbf{f}_\lambda^\dagger(\mathbf{r},\omega)\cdot\mathbf{f}_\lambda(\mathbf{r},\omega) - \sum_{i=1}^{N}\left[\sigma_i^\dagger \boldsymbol{\mu}_i\cdot\mathbf{E}^{(+)}(\mathbf{r_0}) + \sigma_i \mathbf{E}^{(-)}(\mathbf{r_0})\cdot\boldsymbol{\mu}_i\right]. \tag{5.78}$$

The above Hamiltonian, together with a master equation, determine the evolution of the overall system (see Ref. [280]). Since we are interested in a regime in which the EM modes supported by the plasmonic media act solely as mediators of the interaction between the QEs, it is appropriate to work under the Markov approximation, i.e., under the approximation that the coupling between the QEs and the EM field is weak. Thereby, the spontaneous emission of each QE can be found to be determined by contributions arising from all the QEs through the quantities [280],

$$\Gamma_{ij} = \frac{2\omega^2}{\pi\hbar\epsilon_0 c^2}\left[\boldsymbol{\mu}_i\cdot\mathrm{Im}\left\{\hat{\mathbf{G}}(\mathbf{r}_i,\mathbf{r}_j,\omega)\right\}\cdot\boldsymbol{\mu}_j\right], \tag{5.79}$$

where the Green's function $\hat{\mathbf{G}}(\mathbf{r}_i,\mathbf{r}_j,\omega)$ yields the field at point $\mathbf{r}_i$ generated by the QE at $\mathbf{r}_j$. Thus, the spontaneous decay of each QE has contributions arising from its own local field ($i=j$) as well as from the rest of the QEs ($i\neq j$). In the above expression, the term $i=j$ yields to $\Gamma_{ii}=\Gamma$, the spontaneous decay rate given by Eq. 5.29. On the other hand, terms with $i\neq j$ correspond to the contribution to the decay rate of the QE at $\mathbf{r}_i$ with frequency ω_i and dipole moment $\boldsymbol{\mu}_i$ due to the presence of a QE at $\mathbf{r}_j$ and with ω_j and $\boldsymbol{\mu}_j$. Similarly to the expression for the spontaneous decay rate of a single QE, the above equation states that the contribution to the decay rate of a QE due to the presence of other QEs depends on the relative orientation of the QEs' dipole moments,

their oscillation frequency and the imaginary part of the Green's dyadic of the system, which is proportional to the local density of states. Hence, the interaction between QEs is affected by the properties of the environment surrounding them.

Let us now consider the case of two QEs. In order to study their interaction, we introduce the normalized decay factor γ, which characterizes the collective emission of the system composed by the two QEs. This quantity is defined as the ratio of the total decay rate of a system where the two QEs interact through a plasmonic media to the decay rate of two uncoupled QEs though still in the presence of the media. Thus, it accounts for the modification of the collective decay rate due to the presence of the second QE, and reads as

$$\gamma = \frac{\Gamma_{11} + \Gamma_{12} + \Gamma_{21} + \Gamma_{22}}{\Gamma_{11} + \Gamma_{22}}. \tag{5.80}$$

The value of γ distinguishes two regimes: When $\gamma > 1$ the interaction is enhanced due to the presence of the plasmonic medium and the system is said to be superradiant. Correspondingly, when $\gamma < 1$, there is an inhibition of the interaction between the QEs and the system is subradiant. In the following we use factor γ to characterize the interaction between two QEs close to a graphene layer. In particular, we study how the collective interaction between the two emitters can be mediated by the SPPs modes propagating along graphene layers and ribbons.

5.4.2 Interaction between two quantum emitters mediated by SPPs in 2D graphene sheets

Here we study the interaction between two QEs mediated by the SPPs propagating along a 2D graphene sheet. We consider two identical QEs (same resonance frequency, ω_0 and modulus of the dipole moment, $|\boldsymbol{\mu}|$) in the vicinity of a graphene sheet that lies in the $x-y$ plane. The position of each QE, $i = 1, 2$, is $\mathbf{r}_i = (\mathbf{r}_{\parallel,i}, z_i)$, and the in-plane distance between both QEs is $r = |\mathbf{r}_{\parallel,1} - \mathbf{r}_{\parallel,2}|$. Due to its 2D character, graphene allows for two different configurations of the QEs: interaction in reflection (both QEs at the same side of the graphene layer) or in transmission (QEs placed at opposite sides). To characterize the interaction, we study the dependence of the factor γ as given by Eq. 5.80 with the vertical distance from the sheet (z) and with the in-plane distance between the emitters (r).

Let us first consider two QEs interacting through the graphene sheet placed at opposite sides of the sheet, i.e., in the transmission configuration (see the diagram in Fig. 5.8). In order to study the behaviour of their interaction with the distance to the sheet, we locate

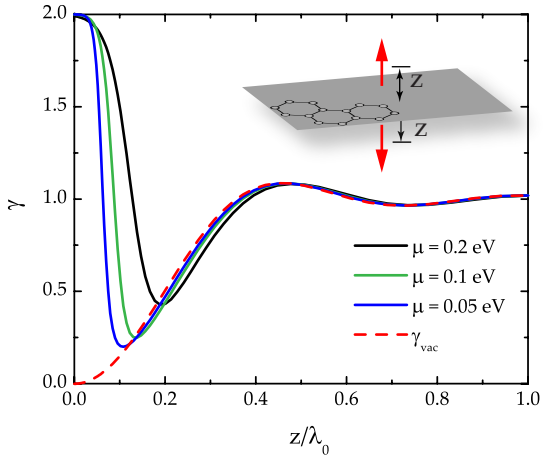

Figure 5.8: Super- ($\gamma > 1$) and subradiance ($\gamma < 1$) between two QEs mediated by a graphene sheet when the they interact in transmission through the sheet. γ is plotted as a function of the normalized vertical distance of the QEs to the graphene sheet for three values of the chemical potential, μ. The dipole moments are perpendicular to the sheet and antiparallel. The red dashed line shows the vacuum interaction γ_{vac}.

the QEs at the same z ($|z_1| = |z_2|$) and at $r = 0$. We assume the dipole moments to be of the same modulus, perpendicular to the sheet and antiparallel, $\boldsymbol{\mu}_1 = -\boldsymbol{\mu}_2 = |\boldsymbol{\mu}|\hat{u}_z$. The collective decay factor, reduces in this case to

$$\gamma = 1 + \frac{\Gamma_{12}^T}{\Gamma_{11}}, \tag{5.81}$$

where the decay rate related to the interaction between the QEs, Γ_{12}^T/γ_0, is given by the Green's function in transmission (see Appendix C). Following Eq. C.34, we can write $\hat{\mathbf{G}}^p(r, z, \omega_0)$ in terms of the transmission coefficient, $t(q)$. This procedure allows us to write the normalized decay rate as

$$\frac{\Gamma_{12}^T}{\gamma_0} = -\frac{3}{2}\mathrm{Re}\left[\int_0^\infty \mathrm{d}q \frac{q^3}{q_z} t(q) e^{2ik_0 q_z z}\right], \tag{5.82}$$

where the minus sign comes from the fact that the dipole moments are antiparallel. The transmission coefficient of the graphene layer is $t(q) = 1/(\alpha q_z + 1)$, with $\alpha = 2\pi\sigma/c$. The γ factor as a function of the normalized distance, z/λ_0, and for three values of the chemical potential $\mu = 0.2$, 0.1, 0.05 eV, is plotted in Fig. 5.8 for the same parameters used in the study of the decay rate and $\beta_{\text{G-SPP}}$ in Fig. 5.4. For comparison, the red dashed line shows γ when the QEs are placed in free space and interact only through

radiative modes, labeled as γ_{vac}. For $z \ll \lambda_0$, $\gamma_{\text{vac}} = 0$ because the opposite phase of the dipole moments inhibits the radiation, and when z increases γ_{vac} oscillates around 1 with λ_0. When the graphene sheet is present, the interaction between the emitters is strongly modified at a subwavelength scale. In the limit of large z, in correspondence with the distances where $\beta \sim 0$ in Fig. 5.4 (b), the emitters couple via radiative modes and γ approaches γ_{vac}. On the other hand, in the range of distances where the plasmonic coupling between the emitters starts to dominate, $\beta \neq 0$, γ deviates from γ_{vac} and the system turns from subradiant to superradiant. For each value of μ (0.2, 0.1 and 0.05 eV), the value of z/λ_0 where β starts to grow from 0 to 1 is the onset of the separation between γ and γ_{vac}. This means that superradiance is due to the interaction being mediated by graphene SPPs. Thus, the superradiant regime, which is controlled by high coupling to SPPs, can be tuned by means of the chemical potential. In the limit $z \ll \lambda_0$, where $\beta = 0$ and non-radiative channels dominate the decay of each QE, the interaction reaches $\gamma = 2$, in contrast to the free-space value in this limit, $\gamma_{\text{vac}} = 0$. The reason why the system turns from subradiant to superradiant when non-radiative modes dominate the interaction is a phase shift provided by the graphene sheet. For $z \ll \lambda_0$, the contribution from modes outside the light line ($q_z = i|q_z|$) dominates the integrals for Γ_{11} (Eq. 5.50) and Γ_{12}^T (Eq. 5.82). While Γ_{11} is controlled by $-\text{Im}\,[r(q)]$, Γ_{12}^T is controlled by $-\text{Im}\,[t(q)]$. Since $t = 1 + r$, the imaginary part of r and t is the same and $\Gamma_{11} = \Gamma_{12}^T$, leading to $\gamma = 2$ in Eq. 5.81.

Let us now study how the interaction evolves with the in-plane distance between the QEs, r. We take two emitters interacting through the graphene sheet in the reflection configuration, as sketched in Fig. 5.9. In this case we place both of them at the same distance z from the sheet, separated by r, and with dipole moments of the same magnitude, parallel and pointing in the vertical direction, $\boldsymbol{\mu}_1 = \boldsymbol{\mu}_2 = |\boldsymbol{\mu}|\hat{u}_z$. In order to determine the γ factor, which in this case reads as

$$\gamma = 1 + \frac{\Gamma_{12}^R}{\Gamma_{11}}, \tag{5.83}$$

we need the interaction decay rate in reflection, Γ_{12}^R. As shown in Appendix C, this is a sum over the free-space and reflected contributions with an in-plane dependence given by the zeroth-order Bessel function, J_0. From Eq. C.32 we have

$$\frac{\Gamma_{12}^R}{\gamma_0} = \frac{3}{2}\text{Re}\left[\int_0^\infty \text{d}q \frac{q^3}{q_z} J_0(k_0 q r)\left[1 - r_p(q) e^{2ik_0 q_z z}\right]\right]. \tag{5.84}$$

The γ factor as a function of the normalized distance, r/λ_0 is plotted in Fig. 5.9 (a) at $\nu = 2.4$ THz and $\mu = 0.2$ eV when the QEs are at three different separations to the sheet:

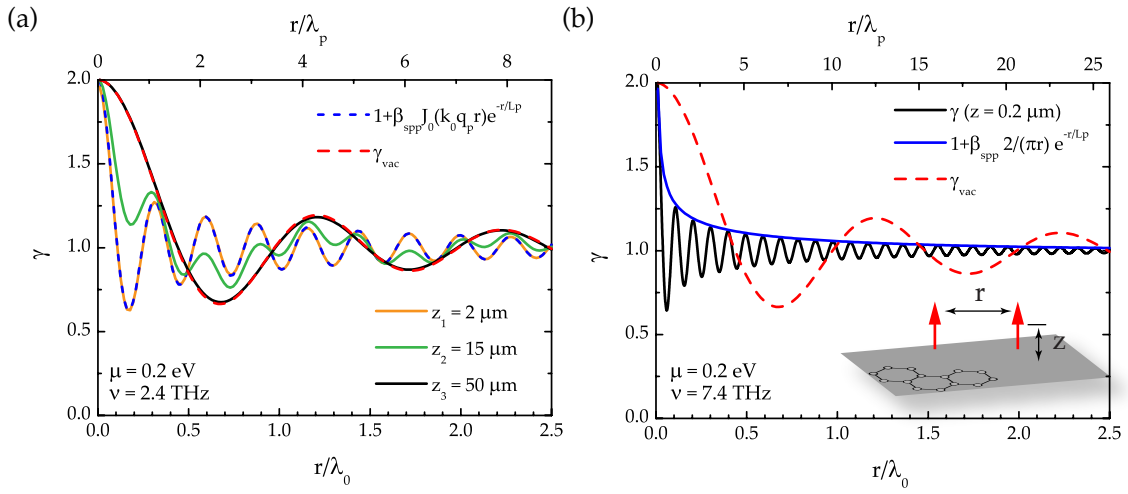

Figure 5.9: Tuning super- and subradiance: γ factor as a function of the in-plane distance r between two QEs in the reflection configuration for two different frequencies. (a) At $\nu = 2.4$ THz, when the QEs are placed at $z_1 = 2\ \mu m$ ($\beta = 0.98$, $\Gamma/\gamma_0 = 105$), $z_2 = 15\ \mu m$ ($\beta = 0.55$, $\Gamma/\gamma_0 = 2$) and $z_3 = 50\ \mu m$ ($\beta = 0.01$, $\Gamma/\gamma_0 = 0.92$). The free-space wavelength is $\lambda_0 = 124$ μm, the plasmon wavelength $\lambda_p = \lambda_0/3.5$ and the propagation length $L_p = 14.9\lambda_p$. The dashed black line corresponds to the free-space interaction and the dashed gray line to Eq. 5.85 for high β. (b) At $\nu = 7.4$ THz, when the QEs are at $z = 0.2\ \mu m$, with $\beta = 0.98$ and $\Gamma_{11}/\gamma_0 = 2250$. The free-space wavelength is $\lambda_0 = 41\ \mu m$, the plasmon wavelength is $\lambda_p = \lambda_0/10$ and the propagation length is $L_p = 20\lambda_p$. The dashed black line shows the free-space γ and the gray line the decay of the interaction.

z_1, z_2, and z_3. First, for $z_1 = 2$ μm, we know from Fig. 5.4 that the coupling to SPPs propagating along the graphene sheet is very efficient, $\beta = 0.98$, and $\Gamma/\gamma_0 \sim 10^2$. In this situation, the interaction between the two QEs is mediated by SPPs, and, consequently, the length scale of the interaction is controlled by the SPP modal wavelength, $\lambda_p = \lambda_0/q_p$, which in this case is $\lambda_p = \lambda_0/3.5$, as opposed to the free-space interaction, dominated by λ_0 (red dashed line). Note that both length scales, r/λ_0 and r/λ_p, are shown in the figure. When $\beta \approx 1$, an analytical expression for γ can be obtained in the pole approximation:

$$\gamma = 1 + \beta J_0(k_0 q_p r) e^{-r/L_p}, \tag{5.85}$$

with q_p being the SPP modal wave vector (Eq. 1.18) and $L_p = \lambda_0/[2\pi \mathrm{Im}(q_p)]$ being the propagation length of the SPP, which is equal to $14.9\lambda_p$ in this case. As can be seen in the plot, this analytical approximation (blue dashed line) coincides with the exact calculation of γ (orange line). Since the propagation length is large enough, the decay length of the interaction is then given by the Bessel function, that decays as $\sqrt{2/(\pi r)}$.

This is a dimensionality factor, coming from the fact that the 3D interaction in free space is confined to the 2D graphene sheet. When the distance to the graphene sheet is increased, β decreases and γ deviates from the analytical expression. For $z_2 = 15$ μm the β factor is 0.55 and the shape of γ (green line) reflects the fact that the QE decays both to SPPs and radiatively. Finally, when the distance to the sheet is large enough to have $\beta \approx 0$, such as $z_3 = 50$ μm, the vacuum interaction is recovered (see black line). Therefore, our results show that a larger interaction length scale and a modification of the super- and subradiant regimes can be achieved in a subwavelength scale for the appropriate choice of parameters.

In addition, the tunability of graphene allows us to reach a regime where the interaction between the two QEs can be controlled at very deep subwavelength scales. Although the tuning can also be done via the chemical potential, μ, here we show a situation where the tuning parameter is the frequency. When the two QEs interact in reflection [see Fig. 5.9 (b)] at 7.4 THz and $\mu = 0.2$ eV, γ (black line) is very different from the one corresponding to the free-space situation (red dashed line). Increasing the frequency while maintaining the chemical potential results in a larger momentum for the SPP, q_p, which leads to a tighter confinement as well as a reduction in the propagation length. Thus, the interaction varies in a $\lambda_p = \lambda_0/10$ scale, as opposed to the free-space interaction, dominated by λ_0. The decay of the γ factor (blue line) is given by the square-root decay characteristic of 2D interactions for distances shorter than the propagation length, which in this case is $L_p = 1.85\lambda_0$ ($19.2\lambda_p$). For larger distances, losses start to dominate and the interaction decays exponentially, according to Eq. 5.85.

5.4.3 Interaction between two quantum emitters mediated by SPPs in 1D graphene ribbons

Further confining SPPs in 1D waveguides provides a platform for long distance interaction between two QEs. Here we consider the coupling between two QEs mediated by the SPPs propagating along 1D graphene ribbons. Compared to the SPPs propagating in a 2D graphene sheet at the same frequency (keeping the same chemical potential, $\mu = 0.2$ eV, and temperature, $T = 300$K), the ribbon-SPPs have a higher q vector, thereby being more tightly confined to the graphene layer. On the other hand, while the coupling of two QEs mediated by 2D graphene SPPs is dominated by the dimensionality factor, $e^{-r/L_p}/\sqrt{r}$ (see Fig. 5.9), in the case of 1D graphene SPPs the coupling is expected to decay as e^{-x/L_p}. This feature enables long range interaction between the QEs provided L_p is long enough. Indeed, when $\beta \approx 1$, the following analytical expression can be written

for γ:

$$\gamma = 1 + \beta e^{-x/L_p}. \tag{5.86}$$

Let us consider a free-standing graphene ribbon of width Δ at $|y| < \Delta/2$, placed at $z = 0$ with its axis along the x direction (see Fig. 5.10). We take $\nu = 2.4$ THz and the fundamental mode of a ribbon of width $\Delta = 5$ μm, that originates from the hybridization of two edge modes and has even parity of E_z with respect to the ribbon axis [281]. The field profile of the fundamental mode, obtained by means of FEM calculations [219], is shown for two situations, where the QE is placed at distances, $z = 3.12$ μm and $z = 12.4$ μm, as shown in Fig. 5.10 (a,b). For a distance to the ribbon of 3.12 μm, i.e. $\lambda_0/40$, $\beta \approx 1$, the SPP mode is excited with a very high efficiency and its field pattern is clearly seen in panel (a). On the other hand, when the QE is not sufficiently close to the ribbon, $\beta \ll 1$ and it couples mostly to radiation, as can be seen in panel (b) for a QE at $z = \lambda_0/10$ where the field snapshot virtually coincides with an spherical wave. For the case with $\beta \approx 1$, Fig. 5.10 (d) shows γ (blue line) for two QEs interacting in reflection through the ribbon-SPP, as sketched in panel (c). Similar to the 2D SPP, a subwavelength modification of the interaction can be achieved. However, since the SPP propagating along the graphene ribbon is much more confined ($\lambda_p = \lambda_0/6.1$), this modification can be achieved in a shorter length scale. Moreover, propagation in 1D allows for a longer interaction range, with an exponential decay given by a propagation length $L_p = 20\lambda_p$. Our results demonstrate that graphene ribbons can be used to control the length scale of the interaction between two QEs thanks to the efficient excitation of SPPs.

Finally, we study the transition across the transverse dimension the ribbon, i.e., how the coupling between the two QEs is affected by the presence of edges (see Fig. 5.11). For this purpose, we consider the evolution of the interaction in the reflection configuration, the same as in Fig. 5.10 (c), and also plot the evolution of $\gamma(x)$ as a function of the lateral distance from the center of the ribbon [see Fig. 5.11 (a)]. Note here that the edge's microscopic geometry (zigzag or armchair) is unimportant since the width of the ribbons considered is larger than 20 nm [282]. As sketched in the inset panel, we displace both QEs simultaneously and perpendicularly to the ribbon axis (along y), from the ribbon's center $y = 0$ and passing through the ribbon's edge at $y = \Delta/2$, up to $y = 2\Delta$. As the figure shows, $\gamma(x)$ evolves from reflecting a high coupling to SPPs at $y = 0$, to following the free-space interaction at $y = 2\Delta$, i.e., β goes from ≈ 1 to ≈ 0 in a length scale of the order of 2Δ. Additionally, we also study the evolution of the interaction between two QEs with opposite dipole moments in the transmission configuration for

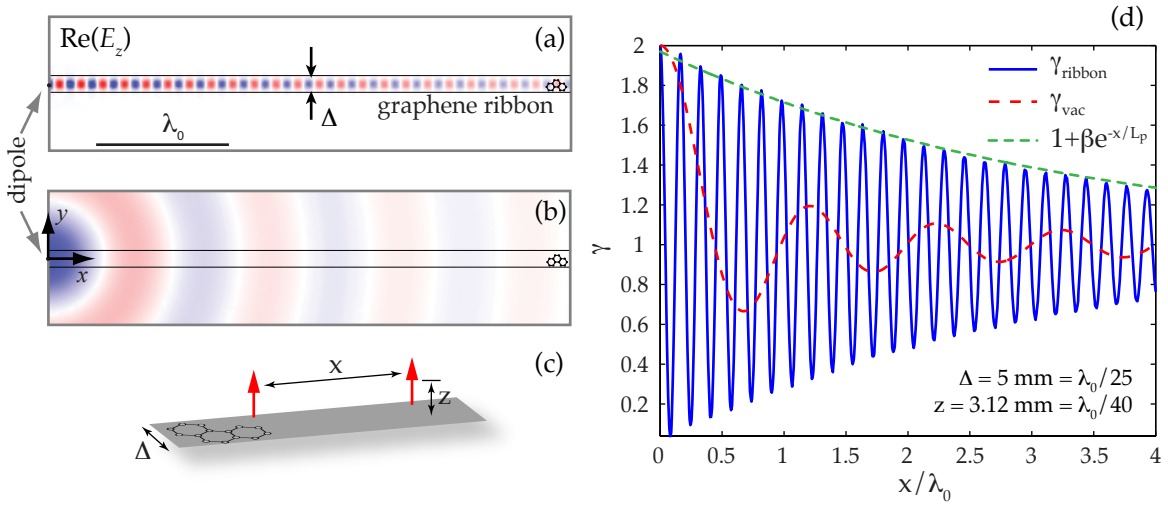

Figure 5.10: Interaction mediated by graphene ribbons. (a,b) Electric field profile for an emitter decaying to the ribbon-SPP. The dipole is placed at $x = 0$, $y = 0$ and $z = \lambda_0/40$ in panel (a) and at $z = \lambda_0/10$ in panel (c) (the same would be obtained for $z > \lambda_0/10$). (c) Sketch showing two emitters separated by x placed at a distance z on top of a graphene ribbon of width Δ. (d) Super-radiance mediated by the ribbon-SPP mode shown in panel (a). The green line shows the exponential decay of the interaction and the red line shows the free space interaction.

two situations. We plot γ at $x = 0$ as a function of y in Fig. 5.11 (b). First, we displace the QEs simultaneously such that both of them are at the same y [see sketch (1)]. At $y = 0$, the emitters couple to the ribbon-SPP and the system is in a superradiant state (red line), as opposed to the situation in free space, that is subradiant (inset panel, red line). When the QEs are displaced from the ribbon's center, but are still on top of the ribbon, i.e. $|y| < \Delta/2$, γ is only slightly modified. Once the QEs pass the ribbon's edge, the coupling to the 1D SPP is reduced, and therefore γ decreases. Subradiance is quickly reached, approaching the free-space value, $\gamma = 0$, which is achieved when the QEs are placed at a distance 2Δ from the ribbon's center. In the second situation, one QE is kept at the ribbon's center and the other is displaced perpendicularly to the ribbon's axis [see sketch (2)]. In this case, the system is always superradiant for the distances considered: γ starts at 2 and approaches 1, while in free space γ is of the order of 0.05 at $y = \Delta$ (blue line in the inset panel). The reason for this lies on the fact that the QE whose position is fixed always couples to the SPP. Remarkably, with only one QE efficiently coupled to the ribbon-SPP, the interaction between both QE is very different to the vacuum case. Our results for both configurations (reflection and transmission) demonstrate that the

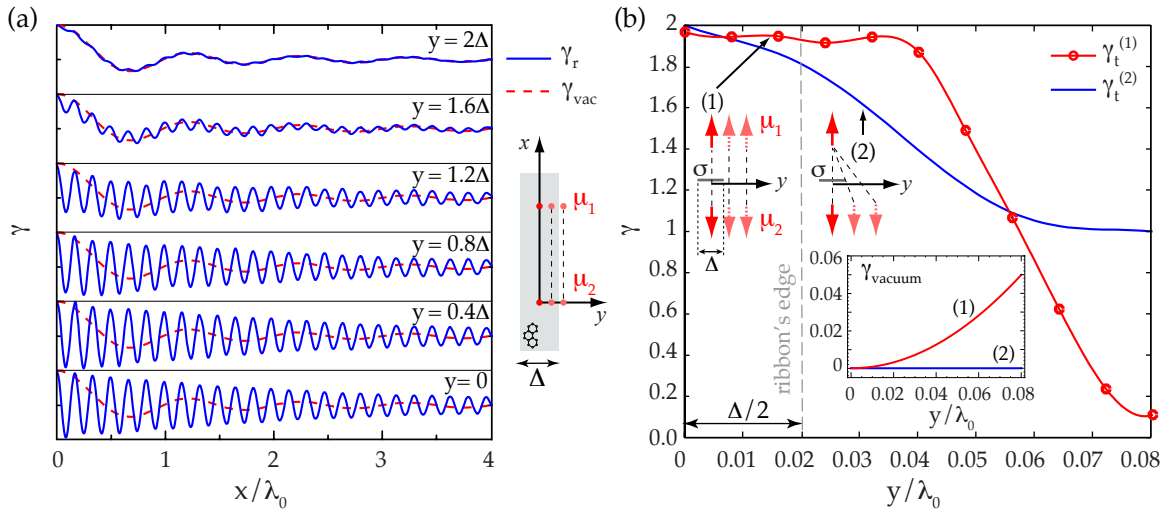

Figure 5.11: Dependence of the coupling between two QEs in graphene ribbons on the lateral separation from the center of the ribbon, $y = 0$. (a) γ factor between two QEs in the reflection configuration as a function of x for several lateral separations from the center of the ribbon (blue lines). The scale in each sub-panel is between 0 and 2. The red line shows the corresponding interaction in vacuum. The inset panel shows a top view of the structure. (b) γ factor as a function of the lateral separation y in the transmission configuration for two cases. First (red line), γ factor when the two QEs are displaced simultaneously, as shown in sketch (1). The dots correspond to numerical simulations and the continuous line is a guide-to-the-eye. Second (blue line), γ factor (from simulations) when the upper QE is fixed at the center of the ribbon and the lower is displaced, as shown in sketch (2). The inset panel shows the corresponding interaction when the QEs are placed in vacuum.

coupling between QEs mediated by the SPPs propagating along 1D graphene ribbons is very insensitive to the lateral displacement and that the effective lateral extension of these SPPs is of the order of $\Delta/2$ measured from the edge's ribbon.

5.5 Strong coupling between an ensemble of quantum emitters and propagating surface plasmons

Reversibility in the dynamics of a single QE coupled to the EM modes of a metal surface (or thin film), as we discussed in Subsection 5.3.2, has not yet been observed in an experiment. In contrast, several experimental studies have shown the emergence of SC, i.e., coherent energy exchange between propagating SPPs and a large number of excitons either in organic molecules [204–209, 211, 216] or in QDs and quantum

wells [212–215]. In this Section we focus on the study of this phenomenon and present its theoretical foundation. For that purpose, we develop a complete quantum treatment that accounts for the coherent coupling between the QEs and SPPs and incorporates the presence of dissipation and dephasing. Our formalism is able to reveal the key physical mechanisms that explain the reported phenomenology and also to determine the physical parameters that optimize the strong coupling. While a semiclassical treatment is also able to reproduce the reported phenomenology (see Section 5.7), our quantum model can deal with more complex aspects as photon statistics, which enables a discussion regarding the classical or quantum nature of this phenomenon.

The Section is organized as follows. We first derive a Hamiltonian for the coherent QEs-SPPs interaction in Subsection 5.5.1. Next, by means of an open quantum system approach, we use a master equation formalism (Subsection 5.5.2) to incorporate dissipation in the metal and internal degrees of freedom within the QEs (*dephasing*) as incoherent decay channels whose effect is to modify the QEs' lifetime. Finally, in Subsection 5.5.3 we study saturation effects and the photon statistics of the system, reporting the conditions needed for the observation of quantum statistics.

5.5.1 Hamiltonian formalism

In the following we develop a full quantum treatment of the QEs-SPPs coupled system that allows us not only to reproduce the reported phenomenology but also to deal with the photon statistics. Our model reproduces the main features of the experimental conditions reported in Refs. [204–208, 211–216]. A sketch of the general structure that mimics the usual experimental configuration can be seen in Fig. 5.12 (a). A collection of N QEs is embedded into a dielectric layer of thickness $\mathcal{W}$, which is placed on top of a thin metal film (thickness h). A second dielectric film below the metal allows for laser excitation of SPPs propagating along the metal/dielectric interface. In some of the experimental setups and in order to avoid quenching of the QEs, a dielectric spacer of width s is located between the QEs and the metal substrate. In the calculations presented in this Thesis, we take $\epsilon_2 = \epsilon_1 = 1$ and we use the dielectric function of the metal (silver), ϵ_m, as tabulated in Ref. [14]. As a minor simplification, we assume a semi-infinite metal substrate instead of the metal film considered in the experiments (these films are thick enough for the SPPs to be very similar to those of a single interface).

As we have already discussed, a QE placed in the vicinity of a metal surface interacts with three different channels: (i) excitation of SPPs that propagate along the metal surface, (ii) radiation of photons into the far field and (iii) dissipation through ohmic

losses in the metal. In Section 5.3 we studied how an individual QE couples to modes at all the $\mathbf{k}$ vectors available in the plasmonic system. We showed that at optical frequencies and intermediate distances between the QE and the metal surface, the effect of the plasmonic media can be treated under the Markov approximation, where the QE's population features an exponential decay at a modified rate given by the density of states at the QE's transition frequency (Subsection 5.3.1). On the other hand, if the QE is placed at very short distances from the metal surface, the effect of high frequencies where absorption is large is very important and may even lead to reversible oscillations in the dynamics of the QE's population (Subsection 5.3.2). Different from this case, in the situation considered in this Section, the collective coupling to the propagating SPP imposes conservation of the $\mathbf{k}$ vector, which prevents the QEs from interacting with high frequency regions of large absorption, as we will see below. Moreover, at the distances and frequencies reported in the experiments, the QE's emission is dominated by coupling to SPPs (see Fig. 5.2). These two features allow us to treat the coupling between the QEs and the SPPs as a coherent channel while dissipation is handled as a perturbation. Since we deal with losses separately, we will rely on a quantization procedure for the EM field in the absence of absorption and use Hamiltonian 5.9 to treat the QE-SPP interaction.

We start by deriving the Hamiltonian that describes the coherent interaction between N QEs and the SPPs confined to the 2D metal/dielectric interface. First, we consider the case of a single QE. As we showed in Subsection 5.2.1, the Hamiltonian is composed of three terms: the QEs free-energy, the SPP field and their interaction. From Eq. 5.9, we can write [7]

$$H = \hbar\omega_0\sigma^\dagger\sigma + \sum_{\mathbf{k}} \hbar\omega(\mathbf{k}) a_{\mathbf{k}}^\dagger a_{\mathbf{k}} + \sum_{\mathbf{k}} \frac{\hbar g_{\boldsymbol{\mu}}(\mathbf{k}, z_0)}{\sqrt{A}} \left(a_{\mathbf{k}}\sigma^\dagger e^{i\mathbf{k}\cdot\mathbf{R}_0} + a_{\mathbf{k}}^\dagger \sigma e^{-i\mathbf{k}\cdot\mathbf{R}_0}\right), \tag{5.87}$$

where $\mathbf{k}$ stands for the parallel momentum and σ ($\sigma^\dagger$) describe the lowering (raising) operators of the QE, located at $(\mathbf{R}_0, z_0)$. The QE has resonance frequency ω_0 and dipole moment $\boldsymbol{\mu}$, that relates to its spontaneous decay rate via Eq. 5.33, $\gamma_0 = \omega_0^3\mu^2/(3\pi\epsilon_0 c^3)$. In addition, $a_{\mathbf{k}}$ and $a_{\mathbf{k}}^\dagger$ are the destruction and creation operators for the SPPs propagating along the 2D metal/dielectric interface characterized by permitivities ϵ_m/ϵ_d. Finally, and different from Eq. 5.9, in the interaction term we have explicitly written the quantization area factor, $1/\sqrt{A}$, and the in-plane dependence of the coupling, $e^{i\mathbf{k}\cdot\mathbf{R}_0}$.

Operators $a_{\mathbf{k}}$ and $a_{\mathbf{k}}^\dagger$ in Hamiltonian 5.87 correspond to a canonical quantization procedure in the absence of losses. Equivalently to Eq. 5.3 for the free space electric field,

[7] Recall that this Hamiltonian is written within the dipolar and rotating wave approximations.

the quantized SPP field at point $\mathbf{r} = (\mathbf{R}, z)$ can be written as [283, 284]

$$\mathbf{E}(\mathbf{r}) = \sum_{\mathbf{k}} \sqrt{\frac{\hbar\omega(\mathbf{k})}{2\epsilon_0 A}} \mathbf{u}_{\mathbf{k}}(z) \left[a_{\mathbf{k}} e^{i\mathbf{k}\cdot\mathbf{R}} + a^{\dagger}{}_{\mathbf{k}} e^{-i\mathbf{k}\cdot\mathbf{R}} \right], \tag{5.88}$$

where the in-plane momentum $\mathbf{k}$ and energy ω are linked by the dispersion relation $k^2(\omega)(\epsilon_m + \epsilon_d) = \epsilon_m \epsilon_d \omega^2/c^2$, with $k = |\mathbf{k}|$. The polarization vector, $\mathbf{u}_{\mathbf{k}}(z)$, is given by:

$$\mathbf{u}_{\mathbf{k}}(z) = \frac{1}{\sqrt{L(\mathbf{k})}} e^{-k_z z} \left(\hat{u}_{\mathbf{k}} + i \frac{|\mathbf{k}|}{k_z} \hat{u}_z \right), \tag{5.89}$$

where $\hat{u}_z$ ($\hat{u}_{\mathbf{k}}$) is the unit vector in the z (in-plane) direction and k_z is the vertical component of the momentum in the dielectric medium, $k_z = \sqrt{k^2 - \epsilon_d k_0^2}$, with $k_0 = \omega/c$. In addition, $L[\mathbf{k}(\omega)]$ is the "effective length" of the mode, that is chosen so that the EM energy of the mode is normalized [284]:

$$L[\mathbf{k}(\omega)] = \frac{\pi}{2} \frac{\epsilon_m(\omega) - \epsilon_d}{\sqrt{\epsilon_d \epsilon_m(\omega)} |\mathbf{k}(\omega)|} \left[\epsilon_m(\omega) + \epsilon_d \left(1 + \omega \frac{d\epsilon_m(\omega)}{d\omega} \right) \right]. \tag{5.90}$$

Finally, we can write an explicit expression for the coupling constant of the dipolar interaction between a given QE and the SPP field, $g_{\boldsymbol{\mu}}(\mathbf{k}; z)$. Following Eq. 5.7 and using the expression for the quantized SPP field, the coupling strength reads as

$$g_{\boldsymbol{\mu}}(\mathbf{k}; z) = \sqrt{\frac{\omega(\mathbf{k})}{2\epsilon_0 L(\mathbf{k})}} e^{-k_z z} \boldsymbol{\mu} \cdot (\hat{u}_{\mathbf{k}} + i \frac{|\mathbf{k}|}{k_z} \hat{u}_z). \tag{5.91}$$

The dependence of $g_{\boldsymbol{\mu}}$ with z is dictated by the decay length of the SPP in the z-direction via the value of k_z. In Fig. 5.12 (b), we render the evolution of $g_{\boldsymbol{\mu}}(\mathbf{k}; z)$ with frequency for two possible orientations of the dipole: parallel to the momentum $\mathbf{k}$ and perpendicular to the metal surface. In both cases, the couplings are evaluated for QEs at $z_0 = 20$ nm and with $h\gamma_0 = 0.1$meV, which corresponds to a lifetime of $\tau_0 = 40$ ps, close to the reported value of 70 ps [276] for the J-aggregates used as QEs in some of the experiments [204, 206, 207]. As shown in Fig. 5.12 (b), the coupling constant between the QE and the SPP mode is larger for the perpendicular orientation, as k_z is always smaller than $|\mathbf{k}|$. By comparing the coupling constant to the β factor for a QE coupled to the SPPs supported by a metal surface given in Fig. 5.3, we see that β is also larger for the perpendicular orientation of the dipole moment. On the other hand, note that $g_{\boldsymbol{\mu}}(\mathbf{k}; z)$ is maximum at $z = 0$ [see Eq. 5.91] and not where β peaks. The reason for this is that we have not included losses when writing Hamiltonian 5.87 while the β factor reflects the fact that lossy modes at high wavevectors are available for the emitter to couple for very small distances to the metal surface.

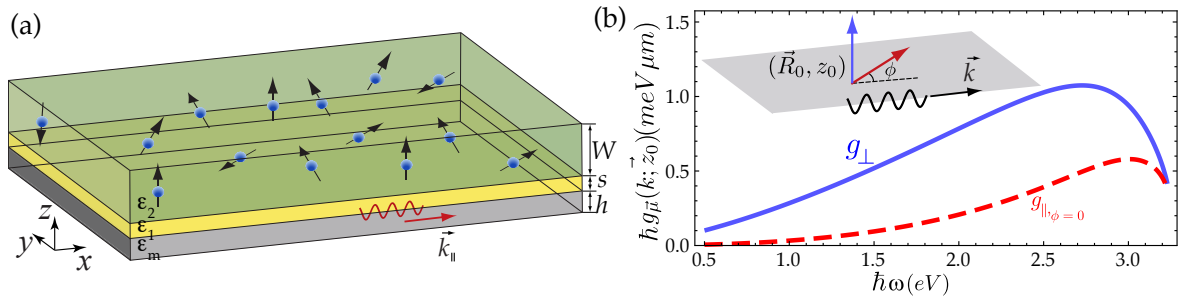

Figure 5.12: Strong coupling between a collection of emitters and SPPs. (a) Schematic picture of the N QEs distributed in a volume of width $\mathcal{W}$ separated by a distance s from a metal film of thickness h. (b) Coupling constant $g_{\boldsymbol{\mu}}(\mathbf{k}; z_0)$ for a single QE with perpendicular (solid blue) and parallel (red dashed) orientations (see inset) placed at $z_0 = 20$ nm and interacting with a SPP of momentum $\mathbf{k}(\omega)$.

Next, we generalize the single-emitter Hamiltonian given by Eq. 5.87 for a collection of N QEs located at positions $\mathbf{r}_i = (\mathbf{R_i}, z_i)$, with $i = 1, ..., N$. As sketched in Fig. 5.12 (a), the QEs are embedded in a dielectric host of thickness $\mathcal{W}$ that is placed on top of the metal surface. A spacer layer (thickness s) is placed between the dielectric host and the metal surface. We model the volume distribution of QEs as N_L layers with N_s QEs each ($N = N_L \times N_s$) and generalize the single QE Hamiltonian. Assuming the same transition frequency for all the emitters, $\omega_i = \omega_0$, the Hamiltonian for the N QEs reads as

$$\begin{aligned} H^N &= \sum_{j=1}^{N_L}\sum_{i=1}^{N_s} \hbar\omega_0 \sigma_{i,j}^\dagger \sigma_{i,j} + \sum_{\mathbf{k}} \hbar\omega(\mathbf{k}) a_{\mathbf{k}}^\dagger a_{\mathbf{k}} \\ &+ \sum_{\mathbf{k}}\sum_{j=1}^{N_L}\sum_{i=1}^{N_s} \frac{\hbar g_{\boldsymbol{\mu}}(\mathbf{k}; z_j)}{\sqrt{A}} \left(a_{\mathbf{k}} \sigma_{i,j}^\dagger e^{i\mathbf{k}\cdot\mathbf{R}_i} + a_{\mathbf{k}}^\dagger \sigma_{i,j} e^{-i\mathbf{k}\cdot\mathbf{R}_i} \right). \end{aligned} \tag{5.92}$$

Here, $\sigma_{i,j}$ and $\sigma_{i,j}^\dagger$ are the QE lowering and raising operators of a QE that is located at $(\mathbf{R}_i, z_j)$. In addition, $a_{\mathbf{k}}$ and $a_{\mathbf{k}}^\dagger$ are the already introduced SPP operators and $g_{\boldsymbol{\mu}}(\mathbf{k}; z_j)$ is the coupling constant between each of the QEs and the SPP, given by Eq. 5.91 and plotted in Fig. 5.12 (b).

To simplify the general Hamiltonian for the collection of emitters, we make a series of assumptions. First, we consider that, in the low excitation regime, the QEs are far from saturation. Hence, their lowering and raising fermionic operators ($\sigma_{i,j}$ and $\sigma_{i,j}^\dagger$), can be mapped into bosonic operators, $b_{i,j}$ and $b_{i,j}^\dagger$, respectively, by means of a Holstein-

Primakoff transformation [285],

$$\sigma_{i,j} = \sqrt{1 - b^{\dagger}{}_{i,j} b_{i,j}} \cdot b_{i,j} \,, \tag{5.93}$$

$$\sigma^{\dagger}{}_{i,j} = b^{\dagger}{}_{i,j} \sqrt{1 - b^{\dagger}{}_{i,j} b_{i,j}} \,. \tag{5.94}$$

Here, $[b_{i,j}, b^{\dagger}{}_{m,n}] = \delta_{mi}\delta_{nj}$. Assuming a low pumping rate, such that $\langle \sigma^{\dagger}{}_{i,j}\sigma_{i,j}\rangle \ll 1$, we have to first order $\sigma_{i,j} \approx b_{i,j}$, thereby arriving to the following total Hamiltonian

$$\begin{aligned} H^N &= \sum_{j=1}^{N_L}\sum_{i=1}^{N_s} \hbar\omega_0 b^{\dagger}_{i,j} b_{i,j} + \sum_{\mathbf{k}} \hbar\omega(\mathbf{k}) a^{\dagger}_{\mathbf{k}} a_{\mathbf{k}} \\ &+ \sum_{\mathbf{k}}\sum_{j=1}^{N_L}\sum_{i=1}^{N_s} \frac{\hbar g_{\boldsymbol{\mu}}(\mathbf{k}; z_j)}{\sqrt{A}} \left(a_{\mathbf{k}} b^{\dagger}_{i,j} e^{i\mathbf{k}\cdot\mathbf{R}_i} + a^{\dagger}_{\mathbf{k}} b_{i,j} e^{-i\mathbf{k}\cdot\mathbf{R}_i} \right) . \end{aligned} \tag{5.95}$$

Second, we construct a collective mode of the N_s emitters in each j-layer in a standard way as

$$D^{\dagger}_{j,\mathbf{q}} = \frac{1}{\sqrt{N_s}} \sum_{i=1}^{N_s} b^{\dagger}_{i,j} e^{i\mathbf{q}\cdot\mathbf{R}_i}. \tag{5.96}$$

In terms of these collective mode operators, the interaction term of the Hamiltonian reads as

$$H^N_{int} = \sum_{\mathbf{k},\mathbf{q}}\sum_{j=1}^{N_L}\sum_{i=1}^{N_s} \frac{\hbar g_{\boldsymbol{\mu}}(\mathbf{k}; z_j)\sqrt{n_s}}{N_s} \left(S(\mathbf{k}-\mathbf{q}) a_{\mathbf{k}} D^{\dagger}_{j,\mathbf{q}} + S^*(\mathbf{k}-\mathbf{q}) a^{\dagger}_{\mathbf{k}} D_{j,\mathbf{q}} \right), \tag{5.97}$$

where $n_s = \frac{N_s}{A}$ is the surface density of emitters. In the above equation we have introduced the structure factor, $S(\mathbf{k})$, of the distribution of QEs in each layer, which is defined as

$$S(\mathbf{k}) = \frac{1}{N_s} \sum_{i=1}^{N_s} e^{i\mathbf{k}\cdot\mathbf{R_i}} \,. \tag{5.98}$$

Next, as in the experiments the ensemble of QEs is disordered, we assume that the structure factor is peaked at zero-momentum, i.e., $S(\mathbf{k}-\mathbf{q}) \approx \delta_{\mathbf{k},\mathbf{q}}$. Within this approximation, the interaction Hamiltonian simplifies to

$$H^N_{int} = \sum_{\mathbf{k}}\sum_{j=1}^{N_L} \hbar g_{\boldsymbol{\mu}}(\mathbf{k}; z_j)\sqrt{n_s} \left(a_{\mathbf{k}} D^{\dagger}_{j,\mathbf{k}} + a^{\dagger}_{\mathbf{k}} D_{j,\mathbf{k}} \right). \tag{5.99}$$

Note here that the collective modes, $D_{j,\mathbf{k}}$, are orthonormal only if the distribution of emitters is homogeneous [8]. Finally, we define a collective mode of the whole ensemble of

[8] The commutation relation of operators $D_{j,\mathbf{k}}$ reads as

$$\left[D_{j,\mathbf{k}}, D^{\dagger}_{j,\mathbf{q}} \right] = \frac{1}{N_s} \sum_{i,i'=1}^{N_s} \left[b_{i,j}, b^{\dagger}_{i',j'} \right] e^{i(\mathbf{k}\cdot\mathbf{R}_i - \mathbf{q}\cdot\mathbf{R}'_i)} = \delta_{jj'} S(\mathbf{k}-\mathbf{q}) \approx \delta_{jj'}\delta_{\mathbf{k},\mathbf{q}}.$$

emitters, $D^{\dagger}_{\mathbf{k}}$, by means of a transformation in which each excitation is weighted by its coupling to SPPs

$$D^{\dagger}_{\mathbf{k}} = \frac{1}{g^N_{\boldsymbol{\mu}}(\mathbf{k})} \sum_{j=1}^{N_L} g_{\boldsymbol{\mu}}(\mathbf{k}; z_j) D^{\dagger}_{j,\mathbf{k}}, \tag{5.100}$$

where $g^N_{\boldsymbol{\mu}}(\mathbf{k})$ is defined such that the collective mode operator is normalized. Based on this, the total Hamiltonian of the N QEs interacting with the SPP modes of a 2D metal film can be written as $H^N = \sum_{\mathbf{k}} H^N_{\mathbf{k}}$, in which the hamiltonian associated with momentum $\mathbf{k}$ has the following expression

$$H^N_{\mathbf{k}} = \hbar\omega_0 D^{\dagger}_{\mathbf{k}} D_{\mathbf{k}} + \hbar\omega_{\mathbf{k}} a^{\dagger}_{\mathbf{k}} a_{\mathbf{k}} + \hbar g^N_{\boldsymbol{\mu}}(\mathbf{k})(a_{\mathbf{k}} D^{\dagger}_{\mathbf{k}} + a^{\dagger}_{\mathbf{k}} D_{\mathbf{k}}). \tag{5.101}$$

The effective coupling constant, $g^N_{\boldsymbol{\mu}}(\mathbf{k})$, is an average over the single QE-SPP coupling constants and reads as

$$g^N_{\boldsymbol{\mu}}(\mathbf{k}) = \sqrt{n_s \sum_{j=1}^{N_L} |g_{\boldsymbol{\mu}}(\mathbf{k}; z)|^2 dz}\,. \tag{5.102}$$

Assuming a continuum of layers in the z-direction with a total thickness $\mathcal{W}$ and a volume density of emitters $n = N_s N_L/(A\mathcal{W})$, the above expression can be written as

$$g^N_{\boldsymbol{\mu}}(\mathbf{k}) = \sqrt{n \int_s^{s+\mathcal{W}} |g_{\boldsymbol{\mu}}(\mathbf{k}; z)|^2 dz}\,. \tag{5.103}$$

The Hamiltonian 5.101 allows an *ab-initio* quantum treatment of the coherent coupling between an ensemble of N QEs and SPPs. This interaction conserves the total momentum of the system composed of the supermode of QEs and the SPP. When evaluating the coupling constant for a momentum $\mathbf{k}$, $g^N_{\boldsymbol{\mu}}(\mathbf{k})$, there is no need to rely on fitting parameters and can be calculated from first principles, as shown below.

In Figure 5.13 (a) we plot the effective coupling constant $g^N_{\boldsymbol{\mu}}$ evaluated at $\mathbf{k}(\omega_0)$ for a density of emitters $n = 10^6 \mu\text{m}^{-3}$ (of the order of the volume densities used in the experiments) as a function of $\mathcal{W}$ and for different values of the spacer width. The magnitude of the collective coupling constant depends on the orientation of the QEs' dipole moments. Here we render the two limiting cases (all dipoles oriented perpendicularly or parallel to the metal surface) as well as an isotropic average over these two orientations, $g_{\text{iso}} = 2g^2_{\parallel}/3 + g^2_{\perp}/3$. Two main conclusions can be extracted from this figure. First, $g^N_{\boldsymbol{\mu}}$ depends strongly on $\mathcal{W}$ but saturates for thick enough films. This saturation is due to

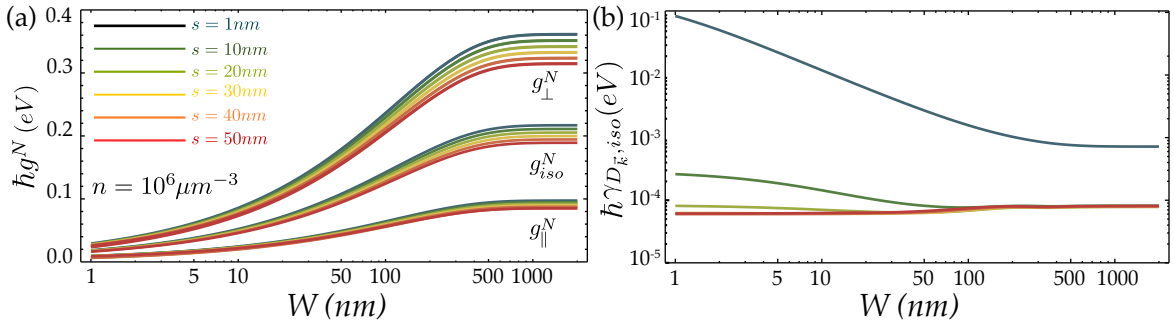

Figure 5.13: Collective coupling constant and losses. (a) Coupling constant, $\hbar g^N(\mathcal{W})$, for separations s ranging from 1 to 50 nm and for parallel, perpendicular and isotropic orientations of the QEs with $h\gamma_0 = 0.1$ meV. (b) Collective mode losses, $\hbar\gamma_{D_{\mathbf{k}}}(\mathcal{W})$, for an isotropic orientation of the QEs and the same range of spacer thickness as in panel (a). The volume density in both panels is $n = 10^6\ \mu\text{m}^{-3}$.

the exponential dependence of $g_{\boldsymbol{\mu}}$ on z, related to the spatial decay of the SPP mode (see Eq. 5.91), and, therefore, is determined by the dielectric environment of the metal film. Second, the dependence of $g_{\boldsymbol{\mu}}^N(\mathbf{k})$ on the width of the spacer layer is not very strong.

Finally, the excitation of the hybrid system needs to be included into the theoretical framework. In order to reproduce the typical experimental configuration, we will assume that SPPs are excited by a coherent laser field. A new term is incorporated into the total Hamiltonian, $H_{\mathbf{k}}^L(t) = \hbar\Omega_{\mathbf{k}}(a_{\mathbf{k}}e^{i\omega_L t} + a_{\mathbf{k}}^\dagger e^{-i\omega_L t})$ [192], in which $\Omega_{\mathbf{k}}$ measures the intensity of the laser field and ω_L is the operating frequency of the laser. In this way, the laser field fixes the SPP parallel momentum, $\mathbf{k}$, implying that only the term $H_{\mathbf{k}}^N$ in the total hamiltonian H^N needs to be taken into account. The final total coherent Hamiltonian then reads as

$$H_{\mathbf{k}} = H_{\mathbf{k}}^N + H_{\mathbf{k}}^L. \tag{5.104}$$

5.5.2 Master equation

The description of the dynamics of the system must be completed by considering both the losses in the ensemble of QEs and the dissipation associated with the SPP mode. We use a Markovian master equation for the density matrix and introduce perturbatively the corresponding Lindblad operators [286] associated with each of the dissipative channels. Recalling that the general expression of a Lindblad term associated with an arbitrary operator c is $\mathcal{L}_c = (2c\rho c^\dagger - c^\dagger c\rho - \rho c^\dagger c)$, the master equation for the density matrix

associated with momentum $\mathbf{k}$, $\rho_{\mathbf{k}}(t)$, can be written as

$$\dot{\rho}_{\mathbf{k}} = i[\rho_{\mathbf{k}}, H^N_{\mathbf{k}} + H^L_{\mathbf{k}}] + \frac{\hbar\gamma_{D_{\mathbf{k}}}}{2}\mathcal{L}_{D_{\mathbf{k}}} + \frac{\hbar\gamma_{a_{\mathbf{k}}}}{2}\mathcal{L}_{a_{\mathbf{k}}} + \frac{\hbar\gamma_{\phi}}{2}\mathcal{L}_{D^\dagger_{\mathbf{k}}D_{\mathbf{k}}}. \tag{5.105}$$

In this equation, we need to provide a decay rate for each decoherence mechanism. First, the decay rate of the SPP mode, $\gamma_{a_{\mathbf{k}}}$, can be calculated from the SPP propagation length, L_{SPP}, and group velocity, v_{g}, as $\gamma_{a_{\mathbf{k}}} = v_{\mathrm{g}}/L_{\mathrm{SPP}}$. The SPP lifetime decreases as the frequency approaches the SPP cut-off frequency, being around $\hbar\gamma_{a_{\mathbf{k}}} \sim 5\,\mathrm{meV}$ for $\hbar\omega_0 = 2\,\mathrm{eV}$.

Second, the decay rate associated with the collective mode of the ensemble of N QEs, $\gamma_{D_{\mathbf{k}}}$, can be obtained from the averaged value of the decay rates for each individual QE, $\gamma_\sigma(z)$, as follows. The losses associated to the N QEs before doing the transformation to the collective mode, are given by the following Lindblad term:

$$\mathcal{L}^N_\sigma[\rho] = \sum_{j=1}^{N_L}\sum_{i=1}^{N_s}\frac{\gamma_\sigma(z_j)}{2}\mathcal{L}_{\sigma_{i,j}}[\rho]. \tag{5.106}$$

Here $\gamma_\sigma(z_j)$ stands for the losses of a single QE, i.e., the coupling of a QE to all EM modes other than SPPs. This magnitude only depends on the z-coordinate and can be obtained from the spontaneous decay rate, Γ, and the β_{spp} factor of the coupling to SPPs as

$$\gamma_\sigma(z_j) = [1 - \beta_{\mathrm{spp}}(z_j)]\,\Gamma(z_j). \tag{5.107}$$

In Section 5.2 we showed that the spontaneous decay rate is given by the imaginary part of the Green's function of the classical problem evaluated at the QE's location through Eq. 5.29. In addition, $\Gamma(z)$ for a QE placed in front of a metal surface was calculated in Section 5.3.1 and plotted in Fig. 5.2 for a QE with $\hbar\omega_0 = 2$ eV. On the other hand, we also showed that β_{spp} can be calculated from the SPP pole in the Green's function, Γ_{spp} (see Eqs. 5.54, 5.55 and 5.59). The Lindblad term for the collective mode $\mathcal{L}_{D_{\mathbf{k}}}$ can be derived from Eq. 5.106 making use of the expression for $D^\dagger_{\mathbf{k}}$ [through Eqs. 5.96 and 5.100]:

$$\mathcal{L}_{D_{\mathbf{k}}}[\rho] = \sum_{\mathbf{k}}\frac{\gamma_{D_{\mathbf{k}}}}{2}\mathcal{L}_{D_{\mathbf{k}}}[\rho] + \sum_{j,j'}^{N_L}\sum_{\mathbf{k},\mathbf{k}'}\frac{\gamma_{D_{j,\mathbf{k}},D_{j',\mathbf{k}'}}}{2}(2D_{j',\mathbf{k}'}\rho D^\dagger_{j,\mathbf{k}} - D^\dagger_{j,\mathbf{k}}D_{j',\mathbf{k}'}\rho - \rho D^\dagger_{j,\mathbf{k}}D_{j',\mathbf{k}'}), \tag{5.108}$$

where we have separated the elements of the sum in $\mathbf{k}$ that conserve momentum and those that connect collective modes from different layers and with different $\mathbf{k}$'s. The second term originates from the inhomogeneity of $\gamma_\sigma(z)$ between different layers (j and j') or different orientations (in the case of an isotropic ensemble). Connecting modes of

different $\mathbf{k}$-vectors implies an incoherent coupling between the collective mode of the N QEs (Dicke state) at $\mathbf{k}$ and the reservoir of dark modes at other $\mathbf{k}'$, thereby yielding an inhomogeneous broadening. However, it can be shown that generally $\gamma_{D_{j,\mathbf{k}},D_{j,\mathbf{k}}} < \gamma_{D_\mathbf{k}}$ and, furthermore, $\gamma_{D_\mathbf{k}}$ is itself generally smaller than other loss mechanisms, as we will see below. Therefore, in our theoretical analysis we neglect the second term in the right-hand side of Eq. (5.108). Regarding the $\mathbf{k}$-conserving term, it involves a decay rate associated to the collective mode that can be written in terms of the decay rate of a single QE given by Eq.(5.107), as follows:

$$\gamma_{D_\mathbf{k}} = \frac{n}{|g^N_{\boldsymbol{\mu}}(\mathbf{k})|^2} \int_s^{s+\mathcal{W}} \mathrm{d}z\, \gamma_\sigma(z) |g^N_{\boldsymbol{\mu}}(\mathbf{k}, z)|^2 \,. \tag{5.109}$$

Notice that, as in the definition of the collective mode (5.100), the losses corresponding to each layer are weighted by a term that is proportional to $g^N_{\boldsymbol{\mu}}(\mathbf{k}, z)$.

The evolution of $\gamma_{D_\mathbf{k}}$ with the dielectric thickness, $\mathcal{W}$, is plotted in Fig. 5.13 (b). An isotropic distribution of QEs is considered, and the dependence with the spacer layer thickness, s, is also presented. Except in the case of a very thin spacer layer ($s = 1$ nm) the plot shows that the QEs' losses do not vary strongly with the geometrical parameters, $\mathcal{W}$ and s. Moreover, $\gamma_{D_\mathbf{k}}$ is of the order of γ_0, which makes this dissipation mechanism negligible when compared to, for instance, the SPP losses $\hbar\gamma_{a_\mathbf{k}} \approx 5\,\mathrm{meV}$. For the case of $s = 1$ nm, the value of $\gamma_{D_\mathbf{k}}$ increases due to the fact that the QEs are very close to the metal surface and quenching is not avoided. However, for dielectric layers of thicknesses $\mathcal{W} \gtrsim 100$ nm, the value of $\hbar\gamma_{D_\mathbf{k}}$ decreases to ≈ 1 meV, which is below the SPP losses.

Finally, in order to be as close as possible to the experimental conditions, the existence of vibro-rotational states in organic molecules must also be taken into account. These degrees of freedom within the QEs can be incorporated into the two-level system model by means of pure dephasing mechanisms, characterized by a dephasing rate, γ_ϕ. A typical value at room temperature for the organic molecules used to observe SC between QEs and SPPs is $\hbar\gamma_\phi = 40\,\mathrm{meV}$ [276].

Once all the ingredients in equation 5.105 have been introduced, the properties of the system, such as populations, can be obtained from it. As we are interested in the stationary properties of the system we solve the linear equation: $\dot{\rho}_\mathbf{k} = 0$, which yields the steady-state density matrix of the system $\rho^{ss}_\mathbf{k}$. Then, any property of the system described by a given operator O can be obtained as: $\langle O \rangle = \mathrm{Tr}\,[O\rho^{ss}_\mathbf{k}]$. The solution of the master equation for $\mathbf{k}_0 = \mathbf{k}(\omega_0)$ (in-plane momentum that displays maximum coupling) yields to coherence functions being proportional to $\exp(iRt)$ where R is the Rabi splitting at

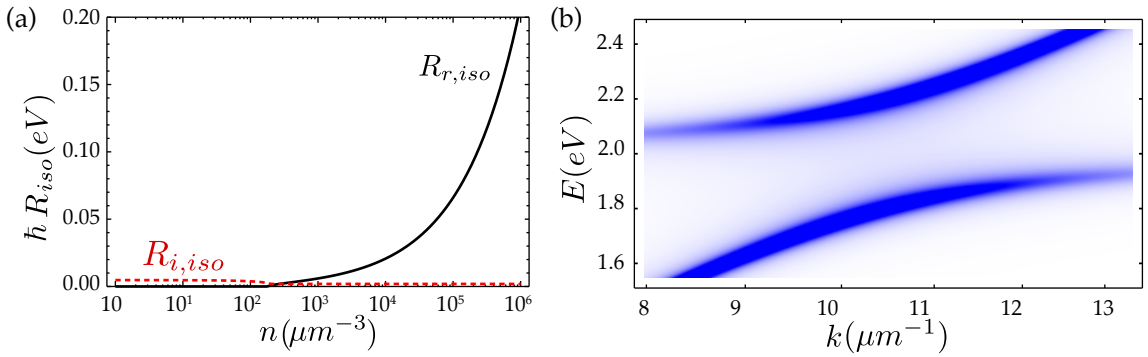

Figure 5.14: (a) Real (solid black) and imaginary (red dashed) parts of the Rabi splitting at resonance for dipoles oriented isotropically, $R_{\rm iso}$, as a function of the density of emitters, n, for the geometrical parameters: $s = 1$ nm, $\mathcal{W} = 500$ nm and $\hbar\gamma_\phi = 40$ meV. (b) Polariton population of a distribution of QEs as a function of $\mathbf{k}$, with the same geometrical parameters as in panel (a) and with $\Omega_{\mathbf{k}} = 0.1g^N$. The volume density in this case is $n = 10^6$ μm $^{-3}$, as in Fig. 5.13.

resonance:

$$R = \sqrt{[g^N_{\boldsymbol{\mu}}(\mathbf{k}_0)]^2 - (\gamma_{D_{\mathbf{k}_0}} + \gamma_\phi - \gamma_{a_{\mathbf{k}_0}})^2/16}. \tag{5.110}$$

Following the standard analysis [278], we will consider that our hybrid system is within the SC regime when the imaginary part of the Rabi splitting is zero. In Fig. 5.14(a), we plot the evolution of $R \equiv R_r + iR_i$ with the volume density n for an ensemble of N QEs whose dipole moments are oriented isotropically. For very low densities (for this set of parameters, $n < 2 \times 10^3 \mu m^{-3}$), R is a purely imaginary number and, therefore, the system operates in the WC regime. This density threshold, n_t, is mainly controlled by γ_ϕ as $\gamma_\phi \gg \gamma_D, \gamma_a$ for this set of decay rates. Notice that as γ_ϕ decreases exponentially when lowering the temperature [276], n_t is expected to be much smaller at very low temperatures (by assuming $\gamma_\phi = 0$ at zero temperature, n_t would be around $20\,\mu m^{-3}$). For high enough densities ($n \approx 10^5 - 10^8 \mu m^{-3}$, typical densities in the experiments [205]), R_r (the so-called vacuum Rabi splitting) is dominated by the coupling constant g^N as $g^N \gg \{\gamma_D, \gamma_a, \gamma_\phi\}$ and $R_r \approx g^N$. As this coupling constant scales as $\sqrt{n}$, so does R_r, as observed in the experiments. Within our formalism, it is also possible to evaluate the absorption spectra, a magnitude that is attainable experimentally. In Fig. 5.14(b) we plot the polariton population (the sum of both the QEs supermode and SPP mode occupations, a magnitude that is proportional to the absorption by the system [287]) versus energy and parallel momentum, showing the anti-crossing between the flat band at ω_0 associated with the collective mode of the N QEs and the dispersive band of the

SPPs. Moreover, our theoretical framework can be confronted with experimental results. In Ref. [205], the metal film was silver, $\mathcal{W} = 50$ nm, and an ensemble of $n = 1.2 \times 10^8$ μm^{-3} of rhodamine 6G molecules were used as QEs ($\gamma 0 = 1$ μeV [288]). This resulted in the observation of a Rabi splitting of 0.115 eV. For those parameters, our theory predicts $R_r = 0.04$ eV for parallel-oriented QEs, $R_r = 0.18$ eV for the perpendicular orientation, and $R_r = 0.10$ eV for an isotropic average, showing a good agreement between theory and experiment.

5.5.3 Saturation effects and quantum statistics

Here we address the fundamental question regarding the classical/quantum nature of the SC regime observed in this type of systems. Although a semiclassical formalism fed with phenomenological parameters is able to reproduce qualitatively the reported absorption spectra (see Section 5.7), this should not be taken as a statement that the system contains no interesting quantum physics. Non-classicality is unambiguosly revealed by the presence of photon antibunching in the dynamics of the strongly coupled system. For this reason, we analyze the behavior of the second-order correlation function, $g^{(2)}$, defined as

$$g^{(2)}(\tau) = \lim_{t\to\infty} \frac{\langle D_{\mathbf{k}}^\dagger(t)(D_{\mathbf{k}}^\dagger D_{\mathbf{k}})(t+\tau)D_{\mathbf{k}}(t)\rangle}{\langle D_{\mathbf{k}}^\dagger D_{\mathbf{k}}(t)\rangle^2}. \tag{5.111}$$

Photon antibunching yields $g^{(2)}(0) < 1$ [184], which reflects the single emitter character of the QEs. As we will show below, only when the intrinsic non-linearity of the QEs is taken into account $g^{(2)}(0)$ can take values < 1. Indeed, within the approximations leading to Hamiltonian 5.101 with $D_{\mathbf{k}}$ constructed from bosonic operators, the system behaves as two coupled harmonic oscillators. In this case, $g^{(2)}(0)$ is always greater or equal to 1 and its time evolution critically depends on the excitation means. For the case of coherent pumping, the system acquires the statistics of the laser field and hence $g^{(2)}(\tau) = 1$, as shown in Fig. 5.15 (a) (blue dotted line). A different case, that of incoherent pumping, is simulated in our theoretical formalism by introducing a Lindblad term, $P_{D_k}\mathcal{L}_{D_{\mathbf{k}}^\dagger}/2$ [278], into the master equation (Eq. 5.105), instead of $H_{\mathbf{k}}^L$. As shown in Fig. 5.15 (a) (green-dashed line), when the collective mode is driven incoherently $g^{(2)}(0) = 2$ and its time dependence presents some Rabi oscillations due to SC but $g^{(2)}(\tau) \geq 1$.

When the intrinsic non-linearity of the QEs is taken into account, with the following Hamiltonian term,

$$H_{nl} = \sum_{\mathbf{k},\mathbf{k}',\mathbf{q}} \hbar U_D D_{\mathbf{k}+\mathbf{q}}^\dagger D_{\mathbf{k}'-\mathbf{q}}^\dagger D_{\mathbf{k}} D_{\mathbf{k}'}\,, \tag{5.112}$$

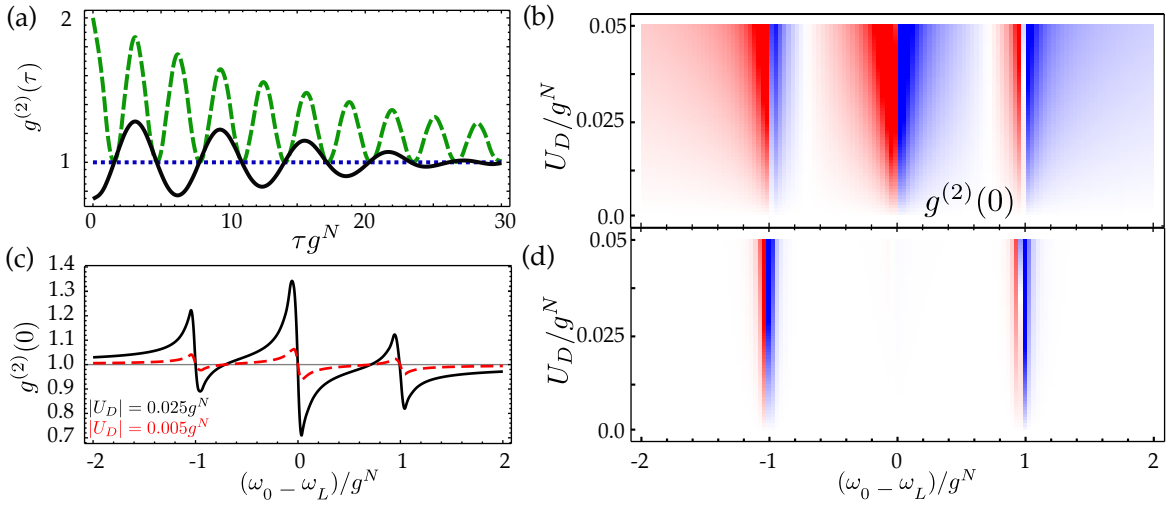

Figure 5.15: Second-order correlation function. (a) Dependence of $g^{(2)}$ on the delay, τ, for a system with $|U_D| = 0.025g^N$ and $\omega_L = \omega_0 + 0.1g^N$ (solid black) and with $|U_D| = 0$ for both incoherent pumping (dashed green) and coherent excitation (dotted blue). (b) Contour plot of $g^{(2)}$ at zero delay as a function of the nonlinearity, $|U_D|/g^N$ and detuning $(\omega_0 - \omega_L)/g^N$. The colour code is 0 blue, 1 white, 2 red. The pumping is coherent and the system parameters are: $s = 10$ nm, $\mathcal{W} = 10$ nm and $n = 10^6$ μm^{-3}, which yields $\hbar g^N \approx 50$ meV, see Fig. 5.13 (a). (c) Two cuts of the contour plot in panel (b) for different nonlinear parameters: $|U_D| = 0.005g^N$ (dashed red) and $|U_D| = 0.025g^N$ (solid black). (d) Contour plot of Mandel parameter, Q, revealing the optimal detuning for the observation of antibunching in this system. The colour code is: < 0 blue, 0 white, > 0 red. In (a-d) we have taken a dephasing rate $\gamma_\phi = 0$.

fingerprints of non-classicality can be found in our system ($g^{(2)}(0) < 1$). The physical origin of such a non-linear term can be twofold [289]: a direct coupling between the QEs, similar to the Coulomb interaction between excitons reported in semiconductor structures, and/or saturation effects. In this last case we can quantify this contribution by introducing the second-order correction within the Holstein-Primakoff approach in the process of replacing the QE lowering and raising operators by the bosonic ones. From Eqs. 5.93-5.94 we can write

$$\sigma_{i,j} \approx (1 - b^\dagger_{i,j} b_{i,j}/2) b_{i,j}. \tag{5.113}$$

This way, the QEs' saturable character is taken into account. With the expression above, the free-energy term of our starting Hamiltonian 5.92 becomes

$$H_0^N = \sum_{j=1}^{N_L} \sum_{i=1}^{N_s} \hbar\omega_0 b^\dagger_{i,j} b_{i,j} - \sum_{j=1}^{N_L} \sum_{i=1}^{N_s} \hbar\omega_0 b^\dagger_{i,j} b^\dagger_{i,j} b_{i,j} b_{i,j}\,. \tag{5.114}$$

The first term in this equation is the first order contribution appearing in Eq.(5.92). On the other hand, the second part of the equation is a non-linear term that can be expressed by means of operators $D_{j,\mathbf{k}}$ as[9]

$$H_{nl} = -\sum_{j=1}^{N_L} \sum_{\mathbf{k},\mathbf{k}',\mathbf{q}} \frac{\hbar\omega_0}{N_s} D^\dagger_{j,\mathbf{k}+\mathbf{q}} D^\dagger_{j,\mathbf{k}'-\mathbf{q}} D_{j,\mathbf{k}} D_{j,\mathbf{k}'} \,. \tag{5.115}$$

In particular, we now focus on a quasi-2D layer of QE's ($\mathcal{W} \to 0$). In this limit, $D_{j,\mathbf{k}} \approx \frac{1}{\sqrt{N_L}} D_{\mathbf{k}}$ and the non-linear term can be written in terms of the collective mode operator $D_{\mathbf{k}}$ as follows:

$$H_{nl} = -\sum_{\mathbf{k},\mathbf{k}',\mathbf{q}} \frac{\hbar\omega_0}{N} D^\dagger_{\mathbf{k}+\mathbf{q}} D^\dagger_{\mathbf{k}'-\mathbf{q}} D_{\mathbf{k}} D_{\mathbf{k}'} \,, \tag{5.116}$$

which is a particular case of Eq.5.112 with $U_D = -\frac{\omega_0}{N}$. Notice that whereas in the *linear* case the key parameter is the volume density n, the saturation contribution to the non-linear term is controlled by the total number of active QEs, N.

In Fig. 5.15 (b), we show the dependence of $g^{(2)}(0)$ on $|U_D|$ and the frequency detuning, $(\omega_0 - \omega_L)$, both expressed in units of g^N. In these calculations we have taken a dephasing rate $\gamma_\phi = 0$ in order to find the most favorable conditions to observe photon antibunching. As we consider pumping to only one $\mathbf{k}$-state, the population of a SPP-mode with parallel momentum $\mathbf{k}'$ is proportional to $\delta(\mathbf{k}-\mathbf{k}')$, canceling out the summation in $\mathbf{k}'$ in Eq. 5.112. In addition, as a first approximation to this problem we neglect also the summation in $\mathbf{q}$. This is justified by the fact that the shape of the SPP dispersion relation does not allow parametric scattering, in which both energy and momentum are conserved, to SPP states with $\mathbf{q} \neq 0$ [290, 291]. Two particular cases ($|U_D| = 0.025g^N$ and $0.005g^N$) are displayed in Fig. 5.15 (c) for a better visualization. If we assumed a saturation origin for U_D, these two cases would correspond to $N \approx 2 \times 10^3$ and $N \approx 10^4$, respectively. Importantly, photon antibunching is observed in both cases and is greater when the laser frequency almost coincides with ω_0 or $\omega_0 \pm g^N$. Finally, in Fig. 5.15 (d) we show a contour plot of the Mandel parameter at zero delay, which is defined as [184]

$$Q(\tau) = n_{D_{\mathbf{k}}} \left[g^{(2)}(\tau) - 1 \right] , \tag{5.117}$$

being $Q > 0$ for photon bunching and $Q < 0$ for antibunching. This definition is convenient because, different from $g^{(2)}(\tau)$, Q is weighted by the population of the mode. Hence, it differentiates regions of $g^{(2)}(\tau) < 1$ but very low population from regions of $g^{(2)}(\tau) < 1$

[9] Using $b^\dagger_{i,j} = \frac{1}{\sqrt{N_s}} \sum_{\mathbf{q}} D^\dagger_{j,\mathbf{q}} e^{-i\mathbf{q}\cdot\mathbf{R}_i}$.

but larger population, which is interesting from the experimental point of view. In the Q plot, the antibunching region at zero detuning disappears because the system is in the SC regime and thereby the population at $\omega_L = \omega_0$ is very low. Therefore, our results suggest that in order to observe noticeable photon antibunching, the laser should be tuned at $\omega_0 \pm g^N$ and the experiments should be performed at very low temperature to avoid dephasing and plasmon losses. Additionally, in order to reduce the number of active QEs, the laser beam should have a very small spot size, and the QEs should be disposed forming quasi-2D layers.

5.6 Conclusions

To summarize, in this Chapter we have studied the interaction between QEs and the EM modes supported by plasmonic structures. We have started by reviewing in Section 5.2 the QED formalism appropriate for treating the coupling of QEs to the EM field. Then, we have considered the coupling of an individual QE to plasmonic media, the SPP-mediated coupling between two QEs and the SC regime between a collection of QEs and propagating SPPs.

In Section 5.3 we have addressed the coupling between an individual QE and the EM modes supported by inhomogeneous plasmonic environments. First, we have considered the modification of the spontaneous decay rate of the QE induced by the presence of the plasmonic media. In particular, we have studied a QE placed close to a metal/dielectric interface as well as a graphene sheet. For both systems, we have identified three different decay channels for the QE: radiation to free space, coupling to SPPs and non radiative decay to lossy processes in the plasmonic medium. We have shown that for intermediate distances between the metal surface or the graphene sheet, the coupling to SPPs is the dominant contribution to the total decay rate. Second, we have studied the dynamics of the QE's population beyond the Markov approximation. For the case of metal/dielectric interfaces, we have explored the conditions under which a single QE interacting with the EM modes supported by the interface shows reversible dynamics. Through numerical and analytical tools, we have identified the parameters that determine both the emergence and the visibility of oscillations in the population of the excited state. We have found that the EM modes of frequencies around the cut-off frequency of the SPP modes, i.e., the most dissipative EM modes of the system, are the most relevant for the observation of reversible dynamics. In addition, in the region of very short distances, we have mapped the problem to an effective dissipative Jaynes Cummings model, yielding

analytical expressions for the coupling and the dynamics.

In Section 5.4 we have studied the tailoring of the interaction between two QEs mediated by SPPs propagating in graphene. We have shown that the interaction between two QEs mediated by the SPPs in 2D graphene sheets can be controlled at a subwavelength scale and can be tuned by means of external parameters through the chemical potential of the sheet. We have studied the appearance of the super- and subradiant regimes, both in the reflection and transmission configurations. Additionally, when the interaction is confined to 1D in graphene ribbons, a longer interaction range between the QEs and a very deep subwavelength control of the interaction can be achieved. By considering the lateral displacement of the QEs from the ribbon's axis, we have also shown that the coupling to the graphene SPPs supported by the ribbon is very robust. Our results show that both graphene sheets and graphene ribbons can be used as efficient platforms to modify the interaction between two QEs in their vicinity.

Finally, in Section 5.5 we have made use of a quantum formalism to study the phenomenon of SC between ensembles of QEs and propagating SPPs in 2D metal surfaces. Based on this formalism, we have predicted a critical density where SC emerges for a given geometry and distribution of QEs, and also determined the optimal geometrical parameters that maximize the SC. These results show that, for experiments carried out at room temperature, QE and SPP losses play a minor role in the emergence of SC. Both coherent coupling between the QEs and SPPs and pure dephasing mechanisms determine the strength of the phenomenon in this case. Additionally, the development of this general quantum framework allows studying the fundamental nature (classical versus quantum) of this phenomenon by analyzing the conditions in which photon antibunching could be observed.

5.7 Appendix: Semiclassical model for strong coupling

In this Appendix we show how a semiclassical model is also able to reproduce the phenomenology reported on the SC regime between a collection of QEs and SPPs.

The SC regime reveals itself through an energy splitting in the dispersion relation of the system of interest. When the interaction strength between two modes is large enough to enable a coherent energy exchange between them, any excitation of the system becomes delocalized. Then, the dispersion relation displays an avoided crossing of the energy levels with a characteristic splitting. It is well known that such a regime can be understood

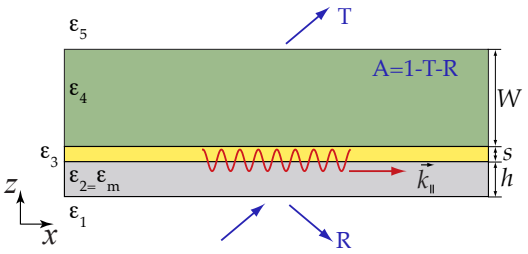

Figure 5.16: Multilayer model for a semiclassical approach to the SC between a collection of QEs and SPPs.

classically. For instance, two coupled classical harmonic oscillators of eigenfrequencies $\omega_{a,b} = \sqrt{k_a/m_{a,b}}$ and coupling constant g, display an avoided crossing of levels with a splitting given by (see for instance Ref. [292])

$$\Delta = \frac{\sqrt{g/m_a}\sqrt{g/m_b}}{\sqrt{\omega'_a}\sqrt{\omega'_b}}, \tag{5.118}$$

with $\omega'_{a,b} = \sqrt{(k_{a,b} + g)/m_{a,b}}$, and where we see that $\Delta \propto g$. Including damping in the model, $\gamma_{a,b}$, results in a broadening of the energy levels. Hence, anticrossing can only be observed if the energy splitting overcomes the sum of the linewidths, i.e. $\Delta > (\gamma_a + \gamma_b)$. Within a quantum formalism, two coupled oscillators show the same results and the anticrossing is usually termed *Rabi* splitting. As a result, the observed avoided crossings between the QEs' level and the propagating SPP mode in Refs. [204–208, 211–215] can be understood within a classical framework.

Here we present a semiclassical approach based on a multilayer model for the QEs-SPPs interacting system studied in Section 5.5 [10]. A sketch of the model, that reproduces the usual experimental configuration, can be seen in Fig. 5.16. First, a dielectric/metal interface of permittivities ϵ_1/ϵ_2, with $\epsilon_1 > 1$ and $\epsilon_2 = \epsilon_m(\omega)$, enables the excitation of SPPs that propagate through the upper metal/spacer/dielectric interface ($\epsilon_2/\epsilon_3/\epsilon_4$). The thickness of the metal film is h and we take it to be silver, with the dielectric function tabulated in Ref. [14]. The thickness of the spacer layer is s and it has $\epsilon_3 = 1$. The dielectric material on top (ϵ_4) is the host for the QEs and has a thickness $\mathcal{W}$. Finally, radiation outcouples through a dielectric/dielectric interface (ϵ_4/ϵ_5), where we take $\epsilon_5 = 1$.

The QEs are modeled through an effective dielectric function, $\epsilon_4 = \epsilon(\omega)$. We start from a quantum model for the polarizability of a 2LS of resonance frequency ω_0 (see Ref.

[10] Similar approaches have been presented to deal with SC in cavity QED systems [293].

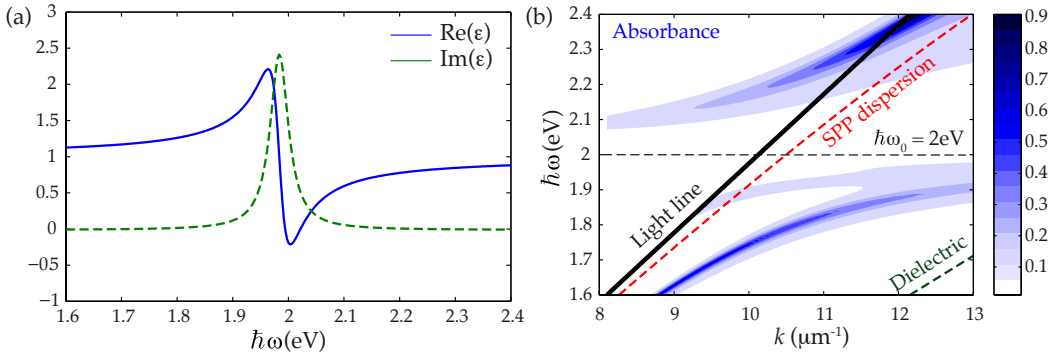

Figure 5.17: Anticrossing in the semiclassical approach. (a) Optical response of the molecules slab as given by Eq. 5.121 and with parameters $\hbar\omega_0 = 2$ eV, $h\gamma_0 = 0.1$ meV, $\hbar\gamma_\phi = 40$ meV and $n = 10^6$ μm^{-3}. (b) Absorbance, $A = 1 - R - T$, in the multilayer medium (colour scale) as a function of frequency and in-plane wave vector. The free-space light line is shown as a thick black line, while the dielectric light-line is shown as a dashed black line. The dispersion relation for the SPPs propagating through the metal film is depicted as a red dashed line. The horizontal dashed line points at the molecules resonance frequency, $\hbar\omega = 2$ eV. The geometrical parameters are $h = 50$ nm, $s = 1$ nm, $W = 500$ nm and $\epsilon_1 = 2.25$.

[11]),

$$\alpha(\omega) = \frac{e^2}{\epsilon_0 m}\frac{f_0}{\omega_0^2 - \omega^2 - i\omega\gamma}, \tag{5.119}$$

where e and m stand for the electron's charge and mass, respectively. In addition, γ stands for the radiative damping of the QEs, which we identify with their dephasing rate, γ_ϕ. The oscillator strength, f_0, accounts for the QEs' dipole moment and can be written in terms of the QEs' free space decay rate, γ_0, as

$$f_0 = \frac{2\pi m\epsilon_0 c^3}{e^2\omega_0^2}\gamma_0. \tag{5.120}$$

Finally, we derive $\epsilon(\omega)$ from a classical dielectric model (see Ref. [294]) as

$$\epsilon(\omega) = \frac{1 + 2/3\, n\,\alpha(\omega)}{1 - 1/3\, n\,\alpha(\omega)}, \tag{5.121}$$

where n is the QEs' number density. The real and imaginary parts (solid blue and dashed green, respectively) of the resulting dielectric function is plotted in Fig. 5.17 (a) for the same parameters considered in Section 5.5: $\hbar\omega_0 = 2$ eV, $h\gamma_0 = 0.1$ meV, $\hbar\gamma_\phi = 40$ meV and $n = 10^6$ μm^{-3}.

Next, we develop a scattering formalism for the multilayer structure and we calculate the absorbance (A) through $A = 1 - R - T$, with R being the reflectance and T the

transmittance. The contour plot in Fig. 5.17 (b) represents the absorbance value as a function of frequency, ω, and in-plane momentum, $\mathbf{k}$, of the excitation. For this calculation, we have considered a multilayer with geometrical set of parameters similar to the experimental setups: $h = 50$ nm, $s = 1$ nm, $W = 500$ nm and $\epsilon_1 = 2.25$. In this case, we have chosen a metal film that is thick enough to avoid the appearance of the short and long range SPP modes, such that it effectively acts as a semi-infinite metal surface. The plot clearly displays an anticrossing between the SPP dispersion and the QEs' energy of the order of those measured in the experiments. In addition, an extra feature appears close to the light line and the QEs' energy level, similar to what is observed in some of the experiments as well as in a recent theoretical calculation [295]. Our results indicate that such feature corresponds to a propagating mode within the dielectric slab that hosts the QEs.

Chapter 6

Conclusions

English

In this Thesis we have presented our contributions to four different topics that lay at the frontier of Plasmonics. These four topics are among the diverse prospects that have been explored in the research field of Plasmonics during the last four years. All the exciting prospects of Plasmonics take advantage of the ability of surface plasmons to confine largely enhanced electromagnetic fields at subwavelength volumes, even beyond the diffraction limit. As a consequence, surface plasmons build a bridge between two different length scales, which enables many novel electromagnetic phenomena with distinct applications. Throughout this Thesis we have explored four topics that exploit the remarkable properties featured by surface plasmons. In the following we summarize the main achievements presented here.

First, we have presented a framework for controlling the propagation of surface plasmons along metal/dielectric interfaces. The subwavelength confinement of surface plasmons opens up a new route to bridge electronics and photonics and many research efforts are devoted to the development of a surface plasmon-based photonics. Our approach makes use of Transformation Optics, a theoretical technique that aims to control and manipulate electromagnetic fields through devising coordinate transformations which are then implemented by means of materials with specifically designed optical properties, i.e., metamaterials. Applying Transformation Optics to Plasmonics allows us to control the flow of surface plasmons propagating along metal surfaces. In particular, we have presented various plasmonic devices working at subwavelength scales and based on patterning solely the dielectric medium that lies on top of the metal surface. Moreover, we have shown that devices relying on isotropic materials can be devised by the

appropriate choice of coordinate transformation.

Next, we have presented a work that aims to transfer the promising prospects of particle Plasmonics to lower frequency regimes, also adding the ingredient of magnetism. We have shown that metal particles with periodically textured surfaces support localized dipolar surface plasmons of electric as well as magnetic characters. These resonances are termed spoof surface plasmons, as they emerge a result of the particle's corrugation instead of the optical properties of metals, as is the case in canonical surface plasmons. For this reason, these geometrically-induced magnetic surface plasmons appear at a broad range of frequencies ranging from the microwave and THz regimes up to the near-IR, as we have demonstrated for realistic metal properties. We have also shown that by corrugating the metal structure with very long grooves, deeply subwavelength magnetic localized modes emerge. Furthermore, we have presented experimental results carried out in the microwave regime that verify our theoretical predictions.

At a different level, we have addressed the use of plasmonic antennas as a platform to manipulate nanoscopic targets at subwavelength scales. We have proposed a plasmonic structure that enables not only the trapping of Rayleigh dielectric or biological objects, but also their transport over long distances. The large field enhancement originated at the vicinity of optical antennas first enables the trapping of such objects in subwavelength volumes. Next, we achieve a directed drift of the targets by means of a combination of geometrical asymmetry and non-equilibrium physics. This is possible by the Brownian ratchet mechanism, that rectifies the Brownian motion of nanoscopic particles even in the absence of an external bias. Achieving a long-distance transport of the targets may find many functions in microfluidics and lab-on-a-chip applications.

Finally, we have studied the effect of plasmonic systems on the interaction between light and matter. In particular, we have shown that the sub-diffraction confined electromagnetic modes supported by flat plasmonic media can greatly enhance the coupling between quantum emitters and photons. For the case of an individual quantum emitter and for weak light-matter coupling strengths, the Markov approximation holds and the emitter's population decays irreversibly at a rate that is different from the free-space spontaneous decay rate. Interestingly, there is a range of distances close to the flat plasmonic structure where coupling to propagating surface plasmons results in an enhanced decay rate for the emitter. We have shown that this fact occurs for both for quantum emitters in the optical regime placed in the vicinity of a metal/dielectric interface and in the THz regime for the case of a graphene sheet. In addition, when the emitter is in a very close proximity to the interface, the emitter's decay rate is greatly enhanced due to electromagnetic modes of very large modal wave vectors associated to fast non radiative

decays within the plasmonic medium. In this case, the coupling strength is enhanced, Markov approximation breaks down, and the emitter's population exhibits reversible dynamics. Next, focusing in weak coupling strengths, we have considered the mediation of the interaction between two emitters by the surface plasmons propagating along graphene sheets and ribbons. The graphene surface plasmon polaritons enable longer interaction ranges between the emitters as well as the emergence of collective super- and subradiant states with modified decay rates. Moreover, the interaction between the emitters can be controlled at subwavelength scales through external parameters thanks to graphene's sensibility to external fields. Finally, we have studied the strong coupling regime for a collection of quantum emitters interacting with the surface plasmons propagating along a metal/dielectric interface. In this case, the ensemble of emitters enables a collective strong coupling with the surface plasmons polaritons. By means of the appropriate quantum framework, we have first reproduced the phenomenology reported in various experiments and then analyzed the conditions under which quantum statistics could be observed.

Castellano

En esta tesis se han presentado las contribuciones que hemos realizado en cuatro temas distintos que se encuentran en la frontera de la Plasmónica. Los temas que hemos tratado se hallan entre las diversas perspectivas que la comunidad científica ha explorado en este campo durante los últimos cuatro años. Todas las expectativas generadas por este área de investigación se basan en la capacidad de los plasmones de superficie de confinar el campo electromagnético en tamaños menores que la longitud de onda de la radiación, incluso superando el límite de la difracción. Como consecuencia de ello, los plasmones de superficie tienden un puente entre dos escalas de longitud muy distintas, lo que permite la aparición de fenómenos electromagnéticos novedosos y variados. A lo largo de esta tesis, hemos explorado cuatro temas que explotan las propiedades características de los plasmones de superficie. A continuación, resumimos los principales resultados expuestos en este manuscrito.

En primer lugar, hemos presentado una serie de herramientas para controlar la propagación de plasmones de superficie a lo largo de la interfaz entre un dieléctrico y un metal. La propiedad que presentan los plasmones de superficie de confinar los campos electromagnéticos a escalas menores que la longitud de onda supone una nueva ruta para combinar la tecnología electrónica con la fotónica. De hecho, numerosos trabajos científicos se han interesado por el desarrollo de una tecnología fotónica basada en plasmones de superficie. Nuestro enfoque se basa en el uso de la Óptica de Transformación, una técnica teórica que consigue controlar y manipular campos electromagnéticos, ideando transformaciones de coordenadas. Dichas transformaciones dan lugar a una serie de parámetros electromagnéticos, que se implementan en la realidad haciendo uso de metamateriales, materiales con propiedades ópticas específicamente diseñadas. Al aplicar la Óptica de Transformación a la Plasmónica, hemos desarrollado formas de control del flujo de plasmones propagándose a lo largo de superficies metálicas. En particular, hemos presentado varios dispositivos plasmónicos de dimensiones menores que la longitud de onda de la radiación involucrada, y que se basan únicamente en estructurar el medio dieléctrico que se encuentra sobre la superficie metálica. Además, hemos demostrado que, eligiendo la transformación de coordenadas de manera apropiada, es posible diseñar dispositivos que requieren solamente el uso de materiales dieléctricos isótropos.

En segundo lugar, hemos expuesto una propuesta para transferir las expectativas generadas por los plasmones localizados en partículas metálicas a regímenes de frecuencia más bajos, incluyendo asimismo modos plasmónicos magnéticos. Hemos mostrado que partículas metálicas con superficies periódicamente corrugadas admiten modos plasmóni-

cos localizados de carácter dipolar eléctrico así como dipolar magnético. Tales resonancias se denominan plasmones de superficie *spoof*, ya que aparecen como resultado de la corrugación de la superficie en lugar de como resultado de las propiedades ópticas de los metales, como ocurre en el caso de plasmones convencionales. Por este motivo, estos modos magnéticos de origen geométrico aparecen en un amplio rango de frecuencias, desde los regímenes de microondas y terahercios hasta el infra-rojo cercano, tal y como hemos demostrado simulando estructuras con propiedades metálicas realistas. También hemos mostrado que al corrugar una estructura puramente metálica con indentaciones muy largas, los modos plasmónicos magnéticos aparecen a longitudes de onda mucho menores que la de la radiación en vacío. Además, hemos presentado unos resultados experimentales que verifican nuestras predicciones teóricas.

Por otra parte, hemos considerado el uso de antenas plasmónicas como plataforma para la manipulación de objetos dieléctricos de dimensiones nanométricas, ya sean éstos tanto nano-partículas como objetos biológicos. Para ello, hemos propuesto una estructura plasmónica que permite no sólo atrapar tales objetos sino también su transporte a lo largo de distancias mucho mayores que sus tamaños. El aumento del campo eléctrico que se genera al iluminar antenas ópticas posibilita localizar dichos objetos de manera controlada en volúmenes menores que la longitud de onda de la fuente de iluminación empleada. Después, y gracias a la acción combinada de una geometría anisótropa y de procesos de fuera de equilibrio, conseguimos un transporte del objeto dieléctrico en una dirección. Esto es posible debido al mecanismo conocido como *ratchet* Browniano, que rectifica el movimiento térmico de una partícula difusiva sin necesidad de aplicar un gradiente de temperatura o una fueza macroscópica. Se espera que el transporte de objetos biológicos encuentre diversos usos en aplicaciones en micro-fluidos y en laboratorios de análisis integrados en micro-chips.

Finalmente, hemos estudiado el efecto producido por estructuras plasmónicas en la interacción entre la luz y la materia. En concreto, hemos demostrado que el confinamiento de los modos electromagnéticos en tamaños menores que el límite de difracción generado en las cercanías de estructuras plasmónicas planas, puede incrementar de manera muy significativa el acoplo entre fotones y emisores. En el caso de un sólo emisor cuántico y asumiendo un acoplo débil, la aproximación *Markov* es válida y el emisor se desexcita de manera irreversible a una tasa distinta a la tasa de de desexcitación espontánea que tiene lugar en vacío. Es de resaltar que hay un rango de distancias entre el emisor y la estructura plasmónica en el cual el acoplo a plasmones de superficie propagantes origina un incremento de la tasa de desexcitación del emisor. Hemos mostrado que este efecto ocurre tanto para emisores ópticos localizados en la cercanía de la interfaz entre un

metal y un dieléctrico, como para el régimen de terahercios en el caso de una lámina de grafeno. Asimismo, cuando el emisor está aún más próximo a dicha interfaz, su tasa de desexcitación sigue incrementándose debido a modos electromagnéticos asociados a procesos no radiativos que disipan energía rápidamente en el medio metálico. En este caso, se incrementa mucho la intensidad del acoplo entre la luz y la materia, de manera que la aproximación *Markov* puede dejar de ser válida y la población del emisor puede presentar una dinámica reversible. En siguiente lugar, y considerando acoplos débiles, hemos estudiado la posibilidad de mediar la interacción entre dos emisores a traves de los plasmones de superficie propagándose a lo largo de láminas y tiras de grafeno. Los plasmones existentes en grafeno dan lugar a interacción de mayor alcance, así como a la aparición de estados colectivos, denominados súper- y sub-radiantes, con tasas de desexcitación modificadas. Además, de esta manera se puede controlar la interacción entre los emisores a escalas menores que la longitud de onda de la radiación a través de parámetros externos gracias a la sensibilidad del grafeno ante a campos aplicados. Por último, hemos estudiado el régimen de acoplo fuerte para un conjunto de emisores cuánticos en interacción con los plasmones de superficie que se propagan a través de la interfaz entre un metal y un dieléctrico. En este caso, el régimen de acoplo fuerte aparece gracias a la acción colectiva de los emisores. A través del desarrollo de un formalismo cuántico apropiado, hemos reproducido la fenomenología encontrada experimentalmente en este tipo de sistemas, además de analizar las condiciones necesarias para la aparición de propiedades cuánticas en la estadística.

Appendix A

Conformal and quasiconformal mappings

In this Appendix we give some technical details on the properties of the conformal and quasiconformal transformations used in Chapter 2.

A.1 Conformal transformations

Consider a transformation from a coordinate grid, $\{\mathbf{x}'\} = \{x', y'\}$, into another, $\{\mathbf{x}\} = \{x, y\}$, given by,

$$w = f(z, \overline{z}) = x(x', y') + iy(x', y'), \tag{A.1}$$

where $z = x' + iy'$ and $w = x + iy$. The above transformation is said to be conformal if the function f depends on z but not on its conjugate $\overline{z}$ and if it is analytical, i.e. $f'(z)$ can be defined. The line element of the conformal transformatiol, $\mathrm{d}z^2$, is related to the euclidean metric $\mathrm{d}s^2 = dx^2 + dy^2$ by a real-valued conformal factor, $\Lambda(z)$, such that $\mathrm{d}s^2 = \Lambda(z)^2 \mathrm{d}z^2$. As a consequence, a conformal transformation maps, to first order, circles into circles. The condition $\partial f / \partial \overline{z}$ implies that a conformal transformation satisfies the Cauchy-Riemann equations,

$$\frac{\partial x}{\partial x'} = \frac{\partial y}{\partial y'}; \quad \frac{\partial x}{\partial y'} = -\frac{\partial y}{\partial x'}. \tag{A.2}$$

Alternatively, these equations can be expressed as Laplace's equations for the functions $x(x', y')$ and $y(x', y')$,

$$\nabla'^2 x = 0; \quad \nabla'^2 y = 0, \tag{A.3}$$

where the Laplacian is taken in the primed coordinate system $\nabla'^2 = \partial^2/\partial x'^2 + \partial^2/\partial y'^2$. Consequently, the metric tensor of the transformation, which is defined as follows,

$$\hat{G} = \left(\frac{\partial x^k}{\partial x^i}\right)\left(\frac{\partial x^k}{\partial x^j}\right), \tag{A.4}$$

is found to be,

$$\hat{G} = \begin{pmatrix} \frac{\partial^2 x'}{\partial x^2} + \frac{\partial^2 y'}{\partial x^2} & 0 \\ 0 & \frac{\partial^2 x'}{\partial x^2} + \frac{\partial^2 y'}{\partial x^2} \end{pmatrix} = \sqrt{g} \cdot \mathbb{I}_{2\times 2}, \tag{A.5}$$

with g being the determinant of the metric tensor.

A.2 Optical conformal mapping

Here we demonstrate that optical conformal mapping technique developed in Ref. [55] is equivalent to Transformation Optics for the particular case of a conformal transformation.

In the limit of ray optics, where the refractive index $n(x, y)$ is nearly constant over the scale of a wavelength $\frac{2\pi}{|\vec{k}|}$, the field amplitude for each polarization satisfies Helmholtz's equation. In virtual space ($z = x' + iy'$), this equation reads as

$$\left(\nabla'^2 + \frac{\omega^2}{c^2} n'^2\right)\psi = 0. \tag{A.6}$$

Let us now consider a transformation $w = w(z)$ from virtual to physical space ($w = x+iy$) such that it is conformal. Making use of the relation between the Laplacian in virtual and physical spaces, $\nabla'^2 = |d\omega/dz|^2 \nabla^2$, we can transform Helmholtz's equation to physical space,

$$\left(\nabla^2 + \frac{\omega^2}{c^2}\left|\frac{dz}{d\omega}\right|^2 n'^2\right)\psi = 0. \tag{A.7}$$

This equation is left invariant if we choose a refractive index of the form [55],

$$n = \left|\frac{dz}{d\omega}\right| n', \tag{A.8}$$

where n' is the background refractive index, n_0. By means of the Cauchy-Riemman equations (A.2) we can express the refractive index in terms of the metric tensor of a conformal transformation,

$$n = n_0 \left|\frac{\mathrm{d}}{\mathrm{d}\omega}(x' + iy')\right| = n_0 \left|\frac{\partial x'}{\partial x} + i\frac{\partial y'}{\partial x}\right| = n_0 \sqrt{\frac{\partial^2 x'}{\partial x^2} + \frac{\partial^2 y'}{\partial x^2}} = n_0 g^{1/4}. \tag{A.9}$$

which is the same expression for the refractive index derived in the main text according to TO (Eq. 2.16).

A.3 Quasiconformal transformations

Quasiconformal transformations are generalizations of conformal mappings which map circles into ellipses to first order. In this case, the relation between its line element, $\mathrm{d}z^2$, and the Euclidean metric is given by the expression,

$$ds^2 = \Lambda(z)^2 \left| dz^2 + H(z,\overline{z}) d\overline{z}^2 \right|^2, \tag{A.10}$$

where the function $H(z,\overline{z}) = \mu(x',y') + i\nu(x',y')$ is zero if the transformation is conformal. A quasiconformal map $w = f(z,\overline{z})$ satisfies the following condition,

$$\frac{\partial f}{\partial \overline{z}} - H(z,\overline{z}) \frac{\partial f}{\partial z} = 0. \tag{A.11}$$

This expression implies a generalized form of the Cauchy-Riemann equations,

$$\begin{aligned} \alpha \frac{\partial x'}{\partial x} + \beta \frac{\partial x'}{\partial y} &= \frac{\partial y'}{\partial y} \\ \beta \frac{\partial x'}{\partial x} + \gamma \frac{\partial x'}{\partial y} &= -\frac{\partial y'}{\partial x}, \end{aligned} \tag{A.12}$$

where $\alpha = \left((1-\mu)^2 + \nu^2\right) / \left(1 - \mu^2 - \nu^2\right)$, $\beta = -2\nu / \left(1 - \mu^2 - \nu^2\right)$ and $\gamma = \left((1+\mu)^2 + \nu^2\right) / \left(1 - \mu^2 - \nu^2\right)$. Finally, a generalized form of Laplace's equation can also be obtained for quasiconformal mappings, reading as follows,

$$\begin{aligned} \frac{\partial^2 x}{\partial x'^2} + \frac{\partial^2 x}{\partial y'^2} + \left(\frac{\partial \beta}{\partial y} + \frac{\partial \alpha}{\partial x} \right) \sqrt{g} = 0, \\ \frac{\partial^2 y}{\partial x'^2} + \frac{\partial^2 y}{\partial y'^2} - \left(\frac{\partial \beta}{\partial x} + \frac{\partial \gamma}{\partial y} \right) \sqrt{g} = 0. \end{aligned} \tag{A.13}$$

Notice that these expressions reduce to Laplace's equation, Eq. A.3, for a conformal transformation ($\alpha = \gamma = 1$ and $\beta = 0$). The equations above imply that quasiconformal mappings yield approximately diagonal metric tensors (see, for instance, Refs. [226, 227]).

Appendix B

Perfect Electrical Conductor

In PEC approximation metals are assumed to have high conductivities, such that the electrons in the metal perfectly shield the EM field. In other words, EM fields can not penetrate in a PEC. The penetration depth of a metal (usually called skin depth), δ, can be used to characterize the PEC limit. It is defined as the inverse of the imaginary part of the wavector inside the metal, $\delta = 1/\mathrm{Im}\, k$. This wavevector is just the product of the free space wavevector, $k_0 = 2\pi/\lambda$, and the refractive index of the metal, $n = \sqrt{\epsilon(\omega)}$: $k = k_0\sqrt{\epsilon(\omega)}$. An important physical quantity to look at when evaluating the validity of the PEC approximation is the ratio between the skin depth and the operating wavelength:

$$\frac{\delta}{\lambda} = \frac{1}{2\pi}\frac{1}{\mathrm{Im}\sqrt{\epsilon(\omega)}}. \tag{B.1}$$

Notice that this normalized magnitude (and not δ) is closely related to the impedance of a metal, $Z_S(\omega) = 1/\sqrt{\epsilon(\omega)}$, which measures how much the parallel component of the electric field at a metal surface, $\vec{E}_{\parallel}$, departs from its PEC value, $\vec{E}_{\parallel} = 0$.

Figure B.1 (b) shows the behavior of δ/λ as a function of the frequency for silver, whose dielectric function is depicted in panel (a). We have modeled the dielectric permittivity of this metal with a Drude formula,

$$\epsilon(\omega) = 1 - \frac{\omega_p^2}{\omega^2 + i\omega_\tau\omega}, \tag{B.2}$$

with $\omega_p = 1.37 \times 10^{16}$ Hz being the plasma frequency and $\omega_\tau = 2.73 \times 10^{13}$ Hz the damping frequency [238]. The ratio between skin depth and wavelength, δ/λ, is of the order of 10^{-5} for GHz frequencies and increases as the frequency increases. Therefore, PEC approximation (that assumes $Z_S = 0$) is a very accurate approximation for very low frequencies and becomes worse for higher frequencies.

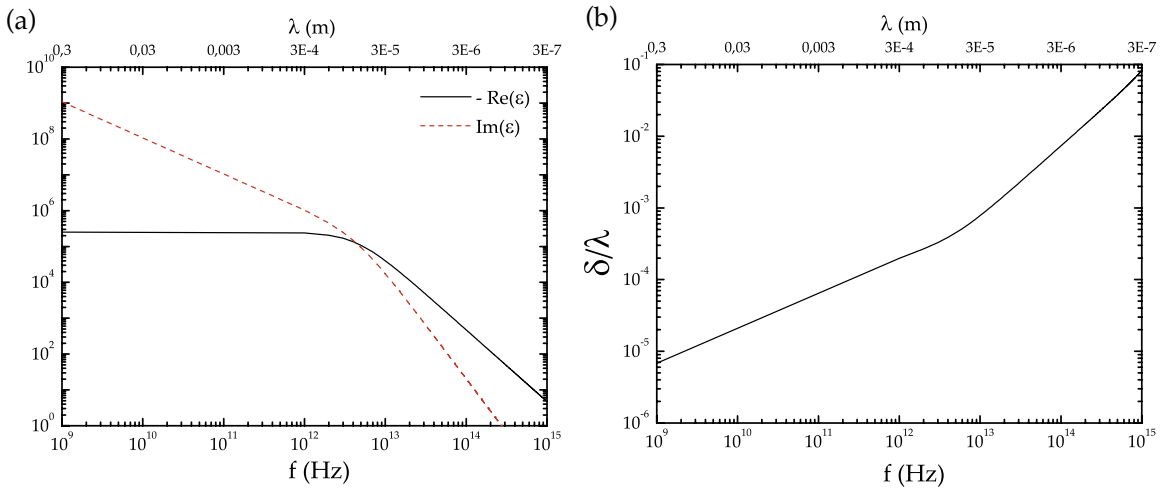

Figure B.1: Silver optical properties. (a) Silver electric permittivity, with parameters from Ref. [238]. (b) Skin depth, δ, normalized to the free-space wavelength, λ.

Appendix C

Green's function mode expansion

C.1 Expansion in normal modes

Here we follow Ref [11] to derive the expansion of the Green's function, $\hat{\mathbf{G}}(\mathbf{r}, \mathbf{r}', \omega)$, in terms of some normal modes, $\mathbf{u}_{\mathbf{k},\lambda}(\mathbf{r}, \omega_{\mathbf{k}})$., which are labeled by the wave vector, $\mathbf{k}$, and the polarization state, $\lambda = 1, 2$. We start by writing the expansion as

$$\hat{\mathbf{G}}(\mathbf{r}, \mathbf{r}', \omega) = \sum_{\mathbf{k},\lambda} \mathbf{A}_{\mathbf{k},\lambda}(\mathbf{r}', \omega)\mathbf{u}_{\mathbf{k},\lambda}(\mathbf{r}, \omega_{\mathbf{k}}), \tag{C.1}$$

where the Green's function satisfies

$$\vec{\nabla} \times \vec{\nabla} \times \hat{\mathbf{G}}(\mathbf{r}, \mathbf{r}', \omega) - \frac{\omega^2}{c^2}\hat{\mathbf{G}}(\mathbf{r}, \mathbf{r}', \omega) = \hat{\mathbf{I}}\delta(\mathbf{r} - \mathbf{r}'), \tag{C.2}$$

and the normal modes satisfy the following Helmholtz equation

$$\vec{\nabla} \times \vec{\nabla} \times \mathbf{u}_{\mathbf{k},\lambda}(\mathbf{r}, \omega_{\mathbf{k}}) - \frac{\omega_{\mathbf{k}}^2}{c^2}\mathbf{u}_{\mathbf{k},\lambda}(\mathbf{r}, \omega_{\mathbf{k}}) = 0, \tag{C.3}$$

and the orthonormality condition

$$\int \mathbf{u}^*_{\mathbf{k}',\lambda}(\mathbf{r}, \omega'_{\mathbf{k}}) \cdot \mathbf{u}_{\mathbf{k},\lambda}(\mathbf{r}, \omega_{\mathbf{k}}) \mathrm{d}^3\mathbf{r} = \delta_{\mathbf{k}\mathbf{k}'}. \tag{C.4}$$

Substituting Eq. C.1 into Eq. C.2 and making use of expression C.3 and the orthonormality relation C.4, we find that the expansion coefficients satisfy

$$\mathbf{A}_{\mathbf{k},\lambda}(\mathbf{r}', \omega)\left[\frac{\omega_{\mathbf{k}}^2}{c^2} - \frac{\omega^2}{c^2}\right] = \mathbf{u}^*_{\mathbf{k},\lambda}(\mathbf{r}, \omega_{\mathbf{k}}). \tag{C.5}$$

Then, we have for the Green's function

$$\hat{\mathbf{G}}(\mathbf{r}, \mathbf{r}', \omega) = \sum_{\mathbf{k},\lambda} \frac{\mathbf{u}^*_{\mathbf{k},\lambda}(\mathbf{r}', \omega_{\mathbf{k}})\mathbf{u}_{\mathbf{k},\lambda}(\mathbf{r}, \omega_{\mathbf{k}})}{(\omega_{\mathbf{k}}^2 - \omega^2)/c^2}. \tag{C.6}$$

which represents the field at point $\mathbf{r} = (x, y, z)$ generated by a dipole located at $\mathbf{r}' = (x', y', z')$.

Now we derive an important expression that relates the imaginary part of the Green's function to the local density of states through the normal modes. We start by taking the imaginary part of the above expression,

$$\mathrm{Im}\left\{\hat{\mathbf{G}}(\mathbf{r}_0, \mathbf{r}_0, \omega)\right\} = c^2 \mathrm{Im}\left\{\lim_{\eta\to 0}\sum_{\mathbf{k},\lambda} \frac{\mathbf{u}^*_{\mathbf{k},\lambda}(\mathbf{r}_0, \omega_{\mathbf{k}})\mathbf{u}_{\mathbf{k},\lambda}(\mathbf{r}_0, \omega_{\mathbf{k}})}{\omega^2_{\mathbf{k}} - (\omega + i\eta)^2}\right\}, \tag{C.7}$$

where we have introduced a small imaginary part $\eta > 0$ in the frequency to perform a contour integral. Integration in the complex plane for $\omega > 0$ yields

$$\mathrm{Im}\left\{\hat{\mathbf{G}}(\mathbf{r}_0, \mathbf{r}_0, \omega)\right\} = \frac{c^2\pi}{2\omega}\sum_{\mathbf{k},\lambda} \mathbf{u}^*_{\mathbf{k},\lambda}(\mathbf{r}_0, \omega_{\mathbf{k}})\mathbf{u}_{\mathbf{k},\lambda}(\mathbf{r}_0, \omega_{\mathbf{k}})\delta(\omega - \omega_{\mathbf{k}}). \tag{C.8}$$

The partial local EM density of states, ρ_μ, can be identified in the right hand side of the above expression following

$$\rho_\mu(\mathbf{r}_0, \omega) = \rho_\mu(\mathbf{r}_0, \omega) = 3\sum_{\mathbf{k},\lambda}\left[\mathbf{n}_\mu \cdot (\mathbf{u}_{\mathbf{k},\lambda}\mathbf{u}^*_{\mathbf{k},\lambda}) \cdot \mathbf{n}_\mu\right]\delta(\omega - \omega_{\mathbf{k},\lambda}). \tag{C.9}$$

Hence, we can write the relation

$$\rho_\mu(\mathbf{r}_0, \omega) = \frac{6\omega}{\pi c^2}\left[\mathbf{n}_\mu \cdot \mathrm{Im}\left\{\hat{\mathbf{G}}(\mathbf{r}_0, \mathbf{r}_0, \omega)\right\} \cdot \mathbf{n}_\mu\right]. \tag{C.10}$$

C.2 Plane wave expansion

Plane waves with p and s polarization constitute a set of normal modes for Maxwell's equations. In this section we make use of this basis to derive the Green's function plane wave expansion. Using the notation $\mathbf{u}_{\mathbf{k},\lambda}(\mathbf{r}, \omega_{\mathbf{k}}) = \langle \mathbf{r}|\mathbf{k}, \lambda\rangle$, the plane wave basis reads as

$$\langle \mathbf{r}|\mathbf{k}, s\rangle = \frac{1}{k_{||}}\begin{pmatrix} -k_y \\ k_x \\ 0 \end{pmatrix} e^{i\mathbf{k}\mathbf{r}}, \quad \langle \mathbf{r}|\mathbf{k}, p\rangle = \frac{k_z}{\sqrt{\epsilon}k_0 k_{||}}\begin{pmatrix} k_x \\ k_y \\ -k^2_{||}/k_z \end{pmatrix} e^{i\mathbf{k}\mathbf{r}}, \tag{C.11}$$

with $k_0 = \omega/c$, $\mathbf{k} = (\mathbf{k}_{||}, k_z) = (k_x, k_y, k_z)$, $k_{||} = \sqrt{k_x^2 + k_y^2}$ and $k_z = \sqrt{\epsilon k_0^2 - k_{||}^2}$ with $\mathrm{Im}(k_z) > 0$. Thus, from Eq. C.6 the Green's function reads as

$$\hat{\mathbf{G}}(\mathbf{r}, \mathbf{r}', \omega) = \sum_\lambda \int \frac{\mathrm{d}^3\mathbf{k}}{(2\pi)^3}\frac{\langle \mathbf{r}|\mathbf{k}, \lambda\rangle\langle \mathbf{k}, \lambda|\mathbf{r}'\rangle}{k^2 - \epsilon k_0^2}. \tag{C.12}$$

In order to treat problems without spatial invariance in the z direction it is convenient to re-define the basis as

$$\langle \mathbf{r}|\mathbf{k},\lambda\rangle = \langle \mathbf{r}|\mathbf{k}_\lambda^\pm\rangle e^{i\mathbf{k}_\pm \mathbf{r}} = \langle \mathbf{r}|\mathbf{k}_\lambda^\pm\rangle e^{i\mathbf{k}_{||}\mathbf{r}_{||}\pm ik_z z}, \tag{C.13}$$

where we have introduced the notation $\mathbf{k}_\pm = (\mathbf{k}_{||}, \pm k_z)$ and "+" must be taken for $z - z' > 0$ while "−" for $z - z' < 0$. The basis is now given by

$$\langle \mathbf{r}|\mathbf{k}_s^\pm\rangle = \frac{1}{k_{||}}\begin{pmatrix} -k_y \\ k_x \\ 0 \end{pmatrix}, \quad \langle \mathbf{r}|\mathbf{k}_p^\pm\rangle = \frac{k_z}{\sqrt{\epsilon}k_0 k_{||}}\begin{pmatrix} k_x \\ k_y \\ \mp k_{||}^2/k_z \end{pmatrix}. \tag{C.14}$$

Performing the integration in k_z in Eq. C.12 yields

$$\hat{\mathbf{G}}(\mathbf{r},\mathbf{r}',\omega) = \frac{i}{8\pi^2}\sum_\lambda \int \mathrm{d}^2\mathbf{k}_{||}\frac{e^{i\mathbf{k}_\pm(\mathbf{r}-\mathbf{r}')}}{k_z}\langle \mathbf{r}|\mathbf{k}_\lambda^\pm\rangle\langle \mathbf{k}_\lambda^\pm|\mathbf{r}'\rangle. \tag{C.15}$$

It is clear from the above equation that $\hat{\mathbf{G}}(\mathbf{r},\mathbf{r}',\omega) = \hat{\mathbf{G}}(\mathbf{r}-\mathbf{r}',\omega)$. Hence, we introduce the notation $\mathbf{R} = \mathbf{r} - \mathbf{r}'$.

C.2.1 Free space Green's function

The total Green's function in free space can be obtained from Eq. C.15 by taking $z - z' > 0$. For the two polarizations we have

$$\hat{\mathbf{G}}_0^s(\mathbf{R},\omega) = \frac{i}{8\pi^2}\int \mathrm{d}^2\mathbf{k}_{||}\frac{e^{i\mathbf{k}\mathbf{R}}}{k_z k_{||}^2}\begin{pmatrix} k_y^2 & -k_x k_y & 0 \\ -k_x k_y & k_x^2 & 0 \\ 0 & 0 & 0 \end{pmatrix}, \tag{C.16}$$

$$\hat{\mathbf{G}}_0^p(\mathbf{R},\omega) = \frac{i}{8\pi^2}\int \mathrm{d}^2\mathbf{k}_{||}\frac{e^{i\mathbf{k}\mathbf{R}}}{k_{||}^2\epsilon k_0^2}\begin{pmatrix} k_x^2 k_z & k_x k_y k_z & k_x k_{||}^2 \\ k_x k_y k_z & k_y^2 k_z & k_y k_{||}^2 \\ k_x k_{||}^2 & k_y k_{||}^2 & k_{||}^4/k_z \end{pmatrix}. \tag{C.17}$$

Summing over the two polarizations we obtain

$$\hat{\mathbf{G}}_0(\mathbf{R},\omega) = \frac{i}{8\pi^2\epsilon k_0^2}\int \mathrm{d}^2\mathbf{k}_{||}\frac{e^{i\mathbf{k}\mathbf{R}}}{k_z}\begin{pmatrix} \epsilon k_0^2 - k_x^2 & -k_x k_y & -k_x k_z \\ -k_x k_y & \epsilon k_0^2 - k_y^2 & -k_y k_z \\ -k_x k_z & -k_y k_z & \epsilon k_0^2 - k_z^2 \end{pmatrix}. \tag{C.18}$$

Equivalently, the Green's dyadic can be expressed in terms of a scalar Green's function, $\mathbf{G}_0(\mathbf{R},\omega)$, as

$$\hat{\mathbf{G}}_0(\mathbf{R},\omega) = \left(\hat{\mathbf{I}} + \frac{1}{\epsilon k_0^2}\nabla\nabla\cdot\right)\mathbf{G}_0(\mathbf{R},\omega), \tag{C.19}$$

with $\mathbf{G}_0(\mathbf{R},\omega)$ satisfying

$$\mathbf{G}_0(\mathbf{R},\omega) = \frac{i}{8\pi^2}\int_0^\infty \mathrm{d}k_{||}\int_0^{2\pi}\mathrm{d}\phi\frac{e^{i\mathbf{k}\mathbf{R}}}{k_z}. \tag{C.20}$$

Performing the angular integration yields

$$\mathbf{G}_0(\mathbf{R},\omega) = \frac{i}{4\pi}\int_0^\infty \mathrm{d}k_{||}J_0(k_{||}|\mathbf{R}_{||}|)\frac{k_{||}}{k_z}e^{ik_z|z-z'|}. \tag{C.21}$$

At the dipole's location we have $\mathbf{R}=0$ and

$$\mathbf{G}_0(\omega) = \frac{i}{4\pi}\int_0^\infty \mathrm{d}k_{||}\frac{k_{||}}{k_z}. \tag{C.22}$$

An useful quantity is its imaginary part, that can be written as

$$\mathrm{Im}\{\mathbf{G}_0(\omega)\} = \frac{1}{4\pi}\mathrm{Re}\left[\int_0^\infty \mathrm{d}k_{||}\frac{k_{||}}{k_z}\right]. \tag{C.23}$$

Introducing the dimensionless wavenumbers $q = k_{||}/k_0$ and $q_z = k_z/k_0 = \sqrt{\epsilon - q^2}$, we arrive to

$$\mathrm{Im}\{\mathbf{G}_0(\omega)\} = \frac{k_0}{4\pi}\mathrm{Re}\left[\int_0^1 \mathrm{d}q\frac{q}{q_z}\right] = \frac{\omega}{6\pi c}, \tag{C.24}$$

where we have made use of the fact that q_z is real only for propagating waves ($0<q<1$) and of the integral $\int_0^1 \mathrm{d}x\, x^3/\sqrt{1-x^2} = 2/3$.

C.2.2 Green's function for a layered structure

We now consider the problem of a point dipole located close to a boundary between two media, a and b. Assume that the dipole is placed at point $\mathbf{r}' = (x', y', z')$ within medium a ($z>0$) and that the plane interface is at $z=0$. The Green's function at point $\mathbf{r} = (x, y, z)$ must be separated in two regions as

$$\hat{\mathbf{G}}(\mathbf{R},\omega) = \hat{\mathbf{G}}_0(\mathbf{R},\omega) + \hat{\mathbf{G}}_R(\mathbf{R},\omega), \quad z>0, \tag{C.25}$$

$$\hat{\mathbf{G}}(\mathbf{R},\omega) = \hat{\mathbf{G}}_T(\mathbf{R},\omega), \quad z<0, \tag{C.26}$$

where $\hat{\mathbf{G}}_0(\mathbf{R},\omega)$ is direct contribution from the dipole, $\hat{\mathbf{G}}_R(\mathbf{R},\omega)$ is the reflected contribution and $\hat{\mathbf{G}}_T(\mathbf{R},\omega)$ is the transmitted part. For each polarization, we have from C.15,

$$\hat{\mathbf{G}}^\lambda(\mathbf{R},\omega) = \frac{i}{8\pi^2}\int\frac{\mathrm{d}^2\mathbf{k}_{||}}{k_z^a}e^{i\mathbf{k}_{||}\mathbf{R}}\left[\langle\mathbf{r}|\mathbf{k}^+_{a\lambda}\rangle\langle\mathbf{k}^+_{a\lambda}|\mathbf{r}'\rangle + r_\lambda\langle\mathbf{r}|\mathbf{k}^+_{a\lambda}\rangle\langle\mathbf{k}^-_{b\lambda}|\mathbf{r}'\rangle e^{ik_z^a(z+z')}\right], \quad z>0, \tag{C.27}$$

$$\hat{\mathbf{G}}^{\lambda}(\mathbf{R},\omega)=\frac{i}{8\pi^2}\int\frac{\mathrm{d}^2\mathbf{k}_{||}}{k_z^a}e^{i\mathbf{k}_{||}\mathbf{R}}t_\lambda\langle\mathbf{r}|\mathbf{k}_{b\lambda}^-\rangle\langle\mathbf{k}_{a\lambda}^-|\mathbf{r}'\rangle e^{i(k_z^a z'-k_z^b z)},\quad z<0, \tag{C.28}$$

where $k_z^a=\sqrt{\epsilon_a k_0^2-k_{||}^2}$ and $k_z^b=\sqrt{\epsilon_b k_0^2-k_{||}^2}$. In this expression we have introduced the reflection, r_λ, and transmission, t_λ, coefficients through the interface for s and p polarizations, given by

$$r_s=\frac{k_z^a-k_z^b}{k_z^a+k_z^b},\quad t_s=\frac{2k_z^a}{k_z^a+k_z^b}, \tag{C.29}$$

$$r_p=\frac{\epsilon_a k_z^b-\epsilon_b k_z^a}{\epsilon_a k_z^b+\epsilon_b k_z^a},\quad t_p=\sqrt{\frac{\epsilon_a}{\epsilon_b}}\frac{2k_z^a\epsilon_b}{\epsilon_a k_z^b+\epsilon_b k_z^a}. \tag{C.30}$$

Finally, we can write

$$\hat{\mathbf{G}}^{s}(\mathbf{R},\omega)=\frac{i}{8\pi^2}\int\frac{\mathrm{d}^2\mathbf{k}_{||}}{k_z^a k_{||}^2}e^{i\mathbf{k}_{||}\mathbf{R}_{||}}\begin{pmatrix}k_y^2 & -k_xk_y & 0\\ -k_xk_y & k_x^2 & 0\\ 0 & 0 & 0\end{pmatrix}\left[1+r_s e^{ik_z^a(z+z')}\right],\quad z>0, \tag{C.31}$$

$$\hat{\mathbf{G}}^{p}(\mathbf{R},\omega)=\frac{i}{8\pi^2}\int\frac{\mathrm{d}^2\mathbf{k}_{||}}{\epsilon_a k_0^2 k_{||}^2}e^{i\mathbf{k}_{||}\mathbf{R}_{||}}\begin{pmatrix}k_x^2k_z^a & k_xk_yk_z^a & k_xk_{||}^2\\ k_xk_yk_z^a & k_y^2k_z^a & k_yk_{||}^2\\ -k_xk_{||}^2 & -k_yk_{||}^2 & -k_{||}^4/k_z^a\end{pmatrix}\left[1+r_p e^{ik_z^a(z+z')}\right],\quad z>0, \tag{C.32}$$

$$\hat{\mathbf{G}}^{s}(\mathbf{R},\omega)=\frac{i}{8\pi^2}\int\frac{\mathrm{d}^2\mathbf{k}_{||}}{k_z^a k_{||}^2}e^{i\mathbf{k}_{||}\mathbf{R}_{||}}\begin{pmatrix}k_y^2 & -k_xk_y & 0\\ -k_xk_y & k_x^2 & 0\\ 0 & 0 & 0\end{pmatrix}t_s e^{i(k_z^a z'-k_z^b z)},\quad z<0, \tag{C.33}$$

$$\hat{\mathbf{G}}^{p}(\mathbf{R},\omega)=\frac{i}{8\pi^2}\int\frac{\mathrm{d}^2\mathbf{k}_{||}}{\sqrt{\epsilon_a\epsilon_b}k_0^2 k_{||}^2}e^{i\mathbf{k}_{||}\mathbf{R}_{||}}\begin{pmatrix}k_x^2k_z^b & k_xk_yk_z^b & k_xk_{||}^2k_z^b/k_z^a\\ k_xk_yk_z^b & k_y^2k_z^b & k_yk_{||}^2k_z^b/k_z^a\\ k_xk_{||}^2 & k_yk_{||}^2 & k_{||}^4/k_z^a\end{pmatrix}t_p e^{i(k_z^a z'-k_z^b z)},\quad z<0. \tag{C.34}$$

Bibliography

[1] J. D. Jackson. *Classical Electrodynamics* (Wiley, 1998), third edition. (cited on pages 1, 8, 18, and 93)

[2] S. Nie and S. Emory. Probing single molecules and single nanoparticles by surface-enhanced raman scattering. Science **275**, 1102 (1997). (cited on p. 1)

[3] S. I. Bozhevolnyi, V. S. Volkov, E. Devaux, J.-Y. Laluet, and T. W. Ebbesen. Channel plasmon subwavelength waveguide components including interferometers and ring resonators. Nature **440**, 508 (2006). (cited on p. 1)

[4] L. Novotny and S. J. Stranick. Near-field optical microscopy and spectroscopy with pointed probes. Annual review of physical chemistry **57**, 303 (2006). (cited on p. 1)

[5] H. A. Atwater and A. Polman. Plasmonics for improved photovoltaic devices. Nature Materials **9**, 865 (2010). (cited on p. 1)

[6] H. Raether. *Surface Plasmons on Smooth and Rough Surfaces and on Gratings* (Springer, 1988). (cited on pages 2 and 6)

[7] W. L. Barnes, A. Dereux, and T. W. Ebbesen. Surface plasmon subwavelength optics. Nature **424**, 824 (2003). (cited on pages 2 and 33)

[8] S. A. Maier and H. A. Atwater. Plasmonics: Localization and guiding of electromagnetic energy in metal/dielectric structures. Journal of Applied Physics **98**, 011101 (2005). (cited on pages 2 and 33)

[9] D. K. Gramotnev and S. I. Bozhevolnyi. Plasmonics beyond the diffraction limit. Nature Photonics **4**, 83 (2010). (cited on pages 2 and 33)

[10] E. Ozbay. Plasmonics: merging photonics and electronics at nanoscale dimensions. Science (New York, N.Y.) **311**, 189 (2006). (cited on p. 2)

[11] L. Novotny and B. Hetch. *Principles of Nanooptics* (Cambridge University Press,

Cambridge, 2006), first edition. (cited on pages 3, 31, 93, 98, 118, 164, and 181)

[12] S. Rodrigo, F. J. García-Vidal, and L. Martín-Moreno. Influence of material properties on extraordinary optical transmission through hole arrays. Physical Review B **77**, 075401 (2008). (cited on pages 3 and 94)

[13] P. B. Johnson and R. W. Christy. Optical constants of noble metals. Physical Review B **6**, 4370 (1972). (cited on pages 3 and 4)

[14] E. Palik. *Handbook of Optical Constants of Solids* (Academic Press Handbook Series (New York), edited by Edward D. Palik, 1985). (cited on pages 3, 4, 125, 148, and 163)

[15] A. Otto. Excitation of nonradiative surface plasma waves in silver by the method of frustrated total reflection. Zeits. Phys. **216**, 398 (1968). (cited on p. 6)

[16] E. Kretschmann and H. Raether. Radiative decay of non radiative surface plasmons excited by light. Z. Naturforschung, A **23**, 2135 (1968). (cited on p. 6)

[17] A. V. Zayats, I. I. Smolyaninov, and A. A. Maradudin. Nano-optics of surface plasmon polaritons. Physics Reports **408**, 131 (2005). (cited on p. 6)

[18] M. Pelton, J. Aizpurua, and G. Bryant. Metal-nanoparticle plasmonics. Laser & Photonics Review **2**, 136 (2008). (cited on p. 8)

[19] S. A. Maier. *Plasmonics fundamentals and applications.* (Springer, Boston, MA, 2007). (cited on p. 8)

[20] P. Bharadwaj, B. Deutsch, and L. Novotny. Optical Antennas. Advances in Optics and Photonics **1**, 438 (2009). (cited on pages 8 and 9)

[21] J. Aizpurua, G. W. Bryant, L. J. Richter, and F. J. García de Abajo. Optical properties of coupled metallic nanorods for field-enhanced spectroscopy. Physical Review B **71**, 235420 (2005). (cited on p. 8)

[22] P. Mühlschlegel, H.-J. Eisler, O. J. F. Martin, B. Hecht, and D. W. Pohl. Resonant optical antennas. Science (New York, N.Y.) **308**, 1607 (2005). (cited on p. 8)

[23] P. J. Schuck, D. P. Fromm, A. Sundaramurthy, G. S. Kino, and W. E. Moerner. Improving the Mismatch between Light and Nanoscale Objects with Gold Bowtie Nanoantennas. Physical Review Letters **94**, 017402 (2005). (cited on p. 8)

[24] G. W. Bryant, F. J. García de Abajo, and J. Aizpurua. Mapping the plasmon

resonances of metallic nanoantennas. Nano letters **8**, 631 (2008). (cited on p. 8)

[25] A. Kinkhabwala, Z. Yu, S. Fan, Y. Avlasevich, K. Müllen, and W. E. Moerner. Large single-molecule fluorescence enhancements produced by a bowtie nanoantenna. Nature Photonics **3**, 654 (2009). (cited on p. 8)

[26] A. G. Curto, G. Volpe, T. H. Taminiau, M. P. Kreuzer, R. Quidant, and N. F. van Hulst. Unidirectional emission of a quantum dot coupled to a nanoantenna. Science (New York, N.Y.) **329**, 930 (2010). (cited on p. 8)

[27] C. Höppener, Z. J. Lapin, P. Bharadwaj, and L. Novotny. Self-Similar Gold-Nanoparticle Antennas for a Cascaded Enhancement of the Optical Field. Physical Review Letters **109**, 017402 (2012). (cited on p. 8)

[28] P. Anger, P. Bharadwaj, and L. Novotny. Enhancement and Quenching of Single-Molecule Fluorescence. Physical Review Letters **96**, 113002 (2006). (cited on pages 8, 28, and 130)

[29] S. Kühn, U. Hakanson, L. Rogobete, and V. Sandoghdar. Enhancement of Single-Molecule Fluorescence Using a Gold Nanoparticle as an Optical Nanoantenna. Physical Review Letters **97**, 017402 (2006). (cited on pages 8, 28, and 130)

[30] L. Novotny. Effective Wavelength Scaling for Optical Antennas. Physical Review Letters **98**, 266802 (2007). (cited on p. 9)

[31] P. Ghenuche, S. Cherukulappurath, T. H. Taminiau, N. F. van Hulst, and R. Quidant. Spectroscopic Mode Mapping of Resonant Plasmon Nanoantennas. Physical Review Letters **101**, 116805 (2008). (cited on p. 9)

[32] L. Novotny and N. F. van Hulst. Antennas for light. Nature Photonics **5**, 83 (2011). (cited on p. 9)

[33] A. H. Castro Neto, N. M. R. Peres, K. S. Novoselov, and A. K. Geim. The electronic properties of graphene. Reviews of Modern Physics **81**, 109 (2009). (cited on p. 9)

[34] F. Bonaccorso, Z. Sun, T. Hasan, and A. C. Ferrari. Graphene photonics and optoelectronics. Nature Photonics **4**, 611 (2010). (cited on p. 9)

[35] M. Liu, X. Yin, E. Ulin-Avila, B. Geng, T. Zentgraf, L. Ju, F. Wang, and X. Zhang. A graphene-based broadband optical modulator. Nature **474**, 64 (2011). (cited on p. 9)

[36] B. Wunsch, T. Stauber, F. Sols, and F. Guinea. Dynamical polarization of graphene at

finite doping. New Journal of Physics **8**, 318 (2006). (cited on p. 9)

[37] E. H. Hwang and S. Das Sarma. Dielectric function, screening, and plasmons in two-dimensional graphene. Physical Review B **75**, 205418 (2007). (cited on p. 9)

[38] K. W. K. Shung. Dielectric function and plasmon structure of stage-1 intercalated graphite. Physical Review B **34**, 979 (1986). (cited on p. 11)

[39] O. Vafek. Thermoplasma Polariton within Scaling Theory of Single-Layer Graphene. Physical Review Letters **97**, 266406 (2006). (cited on p. 11)

[40] G. W. Hanson. Dyadic Green's functions and guided surface waves for a surface conductivity model of graphene. Journal of Applied Physics **103**, 064302 (2008). (cited on p. 11)

[41] M. Jablan, H. Buljan, and M. Soljačić. Plasmonics in graphene at infrared frequencies. Physical Review B **80**, 245435 (2009). (cited on p. 11)

[42] A. A. Dubinov, V. Y. Aleshkin, V. Mitin, T. Otsuji, and V. Ryzhii. Terahertz surface plasmons in optically pumped graphene structures. Journal of Phys.: Condensed Matter **23**, 145302 (2011). (cited on p. 11)

[43] Z. Fei, G. O. Andreev, W. Bao, L. M. Zhang, A. S McLeod, C. Wang, M. K. Stewart, Z. Zhao, G. Dominguez, M. Thiemens, M. M. Fogler, M. J. Tauber, A. H. Castro-Neto, C. N. Lau, F. Keilmann, and D. N. Basov. Infrared nanoscopy of dirac plasmons at the graphene-SiO2 interface. Nano letters **11**, 4701 (2011). (cited on p. 11)

[44] Z. Fei, A. S. Rodin, G. O. Andreev, W. Bao, A. S. McLeod, M. Wagner, L. M. Zhang, Z. Zhao, M. Thiemens, G. Dominguez, M. M. Fogler, A. H. Castro-Neto, C. N. Lau, F. Keilmann, and D. N. Basov. Gate-tuning of graphene plasmons revealed by infrared nano-imaging. Nature **487**, 82 (2012). (cited on p. 11)

[45] J. Chen, M. Badioli, P. Alonso-González, S. Thongrattanasiri, F. Huth, J. Osmond, M. Spasenović, A. Centeno, A. Pesquera, P. Godignon, A. Z. Elorza, N. Camara, F. J. García de Abajo, R. Hillenbrand, and F. H. L. Koppens. Optical nano-imaging of gate-tunable graphene plasmons. Nature **487**, 77 (2012). (cited on p. 11)

[46] F. H. L. Koppens, D. E. Chang, and F. J. García de Abajo. Graphene Plasmonics : A Platform for Strong Light-Matter Interaction. Nano letters **11**, 3370 (2011). (cited on p. 11)

[47] A. Y. Nikitin, F. Guinea, F. J. Garcia-Vidal, and L. Martin-Moreno. Fields radiated by

a nanoemitter in a graphene sheet. Physical Review B **84**, 195446 (2011). (cited on p. 11)

[48] K. A. Velizhanin and A. Efimov. Probing plasmons in graphene by resonance energy transfer. Physical Review B **84**, 085401 (2011). (cited on p. 11)

[49] G. Gómez-Santos and T. Stauber. Fluorescence quenching in graphene: A fundamental ruler and evidence for transverse plasmons. Physical Review B **84**, 165438 (2011). (cited on p. 11)

[50] L. Gaudreau, K. J. Tielrooij, G. E. D. K. Prawiroatmodjo, J. Osmond, F. J. García de Abajo, and F. H. L. Koppens. Universal distance-scaling of nonradiative energy transfer to graphene. Nano letters **13**, 2030 (2013). (cited on p. 11)

[51] J. B. Pendry, D. Schurig, and D. R. Smith. Controlling electromagnetic fields. Science (New York, N.Y.) **312**, 1780 (2006). (cited on pages 12, 13, 15, 33, and 36)

[52] U. Leonhardt and T. G. Philbin. General relativity in electrical engineering. New Journal of Physics **8**, 247 (2006). (cited on pages 12 and 33)

[53] A. J. Ward and J. B. Pendry. Refraction and geometry in Maxwell's equations. Journal of Modern Optics **43**, 773 (1996). (cited on p. 12)

[54] D. Schurig, J. B. Pendry, and D. R. Smith. Calculation of material properties and ray tracing in transformation media. Optics express **14**, 9794 (2006). (cited on pages 12, 13, and 15)

[55] U. Leonhardt. Optical Conformal Mapping. Science **312**, 1777 (2006). (cited on pages 13, 15, 36, 47, 48, and 176)

[56] M. Rahm, S. A. Cummer, D. Schurig, J. B. Pendry, and D. R. Smith. Optical Design of Reflectionless Complex Media by Finite Embedded Coordinate Transformations. Physical Review Letters **100**, 063903 (2008). (cited on pages 14 and 40)

[57] D.-H. Kwon and D. H. Werner. Polarization splitter and polarization rotator designs based on transformation optics. Optics express **16**, 18731 (2008). (cited on p. 14)

[58] H. Chen, J. Ng, C. Lee, Y. Lai, and C. Chan. General transformation for the reduced invisibility cloak. Physical Review B **80**, 085112 (2009). (cited on p. 14)

[59] M. Rahm, D. A. Roberts, J. B. Pendry, and D. R. Smith. Transformation-optical design of adaptive beam bends and beam expanders. Optics express **16**, 11555 (2008).

(cited on p. 14)

[60] D.-H. Kwon and D. H. Werner. Transformation optical designs for wave collimators, flat lenses and right-angle bends. New Journal of Physics **10**, 115023 (2008). (cited on p. 14)

[61] D. A. Roberts, M. Rahm, J. B. Pendry, and D. R. Smith. Transformation-optical design of sharp waveguide bends and corners. Applied Physics Letters **93**, 251111 (2008). (cited on p. 14)

[62] M. Rahm, D. Schurig, D. A. Roberts, S. A. Cummer, D. R. Smith, and J. B. Pendry. Design of electromagnetic cloaks and concentrators using form-invariant coordinate transformations of Maxwell's equations. Photonics and Nanostructures - Fundamentals and Applications **6**, 87 (2008). (cited on p. 14)

[63] D. A. Genov, S. Zhang, and X. Zhang. Mimicking celestial mechanics in metamaterials. Nature Physics **5**, 687 (2009). (cited on p. 14)

[64] S. A. Ramakrishna. Physics of negative refractive index materials. Reports on Progress in Physics **68**, 449 (2005). (cited on pages 14 and 15)

[65] Ziolkowski, R W and N. Engheta. *Metamaterials: Physics and Engineering Explorations* (John Wiley & Sons, Inc., Hoboken, NJ, 2006), first edition. (cited on p. 14)

[66] V. M. Shalaev. Optical negative-index metamaterials. Nature Photonics **1**, 41 (2007). (cited on p. 14)

[67] Cai, W S and Shalaev, V M. *Optical Metamaterials: Fundamentals and Applications* (Springer, New York, 2009), first edition. (cited on p. 14)

[68] Cui, T J, Smith, D R, and Liu, R P. *Metamaterials: Theory, Design and Applications* (Springer, 2009), first edition. (cited on p. 14)

[69] M. Wegener and S. Linden. Shaping optical space with metamaterials feature. Physics Today **63**, 32 (2010). (cited on p. 14)

[70] Y. Liu and X. Zhang. Metamaterials: a new frontier of science and technology. Chemical Society reviews **40**, 2494 (2011). (cited on p. 14)

[71] J. B. Pendry, A. J. Holden, W. J. Stewart, and I. Youngs. Extremely low frequency plasmons in metallic mesostructures. Physical review letters **76**, 4773 (1996). (cited on pages 14 and 15)

[72] J. B. Pendry, A. J. Holden, D. J. Robbins, and W. J. Stewart. Magnetism from conductors and enhanced nonlinear phenomena. IEEE Transactions on Microwave Theory and Techniques **47**, 2075 (1999). (cited on pages 14, 15, and 76)

[73] R. A. Shelby, D. R. Smith, and S. Schultz. Experimental verification of a negative index of refraction. Science (New York, N.Y.) **292**, 77 (2001). (cited on p. 15)

[74] D. R. Smith, J. B. Pendry, and M. C. K. Wiltshire. Metamaterials and negative refractive index. Science (New York, N.Y.) **305**, 788 (2004). (cited on p. 15)

[75] C. M. Soukoulis, S. Linden, and M. Wegener. Negative refractive index at optical wavelengths. Science (New York, N.Y.) **315**, 47 (2007). (cited on p. 15)

[76] H. J. Lezec, J. A. Dionne, and H. A. Atwater. Negative refraction at visible frequencies. Science (New York, N.Y.) **316**, 430 (2007). (cited on p. 15)

[77] J. Yao, Z. Liu, Y. Liu, Y. Wang, C. Sun, G. Bartal, A. M. Stacy, and X. Zhang. Optical negative refraction in bulk metamaterials of nanowires. Science (New York, N.Y.) **321**, 930 (2008). (cited on p. 15)

[78] J. Valentine, S. Zhang, T. Zentgraf, E. Ulin-Avila, D. A. Genov, G. Bartal, and X. Zhang. Three-dimensional optical metamaterial with a negative refractive index. Nature **455**, 376 (2008). (cited on p. 15)

[79] N. Fang, H. Lee, C. Sun, and X. Zhang. Sub–Diffraction-Limited Optical Imaging with a Silver Superlens. Science **308**, 534 (2005). (cited on p. 15)

[80] T. Taubner, D. Korobkin, Y. Urzhumov, G. Shvets, and R. Hillenbrand. Near-field microscopy through a SiC superlens. Science (New York, N.Y.) **313**, 1595 (2006). (cited on p. 15)

[81] X. Zhang and Z. Liu. Superlenses to overcome the diffraction limit. Nature materials **7**, 435 (2008). (cited on p. 15)

[82] S. Zhang, Y.-S. Park, J. Li, X. Lu, W. Zhang, and X. Zhang. Negative Refractive Index in Chiral Metamaterials. Physical Review Letters **102**, 023901 (2009). (cited on p. 15)

[83] J. K. Gansel, M. Thiel, M. S. Rill, M. Decker, K. Bade, V. Saile, G. von Freymann, S. Linden, and M. Wegener. Gold helix photonic metamaterial as broadband circular polarizer. Science (New York, N.Y.) **325**, 1513 (2009). (cited on p. 15)

[84] C. M. Soukoulis and M. Wegener. Past achievements and future challenges in the

development of three-dimensional photonic metamaterials. Nature Photonics **5**, 523 (2011). (cited on p. 15)

[85] O. Hess, J. B. Pendry, S. A. Maier, R. F. Oulton, J. M. Hamm, and K. L. Tsakmakidis. Active nanoplasmonic metamaterials. Nature materials **11**, 573 (2012). (cited on p. 15)

[86] A. V. Kildishev, A. Boltasseva, and V. M. Shalaev. Planar Photonics with Metasurfaces. Science **339**, 1232009 (2013). (cited on pages 15 and 83)

[87] M. C. K. Wiltshire, J. B. Pendry, I. R. Young, D. J. Larkman, D. J. Gilderdale, and J. V. Hajnal. Microstructured Magnetic Materials for RF Flux Guides in Magnetic Resonance Imaging. Science **291**, 849 (2001). (cited on p. 15)

[88] D. Schurig, J. J. Mock, B. J. Justice, S. A. Cummer, J. B. Pendry, A. F. Starr, and D. R. Smith. Metamaterial Electromagnetic Cloak at Microwave Frequencies. Science **314**, 977 (2006). (cited on pages 15, 16, and 36)

[89] J. Valentine, J. Li, T. Zentgraf, G. Bartal, and X. Zhang. An optical cloak made of dielectrics. Nature materials **8**, 568 (2009). (cited on pages 16, 17, and 48)

[90] T. Ergin, N. Stenger, P. Brenner, J. B. Pendry, and M. Wegener. Three-dimensional invisibility cloak at optical wavelengths. Science (New York, N.Y.) **328**, 337 (2010). (cited on pages 16 and 17)

[91] B. Zhang, Y. Luo, X. Liu, and G. Barbastathis. Macroscopic Invisibility Cloak for Visible Light. Physical Review Letters **106**, 033901 (2011). (cited on pages 16 and 17)

[92] H. Chen, C. T. Chan, and P. Sheng. Transformation optics and metamaterials. Nature materials **9**, 387 (2010). (cited on p. 15)

[93] J. Li and J. B. Pendry. Hiding under the Carpet: A New Strategy for Cloaking. Physical Review Letters **101**, 203901 (2008). (cited on pages 16, 48, and 54)

[94] R. Liu, C. Ji, J. J. Mock, J. Y. Chin, T. J. Cui, and D. R. Smith. Broadband Ground-Plane Cloak. Science **323**, 366 (2009). (cited on pages 17 and 48)

[95] L. H. Gabrielli, J. Cardenas, C. B. Poitras, and M. Lipson. Silicon nanostructure cloak operating at optical frequencies. Nature Photonics **3**, 461 (2009). (cited on pages 17 and 48)

[96] X. Chen, Y. Luo, J. Zhang, K. Jiang, J. B. Pendry, and S. Zhang. Macroscopic invisibility cloaking of visible light. Nature communications **2**, 176 (2011).

(cited on p. 17)

[97] P. A. Huidobro, M. L. Nesterov, L. Martín-Moreno, and F. J. García-Vidal. Transformation optics for plasmonics. Nano Letters **10**, 1985 (2010). (cited on pages 17, 18, and 34)

[98] Y. Liu, T. Zentgraf, G. Bartal, and X. Zhang. Transformational plasmon optics. Nano letters **10**, 1991 (2010). (cited on pages 17, 18, 34, and 47)

[99] J. Renger, M. Kadic, G. Dupont, S. S. Aćimović, S. Guenneau, R. Quidant, and S. Enoch. Hidden progress: broadband plasmonic invisibility. Optics express **18**, 15757 (2010). (cited on pages 17, 34, 58, and 59)

[100] T. Zentgraf, Y. Liu, M. H. Mikkelsen, J. Valentine, and X. Zhang. Plasmonic Luneburg and Eaton lenses. Nature nanotechnology **6**, 151 (2011). (cited on pages 17, 34, 58, 59, 60, and 61)

[101] M. Kadic, S. Guenneau, S. Enoch, P. A. Huidobro, L. Martín-Moreno, F. J. García-Vidal, J. Renger, and R. Quidant. Transformation plasmonics. Nanophotonics **1**, 51 (2012). (cited on pages 17, 57, and 58)

[102] Y. Liu and X. Zhang. Recent advances in transformation optics. Nanoscale **4**, 5277 (2012). (cited on p. 17)

[103] W. Cai and M. L. Brongersma. Nanoscale optics: Plasmonics gets transformed. Nature nanotechnology **5**, 485 (2010). (cited on pages 17 and 18)

[104] A. Vakil and N. Engheta. Transformation optics using graphene. Science (New York, N.Y.) **332**, 1291 (2011). (cited on p. 17)

[105] P. A. Huidobro, M. L. Nesterov, L. Martín-Moreno, and F. J. García-Vidal. Moulding the flow of surface plasmons using conformal and quasiconformal mappings. New Journal of Physics **13**, 033011 (2011). (cited on pages 17 and 34)

[106] A. Aubry, D. Y. Lei, A. I. Fernández-Domínguez, Y. Sonnefraud, S. A. Maier, and J. B. Pendry. Plasmonic light-harvesting devices over the whole visible spectrum. Nano letters **10**, 2574 (2010). (cited on pages 17 and 47)

[107] Y. Luo, J. B. Pendry, and A. Aubry. Surface plasmons and singularities. Nano letters **10**, 4186 (2010). (cited on p. 17)

[108] A. I. Fernández-Domínguez, S. A. Maier, and J. B. Pendry. Collection and

Concentration of Light by Touching Spheres: A Transformation Optics Approach. Physical Review Letters **105**, 266807 (2010). (cited on p. 17)

[109] A. I. Fernández-Domínguez, Y. Luo, A. Wiener, J. B. Pendry, and S. A. Maier. Theory of three-dimensional nanocrescent light harvesters. Nano letters **12**, 5946 (2012). (cited on pages 17 and 18)

[110] A. I. Fernández-Domínguez, A. Wiener, F. J. García-Vidal, S. A. Maier, and J. B. Pendry. Transformation-Optics Description of Nonlocal Effects in Plasmonic Nanostructures. Physical Review Letters **108**, 106802 (2012). (cited on p. 18)

[111] A. I. Fernández-Domínguez, P. Zhang, Y. Luo, S. A. Maier, F. J. García-Vidal, and J. B. Pendry. Transformation-optics insight into nonlocal effects in separated nanowires. Physical Review B **86**, 241110 (2012). (cited on p. 18)

[112] R. Zhao, Y. Luo, A. I. Fernández-Domínguez, and J. B. Pendry. Description of van der Waals Interactions Using Transformation Optics. Physical Review Letters **111**, 033602 (2013). (cited on p. 18)

[113] J. B. Pendry, A. I. Fernández-Domínguez, Y. Luo, and R. Zhao. Capturing photons with transformation optics. Nature Physics **9**, 518 (2013). (cited on p. 18)

[114] J. Zenneck. Propagation of plane electromagnetic waves along a plane conducting surface. Ann. Phys.(Leipzig) **23**, 846 (1907). (cited on p. 18)

[115] A. Sommerfeld. Propagation of electrodynamic waves along a cylindric conductor. Ann. Phys. und Chemie **67**, 233 (1899). (cited on p. 18)

[116] B. A. Munk. *Frequency Selective Surfaces: Theory and Design* (Wiley-Interscience, 2000), first edition. (cited on p. 18)

[117] J. B. Pendry, L. Martín-Moreno, and F. J. García-Vidal. Mimicking surface plasmons with structured surfaces. Science (New York) **305**, 847 (2004). (cited on pages 18, 19, 20, 21, and 63)

[118] F. J. García-Vidal, L. Martín-Moreno, and J. B. Pendry. Surfaces with holes in them: new plasmonic metamaterials. Journal of Optics A: Pure and Applied Optics **7**, S97 (2005). (cited on pages 18, 19, 20, 21, and 63)

[119] B. Ferguson and X.-C. Zhang. Materials for terahertz science and technology. Nature materials **1**, 26 (2002). (cited on p. 21)

[120] A. P. Hibbins, B. R. Evans, and J. R. Sambles. Experimental verification of designer surface plasmons. Science (New York, N.Y.) **308**, 670 (2005). (cited on pages 21 and 63)

[121] A. Hibbins, M. Lockyear, I. Hooper, and J. Sambles. Waveguide Arrays as Plasmonic Metamaterials: Transmission below Cutoff. Physical Review Letters **96**, 073904 (2006). (cited on pages 21 and 63)

[122] C. R. Williams, S. R. Andrews, S. A. Maier, A. I. Fernández-Domínguez, L. Martín-Moreno, and F. J. García-Vidal. Highly confined guiding of terahertz surface plasmon polaritons on structured metal surfaces. Nature Photonics **2**, 175 (2008). (cited on pages 21 and 63)

[123] N. Yu, Q. J. Wang, M. A. Kats, J. A. Fan, S. P. Khanna, L. Li, A. G. Davies, E. H. Linfield, and F. Capasso. Designer spoof surface plasmon structures collimate terahertz laser beams. Nature materials **9**, 730 (2010). (cited on pages 21 and 63)

[124] F. J. García de Abajo and J. J. Sáenz. Electromagnetic Surface Modes in Structured Perfect-Conductor Surfaces. Physical Review Letters **95**, 233901 (2005). (cited on pages 21 and 63)

[125] E. Hendry, A. P. Hibbins, and J. R. Sambles. Importance of diffraction in determining the dispersion of designer surface plasmons. Physical Review B **78**, 235426 (2008). (cited on pages 21 and 63)

[126] S. A. Maier, S. A. Andrews, L. Martín-Moreno, and F. García-Vidal. Terahertz Surface Plasmon-Polariton Propagation and Focusing on Periodically Corrugated Metal Wires. Physical Review Letters **97**, 176805 (2006). (cited on pages 21 and 63)

[127] A. I. Fernández-Domínguez, E. Moreno, L. Martín-Moreno, and F. J. García-Vidal. Terahertz wedge plasmon polaritons. Optics letters **34**, 2063 (2009). (cited on pages 21 and 63)

[128] A. I. Fernández-Domínguez, E. Moreno, L. Martín-Moreno, and F. García-Vidal. Guiding terahertz waves along subwavelength channels. Physical Review B **79**, 233104 (2009). (cited on pages 21 and 63)

[129] D. Martín-Cano, M. L. Nesterov, A. I. Fernández-Domínguez, F. J. García-Vidal, L. Martín-Moreno, and E. Moreno. Domino plasmons for subwavelength terahertz circuitry. Optics express **18**, 754 (2010). (cited on pages 21 and 63)

[130] M. A. Kats, D. Woolf, R. Blanchard, N. Yu, and F. Capasso. Spoof plasmon analogue

of metal-insulator-metal waveguides. Optics express **19**, 14860 (2011). (cited on pages 21 and 63)

[131] D. Martín-Cano, O. Quevedo-Teruel, E. Moreno, L. Martín-Moreno, and F. J. García-Vidal. Waveguided spoof surface plasmons with deep-subwavelength lateral confinement. Optics letters **36**, 4635 (2011). (cited on pages 21 and 63)

[132] A. I. Fernández-Domínguez, C. R. Williams, F. J. García-Vidal, L. Martín-Moreno, S. R. Andrews, and S. A. Maier. Terahertz surface plasmon polaritons on a helically grooved wire. Applied Physics Letters **93**, 141109 (2008). (cited on pages 21 and 63)

[133] E. M. G. Brock, E. Hendry, and A. P. Hibbins. Subwavelength lateral confinement of microwave surface waves. Applied Physics Letters **99**, 051108 (2011). (cited on pages 21 and 63)

[134] M. L. Nesterov, D. Martin-Cano, A. I. Fernández-Domínguez, E. Moreno, L. Martín-Moreno, and F. J. García-Vidal. Geometrically induced modification of surface plasmons in the optical and telecom regimes. Optics letters **35**, 423 (2010). (cited on pages 21 and 63)

[135] X. Shen, T. J. Cui, D. Martín-cano, and F. J. García-vidal. Conformal surface plasmons propagating on ultrathin and flexible films. Proceedings of the National Academy of Sciences **110**, 40 (2013). (cited on pages 21 and 63)

[136] A. Pors, E. Moreno, L. Martín-Moreno, J. B. Pendry, and F. J. García-Vidal. Localized Spoof Plasmons Arise while Texturing Closed Surfaces. Physical Review Letters **108**, 223905 (2012). (cited on pages 21, 22, 63, 65, and 70)

[137] D. G. Grier. A revolution in optical manipulation. Nature **424**, 810 (2003). (cited on p. 22)

[138] A. Ashkin and J. M. Dziedzic. Optical trapping and manipulation of viruses and bacteria. Science (New York, N.Y.) **235**, 1517 (1987). (cited on p. 22)

[139] A. Ashkin, J. M. Dziedzic, and T. Yamanel. Optical trapping and manipulation of single cells using infrared laser beams. Nature **330**, 469 (1987). (cited on p. 22)

[140] M. L. Juan, M. Righini, and R. Quidant. Plasmon nano-optical tweezers. Nature Photonics **5**, 349 (2011). (cited on pages 22 and 89)

[141] S. Kawata and T. Sugiura. Movement of micrometer-sized particles in the evanescent field of a laser beam. Optics letters **17**, 772 (1992). (cited on p. 22)

[142] C. Girard, A. Dereux, and O. J. F. Martin. Theoretical analysis of light-inductive forces in scanning probe microscopy. Physical Review B **49**, 13 872 (1994). (cited on p. 22)

[143] L. Novotny, R. X. Bian, and X. S. Xie. Theory of Nanometric Optical Tweezers. Physical Review Letters **79**, 645 (1997). (cited on pages 22 and 23)

[144] P. Chaumet, A. Rahmani, and M. Nieto-Vesperinas. Optical Trapping and Manipulation of Nano-objects with an Apertureless Probe. Physical Review Letters **88**, 123601 (2002). (cited on p. 22)

[145] R. Quidant, D. Petrov, and G. Badenes. Radiation forces on a Rayleigh dielectric sphere in a patterned optical near field. Optics letters **30**, 1009 (2005). (cited on p. 22)

[146] M. Righini, C. Girard, and R. Quidant. Light-induced manipulation with surface plasmons. Journal of Optics A: Pure and Applied Optics **10**, 093001 (2008). (cited on p. 23)

[147] M. Righini, A. S. Zelenina, C. Girard, and R. Quidant. Parallel and selective trapping in a patterned plasmonic landscape. Nature Physics **3**, 477 (2007). (cited on pages 23, 24, and 89)

[148] M. Righini, G. Volpe, C. Girard, D. Petrov, and R. Quidant. Surface Plasmon Optical Tweezers: Tunable Optical Manipulation in the Femtonewton Range. Physical Review Letters **100**, 186804 (2008). (cited on pages 23 and 89)

[149] G. Volpe, R. Quidant, G. Badenes, and D. Petrov. Surface Plasmon Radiation Forces. Physical Review Letters **96**, 238101 (2006). (cited on pages 24 and 89)

[150] A. N. Grigorenko, N. W. Roberts, M. R. Dickinson, and Y. Zhang. Nanometric optical tweezers based on nanostructured substrates. Nature Photonics **2**, 365 (2008). (cited on pages 24 and 89)

[151] M. Righini, P. Ghenuche, S. Cherukulappurath, V. Myroshnychenko, F. J. García de Abajo, and R. Quidant. Nano-optical trapping of Rayleigh particles and Escherichia coli bacteria with resonant optical antennas. Nano letters **9**, 3387 (2009). (cited on pages 24, 89, and 107)

[152] W. Zhang, L. Huang, C. Santschi, and O. J. F. Martin. Trapping and sensing 10 nm metal nanoparticles using plasmonic dipole antennas. Nano letters **10**, 1006 (2010). (cited on p. 25)

[153] D. Erickson, X. Serey, Y.-F. Chen, and S. Mandal. Nanomanipulation using near field

photonics. Lab on a chip **11**, 995 (2011). (cited on pages 25 and 89)

[154] J. Kim. Joining plasmonics with microfluidics: from convenience to inevitability. Lab on a chip **12**, 3611 (2012). (cited on p. 25)

[155] P. A. Huidobro, S. Ota, X. Yang, X. Yin, F. J. García-Vidal, and X. Zhang. Plasmonic Brownian ratchet. Physical Review B **88**, 201401(R) (2013). (cited on p. 25)

[156] C. Monroe. Quantum information processing with atoms and photons. Nature **416**, 238 (2002). (cited on pages 26 and 109)

[157] J. M. Raimond, M. Brune, and S. Haroche. Colloquium: Manipulating quantum entanglement with atoms and photons in a cavity. Reviews of Modern Physics **73**, 565 (2001). (cited on pages 26 and 31)

[158] J. Mckeever, A. Boca, A. D. Boozer, R. Miller, J. R. Buck, A. Kuzmich, and H. J. Kimble. Deterministic Generation of Single Photons from One Atom. Science **303**, 1992 (2004). (cited on p. 26)

[159] K. Hennessy, A. Badolato, M. Winger, D. Gerace, M. Atatüre, S. Gulde, S. Fält, E. L. Hu, and A. Imamoğlu. Quantum nature of a strongly coupled single quantum dot-cavity system. Nature **445**, 896 (2007). (cited on p. 26)

[160] C. Kurtsiefer, S. Mayer, P. Zarda, and H. Weinfurter. Stable solid-state source of single photons. Physical review letters **85**, 290 (2000). (cited on p. 26)

[161] X. Zhu, S. Saito, A. Kemp, K. Kakuyanagi, S.-i. Karimoto, H. Nakano, W. J. Munro, Y. Tokura, M. S. Everitt, K. Nemoto, M. Kasu, N. Mizuochi, and K. Semba. Coherent coupling of a superconducting flux qubit to an electron spin ensemble in diamond. Nature **478**, 221 (2011). (cited on p. 26)

[162] M. S. Tame, K. R. McEnery, S. K. Özdemir, J. Lee, S. A. Maier, and M. S. Kim. Quantum plasmonics. Nature Physics **9**, 329 (2013). (cited on p. 26)

[163] E. Altewischer, M. P. van Exter, and J. P. Woerdman. Plasmon-assisted transmission of entangled photons. Nature **418**, 304 (2002). (cited on p. 26)

[164] E. Moreno, F. J. García-Vidal, D. Erni, J. I. Cirac, and L. Martín-Moreno. Theory of Plasmon-Assisted Transmission of Entangled Photons. Physical Review Letters **92**, 236801 (2004). (cited on p. 26)

[165] S. Fasel, F. Robin, E. Moreno, D. Erni, N. Gisin, and H. Zbinden. Energy-Time

Entanglement Preservation in Plasmon-Assisted Light Transmission. Physical Review Letters **94**, 110501 (2005). (cited on p. 26)

[166] A. Huck, S. Smolka, P. Lodahl, A. S. Sorensen, A. Boltasseva, J. Janousek, and U. Andersen. Demonstration of Quadrature-Squeezed Surface Plasmons in a Gold Waveguide. Physical Review Letters **102**, 246802 (2009). (cited on p. 26)

[167] R. Kolesov, B. Grotz, G. Balasubramanian, R. J. Stöhr, A. A. L. Nicolet, P. R. Hemmer, F. Jelezko, and J. Wrachtrup. Wave-particle duality of single surface plasmon polaritons. Nature Physics **5**, 470 (2009). (cited on p. 26)

[168] Q. P. Halperin. Quantum size effects in metal particles. Reviews of Modern Physics **58**, 533 (1986). (cited on p. 27)

[169] J. A. Scholl, A. L. Koh, and J. A. Dionne. Quantum plasmon resonances of individual metallic nanoparticles. Nature **483**, 421 (2012). (cited on p. 27)

[170] E. Townsend and G. W. Bryant. Plasmonic properties of metallic nanoparticles: the effects of size quantization. Nano letters **12**, 429 (2012). (cited on p. 27)

[171] R. Esteban, A. G. Borisov, P. Nordlander, and J. Aizpurua. Bridging quantum and classical plasmonics with a quantum-corrected model. Nature communications **3**, 825 (2012). (cited on p. 27)

[172] K. J. Savage, M. M. Hawkeye, R. Esteban, A. G. Borisov, J. Aizpurua, and J. J. Baumberg. Revealing the quantum regime in tunnelling plasmonics. Nature **491**, 574 (2012). (cited on p. 27)

[173] J. A. Scholl, A. García-Etxarri, A. L. Koh, and J. A. Dionne. Observation of quantum tunneling between two plasmonic nanoparticles. Nano letters **13**, 564 (2013). (cited on p. 27)

[174] K. H. Drexhage, H. Kuhn, and F. P. Schafer. Variation of the fluorescence decay time of a molecule in front of a mirror. Berichte der Bunsengesellschaft fur physikalische Chemie **72**, 329 (1968). (cited on pages 27, 109, and 130)

[175] R. R. Chance. Lifetime of an emitting molecule near a partially reflecting surface. The Journal of Chemical Physics **60**, 2744 (1974). (cited on pages 27, 109, and 130)

[176] K. H. Drexhage. Interaction of light with monomolecular dye layers. In *Progress in Optics XII*, 165 (1974). (cited on pages 27, 109, and 130)

[177] R. M. Amos and W. L. Barnes. Modification of the spontaneous emission rate of Eu ions close to a thin metal mirror. Physical Review B **55**, 7249 (1997). (cited on pages 27, 28, 109, and 130)

[178] E. M. Purcell, H. C. Torrey, and R. V. Pound. Resonance absorption by nuclear magnetic moments in a solid. Physical Review **69**, 681 (1946). (cited on pages 27, 109, 118, and 122)

[179] G. W. Ford and W. H. Weber. Electromagnetic Iinteractions Of Molecules With Metal Surfaces. Phys. Rep. **113**, 195 (1984). (cited on pages 27, 122, 124, 125, 130, 133, and 135)

[180] W. L. Barnes. Topical review Fluorescence near interfaces : the role of photonic mode. Journal of Modern Optics **45** (1998). (cited on pages 27, 122, 124, 130, 133, and 135)

[181] D. Chang, A. S. Sorensen, P. Hemmer, and M. Lukin. Quantum Optics with Surface Plasmons. Physical Review Letters **97**, 053002 (2006). (cited on pages 28, 30, 130, and 135)

[182] A. V. Akimov, A. Mukherjee, C. L. Yu, D. E. Chang, A. S. Zibrov, P. R. Hemmer, H. Park, and M. D. Lukin. Generation of single optical plasmons in metallic nanowires coupled to quantum dots. Nature **450**, 402 (2007). (cited on pages 28, 29, 130, and 134)

[183] A. L. Falk, F. H. L. Koppens, C. L. Yu, K. Kang, N. de Leon Snapp, A. V. Akimov, M.-H. Jo, M. D. Lukin, and H. Park. Near-field electrical detection of optical plasmons and single-plasmon sources. Nature Physics **5**, 475 (2009). (cited on pages 28 and 130)

[184] L. Mandel and E. Wolf. *Optical coherence and quantum optics* (Cambridge University Press, Cambridge, UK, 1995). (cited on pages 28, 158, and 160)

[185] A. Huck, S. Kumar, A. Shakoor, and U. L. Andersen. Controlled Coupling of a Single Nitrogen-Vacancy Center to a Silver Nanowire. Physical Review Letters **106**, 096801 (2011). (cited on pages 29 and 130)

[186] V. J. Sorger, N. Pholchai, E. Cubukcu, R. F. Oulton, P. Kolchin, C. Borschel, M. Gnauck, C. Ronning, and X. Zhang. Strongly enhanced molecular fluorescence inside a nanoscale waveguide gap. Nano letters **11**, 4907 (2011). (cited on pages 29 and 130)

[187] N. P. de Leon, B. J. Shields, C. L. Yu, D. E. Englund, A. V. Akimov, M. D. Lukin, and H. Park. Tailoring Light-Matter Interaction with a Nanoscale Plasmon Resonator. Physical Review Letters **108**, 226803 (2012). (cited on pages 29 and 130)

[188] D. E. Chang, A. S. Sø rensen, E. a. Demler, and M. D. Lukin. A single-photon transistor using nanoscale surface plasmons. Nature Physics **3**, 807 (2007). (cited on p. 29)

[189] P. Kolchin, R. F. Oulton, and X. Zhang. Nonlinear Quantum Optics in a Waveguide: Distinct Single Photons Strongly Interacting at the Single Atom Level. Physical Review Letters **106**, 113601 (2011). (cited on p. 29)

[190] D. Martín-Cano, L. Martín-Moreno, F. J. García-Vidal, and E. Moreno. Resonance energy transfer and superradiance mediated by plasmonic nanowaveguides. Nano letters **10**, 3129 (2010). (cited on pages 29 and 138)

[191] R. H. Dicke. Coherence in Spontaneous Radiation Processes. Physical Review **93**, 99 (1954). (cited on pages 30 and 138)

[192] A. González-Tudela, D. Martín-Cano, E. Moreno, L. Martín-Moreno, C. Tejedor, and F. J. García-Vidal. Entanglement of Two Qubits Mediated by One-Dimensional Plasmonic Waveguides. Physical Review Letters **106**, 020501 (2011). (cited on pages 30, 138, and 154)

[193] D. Dzsotjan, J. Kästel, and M. Fleischhauer. Dipole-dipole shift of quantum emitters coupled to surface plasmons of a nanowire. Physical Review B **84**, 075419 (2011). (cited on p. 30)

[194] D. Martín-Cano, A. González-Tudela, L. Martín-Moreno, F. J. García-Vidal, C. Tejedor, and E. Moreno. Dissipation-driven generation of two-qubit entanglement mediated by plasmonic waveguides. Physical Review B **84**, 235306 (2011). (cited on p. 30)

[195] A. González-Tudela and D. Porras. Mesoscopic Entanglement Induced by Spontaneous Emission in Solid-State Quantum Optics. Physical Review Letters **110**, 080502 (2013). (cited on p. 30)

[196] A. Trügler and U. Hohenester. Strong coupling between a metallic nanoparticle and a single molecule. Physical Review B **77**, 115403 (2008). (cited on pages 30, 109, and 130)

[197] S. Savasta, R. Saija, A. Ridolfo, O. Di Stefano, P. Denti, and F. Borghese. Nanopolaritons: vacuum Rabi splitting with a single quantum dot in the center of a dimer nanoantenna. ACS nano **4**, 6369 (2010). (cited on pages 30, 109, and 130)

[198] C. Van Vlack, P. T. S. Kristensen, and S. Hughes. Spontaneous emission spectra and quantum light-matter interactions from a strongly coupled quantum dot metal-nanoparticle system. Physical Review B **85**, 075303 (2012).

(cited on pages 30, 109, and 130)

[199] M. M. Dvoynenko and J.-K. Wang. Revisiting strong coupling between a single molecule and surface plasmons. Optics letters **38**, 760 (2013). (cited on pages 30, 109, and 130)

[200] D. Chang, A. S. Sorensen, P. Hemmer, and M. Lukin. Strong coupling of single emitters to surface plasmons. Physical Review B **76**, 035420 (2007).
(cited on pages 30, 110, 130, and 136)

[201] Y. Chen, G. Chen, D. Chuu, and T. Brandes. Quantum-dot exciton dynamics with a surface plasmon: Band-edge quantum optics. Physical Review A **79**, 033815 (2009).
(cited on pages 30, 110, 130, and 136)

[202] A. González-Tudela, F. J. Rodríguez, L. Quiroga, and C. Tejedor. Dissipative dynamics of a solid-state qubit coupled to surface plasmons: From non-Markov to Markov regimes. Physical Review B **82**, 115334 (2010). (cited on pages 30, 110, 130, 133, and 136)

[203] T. Hümmer, F. J. García-Vidal, L. Martín-Moreno, and D. Zueco. Weak and strong coupling regimes in plasmonic QED. Physical Review B **87**, 115419 (2013).
(cited on pages 30, 110, and 130)

[204] J. Bellessa, C. Bonnand, J. Plenet, and J. Mugnier. Strong Coupling between Surface Plasmons and Excitons in an Organic Semiconductor. Physical Review Letters **93**, 036404 (2004). (cited on pages 30, 31, 32, 110, 147, 148, 150, and 163)

[205] T. Hakala, J. Toppari, A. Kuzyk, M. Pettersson, H. Tikkanen, H. Kunttu, and P. Törmä. Vacuum Rabi Splitting and Strong-Coupling Dynamics for Surface-Plasmon Polaritons and Rhodamine 6G Molecules. Physical Review Letters **103**, 053602 (2009).
(cited on pages 30, 32, 110, 147, 148, 157, 158, and 163)

[206] S. Aberra Guebrou, C. Symonds, E. Homeyer, J. C. Plenet, Y. N. Gartstein, V. M. Agranovich, and J. Bellessa. Coherent Emission from a Disordered Organic Semiconductor Induced by Strong Coupling with Surface Plasmons. Physical Review Letters **108**, 066401 (2012). (cited on pages 30, 110, 147, 148, 150, and 163)

[207] J. Dintinger, S. Klein, F. Bustos, W. L. Barnes, and T. W. Ebbesen. Strong coupling between surface plasmon-polaritons and organic molecules in subwavelength hole arrays. Physical Review B **71**, 035424 (2005). (cited on pages 30, 110, 147, 148, 150, and 163)

[208] P. Vasa, R. Pomraenke, G. Cirmi, E. De Re, W. Wang, S. Schwieger, D. Leipold, E. Runge, G. Cerullo, and C. Lienau. Ultrafast manipulation of strong coupling in

metal-molecular aggregate hybrid nanostructures. ACS nano **4**, 7559 (2010). (cited on pages 30, 110, 147, 148, and 163)

[209] T. Schwartz, J. A. Hutchison, C. Genet, and T. W. Ebbesen. Reversible Switching of Ultrastrong Light-Molecule Coupling. Physical Review Letters **106**, 196405 (2011). (cited on pages 30, 110, and 147)

[210] J. A. Hutchison, T. Schwartz, C. Genet, E. Devaux, and T. W. Ebbesen. Modifying chemical landscapes by coupling to vacuum fields. Angewandte Chemie (International ed. in English) **51**, 1592 (2012). (cited on pages 31 and 110)

[211] J. A. Hutchison, A. Liscio, T. Schwartz, A. Canaguier-Durand, C. Genet, V. Palermo, P. Samorì, and T. W. Ebbesen. Tuning the work-function via strong coupling. Advanced materials (Deerfield Beach, Fla.) **25**, 2481 (2013). (cited on pages 31, 110, 147, 148, and 163)

[212] P. Vasa, R. Pomraenke, S. Schwieger, Y. Mazur, V. Kunets, P. Srinivasan, E. Johnson, J. Kihm, D. Kim, E. Runge, G. Salamo, and C. Lienau. Coherent Exciton–Surface-Plasmon-Polariton Interaction in Hybrid Metal-Semiconductor Nanostructures. Physical Review Letters **101**, 116801 (2008). (cited on pages 31, 32, 110, 148, and 163)

[213] J. Bellessa, C. Symonds, C. Meynaud, J. Plenet, E. Cambril, A. Miard, L. Ferlazzo, and A. Lemaître. Exciton/plasmon polaritons in GaAs/AlGaAs heterostructures near a metallic layer. Physical Review B **78**, 205326 (2008). (cited on pages 31, 110, 148, and 163)

[214] D. E. Gómez, K. C. Vernon, P. Mulvaney, and T. J. Davis. Surface plasmon mediated strong exciton-photon coupling in semiconductor nanocrystals. Nano letters **10**, 274 (2010). (cited on pages 31, 32, 110, 148, and 163)

[215] D. E. Gomez, K. C. Vernon, P. Mulvaney, and T. J. Davis. Coherent superposition of exciton states in quantum dots induced by surface plasmons. Applied Physics Letters **96**, 073108 (2010). (cited on pages 31, 110, 148, and 163)

[216] P. Vasa, W. Wang, R. Pomraenke, M. Lammers, M. Maiuri, C. Manzoni, G. Cerullo, and C. Lienau. Real-time observation of ultrafast Rabi oscillations between excitons and plasmons in metal nanostructures with J-aggregates. Nature Photonics **7**, 128 (2013). (cited on pages 31, 110, 147, and 148)

[217] P. A. Huidobro, A. Y. Nikitin, C. González-Ballestero, L. Martín-Moreno, and F. J.

García-Vidal. Superradiance mediated by graphene surface plasmons. Physical Review B **85**, 155438 (2012). (cited on p. 31)

[218] A. González-Tudela, P. A. Huidobro, L. Martín-Moreno, C. Tejedor, and F. J. García-Vidal. Theory of Strong Coupling between Quantum Emitters and Propagating Surface Plasmons. Physical Review Letters **110**, 126801 (2013). (cited on pages 32 and 138)

[219] COMSOL. *Multiphysics 4.2a.* (cited on pages 34, 65, 94, and 145)

[220] I. I. Smolyaninov, Y. J. Hung, and C. C. Davis. Two-dimensional metamaterial structure exhibiting reduced visibility at 500nm. Optics letters **33**, 1342 (2008). (cited on p. 39)

[221] M. Yan, Z. Ruan, and M. Qiu. Cylindrical Invisibility Cloak with Simplified Material Parameters is Inherently Visible. Physical Review Letters **99**, 233901 (2007). (cited on p. 39)

[222] M. Schmiele, V. S. Varma, C. Rockstuhl, and F. Lederer. Designing optical elements from isotropic materials by using transformation optics. Physical Review A **81**, 033837 (2010). (cited on pages 40, 47, 51, and 52)

[223] D.-H. Kwon and D. H. Werner. Transformation optical designs for wave collimators, flat lenses and right-angle bends. New Journal of Physics **10**, 115023 (2008). (cited on pages 43 and 44)

[224] N. I. Landy and W. J. Padilla. Guiding light with conformal transformations. Optics express **17**, 14872 (2009). (cited on p. 47)

[225] Z. L. Mei and T. J. Cui. Arbitrary bending of electromagnetic waves using isotropic materials. Journal of Applied Physics **105**, 104913 (2009). (cited on p. 47)

[226] Knupp, P and Steinberg, S. *Fundamentals of Grid Generation* (CRC Press, Boca Raton, FL, 1994), first edition. (cited on pages 48 and 177)

[227] Farrashkhalvat, M and Miles, J P. *Basic Structured Grid Generation* (Eselvier, Amsterdam, 2003), first edition. (cited on pages 48 and 177)

[228] Z. Chang, X. Zhou, J. Hu, and G. Hu. Design method for quasi-isotropic transformation materials based on inverse Laplace's equation with sliding boundaries. Optics express **18**, 6089 (2010). (cited on p. 48)

[229] J. Hu, X. Zhou, and G. Hu. Nonsingular two dimensional cloak of arbitrary shape.

Applied Physics Letters **95**, 011107 (2009). (cited on p. 48)

[230] C. F. Bohren and D. R. Huffman. *Absorption and scattering of light by small particles* (John Wiley and Sons, 1983). (cited on p. 67)

[231] A. García-Etxarri, R. Gómez-Medina, L. S. Froufe-Pérez, C. López, L. Chantada, F. Scheffold, J. Aizpurua, M. Nieto-Vesperinas, and J. J. Sáenz. Strong magnetic response of submicron silicon particles in the infrared. Optics express **19**, 4815 (2011). (cited on p. 73)

[232] A. I. Kuznetsov, A. E. Miroshnichenko, Y. H. Fu, J. Zhang, and B. Luk'yanchuk. Magnetic light. Scientific reports **2**, 492 (2012). (cited on p. 73)

[233] J. D. Dyson. The Equiangular Spiral Antenna. IEEE Transactions on antennas and propagation **2**, 181 (1959). (cited on p. 76)

[234] J. A. Kaiser. The Archimedean Two-Wire Spiral Antenna. IEEE Transactions on antennas and propagation **8**, 312 (1960). (cited on p. 76)

[235] C. A. Balanis. *Antenna Theory: Analysis and Design* (Wiley-Interscience, 2005), 3rd edition. (cited on p. 76)

[236] J. Baena, R. Marqués, F. Medina, and J. Martel. Artificial magnetic metamaterial design by using spiral resonators. Physical Review B **69**, 014402 (2004). (cited on p. 76)

[237] F. Bilotti, A. Toscano, and L. Vegni. Design of Spiral and Multiple Split-Ring Resonators for the Realization of Miniaturized Metamaterial Samples. IEEE Transactions on Antennas and Propagation **55**, 2258 (2007). (cited on p. 76)

[238] M. A. Ordal, L. L. Long, R. J. Bell, S. E. Bell, R. R. Bell, R. W. Alexander, and C. A. Ward. Optical properties of the metals Al, Co, Cu, Au, Fe, Pb, Ni, Pd, Pt, Ag, Ti, and W in the infrared and far infrared. Applied Optics **22**, 1099 (1983). (cited on pages 79, 80, 179, and 180)

[239] CST. *Microwave Studio*. (cited on p. 82)

[240] N. Yu, P. Genevet, M. A. Kats, F. Aieta, J.-P. Tetienne, F. Capasso, and Z. Gaburro. Light propagation with phase discontinuities: generalized laws of reflection and refraction. Science (New York) **334**, 333 (2011). (cited on p. 83)

[241] J. D. Joannopoulos, S. G. Johnson, J. N. Winn, and R. D. Meade. *Photonic Crystals: Molding the Flow of Light (Second Edition)* (Princeton University Press, 2008), 2

edition. (cited on p. 85)

[242] K. Wang, E. Schonbrun, and K. B. Crozier. Propulsion of gold nanoparticles with surface plasmon polaritons: evidence of enhanced optical force from near-field coupling between gold particle and gold film. Nano letters **9**, 2623 (2009). (cited on p. 89)

[243] A. Cuche, B. Stein, A. Canaguier-Durand, E. Devaux, C. Genet, and T. W. Ebbesen. Brownian motion in a designer force field: dynamical effects of negative refraction on nanoparticles. Nano letters **12**, 4329 (2012). (cited on p. 89)

[244] A. Einstein. Investigations on the theory of the brownian movement. Ann Phys **17**, 549 (1905). (cited on p. 89)

[245] R. P. Feynmann, R. B. Leighton, and M. Sands. *Feynmann Lectures in Physics* (Addison-wesley, Reading, 1966). (cited on p. 89)

[246] P. Reimann. Brownian motors: noisy transport far from equilibrium. Physics Reports **361**, 57 (2002). (cited on p. 89)

[247] P. Hänggi and F. Marchesoni. Artificial Brownian motors: Controlling transport on the nanoscale. Reviews of Modern Physics **81**, 387 (2009). (cited on p. 90)

[248] M. Takano, T. P. Terada, and M. Sasai. Unidirectional Brownian motion observed in an in silico single molecule experiment of an actomyosin motor. Proceedings of the National Academy of Sciences **107**, 7769 (2010). (cited on p. 90)

[249] J. Rousselet, L. Salome, A. Ajdari, and J. Prost. Directional motion of brownian particles induced by a periodic asymmetric potential. Nature **370**, 446 (1994). (cited on p. 90)

[250] L. P. Faucheux, L. S. Bourdieu, P. D. Kaplan, and A. J. Libchaber. Optical thermal ratchet. Physical Review Letters **74**, 7 (1995). (cited on pages 90 and 104)

[251] R. D. Astumian. Thermodynamics and Kinetics of a Brownian Motor. Science **276**, 917 (1997). (cited on p. 90)

[252] J. S. Bader, R. W. Hammond, S. A. Henck, M. W. Deem, G. A. McDermott, J. M. Bustillo, J. W. Simpson, G. T. Mulhern, and J. M. Rothberg. DNA transport by a micromachined Brownian ratchet device. Proceedings of the National Academy of Sciences **96**, 13165 (1999). (cited on p. 90)

[253] A. van Oudenaarden. Brownian Ratchets: Molecular Separations in Lipid Bilayers

Supported on Patterned Arrays. Science **285**, 1046 (1999). (cited on p. 90)

[254] A. Ros, R. Eichhorn, J. Regtmeier, T. Tu Duong, P. Reimann, and D. Anselmetti. Absolute negative particle mobility. Nature **436**, 928 (2005). (cited on p. 90)

[255] I. Zapata, S. Albaladejo, J. Parrondo, J. J. Sáenz, and F. Sols. Deterministic Ratchet from Stationary Light Fields. Physical Review Letters **103**, 130601 (2009). (cited on p. 90)

[256] R. Di Leonardo, L. Angelani, D. Dell'arciprete, G. Ruocco, V. Iebba, S. Schippa, M. P. Conte, F. Mecarini, F. De Angelis, and E. Di Fabrizio. Bacterial ratchet motors. Proceedings of the National Academy of Sciences **107**, 9541 (2010). (cited on p. 90)

[257] A. Song, A. Lorke, A. Kriele, J. Kotthaus, W. Wegscheider, and M. Bichler. Nonlinear Electron Transport in an Asymmetric Microjunction: A Ballistic Rectifier. Physical Review Letters **80**, 3831 (1998). (cited on p. 90)

[258] H. Linke, T. E. Humphrey, A. Löfgren, A. O. Sushkov, R. Newbury, R. P. Taylor, and P. Omling. Experimental Tunneling Ratchets. Science **286**, 2314 (1999). (cited on p. 90)

[259] J. E. Villegas, S. Savel'ev, F. Nori, E. M. Gonzalez, J. V. Anguita, R. García, and J. L. Vicent. A superconducting reversible rectifier that controls the motion of magnetic flux quanta. Science (New York) **302**, 1188 (2003). (cited on p. 90)

[260] V. Khrapai, S. Ludwig, J. Kotthaus, H. Tranitz, and W. Wegscheider. Double-Dot Quantum Ratchet Driven by an Independently Biased Quantum Point Contact. Physical Review Letters **97**, 176803 (2006). (cited on p. 90)

[261] M. V. Costache and S. O. Valenzuela. Experimental spin ratchet. Science (New York) **330**, 1645 (2010). (cited on p. 90)

[262] S. Zhang, Z. Ye, Y. Wang, Y. Park, G. Bartal, M. Mrejen, X. Yin, and X. Zhang. Anti-Hermitian Plasmon Coupling of an Array of Gold Thin-Film Antennas for Controlling Light at the Nanoscale. Physical Review Letters **109**, 193902 (2012). (cited on p. 92)

[263] D. Frenkel and B. Smit. *Understanding Molecular Simulation, Second Edition: From Algorithms to Applications (Computational Science)* (Academic Press, 2001), second edition. (cited on pages 100 and 102)

[264] P. Langevin. Sur la théorie du mouvement brownien. C. R. Acad. Sci. Paris **146**, 530

(1908). (cited on p. 101)

[265] G. Baffou and R. Quidant. Thermo-plasmonics: using metallic nanostructures as nano-sources of heat. Laser & Photonics Reviews **7**, 171 (2013). (cited on p. 107)

[266] K. Wang, E. Schonbrun, P. Steinvurzel, and K. B. Crozier. Trapping and rotating nanoparticles using a plasmonic nano-tweezer with an integrated heat sink. Nature communications **2**, 469 (2011). (cited on p. 107)

[267] H.-P. Breuer and F. Petruccione. *The Theory of Open Quantum Systems* (Oxford, 2002). (cited on pages 112, 135, and 136)

[268] B. Huttner and S. M. Barnett. Quantization of the electromagnetic field in dielectrics. Physical Review A **46** (1992). (cited on p. 113)

[269] T. Gruner and D. Welsch. Green-function approach to the radiation-field quantization for homogeneous and inhomogeneous Kramers-Kronig dielectrics. Physical review. A **53**, 1818 (1996). (cited on p. 113)

[270] S. Scheel and S. Y. Buhmann. Macroscopic quantum electrodynamics. Concepts and applications. Acta Physica Slovaca **58**, 675 (2008). (cited on pages 113 and 116)

[271] E. Hwang, S. Adam, and S. Sarma. Carrier Transport in Two-Dimensional Graphene Layers. Physical Review Letters **98**, 186806 (2007). (cited on p. 127)

[272] C. A. Marocico and J. Knoester. Effect of surface-plasmon polaritons on spontaneous emission and intermolecular energy-transfer rates in multilayered geometries. Physical Review A **84**, 053824 (2011). (cited on p. 128)

[273] E. Castanié, M. Boffety, and R. Carminati. Fluorescence quenching by a metal nanoparticle in the extreme near-field regime. Optics Letters **35**, 291 (2010). (cited on pages 132 and 135)

[274] J. Wilkie and Y. M. Wong. A linearly scaling grid method for generalized Langevin and other integrodifferential equations. Journal of Physics A: Mathematical and Theoretical **41**, 335005 (2008). (cited on p. 133)

[275] A. Faraon, C. Santori, Z. Huang, V. M. Acosta, and R. G. Beausoleil. Coupling of Nitrogen-Vacancy Centers to Photonic Crystal Cavities in Monocrystalline Diamond. Physical Review Letters **109**, 033604 (2012). (cited on p. 134)

[276] H. Fidder, J. Knoester, and D. A. Wiersma. Superradiant emission and optical

dephasing in J-aggregates. Chemical Physical Letters **171**, 529 (1990). (cited on pages 134, 150, 156, and 157)

[277] P. Bharadwaj and L. Novotny. Spectral dependence of single molecule fluorescence enhancement. Optics express **15**, 14266 (2007). (cited on p. 135)

[278] F. Laussy, E. del Valle, and C. Tejedor. Strong Coupling of Quantum Dots in Microcavities. Physical Review Letters **101**, 083601 (2008). (cited on pages 136, 157, and 158)

[279] A. González-Tudela, E. del Valle, E. Cancellieri, C. Tejedor, D. Sanvitto, and F. P. Laussy. Effect of pure dephasing on the Jaynes-Cummings nonlinearities. Optics express **18**, 7002 (2010). (cited on p. 138)

[280] H. Dung, L. Knöll, and D.-G. Welsch. Resonant dipole-dipole interaction in the presence of dispersing and absorbing surroundings. Physical Review A **66**, 063810 (2002). (cited on p. 139)

[281] A. Y. Nikitin, F. Guinea, F. J. García-Vidal, and L. Martín-Moreno. Edge and waveguide terahertz surface plasmon modes in graphene microribbons. Physical Review B **84**, 161407 (2011). (cited on p. 145)

[282] S. Thongrattanasiri, A. Manjavacas, and F. J. García de Abajo. Quantum Finite-Size Effects in Graphene Plasmons. ACS nano **6**, 1766 (2012). (cited on p. 145)

[283] M. Tame, C. Lee, J. Lee, D. Ballester, M. Paternostro, a. Zayats, and M. Kim. Single-Photon Excitation of Surface Plasmon Polaritons. Physical Review Letters **101**, 190504 (2008). (cited on p. 150)

[284] A. Archambault, F. Marquier, J.-J. Greffet, and C. Arnold. Quantum theory of spontaneous and stimulated emission of surface plasmons. Physical Review B **82**, 035411 (2010). (cited on p. 150)

[285] T. Holstein and H. Primakoff. Field dependence of the intrinsic domain magnetization of a ferromagnet. Physical Review **58**, 1098 (1940). (cited on p. 152)

[286] H. Carmichael. *Statistical Methods in Quantum Optics I* (Springer, 1999). (cited on p. 154)

[287] R. Loudon. *The quantum theory of light* (Oxford Science Publications, 2000), 3 edition. (cited on p. 157)

[288] W. P. Ambrose, P. M. Goodwin, J. C. Martin, and R. A. Keller. Alterations of single molecule fluorescence lifetimes in near-field optical microscopy. Science (New York) **265**, 364 (1994). (cited on p. 158)

[289] C. Ciuti, P. Schwendimann, B. Deveaud, and A. Quattropani. Theory of the angle-resonant polariton amplifier. Physical Review B **62**, R4825 (2000). (cited on p. 159)

[290] C. Ciuti, P. Schwendimann, and A. Quattropani. Parametric luminescence of microcavity polaritons. Physical Review B **63**, 041303 (2001). (cited on p. 160)

[291] A. Verger, C. Ciuti, and I. Carusotto. Polariton quantum blockade in a photonic dot. Physical Review B **73**, 193306 (2006). (cited on p. 160)

[292] L. Novotny. Strong coupling, energy splitting, and level crossings: A classical perspective. American Journal of Physics **78**, 1199 (2010). (cited on p. 163)

[293] Y. Zhu, D. J. Gauthier, S. E. Morin, Q. Wu, H. J. Carmichael, and T. W. Mossberg. Vacuum Rabi Splitting as a feature of linear-dispersion theory: analysis and experimental observations. Physical Review Letters **64**, 2499 (1990). (cited on p. 163)

[294] M. Born and E. Wolf. *Principles of Optics* (Cambridge University Press, 1999), 7 edition. (cited on p. 164)

[295] A. Salomon, R. J. Gordon, Y. Prior, T. Seideman, and M. Sukharev. Strong Coupling between Molecular Excited States and Surface Plasmon Modes of a Slit Array in a Thin Metal Film. Physical Review Letters **109**, 073002 (2012). (cited on p. 165)

List of Figures

List of Tables

List of publications

Publications related to the content of this Thesis:

1. *Transformation optics for plasmonics.* **P. A. Huidobro**, M. L. Nesterov, L. Martín-Moreno, and F.J. García-Vidal. Nano Letters, 10(6), 1985-90 (2010).
   Highlighted in *Nanoscale optics: Plasmonics gets transformed.* Nature nanotechnology, 5(7), 485 (2010).

2. *Moulding the flow of surface plasmons using conformal and quasiconformal mappings.* **P.A. Huidobro**, M.L. Nesterov, L. Martín-Moreno, and F.J. García-Vidal. New Journal of Physics, 13(3), 033011 (2011).

3. *Superradiance mediated by graphene surface plasmons.* **P.A. Huidobro**, A.Y. Nikitin, C. González-Ballestero, L. Martín-Moreno, and F.J. García-Vidal. Physical Review B, 85(15), 155438 (2012).

4. *Transformation plasmonics.* M. Kadic, S. Guenneau, S. Enoch, **P.A. Huidobro**, L. Martín-Moreno, F.J. García-Vidal., J. Renger and R. Quidant. Nanophotonics, 1(1), 51-64 (2012).

5. *Theory of Strong Coupling between Quantum Emitters and Propagating Surface Plasmons.* A. González-Tudela, **P.A. Huidobro**, L. Martín-Moreno, C. Tejedor and F.J. García-Vidal. Physical Review Letters, 110(12), 126801 (2013).

6. *Plasmonic Brownian Ratchet* **P.A. Huidobro**, S. Ota, X. Yang, X. Yin, F.J. Garcia-Vídal and X. Zhang. Physical Review B (Rapid Communications) 88(20) 201401(R) (2013).
   Highlighted as Editor's Suggestion.

7. *Magnetic Localized Surface Plasmons* **P.A. Huidobro**, X. Shen, J. Cuerda, E. Moreno, L. Martín-Moreno, F.J. García-Vidal, T.J. Cui and J.B. Pendry. Submitted (2013).

8. *Reversible dynamics of single quantum emitters near metal-dielectric interfaces* A. González-Tudela, **P.A. Huidobro**, L. Martín-Moreno, C. Tejedor and F.J. García-Vidal. Submitted (2013).

Other publications:

9. *Confining and slowing airborne sound with a corrugated metawire.* J. Christensen, **P.A. Huidobro**, L. Martín-Moreno, and F.J. García-Vidal. Applied Physics Letters, 93(8), 083502 (2008).

10. *Emergence of Anderson localization in plasmonic waveguides.* F. Rüting, **P.A. Huidobro**, and F.J. García-Vidal. Optics letters, 36(22), 4341-3 (2011).

Book Chapters:

11. *Quantum Plasmonics.* D. Martín-Cano, **P.A. Huidobro**, E-Moreno, and F.J. García-Vidal. In *Modern Plasmonics,* Eselvier, (2014).